Physics Area - PhD course in Theoretical Particle Physics

SISSA, Trieste

Present and future tools for testing the Standard Model and beyond

Supervisor:
David Marzocca

Candidate:
Francesco Garosi

ACADEMIC YEAR 2023/2024

Acknowledgments

Voglio iniziare ringraziando le due persone più importanti: i miei genitori Carlo e Paola. Mi hanno sempre supportato e incoraggiato ad andare avanti: non so dove sarei ora senza di voi. Grazie anche a tutto il resto della mia famiglia, in particolare ai miei cugini Lorenzo e Serena e a mio zio Fausto, per aver sempre condiviso con me i momenti importanti. Grazie a tutti voi i miei rientri a Venturina sono sempre fantastici. Un pensiero speciale ai miei nonni, che purtroppo ho perso durante questi 4 anni: grazie per tutto il supporto e la gioia che mostravate per i miei risultati, il vostro ricordo mi spinge a continuare sulla strada che ho scelto.

Passando alla Fisica, devo cominciare dal mio supervisor, David Marzocca: grazie per la tua guida e per la tua pazienza e per avermi insegnato moltissimo durante gli ultimi tre anni. Un ringraziamento anche a tutto il gruppo di TPP, in particolare ad Aleksandr Azatov, Matteo Bertolini, Andrea Romanino e Marco Serone per i bellissimi corsi del primo anno. Ringrazio Andrea Wulzer e tutto il gruppo teorico dell'IFAE di Barcellona, per avermi ospitato per tre mesi. Lì ho imparato moltissimo e ho avuto modo di scoprire una città meravigliosa. Un grazie anche ai dottorandi e PostDoc che hanno collaborato con me: Marco Cardinali, Alfredo Stanzione, Antonio Rodriguez-Sanchez e Sokratis Trifinopoulos. Un ringraziamento anche a Dario Buttazzo, Jorge de Blas, Roberto Franceschini e Fabio Maltoni per aver accettato di essere i membri esterni della commissione per la mia discussione. Infine grazie a Massimo d'Elia, il mio relatore per entrambe le tesi di laurea, per la gentilezza e la guida fondamentale nella scrittura del mio primo paper, e a Franca Berghi, la mia professoressa del liceo: se ho deciso di studiare Fisica è anche merito suo.

Devo poi ringraziare tutti i fantastici amici che ho conosciuto durante questi 4 anni: grazie per aver reso migliore la vita in SISSA e fuori. Inizio con i fantastici "Freschi di Zona" dell'ufficio 431: grazie di cuore all'Armochromogirl Fabiana, a Bubbleman Giulio e a Mr. Alla Doc Saman per aver reso l'ufficio una famiglia, per le incredibili cene 431 e per la nascita della Barmacia, che ormai è diventata il nostro bar preferito. Grazie a Cristiano e Delpo per le partite a tennis e a Samuele, Valentina e Vania per i mitici sfoglini. Grazie ad Andrea, Cristoforo, Daniele, Davide, Diego 1, Diego 2, Frago, Giuà, Giovanni, Jacopo, Mavi, Max e Stephane per i pranzi, le cene, le giornate a Barcola e le gite fuori Trieste. Un ringraziamento anche agli amici conosciuti a Barcellona, per avermi subito incluso nel gruppo e avermi fatto trovare la stessa atmosfera che c'è in SISSA: Angel Gil Muyor, M.

Herrero-Valea, Silvia Gasparotto, Francesco Sciotti, Fabio Van Dissel e George Zahariade.

Non posso poi non dire grazie ai miei amici dell'Univerisità, che sono stati importantissimi durante quei cinque anni e lo sono ancora. Ad Antonio e Filippo per essere venuti a Trieste, a Riccardo per avermi fatto conoscere Castelldefels e a Lorenzo per la fantastica organizzazione di NePSi-2023 e per le chiacchierate, anche di Fisica. Grazie a tutti per le rimpatriate, per lo più a Pisa, che spero continuino anche in futuro.

Dulcis in fundo, i miei amici del liceo: è sempre una gioia rivedervi quando torno a casa. Grazie a Lisa e Mirco per i capodanni da voi, a Letizia per le perle di Paolo e Sofia, a Eleonora per i Lucca Comics, a Leonardo per pensare sempre a tutti noi ed averci dato molte occasioni di rivederci, e poi a Luca, Martina, Riccardo e Simone. Infine un grazie speciale ai "Fratelli di Venturina" Alessio e Giovanni: per le partite ad Age of the Rings e a Catan, le mangiate e le costanti chiacchierate.

Abstract

Despite its incredible success in describing physics in a wide range of energies up to the electroweak (EW) scale, the Standard Model (SM) cannot explain many observed phenomena, such as the presence of dark matter, the matter-antimatter asymmetry or neutrino masses. Furthermore, theoretical issues like the Higgs hierarchy or the flavor problem suggest the existence of physic beyond the Standard Model (BSM). Therefore a huge effort has been dedicated to the formulation of BSM models capable of explaining such deviations, and at the same time to the analysis of their signatures at present and future experiments, to constrain the options and to find ways to potentially discover new physics.

The first part of this thesis is mainly related to muon colliders (MuC), which represent one of the most promising option to explore the high-energy frontier. These machines, operating at the TeV scale, can test short-distance physics with the potential of discovering new particles, reaching at the same time high precision in the measurement of EW observables. We present one of the main novelties in the analysis of TeV-scale EW processes at lepton colliders, i.e. the partonic description of lepton collisions. This allows to systematically study processes involving collinear initial state radiation (ISR), whose cross sections dominate over those for lepton annihilation at high energies. We show the calculation of the parton distribution functions (PDFs) and discuss their features, with explicit applications to MuC processes. In particular, the impact of the muon neutrino PDF is studied and compared with the expected experimental precision of muon colliders. We also consider signatures relevant for $B-$meson decays, exploring the potential of MuC to discover new physics in some benchmark models. The latter analysis is extended to the complementary hadronic proposal, namely FCC-hh, and a comparison between the prospects at the two machines is presented.

The second part of the thesis focuses instead on the use of present measurements of a large set of low-energy observables to constrain new physics in a model-independent way, within the framework of the Standard Model Effective Field Theory (SMEFT). Bounds on Wilson coefficients of top-quark operators are derived through a global analysis, and implications for explicit new physics models are discussed.

Declaration

I hereby declare that, except where specific reference is made to the work of others, the contents of this thesis are original and have not been submitted in whole or in part for consideration for any other degree or qualification in this or any other university.

The discussion is based on the following works:

1. A. Azatov, F. Garosi, A. Greljo, D. Marzocca, J. Salko and S. Trifinopoulos, *New Physics in $b \to s\mu\mu$: FCC-hh or a Muon Collider?*, *JHEP* **10** (2022) 149, arXiv:2205.13552 [hep-ph].

2. F. Garosi, D. Marzocca and S. Trifinopoulos, *LePDF: Standard Model PDFs for High-Energy Lepton Colliders*, *JHEP* **09** (2023) 107, arXiv:2303.16964 [hep-ph].

3. F. Garosi, D. Marzocca, A. Rodriguez-Sanchez and A. Stanzione, *Indirect constraints on top quark operators from a global SMEFT analysis*, *JHEP* **12** (2023) 129, arXiv:2310.00047 [hep-ph].

4. R. Capdevilla, F. Garosi, D. Marzocca, and B. Stechauner, *On the neutrino content of the muon at Muon Colliders*, in preparation.

Contents

Chapter 1

Introduction

At present, the Large Hadron Collider (LHC) at CERN is our only tool for direct exploration of physics at the electroweak scale and above, and the high-luminosity phase is planned to last until the early 2040s. It proved to be a formidable machine for both searches of new heavy particles as well as precision studies at the electroweak scale, of which the Higgs boson discovery by the ATLAS and CMS collaborations [1, 2] is a prime example. The precision Higgs measurements which followed all agree quite well with the Standard Model predictions. In the meantime, the two collaborations have searched for many hypothetical new particles at the energy frontier. This effort was so far unsuccessful, confirming the SM in spite of naturalness arguments that suggested the presence of new physics at (or below) the TeV scale. However, some observed phenomena, like the presence of dark matter, the matter-antimatter asymmetry of the universe or neutrino masses, cannot be explained within the SM, meaning that new physics must be there. Due to the absence of deviations from the SM at the current experiments, to find signatures of BSM physics is therefore necessary to increase the precision and the energy of the experiments. Deviations from the SM may appear in more precise measurements, while the increase of the energy may offer the potential to discover new heavy particles, or at least to exclude their presence. In light of this, discussions about building new colliders are taking place [3], with the 100 TeV future circular hadron collider (FCC-hh) [4–6] as the natural successor of LHC. Nevertheless, the next large-scale experiment in high-energy physics is likely to be a lepton collider. The proposed options include circular or linear electron-positron colliders (FCC-ee [7] and CEPC [8] for the former, ILC [9], CLIC [10] and CCC [11] for the latter) as well as $\mu^+\mu^-$ colliders [12–17]. Among these, the linear e^+e^- colliders and the muon colliders could achieve multi-TeV center-of-mass energies. In particular, muon colliders represent with FCC-hh the most promising option in the energy frontier, while the next generation of EW and Higgs factories will explore the precision frontier, with FCC-ee, ILC, and CLIC as the most promising proposals in this regard.

An interesting feature of lepton colliders is that TeV-scale processes involving vector boson fusion and soft-collinear radiation dominate over lepton annihilation [18]. This is

why it is commonly said that *a muon collider is a vector boson collider*. It turns out that, while leptons are elementary particles in the SM, the process of collinear emission of initial state radiation, with transverse momentum p_T much smaller than the energy of the hard scattering process, can be factorized and a description in terms of parton distribution functions can be introduced, similarly to what is done in the case of proton colliders and the parton content of a proton. A precise calculation of lepton PDFs (LePDFs) is then needed for a proper study of some MuC processes.

Opposite to the high-energy searches, a crucial role is still played by low-energy observables, whose precise determination may constrain the parameter space on new physics scenarios. A model-independent analysis can be performed through the SMEFT, describing the contribution of new physics through the coefficients of higher dimensional operators. Bounds on such coefficients can be derived starting from the experimental measurements, and information on the scale of new physics can be extracted consequently.

The thesis is structured as follows. In Chapter 2 we recall some fundamental concepts that are needed for the rest of the thesis. We start with a review of the Standard Model, focusing on the fermion sector and highlighting the role of the third family. Then we introduce the concept of factorization and PDFs for lepton collisions, showing their role in MuC analyses. We conclude the Chapter with the presentation of the Standard Model Effective Field Theory, of which we review some selected topics, such as 4-fermion operators and the procedure of integrating out heavy fields.

In Chapter 3 we focus on PDFs for lepton colliders, showing our numerical computation, discussing their main features, and comparing them with the results present in the literature. The Chapter ends with the study of the impact of muon neutrino PDF on processes at muon colliders.

Chapter 4 is dedicated to the comparison between MuC and FCC-hh sensitivity to signatures of new physics relevant for $B-$meson decays, showing the potential of new physics discovery of such machines in some benchmark models. Such models were mainly motivated by the $R_{K^{(*)}}$ flavor anomalies present at the time of our work [19, 20], and in December 2022 the LHCb collaboration announced that they were due to experimental systematics [21]. Even though the prospects for the models explicitly addressing the past anomalies are no longer relevant, we show them anyway, since the same strategy may be used in the future if new discrepancies will show up.

Finally in Chapter 5 we derive bounds on Wilson coefficients of top-quark effective operators through a global analysis. We also compare our results with direct LHC bounds and show applications to specific new physics models.

Chapter 2

Fundamentals

2.1 The Standard Model

We start with a brief review of the Standard Model [22–26], in order to introduce all the ingredients we will use and to set the notation. SM is the most general renormalizable gauge theory with gauge group $G_{SM} = SU(3)_c \times SU(2)_L \times U(1)_Y$. We denote the corresponding gauge fields as G_A ($A = \{1, \dots, 8\}$), W_a ($a = \{1, 2, 3\}$) and B. The matter fields with their quantum numbers under G_{SM} are reported in Table 2.1: the fermions f_i, $f = \{q, l, u_R, d_R, e_R\}$ come in three copies, called families, while the Higgs field is a complex scalar.

The SM Lagrangian can be split in pure gauge, fermions, Higgs and Yukawa parts as follows:

$$\begin{aligned}
\mathcal{L}_{SM} &= \mathcal{L}_G + \mathcal{L}_f + \mathcal{L}_H + \mathcal{L}_Y, \\
\mathcal{L}_G &= -\frac{1}{4} G^A_{\mu\nu} G_A^{\mu\nu} - \frac{1}{4} W^a_{\mu\nu} W_a^{\mu\nu} - \frac{1}{4} B_{\mu\nu} B^{\mu\nu}, \\
\mathcal{L}_f &= i \sum_f \bar{f}^i \not{D} f^i, \\
\mathcal{L}_H &= |D_\mu H|^2 - V(H^\dagger H) = |D_\mu H|^2 - \lambda \left(H^\dagger H - \frac{v^2}{2} \right)^2, \\
\mathcal{L}_Y &= -Y^u_{ij} \bar{q}^i u^j_R \widetilde{H} - Y^d_{ij} \bar{q}^i d^j_R H - Y^e_{ij} \bar{l}^i e^j_R H + \text{h.c.},
\end{aligned} \tag{2.1}$$

where the indices i and j label the families of the fermions and we refer to them as flavor indices. The conjugate Higgs field is defined as $\widetilde{H} \equiv \epsilon H^*$.

The potential $V(H^\dagger H)$ has a minimum away from the origin, so H develops a non zero vacuum expectation value (vev) $\langle H \rangle$. We parametrize the vev and the fluctuations H' around it as

$$\langle H \rangle = \begin{pmatrix} 0 \\ \frac{v}{\sqrt{2}} \end{pmatrix}, \qquad H' = \begin{pmatrix} h^+ \\ \frac{h - i h_3}{\sqrt{2}} \end{pmatrix}, \tag{2.2}$$

	Field	$SU(3)_c$	$SU(2)_L$	$U(1)_Y$	Lorentz
Left-handed quark doublets	$q^i = \begin{pmatrix} u_L^i \\ d_L^i \end{pmatrix}$	**3**	**2**	$\frac{1}{6}$	$\left(\frac{1}{2}, 0\right)$
Left-handed lepton doublets	$l^i = \begin{pmatrix} \nu_L^i \\ e_L^i \end{pmatrix}$	**1**	**2**	$-\frac{1}{2}$	$\left(\frac{1}{2}, 0\right)$
Right-handed up quarks	u_R^i	**3**	**1**	$\frac{2}{3}$	$\left(0, \frac{1}{2}\right)$
Right-handed down quarks	d_R^i	**3**	**1**	$-\frac{1}{3}$	$\left(0, \frac{1}{2}\right)$
Right-handed leptons	e_R^i	**1**	**1**	-1	$\left(0, \frac{1}{2}\right)$
Higgs doublet	H	**1**	**2**	$\frac{1}{2}$	$(0, 0)$

Table 2.1: SM matter fields and their quantum numbers. Left-handed up and down quarks form doublets of $SU(2)_L$, as well as neutrinos and left-handed leptons, while right-handed fermions are singlets. i is the flavor index.

with $v = 246\,\text{GeV}$, so that

$$H = \langle H \rangle + H' = \begin{pmatrix} h^+ \\ h_0 \end{pmatrix} = \begin{pmatrix} h^+ \\ \frac{v+h-ih_3}{\sqrt{2}} \end{pmatrix}. \tag{2.3}$$

The covariant derivative D_μ is defined as

$$D_\mu = \partial_\mu - ig_3 G_\mu^A T_A - ig_2 W_\mu^a t_a - ig_1 Y B_\mu, \tag{2.4}$$

where Y is the hypercharge, $T_A = \lambda^A/2$ and $t_a = \sigma^a/2$ are $SU(3)$ and $SU(2)$ generators respectively, while λ^A and σ^a are the Gell-Man and Pauli matrices. $\{g_1, g_2, g_3\}$ are the gauge couplings.

The Higgs vev $\langle H \rangle$ breaks spontaneously $SU(2)_L \times U(1)_Y$ to $U(1)_{\text{em}}$, generated by the electric charge:

$$Q = t_3 + Y. \tag{2.5}$$

2.1.1 Gauge and Higgs sectors

Due to the symmetry breaking, we end up with a massless gauge boson associated to $U(1)_{\text{em}}$, i.e. the photon (A), and three massive ones, of which two are charged ($W^\pm$) and one is neutral (Z). $W^\pm$ are complex combinations of $W_{1,2}$:

$$W_\mu^\pm = \frac{W_\mu^1 \mp iW_\mu^2}{\sqrt{2}}, \tag{2.6}$$

while Z and A are obtained rotating W_3 and B by an angle θ_W, known as the Weinberg angle:

$$\begin{pmatrix} Z_\mu \\ A_\mu \end{pmatrix} = \begin{pmatrix} c_W & -s_W \\ s_W & c_W \end{pmatrix} \begin{pmatrix} W_\mu^3 \\ B_\mu \end{pmatrix}. \tag{2.7}$$

Here we defined

$$c_W = \cos\theta_W = \frac{g_2}{\sqrt{g_1^2+g_2^2}}, \qquad s_W = \sin\theta_W = \frac{g_1}{\sqrt{g_1^2+g_2^2}}. \tag{2.8}$$

In terms of these new fields, the covariant derivative can be written as

$$D_\mu = \partial_\mu - ig_3 G_\mu^A T_A - i\frac{g_2}{\sqrt{2}}(W_\mu^+ t_+ + W_\mu^- t_-) - ieQA_\mu - i\frac{g_2}{c_W}\left(t_3 - Qs_W^2\right) Z_\mu, \tag{2.9}$$

where $t_\pm = t_1 \pm it_2$ and the electromagnetic coupling e is given by

$$e = g_2 s_W = g_1 c_W. \tag{2.10}$$

To shorten the notation, we also define

$$Q^Z = t_3 - Qs_W^2. \tag{2.11}$$

Expanding $|D_\mu H|^2$ we can read the gauge bosons' masses:

$$|D_\mu H|^2 = \frac{g_2^2 v^2}{4} W_\mu^+ W^{\mu-} + \frac{1}{2}\frac{(g_1^2+g_2^2)v^2}{4} Z_\mu Z^\mu + \text{interactions}, \tag{2.12}$$

i.e.

$$m_W^2 = \frac{g_2^2 v^2}{4}, \qquad m_Z^2 = \frac{(g_1^2+g_2^2)v^2}{4} = \frac{m_W^2}{c_W^2}, \qquad m_A^2 = 0. \tag{2.13}$$

Then from the Higgs potential $V(H^\dagger H)$ we obtain the mass of the scalar particles. h is the physical Higgs boson, while $h^\pm$ and h_3 are the Goldstone bosons associated to the breaking:

$$V(H^\dagger H) = \lambda v^2 h^2 + \text{interactions}, \tag{2.14}$$

which means

$$m_h^2 = 2\lambda v^2, \qquad m_{h^\pm}^2 = m_{h_3}^2 = 0. \tag{2.15}$$

Summing up, h is the physical, massive Higgs boson, while $h^\pm$ and h_3 are the Goldstone bosons associated to the breaking. They are eaten up by $W^\pm$ and Z, which acquire mass and longitudinal component. Finally the photon A, the gauge boson associated to the unbroken group $U(1)_{\text{em}}$, remains massless. Note that the $SU(3)_c$ sector is unaffected by the symmetry breaking, being the Higgs field neutral under it, and so the corresponding gauge bosons, called gluons, remain massless. This sector is often studied alone and the resulting theory is called Quantum Chromodynamics (QCD).

The interactions within the gauge and Higgs sectors can be found expanding the SM Lagrangian, including also the gauge fixing terms:

$$\mathcal{L}_{g.f.} = -\frac{1}{2\xi}\sum_V \left(\partial_\mu V^\mu + (g_V \xi H'^\dagger i T \langle H\rangle + \text{h.c.})\right)^2, \tag{2.16}$$

where $V = \{G_A, W_a, B\}$. We do not report here the expanded Lagrangian, see Appendix A.1 for the cubic part.

2.1.2 Fermionic sector

We are left with the fermionic sector. Being it one of the most intriguing pieces of the SM, this time we focus both on the spectrum and the interactions with the Higgs and the gauge bosons. The latter come from $\mathcal{L}_f$:

$$\mathcal{L}_f = \sum_f i\bar{f}\gamma^\mu\partial_\mu f + g_3 G^A_\mu j^\mu_{sA} + eA_\mu j^\mu_{\rm em} + \frac{g_2}{c_W} Z_\mu j^\mu_n + \frac{g_2}{\sqrt{2}}(W^+_\mu j^\mu_- + \text{h.c.}), \tag{2.17}$$

where we introduced the strong, electromagnetic, neutral and charged currents j_s, $j_{\rm em}$, j_n and $j_\pm$, defined as (flavor indices are omitted):

$$\begin{aligned} j^\mu_{sA} &= \bar{u}\gamma^\mu T_A u + \bar{d}\gamma^\mu T_A d, \\ j^\mu_{em} &= \sum_f Q_f \bar{f}\gamma^\mu f, \\ j^\mu_n &= \sum_f Q^Z_f \bar{f}\gamma^\mu f, \\ j^\mu_- &= (j^\mu_+)^\dagger = \bar{u}_L\gamma^\mu d_L + \bar{\nu}_L\gamma^\mu e_L. \end{aligned} \tag{2.18}$$

The mass matrices are obtained from the term of the Yukawa Lagrangian proportional to the Higgs vev

$$\mathcal{L}_Y = -\frac{v}{\sqrt{2}}(Y^u_{ij}\bar{u}^i_L u^j_R + Y^d_{ij}\bar{d}^i_L d^j_R + Y^e_{ij}\bar{e}^i_L e^j_R) + \text{h.c.} + \text{interactions}, \tag{2.19}$$

i.e.

$$m_{ij} = \frac{v}{\sqrt{2}} Y_{ij}. \tag{2.20}$$

To find the mass eigenstates, we diagonalize each Yukawa matrix Y^X, $X = \{u, d, e\}$, with two unitary matrices

$$\begin{aligned} Y^X &= U^{X\dagger}_L Y^X_{\rm diag} U^X_R, \\ Y^u_{\rm diag} &= \text{diag}\,(y_u, y_c, y_t), \\ Y^d_{\rm diag} &= \text{diag}\,(y_d, y_s, y_b), \\ Y^e_{\rm diag} &= \text{diag}\,(y_e, y_\mu, y_\tau), \end{aligned} \tag{2.21}$$

and redefine the fermion fields through the same unitary rotations, which can be performed safely since they leave the kinetic term invariant:

$$\begin{aligned} u'_{L,R} &= U^u_{L,R} u_{L,R}, \\ d'_{L,R} &= U^d_{L,R} d_{L,R}, \\ e'_{L,R} &= U^e_{L,R} e_{L,R}. \end{aligned} \tag{2.22}$$

After the rotations we obtain diagonal Yukawa matrices and so the primed fields are mass eigenstates, with mass

$$m_i = \frac{v}{\sqrt{2}} y_i, \tag{2.23}$$

where y_i are the eigenvalues of the Yukawa matrices, as in Eq. (2.21).

Clearly this redefinition does not affect the strong, electromagnetic and neutral currents, since the matrices U cancel out, and therefore at tree-level there are no flavor-changing processes mediated by a neutral particle at tree-level. Processes of this kind are known as flavor-changing neutral currents (FCNC) and they appear in the SM only at loop-level.

Moving to the charged currents, the leptonic part can be left invariant through a redefinition of the neutrino fields:

$$\nu'_L = U^e_L \nu_L. \tag{2.24}$$

This is possible because in the SM neutrinos are massless and we can use the same rotation for e_L and ν_L. For the quarks we are instead forced to use different matrices and the charged currents are modified as

$$\bar{u}_L \gamma^\mu d_L = \bar{u}'_L \gamma^\mu U^u_L U^{d\dagger}_L d'_L \equiv \bar{u}'_L \gamma^\mu V d'_L, \tag{2.25}$$

where $V = U^u_L U^{d\dagger}_L$ is the Cabibbo-Kobayashi-Maskawa (CKM) matrix [27]. In the rest of this work, if not explicitly stated, we will use diagonal Yukawa matrices and the mass eigenstates, omitting the $'$.

All of this can be seen in terms of global symmetries. Neglecting Yukawa interactions, the SM Lagrangian is invariant under five independent $U(3)$ rotations, acting on each one of the fermionic fields:

$$G_F = U(3)_q \times U(3)_u \times U(3)_d \times U(3)_l \times U(3)_e, \tag{2.26}$$

$$f_i \to f'_i = (U^f)_{ij} f_j. \tag{2.27}$$

Yukawa interactions break this flavor degeneracy inducing a mixing between families. The only residual symmetries are the baryon number $U(1)_B$ and the three individual lepton numbers $U(1)_e \times U(1)_\mu \times U(1)_\tau$. We see that Eqs. (2.22) and (2.24) look like G_F transformations, except for the fact that u_L and d_L rotations are different, with the appearance of the CKM matrix in the quark charged currents. Using only G_F transformations we can just choose a flavor basis in which only one of the Yukawa matrices $Y^{u,d}$ is diagonal:

$$Y^u = \mathrm{diag}\,(y_u, y_c, y_t)\,, \qquad Y^d = V\,\mathrm{diag}\,(y_d, y_s, y_b)\,, \tag{2.28}$$

$$Y^u = V^\dagger \mathrm{diag}\,(y_u, y_c, y_t)\,, \qquad Y^d = \mathrm{diag}\,(y_d, y_s, y_b)\,. \tag{2.29}$$

We refer to the two options as up-quark and down-quark basis respectively. Note that in the absence of Yukawa interactions V is just the identity and no mixing occurs.

2.1.3 Flavor problem

From the discussion above, we end up with 13 flavor parameters: the 9 fermion masses and the 4 parameters of the CKM matrix, that being unitary is characterized by 3 angles

and a phase. These parameters show a huge hierarchy. For the most recent experimental values, we refer to the Review of Particle Physics 2024 by the Particle Data Group collaboration [28] and the references therein. Using Eq. (2.23) and the measured masses, we obtain the following values for the Yukawa couplings:

$$\begin{aligned}(y_u, y_c, y_t) &\approx \left(10^{-5}, 7\times 10^{-3}, 1\right),\\ (y_d, y_s, y_b) &\approx \left(3\times 10^{-5}, 5\times 10^{-4}, 2.4\times 10^{-2}\right),\\ (y_e, y_\mu, y_\tau) &\approx \left(3\times 10^{-6}, 6\times 10^{-4}, 10^{-2}\right).\end{aligned} \tag{2.30}$$

For the CKM, it is convenient to use the Wolfenstein parametrisation:

$$V = \begin{pmatrix} V_{ud} & V_{us} & V_{ub} \\ V_{cd} & V_{cs} & V_{cb} \\ V_{td} & V_{ts} & V_{tb} \end{pmatrix} = \begin{pmatrix} 1-\frac{\lambda^2}{2} & \lambda & A\lambda^3(\bar\rho - i\bar\eta) \\ -\lambda & 1-\frac{\lambda^2}{2} & A\lambda^2 \\ A\lambda^3(1-\bar\rho - i\bar\eta) & -A\lambda^2 & 1 \end{pmatrix} + \mathcal{O}(\lambda^4), \tag{2.31}$$

where the parameters take the following values:

$$\begin{aligned}\lambda &= 0.22501 \pm 0.00068,\\ A &= 0.826^{+0.016}_{-0.015},\\ \bar\rho &= 0.1591 \pm 0.0094,\\ \bar\eta &= 0.3523^{+0.0073}_{-0.0071}.\end{aligned} \tag{2.32}$$

λ is related to the Cabibbo angle θ_C describing the mixing between the first two generations: $\lambda = \sin\theta_C$. The most precise determination of this parameter comes from nuclear beta decays (i.e. through the determination of $V_{ud} \sim \cos\theta_C$), but it shows some tensions with the other measurements. These tensions are known as Cabibbo angle anomalies, see for instance [29] for a quick review and possible explanations.

Back to the Yukawas, we see from Eq. (2.30) that the third family is always much heavier than the first two. Clearly the same holds in other bases: for instance in the down-quark basis of Eq. (2.29), where Y^d is diagonal, Y^u takes the following form (in modulus):

$$Y^u \approx \begin{pmatrix} 10^{-5} & 2\times 10^{-3} & 9\times 10^{-3} \\ 3\times 10^{-6} & 7\times 10^{-3} & 4\times 10^{-2} \\ 5\times 10^{-8} & 3\times 10^{-4} & 1 \end{pmatrix} \tag{2.33}$$

We see that the 2×2 block corresponding to the first two families contains negligible values with respect to the $\mathcal{O}(1)$ top Yukawa. This pattern of parameters does not look accidental and in particular we observe an approximate $U(2)^5$ symmetry, under which the first two families transform as a doublet and the third one is a singlet. All of this leads to the so called SM flavor problem, hinting at a deeper explanation of the observed structures. For instance we may think of new physics models that respect the approximate $U(2)^5$ symmetry [30–32]. We will see some examples of this kind in Chapter 4.

2.1.4 Running couplings

We conclude this short SM review with the running couplings. Due to renormalization the coupling constants acquire a dependence on the energy scale Q, encoded in the beta functions:

$$\beta(\alpha_x) \equiv Q\frac{d\alpha_x}{dQ} = -\beta_0\alpha_x^2 + \mathcal{O}(\alpha_x^3), \tag{2.34}$$

where we explicitly wrote only the one-loop coefficient β_0 and α_x is defined as

$$\alpha_x = \frac{g_x^2}{4\pi}, \tag{2.35}$$

where g_x is a coupling constant. In the SM gauge sector, $g_x = \{g_1, g_2, g_3, e\}$.

For a $SU(N)$ gauge theory with n_s scalar fields and n_f chiral fermions in the fundamental representation, as the $SU(3)_c$ and $SU(2)_L$ sectors of the SM, β_0 is given by

$$\beta_0^{SU(N)} = \frac{1}{6\pi}\left(11N - n_f - \frac{n_s}{2}\right), \tag{2.36}$$

while in case of a $U(1)$ theory it becomes

$$\beta_0^{U(1)} = -\frac{1}{6\pi}\left(2\sum_f Q_f^2 + \sum_s Q_s^2\right), \tag{2.37}$$

where f runs over the chiral fermions, s over the scalars and $Q_{f,s}$ is the corresponding electric charge. Integrating Eq. (2.34) starting from the scale Q_0 one gets the one-loop running of the couplings:

$$\alpha^{(1)}(Q) = \frac{\alpha(Q_0)}{1 + \beta_0\alpha(Q_0)\ln(\frac{Q}{Q_0})}. \tag{2.38}$$

For the three SM couplings, applying Eqs. (2.36) and (2.37), we obtain that the one-loop coefficients of the beta functions are

$$\beta_0^{U(1)_Y} = -\frac{41}{12\pi}, \qquad \beta_0^{SU(2)_L} = \frac{19}{12\pi}, \qquad \beta_0^{SU(3)_c} = \frac{7}{2\pi}. \tag{2.39}$$

For the Yukawa couplings the running is different, since it receives contributions also from QCD. Focusing on the top Yukawa and defining $\alpha_y = y_t^2/4\pi$, its renormalization group equation (RGE) is [33]

$$Q\frac{d\alpha_y}{dt} = \beta_y\alpha_y^2 - \beta_s\alpha_y\alpha_3, \tag{2.40}$$

with $\beta_y = 9/4\pi$ and $\beta_s = 4/\pi$. The one-loop solution of this equation is

$$\alpha_y(Q) = \left(\frac{9}{2\alpha_3(Q)} - \left[\frac{9}{2\alpha_3(Q_0)} - \frac{1}{\alpha_y(Q_0)}\right]\left(\frac{\alpha_3(Q_0)}{\alpha_3(Q)}\right)^{8/7}\right)^{-1}. \tag{2.41}$$

We report in Table 2.2 the numerical boundary conditions $\alpha(Q_0)$ at $Q = 200$ GeV, as in [34].

Parameter	α_3	α_2	α_1	α_{y_t}
Value	0.1057	0.03329	0.01025	0.0679

Table 2.2: Numerical inputs for the SM parameters at a scale $Q = 200$ GeV from [34].

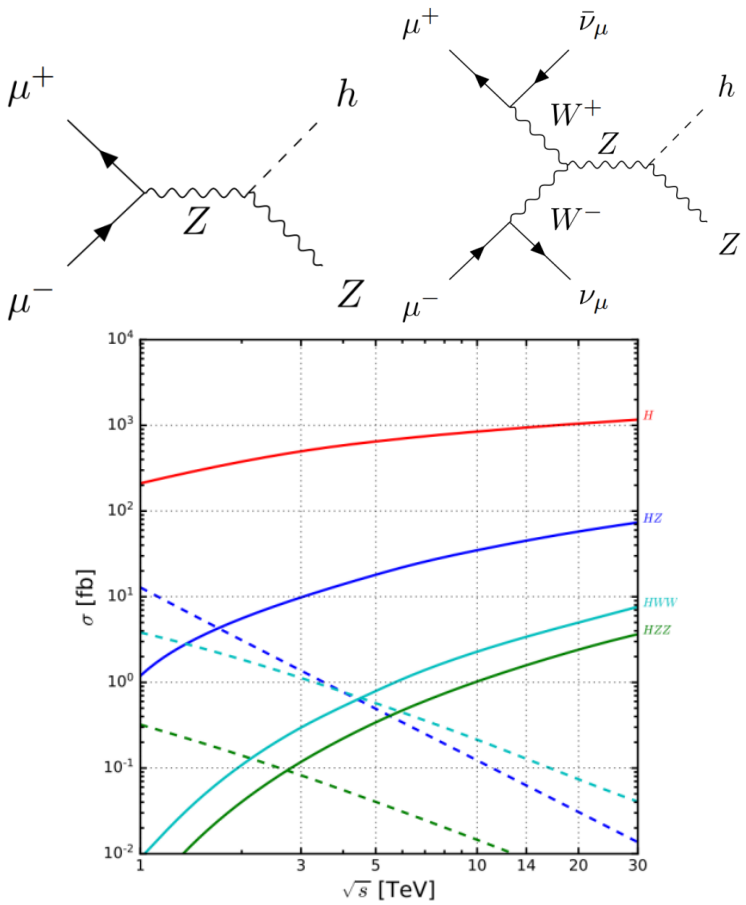

Figure 2.1: Example of typical annihilation (upper-left) and vector boson fusion (upper right) processes at MuC and their cross sections [18] (bottom).

2.2 Factorization for high-energy lepton colliders

In this Section we recall the basics of factorization, introducing the concepts of splitting functions and DGLAP equations that will be used in the rest of this thesis. This formalism has a direct application to high-energy lepton colliders, since TeV-scale processes involving vector boson fusion (VBF) and ISR dominate over lepton annihilation, as shown in Figure 2.1.

2.2.1 Derivation of the DGLAP equations

The case of collinear photon emission from an electron is known since almost a century and at leading order can be described using the effective photon approximation (EPA)[35–38]

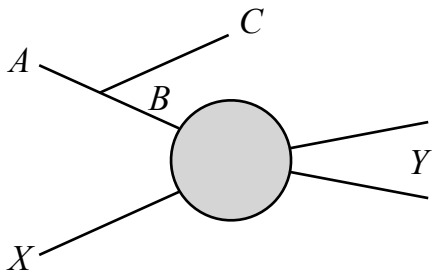

Figure 2.2: Diagram of a process $AX \to CY$ with an initial-state splitting $A \to BC$.

with a photon PDF given by

$$f_\gamma^{\mathrm{EPA}}(x) = \frac{\alpha_\gamma}{2\pi} P_{\gamma e}(x) \log \frac{E^2}{m_e^2} \,, \tag{2.42}$$

where E is the energy of the initial electron and $P_{\gamma e}(x) = \frac{1+(1-x)^2}{x}$ is the splitting function, that describes the probability of an electron to emit a photon with a fraction x of its energy and virtuality $-p_T^2/(1-x)$.

When $E \gg m_e$ the large logarithms can be resummed in order to improve the perturbative expansion, and the factorization scale Q is introduced. Invariance of the physics under the factorization scale leads to the DGLAP equations [39–41]. We show a simple derivation in what follows.

Consider a generic parton-level splitting $A \to B + C$ followed by the hard scattering $B + X \to Y$, as in Figure 2.2. Defining z as the fraction of the energy of A carried by B, the kinematics, up to quadratic order in the transverse momentum p_T, is the following:

$$p_A^\mu = \left(E_A, 0, 0, \sqrt{E_A^2 - m_A^2} \right) , \tag{2.43}$$

$$p_B^\mu = \left(zE_A, p_T, 0, \sqrt{E_A^2 - m_A^2} - \sqrt{\bar{z}^2 E_A^2 - m_C^2} + \frac{p_T^2}{2\sqrt{\bar{z}^2 E_A^2 - m_C^2}} \right) , \tag{2.44}$$

$$p_C^\mu = \left(\bar{z}E_A, -p_T, 0, \sqrt{\bar{z}^2 E_A^2 - m_C^2} - \frac{p_T^2}{2\sqrt{\bar{z}^2 E_A^2 - m_C^2}} \right) , \tag{2.45}$$

where $\bar{z} \equiv 1 - z$. In this way, neglecting $\mathcal{O}(p_T^4)$ terms, the emitted particle C is correctly on-shell ($p_C^2 = m_C^2$), while for the particle B we have

$$p_B^2 = m_A^2 + m_C^2 - 2\bar{z}E_A^2 + 2\sqrt{(E_A^2 - m_A^2)(\bar{z}^2 E_A^2 - m_C^2)} - \sqrt{\frac{(E_A^2 - m_A^2)}{(\bar{z}^2 E_A^2 - m_C^2)}} p_T^2. \tag{2.46}$$

Since we are working with high-energy initial beams, we can expand p_B^2 neglecting terms of order m/E and p_T/E or higher, so that we obtain for the virtuality of the particle B

$$m_B^2 - p_B^2 = \frac{1}{\bar{z}}(p_T^2 + zm_C^2 + \bar{z}m_B^2 - z\bar{z}m_A^2) + \mathcal{O}\left(\frac{m^2}{E^2}, \frac{p_T^2}{E^2} \right) \equiv \frac{\widetilde{p}_T^2}{\bar{z}} \,. \tag{2.47}$$

The cross section of the process $A + X \to C + Y$ is given by

$$d\sigma_{AX\to CY} = \frac{(2\pi)^4\delta^{(4)}(p + p_X - k - p_Y)}{\Phi_{in} 4E_A E_X}|\mathcal{M}_{A+X\to C+Y}|^2 \frac{d^3k}{(2\pi)^3 2E_C} d\Pi_Y, \tag{2.48}$$

where Φ_{in} is the incoming flux and Π_Y is Y phase space. When the energy of the hard scattering $\sqrt{\hat{s}}$ is much larger than the masses of the particles and the p_T of the radiation emitted, the total amplitude $\mathcal{M}$ factorizes, see [42] for a recent review:

$$\mathcal{M}_{AX\to CY} = \mathcal{M}_{A\to BC}\frac{1}{q^2 - m_B^2}\mathcal{M}_{BX\to Y}. \tag{2.49}$$

After the integration over the final state phase space, the cross section of the process can be written as

$$\begin{aligned}\sigma_{A+X\to C+Y} &= \int \frac{dp_T^2 dz}{16\pi^2 \widetilde{p}_T^4}|\mathcal{M}_{A\to BC}|^2 z\bar{z}\sigma_{B+X\to Y} \\ &\equiv \int dp_T^2 \int_0^1 dz \frac{d\mathcal{P}_{A\to B+C}}{dz dp_T^2}(z, p_T^2)\sigma_{B+X\to Y},\end{aligned} \tag{2.50}$$

where $\sigma_{B+X\to Y}$ is the cross section of the hard scattering and we defined

$$\frac{d\mathcal{P}_{A\to B+C}}{dz dp_T^2}(z, p_T^2) = \frac{1}{16\pi^2 \widetilde{p}_T^4} z\bar{z}|\mathcal{M}_{A\to B+C}|^2. \tag{2.51}$$

Now consider the initial lepton beam (electron or muon): its parton content can be described using the PDFs $f_A(x, Q^2)$, that represent the probability of finding a particle A in the beam at the factorization scale Q with fraction x of its energy. Then a cross section involving the initial lepton can be written as

$$\sigma_{\ell+X\to Y} = \sum_A \int_0^1 dx f_A(x)\sigma_{A_x+X\to Y}, \tag{2.52}$$

where $\sigma_{A_x+X\to Y}$ represents the partonic cross section, with the parton A carrying a fraction x of the beam energy. When we consider the emission of soft radiation we must add to this process the ones with the splitting of the parton A, whose cross section is reported in Eq. (2.50). The total cross section with ISR reads

$$\begin{aligned}\sigma_{\text{TOT}} &= \sum_B \int_0^1 dx \left[f_B(x) + \sum_{A,C} \int_0^{Q^2} dp_T^2 \int_x^1 \frac{dz}{z} \frac{d\mathcal{P}_{A\to B+C}}{dz dp_T^2}\left(z, p_T^2\right) f_A\left(\frac{x}{z}, p_T^2\right)\right] \sigma_{B_x+X\to Y} \\ &\equiv \sum_B \int_0^1 dx f_B(x, Q^2)\sigma_{B_x+X\to Y}.\end{aligned} \tag{2.53}$$

Invariance of the cross section on the factorization scale Q, that we choose to be the p_T of the emitted parton, gives

$$\frac{df_B(x, Q^2)}{dQ^2} = \sum_{A,C} \int_x^1 \frac{dz}{z} \frac{d\mathcal{P}_{A\to B+C}}{dz dp_T^2}\left(z, Q^2\right) f_A\left(\frac{x}{z}, Q^2\right) \ . \tag{2.54}$$

Standard matrix elements, present in massless theories, are typically parametrized as

$$|\mathcal{M}_{A\to B+C}|^2 \equiv 8\pi\alpha_{ABC}\frac{p_T^2}{z\bar{z}}P_{BA}^C(z)\ , \tag{2.55}$$

where $P_{BA}^C(z)$ is the splitting function associated to $A \to B + C$ and α_{ABC} is the corresponding coupling. In presence of massive partons the so-called ultra-collinear matrix elements appear, proportional to m^2 instead of p_T^2. In the SM, where all the masses of elementary particles are proportional to the Higgs vev v, they can be parametrized with new splitting functions U_{BA}^C as

$$|\mathcal{M}_{A\to B+C}|^2 = \frac{v^2}{z\bar{z}}U_{BA}^C(z)\ . \tag{2.56}$$

The evolution equation for a parton B in the SM is then given by

$$\frac{df_B(x,t)}{dt} = \sum_{A,C}\frac{\alpha_{ABC}}{2\pi}\widetilde{P}_{BA}^C \otimes f_A + \frac{v^2}{16\pi^2Q^2}\sum_{A,C}\widetilde{U}_{BA}^C \otimes f_A\ , \tag{2.57}$$

where $\widetilde{P}$ and $\widetilde{U}$ are the splitting functions for massive partons. They include the modified propagator of the particle B and are obtained from those for massless ones with just a rescaling:

$$\widetilde{P}_{BA}^C(z,Q^2) = \left(\frac{Q^2}{\widetilde{p}_T^2}\right)^2 P_{BA}^C(z)\ , \tag{2.58}$$

where $\widetilde{p}_T$ is the one defined in Eq. (2.47) with $p_T \to Q$. To shorten the notation, we used the symbol $\otimes$ to indicate the convolution:

$$P \otimes f \equiv \int_x^1 \frac{dz}{z}P(z)f\left(\frac{x}{z}\right). \tag{2.59}$$

We defined the evolution variable t as

$$t \equiv \log\left(Q^2/m_{\ell_v}^2\right)\ , \tag{2.60}$$

where ℓ_v is the valence lepton, i.e. the electron or the muon depending on the type of beam considered.

2.2.2 Virtual corrections

Eq. (2.57) is not complete: some of the $d\mathcal{P}$ terms are divergent in the soft limit $z \to 1$ and we must add virtual corrections to cancel the divergences. These corrections do not modify the nature of the parton and lead to the full form of the DGLAP equations:

$$Q^2\frac{df_B(x,Q^2)}{dQ^2} = P_B^v(x,Q^2)f_B(x,Q^2) + \sum_{A,C}\int_x^1\frac{dz}{z}Q^2\frac{d\mathcal{P}_{A\to B+C}}{dzdp_T^2}\left(z,Q^2\right)f_A\left(\frac{x}{z},Q^2\right)\ , \tag{2.61}$$

where P_B^v represents the virtual corrections. The full set of splitting functions and DGLAP equations in the SM are reported in Appendix A.

Virtual corrections can be easily computed using momentum conservation, i.e. the sum of the momenta of the partons must be equal to the total momentum of the beam. Each parton carries a fraction x of the total momentum and weighting with the PDFs we get

$$\sum_i \int_0^1 dx\, x f_i(x,t) = \sum_i f_i^{(2)}(t) = 1 \quad \forall t \ , \tag{2.62}$$

where $f_i^{(2)}$ represents the $n = 2$ Mellin transform of the PDF:

$$f^{(n)} = \int_0^1 \frac{dx}{x} x^n f(x) \ . \tag{2.63}$$

Deriving in t and using Eq. (2.61) we obtain for each particle A

$$P_A^v = -\sum_{B,C} \left(\frac{\alpha_{ABC}}{2\pi} \widetilde{P}_{BA}^{C(2)} + \frac{v^2}{16\pi^2 Q^2} \widetilde{U}_{BA}^{C(2)} \right) \ . \tag{2.64}$$

To deal with divergences in the computation of the Mellin transforms, we use the + distribution, defined as

$$\begin{aligned} \int_x^1 dz \frac{f(z)}{(1-z)_+} &= \int_x^1 dz \frac{f(z) - f(1)}{1-z} - f(1) \int_0^x \frac{dz}{1-z} \\ &= \int_x^1 dz \frac{f(z) - f(1)}{1-z} + f(1) \log(1-x). \end{aligned} \tag{2.65}$$

2.2.3 Features of lepton PDFs

In case of a proton, due to its non-perturbative nature, the initial conditions for the system must be fitted from collider data. For a lepton, instead, the initial conditions can be computed perturbatively and the system can be solved from first principles. The initial condition for the valence lepton is

$$f_{\ell_v}(x, m_{\ell_v}^2) = \delta(1-x) + \mathcal{O}(\alpha) \ , \tag{2.66}$$

for initially unpolarized beams, while all other PDFs vanish for $Q^2 = m_{\ell_v}^2$ at this order. These initial conditions just represent the fact that at leading order all the energy is stored in the valence lepton at its mass scale. Next-to-leading order (NLO) corrections to the initial conditions have also been computed [43] and become relevant when next-to-leading log (NLL) evolution is considered [44, 45].

In case of multi-TeV lepton colliders one can be interested in factorization scales much higher than the electroweak scale. In this case all SM interactions and fields should be considered [46]. In this aspect, lepton colliders differ qualitatively from hadron colliders. For the latter, QCD interactions are the dominant contributions to the DGLAP evolution in the whole energy range (see however e.g. Refs. [47–51] about the photon and lepton content of the proton). In the case of lepton colliders, instead, EW interactions are the leading ones, with QCD playing an important but not dominant role.

Furthermore, the facts that the SM gauge group is non abelian, that it is spontaneously broken at the electroweak scale, and that interactions are chiral have several crucial implications for the evaluation of collinear radiation in this regime. The non abelian nature of EW interactions imply a lack of cancellation of infrared (IR) divergencies between virtual corrections and real emission, which generates Sudakov double logarithms [52–54]. Electroweak symmetry breaking effects have been shown to provide important contributions and to be the dominant ones in case of longitudinal polarizations of electroweak gauge bosons [55]. Finally, since the SM interactions are chiral, PDFs become polarized above the EW scale [56]. See Chapter 3 for a detailed discussion of these effects and the computation of lepton PDFs.

2.3 The Standard Model Effective Field Theory

Supposing that new physics is heavier than the electroweak scale, we can integrate out the new heavy fields and effectively describe their impact at low energies through higher dimensional operators. The resulting effective field theory (EFT) is the SMEFT [57, 58], whose Lagrangian is obtained dropping the condition of renormalizability, i.e. adding to the SM Lagrangian the full set of higher dimensional operators that are G_{SM} singlets and are built with SM fields:

$$\mathcal{L}_{\text{SMEFT}} = \mathcal{L}_{SM} + \sum_{d>4} \sum_{i} \frac{c_i^{(d)}}{\Lambda_i^{d-4}} \mathcal{O}_i^{(d)}. \tag{2.67}$$

Here the quantities Λ_i represent the characteristic scales at which the operators $\mathcal{O}_i^{(d)}$ are generated, and the smallest of them acts as a cut-off above which the SMEFT description breaks down. The coefficients c_i are dimensionless and the combinations $C_i \equiv c_i^{(d)}/\Lambda_i^{d-4}$ are called Wilson coefficients. If the ultraviolet (UV) theory is known, they can be determined integrating out the new heavy fields or matching the results for amplitudes obtained using the effective and the full descriptions. Otherwise we can put bounds on them using the present experimental data. Note that the contribution of higher dimensional operators to any amplitude will be suppressed wrt the SM by a factor $(E/\Lambda_i)^{d-4}$, meaning that only the first terms of the series will be important at low energies.

The only operator appearing at dimension 5 is

$$\mathcal{O}_W^{i,j} = \left(\widetilde{H}^\dagger l_i\right)^T \mathcal{C} \left(\widetilde{H}^\dagger l_j\right), \tag{2.68}$$

where $\mathcal{C} = i\gamma^0\gamma^2$ is the charge conjugation matrix. O_W is called Weinberg operator and it generates non-zero neutrino masses, producing a Majorana mass term once the Higgs gets a vev. In the rest of this thesis we will not be interested in the effects of this operator and we will focus on dimension-6 operators only. They are reported in Tables 2.3, 2.4 and 2.5 in the Warsaw basis [58], for a total of 63 operators, neglecting the flavor structure. Note

X^3		f^2H^3		H^6 and H^4D^2	
$\mathcal{O}_G$	$f^{ABC}G_\mu^{A\nu}G_\nu^{B\rho}G_\rho^{C\mu}$	$\mathcal{O}_{uH}$	$\left(H^\dagger H\right)\left(\bar{q}u\widetilde{H}\right)$	$\mathcal{O}_H$	$\left(H^\dagger H\right)^3$
$\mathcal{O}_{\widetilde{G}}$	$f^{ABC}\widetilde{G}_\mu^{A\nu}G_\nu^{B\rho}G_\rho^{C\mu}$	$\mathcal{O}_{dH}$	$\left(H^\dagger H\right)\left(\bar{q}dH\right)$	$\mathcal{O}_{H\Box}$	$\left(H^\dagger H\right)\Box\left(H^\dagger H\right)$
$\mathcal{O}_W$	$\epsilon^{abc}W_\mu^{a\nu}W_\nu^{b\rho}W_\rho^{c\mu}$	$\mathcal{O}_{eH}$	$\left(H^\dagger H\right)\left(\bar{l}eH\right)$	$\mathcal{O}_{HD}$	$\left(H^\dagger D^\mu H\right)^\dagger\left(H^\dagger D_\mu H\right)$
$\mathcal{O}_{\widetilde{W}}$	$\epsilon^{abc}\widetilde{W}_\mu^{a\nu}W_\nu^{b\rho}W_\rho^{c\mu}$				
f^2HX		H^2X^2		DH^2f^2	
$\mathcal{O}_{eW}$	$\left(\bar{l}\sigma^{\mu\nu}e\right)\tau^a HW_{\mu\nu}^a$	$\mathcal{O}_{HG}$	$\left(H^\dagger H\right)G_{\mu\nu}^A G_B^{\mu\nu}$	$\mathcal{O}_{Hl}^{(1)}$	$\left(H^\dagger i\overleftrightarrow{D}_\mu H\right)\left(\bar{l}\gamma^\mu l\right)$
$\mathcal{O}_{eB}$	$\left(\bar{l}\sigma^{\mu\nu}e\right)HB_{\mu\nu}$	$\mathcal{O}_{H\widetilde{G}}$	$\left(H^\dagger H\right)\widetilde{G}_{\mu\nu}^A G_B^{\mu\nu}$	$\mathcal{O}_{Hl}^{(3)}$	$\left(H^\dagger i\overleftrightarrow{D}_\mu^a H\right)\left(\bar{l}\tau^a\gamma^\mu l\right)$
$\mathcal{O}_{uG}$	$\left(\bar{q}\sigma^{\mu\nu}T^A u\right)\widetilde{H}G_{\mu\nu}^A$	$\mathcal{O}_{HW}$	$\left(H^\dagger H\right)W_{\mu\nu}^a W_b^{\mu\nu}$	$\mathcal{O}_{He}$	$\left(H^\dagger i\overleftrightarrow{D}_\mu H\right)\left(\bar{e}\gamma^\mu e\right)$
$\mathcal{O}_{uW}$	$\left(\bar{q}\sigma^{\mu\nu}\tau^a u\right)\widetilde{H}W_{\mu\nu}^a$	$\mathcal{O}_{H\widetilde{W}}$	$\left(H^\dagger H\right)\widetilde{W}_{\mu\nu}^a W_b^{\mu\nu}$	$\mathcal{O}_{Hq}^{(1)}$	$\left(H^\dagger i\overleftrightarrow{D}_\mu H\right)\left(\bar{q}\gamma^\mu q\right)$
$\mathcal{O}_{uB}$	$\left(\bar{q}\sigma^{\mu\nu}u\right)\widetilde{H}B_{\mu\nu}$	$\mathcal{O}_{HB}$	$\left(H^\dagger H\right)B_{\mu\nu}B^{\mu\nu}$	$\mathcal{O}_{Hq}^{(3)}$	$\left(H^\dagger i\overleftrightarrow{D}_\mu^a H\right)\left(\bar{q}\tau^a\gamma^\mu q\right)$
$\mathcal{O}_{dG}$	$\left(\bar{q}\sigma^{\mu\nu}T^A d\right)HG_{\mu\nu}^A$	$\mathcal{O}_{H\widetilde{B}}$	$\left(H^\dagger H\right)\widetilde{B}_{\mu\nu}B^{\mu\nu}$	$\mathcal{O}_{Hu}$	$\left(H^\dagger i\overleftrightarrow{D}_\mu H\right)\left(\bar{u}\gamma^\mu u\right)$
$\mathcal{O}_{dW}$	$\left(\bar{q}\sigma^{\mu\nu}\tau^a d\right)HW_{\mu\nu}^a$	$\mathcal{O}_{HWB}$	$\left(H^\dagger\tau^a H\right)W_{\mu\nu}^a B^{\mu\nu}$	$\mathcal{O}_{Hd}$	$\left(H^\dagger i\overleftrightarrow{D}_\mu H\right)\left(\bar{d}\gamma^\mu d\right)$
$\mathcal{O}_{dB}$	$\left(\bar{q}\sigma^{\mu\nu}d\right)HB_{\mu\nu}$	$\mathcal{O}_{H\widetilde{B}}$	$\left(H^\dagger\tau^a H\right)\widetilde{W}_{\mu\nu}^a B^{\mu\nu}$	$\mathcal{O}_{Hud}$	$\left(H^\dagger i\overleftrightarrow{D}_\mu H\right)\left(\bar{u}\gamma^\mu d\right)$

Table 2.3: SMEFT operators in the Warsaw basis excluding the 4-fermion. Flavor indices and the subscript R for u, d and e are omitted. The left-right covariant derivatives are defined as $H^\dagger\overleftrightarrow{D}_\mu H \equiv H^\dagger D_\mu H - D_\mu H^\dagger H$ and $H^\dagger\overleftrightarrow{D}_\mu^a H \equiv H^\dagger\tau^a D_\mu H - D_\mu H^\dagger\tau^a H$.

Four leptons		Semi-leptonic		Four quarks	
$\mathcal{O}_{ll}$	$\left(\bar{l}\gamma_\mu l\right)\left(\bar{l}\gamma^\mu l\right)$	$\mathcal{O}_{lq}^{(1)}$	$\left(\bar{l}\gamma_\mu l\right)\left(\bar{q}\gamma^\mu q\right)$	$\mathcal{O}_{qq}^{(1)}$	$\left(\bar{q}\gamma_\mu q\right)\left(\bar{q}\gamma^\mu q\right)$
$\mathcal{O}_{ee}$	$\left(\bar{e}\gamma_\mu e\right)\left(\bar{e}\gamma^\mu e\right)$	$\mathcal{O}_{lq}^{(3)}$	$\left(\bar{l}\gamma_\mu \tau^a l\right)\left(\bar{q}\gamma^\mu \tau^a q\right)$	$\mathcal{O}_{qq}^{(3)}$	$\left(\bar{q}\gamma_\mu \tau^a q\right)\left(\bar{q}\gamma^\mu \tau^a q\right)$
$\mathcal{O}_{le}$	$\left(\bar{l}\gamma_\mu l\right)\left(\bar{e}\gamma^\mu e\right)$	$\mathcal{O}_{eu}$	$\left(\bar{e}\gamma_\mu e\right)\left(\bar{u}\gamma^\mu u\right)$	$\mathcal{O}_{uu}$	$\left(\bar{u}\gamma_\mu u\right)\left(\bar{u}\gamma^\mu u\right)$
		$\mathcal{O}_{ed}$	$\left(\bar{e}\gamma_\mu e\right)\left(\bar{d}\gamma^\mu d\right)$	$\mathcal{O}_{dd}$	$\left(\bar{d}\gamma_\mu d\right)\left(\bar{d}\gamma^\mu d\right)$
		$\mathcal{O}_{lu}$	$\left(\bar{l}\gamma_\mu l\right)\left(\bar{u}\gamma^\mu u\right)$	$\mathcal{O}_{ud}^{(1)}$	$\left(\bar{u}\gamma_\mu u\right)\left(\bar{d}\gamma^\mu d\right)$
		$\mathcal{O}_{ld}$	$\left(\bar{l}\gamma_\mu l\right)\left(\bar{d}\gamma^\mu d\right)$	$\mathcal{O}_{ud}^{(8)}$	$\left(\bar{u}\gamma_\mu T^A u\right)\left(\bar{d}\gamma^\mu T^A d\right)$
		$\mathcal{O}_{qe}$	$\left(\bar{q}\gamma_\mu q\right)\left(\bar{e}\gamma^\mu e\right)$	$\mathcal{O}_{qu}^{(1)}$	$\left(\bar{q}\gamma_\mu q\right)\left(\bar{u}\gamma^\mu u\right)$
		$\mathcal{O}_{ledq}$	$\left(\bar{l}e\right)\left(\bar{d}q\right)$	$\mathcal{O}_{qu}^{(8)}$	$\left(\bar{q}\gamma_\mu T^A q\right)\left(\bar{u}\gamma^\mu T^A u\right)$
		$\mathcal{O}_{lequ}^{(1)}$	$\left(\bar{l}\gamma_\mu e\right)\epsilon\left(\bar{q}\gamma^\mu u\right)$	$\mathcal{O}_{qd}^{(1)}$	$\left(\bar{q}\gamma_\mu q\right)\left(\bar{d}\gamma^\mu d\right)$
		$\mathcal{O}_{lequ}^{(3)}$	$\left(\bar{l}\sigma_{\mu\nu} e\right)\epsilon\left(\bar{q}\sigma_{\mu\nu} u\right)$	$\mathcal{O}_{qd}^{(8)}$	$\left(\bar{q}\gamma_\mu T^A q\right)\left(\bar{d}\gamma^\mu T^A d\right)$
				$\mathcal{O}_{quqd}^{(1)}$	$\left(\bar{q}u\right)\epsilon\left(\bar{q}d\right)$
				$\mathcal{O}_{quqd}^{(8)}$	$\left(\bar{q}T^A u\right)\epsilon\left(\bar{q}T^A d\right)$

Table 2.4: SMEFT 4-fermion operators in the Warsaw basis. Flavor indices and the subscript R for u, d and e are omitted.

$\mathcal{O}_{duql}$	$\left(d^T\mathcal{C}u\right)\left(q^T\mathcal{C}l\right)$
$\mathcal{O}_{qque}$	$\left(q^T\mathcal{C}q\right)\left(u^T\mathcal{C}e\right)$
$\mathcal{O}_{qqql}$	$\epsilon_{im}\epsilon_{jk}\left(q_i^T\mathcal{C}q_j\right)\left(q_k^T\mathcal{C}l_m\right)$
$\mathcal{O}_{duue}$	$\left(d^T\mathcal{C}u\right)\left(u^T\mathcal{C}e\right)$

Table 2.5: SMEFT baryon and lepton number violating operators in the Warsaw basis. Flavor indices and the subscript R for u, d and e are omitted.

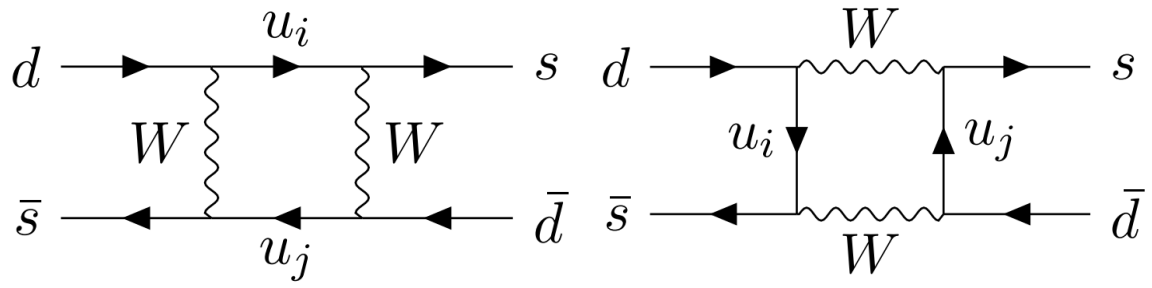

Figure 2.3: Feynman diagrams for kaon mixing.

that 4 of these 63 operators violate baryon number: their presence is due to the fact that it can be broken by new physics, being it just an accidental symmetry of the SM.

These operators form a basis in the sense that we cannot obtain one of them with linear combinations of the others, field redefinitions or addition of total derivatives.

2.3.1 4-fermion operators and minimal flavor violation

Now we focus on 4-fermion operators, which introduce additional interactions between fermions. Being not forbidden by symmetries, they receive a SM contribution at loop level, once heavy fields (Higgs, W, Z and the top quark) have been integrated out. The corresponding Wilson coefficients can be computed by matching with the SM amplitudes. Processes of this kind become excellent probes of new physics when the SM amplitude is small enough and therefore can be compared with the contributions coming from the heavy fields. This is, for instance, the case of lepton flavor universality violating processes, as we will see in Chapter 4.

Here we just show, as an example, the case of meson mixing, which we will also use in Chapter 5 in the global analysis of the effects of top-quark operators. Meson mixing is a so called $\Delta F = 2$ process, in which flavor changes by two units. For concreteness, let us consider neutral kaons, $K^0 = (d, \bar{s})$ and $\bar{K}^0 = (\bar{d}, s)$. The transition between the two mesons occurs at one loop in the SM via the box diagrams in Figure 2.3. Computing the amplitude and taking the limit of heavy top-quark and W, one gets the following result:

$$\mathcal{M}(K^0 \leftrightarrow \bar{K}^0) = \frac{G_F^2 m_W^2}{4\pi^2} \left(\bar{s}_L \gamma^\mu d_L\right)^2 \left[\lambda_t^2 s_0(x_t) + \lambda_c \lambda_t s_0(x_c, x_t) + \lambda_c^2 s_0(x_c)\right], \tag{2.69}$$

where we defined $\lambda_i = V_{id} V_{is}^*$ and $x_i = m_i/m_W$, while $s_0(x) \approx x^2$ and $s_0(x, y) \approx xy$ are loop functions. Using the Wolfenstein parametrization of the CKM matrix, Eq. (2.31), we obtain that the Wilson coefficient of the generated operator $\left(\bar{s}_L \gamma^\mu d_L\right)^2 \subset \mathcal{O}_{qq}^{(1)}$ is roughly given by

$$C_{sd} \sim \frac{G_F^2}{4\pi^2} \left(\lambda^{10} m_t^2 + \lambda^6 m_t m_c + \lambda^2 m_c^2\right), \tag{2.70}$$

that corresponds to $\Lambda \sim 10^3\,\text{TeV}$ for $c_{sd} \sim \mathcal{O}(1)$. This is an example of the GIM mechanism [59]: $\Delta F = 2$ transitions, and FCNC processes in general, are suppressed due to the peculiar flavor structure (i.e. the values of the CKM matrix and of the quark masses).

The presence of tight bounds above the TeV scale predicted by naturalness arguments leads to the so-called new physics flavor problem, since such bounds can be lowered only making hypothesis on the flavor structure of new physics. The strongest possible assumption is the so called minimal flavor violation (MFV) [60]: in this scenario Yukawa matrices are generated at an inaccessible scale as vev of some heavy fields and they are the only source of breaking of the global accidental symmetry group G_F defined in Eq. (2.26). To find how Yukawa matrices enter in the Wilson coefficients of higher-dimensional operators, we promote them to spurions in order to have G_F formally restored. From the Yukawa Lagrangian in Eq. (2.1), we see that these spurions must transform in the following representations of G_F:

$$Y^u \sim (3, \bar{3}, 1, 1, 1)\,, \qquad Y^d \sim (3, 1, \bar{3}, 1, 1)\,, \qquad Y^e \sim (1, 1, 1, 3, \bar{3})\,. \tag{2.71}$$

For instance, the operator $\mathcal{O}_{qq}^{(1)}$, responsible for meson mixing, can be made G_F singlet in the following way:

$$C_{qq}^{(1)ijkm}\left(\bar{q}_i\gamma_\mu q_j\right)\left(\bar{q}_k\gamma^\mu q_m\right) \Longrightarrow \left[\bar{q}_i\gamma_\mu \left(Y^u Y^{u\dagger}\right)_{ij} q_j\right]^2. \tag{2.72}$$

In the down quark basis in Eq. (2.29), this corresponds to a Wilson coefficient of $\mathcal{O}(10^{-7})$, i.e. the scale reduces to few TeV.

2.3.2 Integrating out heavy fields

We conclude this short SMEFT review with an explicit example of how to integrate out heavy fields. Let us consider a new physics scenario in which an additional vector boson Z' is present, interacting with fermions with the following Lagrangian[1]:

$$\mathcal{L}_{Z'} \supset \frac{M_{Z'}^2}{2} Z'_\mu Z'^\mu - g' Z'_\mu \left[-\bar{\mu}\gamma^\mu\mu + \frac{\epsilon}{3}\left(\bar{b}_L\gamma^\mu s_L + \bar{s}_L\gamma^\mu b_L\right)\right] \equiv \frac{M_{Z'}^2}{2} Z'_\mu Z'^\mu - g' Z'_\mu j'^\mu. \tag{2.73}$$

We can integrate out Z' solving the corresponding equation of motion and plugging back the result into the Lagrangian. Neglecting derivatives, that give rise to higher dimensional operators, we get

$$0 = \frac{\delta \mathcal{L}_{Z'}}{\delta Z'^\mu} \supset M_{Z'}^2 Z'_\mu - g' j'_\mu \Longrightarrow Z'_\mu = \frac{g'}{M_{Z'}^2} j'_\mu. \tag{2.74}$$

Plugging back this result in Eq. (2.73) we obtain

$$\mathcal{L} \supset -\frac{g'}{2M_{Z'}^2} j'_\mu j'^\mu \supset \frac{\epsilon g'}{3M_{Z'}^2}\left(\bar{\mu}\gamma_\mu\mu\right)\left(\bar{b}_L\gamma^\mu s_L + \text{h.c.}\right). \tag{2.75}$$

We see that integrating out the Z' we generate a dimension-6 4-fermion operator, known in the literature as $\mathcal{O}_9^{ijkl}$ [61]:

$$\mathcal{O}_9^{ijkl} = \left(\bar{d}_L^i\gamma^\mu d_L^j\right)\left(\bar{e}^k\gamma_\mu e^l\right), \tag{2.76}$$

[1]Here we write only the terms that we need in order to show how to integrate out Z'. In Chapter 4 we will discuss more in details Z' models and study the possibilities of future colliders to discover or exclude such scenarios.

where in this specific case $i = j = 2, 3$ and $k, l = 2$. The corresponding Wilson coefficient is

$$C_9 = \frac{\epsilon g'}{3M_{Z'}^2}. \tag{2.77}$$

Note that this operator does not appear in the Warsaw basis, being it a linear combination of $\mathcal{O}_{qe}$ and $\mathcal{O}_{lq}^{(1)}$:

$$\mathcal{O}_{lq}^{(1)kl,ij} + \mathcal{O}_{qe}^{ij,kl} = \left(\bar{q}^i \gamma^\mu q^j\right) \left(\bar{e}^k \gamma_\mu e^l\right) \supset \mathcal{O}_9^{ijkl}. \tag{2.78}$$

Chapter 3

Parton distribution functions of leptons

In this Chapter we show our numerical solution of the DGLAP equations for lepton parton distribution functions from the valence lepton mass scale, with the LO initial conditions in Eq. (2.66), up to multi-TeV scales, taking into account all SM interactions, including the effects mentioned in Section 2.2.3. For concreteness, we consider the muon as the initial lepton, since muon colliders could achieve higher energies, for which the discussion is more relevant. However, all results can be equally applied to e^+e^- colliders with suitable substitutions. A similar study has already been performed in the literature, specifically in Refs. [62, 63], and we compare our results with the plots presented in those works. We also compare against approximate solutions obtained by solving iteratively, at fixed-order, the DGLAP equations, which provide the analogous of the Effective Vector Boson Approximation (EVA) [18, 64, 65]. As a direct application of LePDFs, we investigate processes at the muon collider that are sensitive to the muon neutrino PDF, offering a potential cross-check for theoretical predictions.

The Chapter is organized as follows. We start in Section 3.1 presenting the evolution below the EW scale, where only QED and QCD interactions are relevant. In Section 3.2 we discuss the main aspects of the evolution above the EW scale, focusing on EW effects. Our results are collected in Section 3.3[1], where we show several notable features of LePDFs, and a comparison with the EVA is presented. Section 3.4 is dedicated to the study of the impact of muon neutrino PDF at MuC to the processes $\mu\bar{\mu} \to e^-\bar{\nu}_e$ and $\mu\bar{\mu} \to W^-\gamma$, where μ ($\bar{\mu}$) represents the muon (antimuon) beam with its full parton content. Similarly, in Section 3.5 we study the impact of neutrino PDF on single Higgs production at MuC, comparing our results with the expected experimental sensitivity. We summarize in Section 3.6, while many details of the computations, the numerical implementation and the formatting of LePDF files are collected in Appendices A-B-C.

[1]The numerical results for the LePDFs can be downloaded from GitHub at the link: `https://github.com/DavidMarzocca/LePDF`.

3.1 QED and QCD evolution

For factorization scales below the EW scale the relevant degrees of freedom are light quarks and charged leptons, with vectorlike QED and QCD interactions. Neutrinos, while having negligible masses, become relevant only above the EW scale where the W boson can go on-shell.[2] Because the initial condition and the evolution equations are vectorlike, in this regime no polarization effects are induced, i.e. PDFs will be the same for both fermion chiralities or gauge boson polarizations.

In the DGLAP evolution from the muon mass up to the EW scale one encounters several mass thresholds for each fermion species as well as at the QCD scale $Q_{\rm QCD}$. The latter sets the onset of QCD interactions, which become relevant after the $\gamma \to q\bar{q}$ splitting. This can be interpreted as the QCD structure of a photon, and can be divided into a perturbative and a non-perturbative component, mainly due to the photon mixing with QCD vector mesons [69–73]. The latter one will be power-suppressed at the large scales we are eventually interested in, so we neglect it. The choice of $Q_{\rm QCD}$ depends on how many resonances are included in the non-perturbative component and a value close to m_ρ has been argued to provide a good benchmark [71–73]. In practice, we follow the prescription of Refs. [63, 71] with $Q_{\rm QCD} = 0.7$ GeV.[3]

At each threshold a matching should be performed. Therefore, from m_μ to $Q_{\rm QCD}$ we consider only QED interactions, including only the light fermions (e, μ, u, d, s). At $Q_{\rm QCD}$ we match the PDFs and continue the evolution up to the charm mass scale adding also QCD interactions and setting the initial condition for the gluon PDF as $f_g(x, Q_{\rm QCD}) = 0$. At $Q = m_c$ we perform another matching and we do the same at m_τ and m_b, including at each threshold the corresponding fermion and setting $f_i(x, m_i) = f_{\bar{i}}(x, m_i) = 0$ as initial conditions ($i = \{c, \tau, b\}$). We finally continue the evolution up to the EW scale $Q_{\rm EW}$.

Given the C and P symmetries of QED and QCD, and the fact that some particles share

[2] A possible effect of neutrinos even below the EW scale is due to neutrinos from muon decay $\mu^- \to e^- \bar{\nu}_e \nu_\mu$ which present IR singularities in the physical region when scattering with the incoming μ^+ (or viceversa) [66]. In case of muon colliders such singularities are cutoff by the finite width of the muon beam [67, 68]. We neglect such effects with our PDF formalism, assuming that it can be described independently of PDFs.

[3] We study the dependence of our results on $Q_{\rm QCD}$ by running the evolution also for values $Q_{\rm QCD} = 0.52(1.0)$ GeV and interpreting the differences as theory uncertainty on our final results due to non-perturbative QCD dynamics, see the dedicated discussion in Section 3.3.7.

the same evolution equations and initial conditions, below $Q_{\rm EW}$ several PDFs are related:

$$\begin{aligned}
f_e &= f_{\bar{e}} = f_{\bar{\mu}} \ , \\
f_\tau &= f_{\bar{\tau}} \ , \\
f_u &= f_{\bar{u}} \ , \\
f_c &= f_{\bar{c}} \ , \\
f_d &= f_{\bar{d}} = f_s = f_{\bar{s}} \ , \\
f_b &= f_{\bar{b}} \ .
\end{aligned} \tag{3.1}$$

The DGLAP equations, according to Eq. (2.61), are then given by

$$\begin{aligned}
\frac{df_\ell}{dt} =& P^v_\ell f_\ell + \frac{\alpha_\gamma(t)}{2\pi}\left[P^V_{ff}\otimes f_\ell + P^f_{fV}\otimes f_\gamma\right] \ , \\
\frac{df_{q^u}}{dt} =& P^v_{q^u} f_{q^u} + \frac{\alpha_\gamma(t)}{2\pi} Q_u^2\left[P^V_{ff}\otimes f_{q^u} + N_c P^f_{fV}\otimes f_\gamma\right] \\
&+ \frac{\alpha_3(t)}{2\pi}\left[C_F P^V_{ff}\otimes f_{q^u} + T_F P^f_{fV}\otimes f_g\right] \ , \\
\frac{df_{q^d}}{dt} =& P^v_{q^d} f_{q^d} + \frac{\alpha_\gamma(t)}{2\pi} Q_d^2\left[P^V_{ff}\otimes f_{q^d} + N_c P^f_{fV}\otimes f_\gamma\right] \\
&+ \frac{\alpha_3(t)}{2\pi}\left[C_F P^V_{ff}\otimes f_{q^d} + T_F P^f_{fV}\otimes f_g\right] \ , \\
\frac{df_\gamma}{dt} =& P^v_\gamma f_\gamma + \frac{\alpha_\gamma(t)}{2\pi}\sum_f Q_f^2 P^f_{Vf}\otimes\left(f_f + f_{\bar{f}}\right) \ , \\
\frac{df_g}{dt} =& P^v_g f_g + \frac{\alpha_3(t)}{2\pi}\left[C_A P_{VV}\otimes f_g + C_F P^f_{Vf}\otimes\sum_q\left(f_q + f_{\bar{q}}\right)\right] \ ,
\end{aligned} \tag{3.2}$$

where $\ell = \{e,\mu,\tau\}$, $q^u = \{u,c\}$, $q^d = \{d,s,b\}$. The evolution variable t is defined in Eq. (2.60), the splitting functions are listed in Appendix A.2, and the group factors C_F, C_A and T_F are reported in Appendix A.3.

The virtual coefficients P^v_f, P^v_γ and P^v_g are computed using Eq. (2.64) applied to fermions, photon and gluon respectively:

$$\begin{aligned}
P^v_f &= -\left(P^{V(2)}_{ff} + P^{f(2)}_{Vf}\right)\left(\frac{\alpha_\gamma}{2\pi}Q_f^2 + \frac{\alpha_3}{2\pi}C_F\delta_{f,q}\right) = \frac{3}{2}\left(\frac{\alpha_\gamma}{2\pi}Q_f^2 + \frac{\alpha_3}{2\pi}C_F\delta_{f,q}\right) \ , \\
P^v_\gamma &= -2\frac{\alpha_\gamma}{2\pi}N_f^{\rm QED}P^{f(2)}_{fV} = -\frac{2}{3}\frac{\alpha_\gamma}{2\pi}N_f^{\rm QED} \ , \\
P^v_g &= -\frac{\alpha_3}{2\pi}\left(2T_F N_q P^{f(2)}_{fV} + C_A P^{V(2)}_{VV}\right) = \frac{\alpha_3}{2\pi}\left(\frac{11}{6}C_A - \frac{2}{3}T_F N_q\right) \ ,
\end{aligned} \tag{3.3}$$

where $\delta_{f,q}$ is one for quarks and zero otherwise. $N_f^{\rm QED} = N_\ell Q_\ell^2 + N_c(N_u Q_u^2 + N_d Q_d^2)$ is the effective number of fermions in QED and N_q is the number of quarks. Notice that the number of leptons (N_ℓ), up and down quarks (N_u and N_d) are not constant due to the thresholds. We also have to take into account the renormalization group (RG) evolution of the couplings: in particular we evaluate the QCD coupling using the 3-loop result [74]

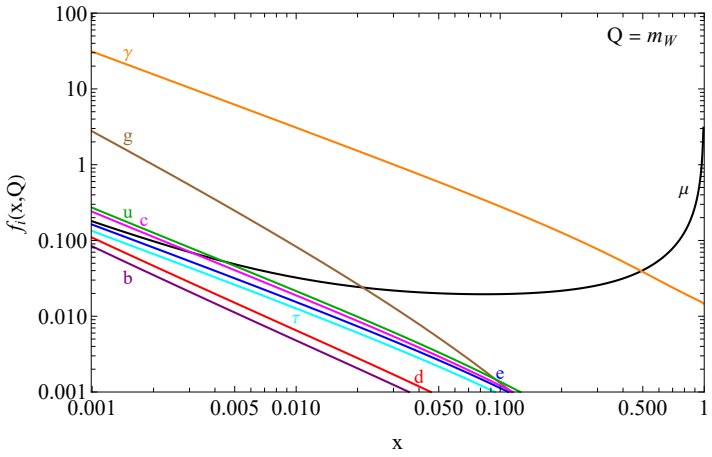

Figure 3.1: PDFs of a muon evaluated at the EW scale $Q_{EW} = m_W$.

with mass thresholds for the charm, bottom, and top quarks, while for QED we just use the one-loop formula in Eq. (2.38), that in the variable t becomes

$$\alpha^{(1)}(t) = \frac{\alpha(t_0)}{1 + \frac{1}{2}\beta_0\alpha(t_0)(t - t_0)}. \tag{3.4}$$

Since we use this setup only up to the EW scale, we take the boundary condition at that scale: $\alpha_\gamma(t_0) = \alpha_\gamma(t_{\rm EW}) = 0.00783581$. At each threshold a matching is performed, since the beta function coefficient is not fixed: using Eq. (2.37) we obtain

$$\beta_0^\gamma = -\frac{2}{3\pi}N_f^{\rm QED} = \begin{cases} -\frac{8}{3\pi} & t < t_c \\ -\frac{32}{9\pi} & t_c \le t < t_\tau \\ -\frac{38}{9\pi} & t_\tau \le t < t_b \\ -\frac{40}{9\pi} & t_b \le t_{\rm EW} \end{cases} \tag{3.5}$$

In Figure 3.1 we show our numerical results for a muon, at the EW scale $Q_{\rm EW} = m_W$. As can be seen, at small x the gluon PDF becomes rather important, while quark PDFs have a size similar to the muon itself or sea leptons[4], as already shown in Refs. [62, 63].

3.1.1 Iterative solution for QED

By solving iteratively the DGLAP equations order by order in $\alpha_\gamma t$, one gets approximate solutions for the PDFs. The LO contribution for the photon PDF is given by Eq. (2.42) with the crucial substitution $E \to Q$. Neglecting the τ mass threshold and including terms

[4]We call sea leptons all the leptons that are not the muon. As shown in Eq. (3.1), electron, positron and antimuon PDFs are the same due to CP and initial conditions, while the threshold makes τ and $\bar{\tau}$ PDFs different. Neglecting the threshold, all sea leptons PDFs are equal.

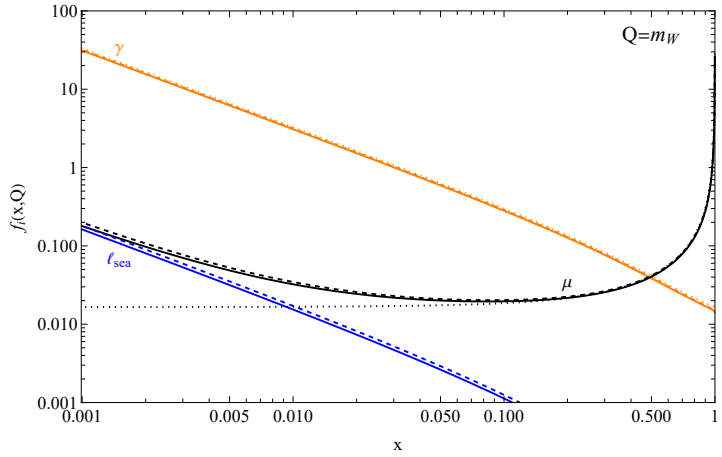

Figure 3.2: Muon, photon and sea leptons PDFs evaluated at the EW scale $Q_{EW} = m_W$. Solid lines correspond to the numerical results, while dotted and dashed lines represent the LO and NLO approximated solutions respectively.

up to $\mathcal{O}(\alpha^2 t^2)$ we get

$$\begin{aligned} f_\mu^{(\alpha^2)}(x,t) &= \delta(1-x) + \frac{\alpha_\gamma}{2\pi}\, t \left(\frac{3}{2}\delta(1-x) + P_{ff}^V(x)\right) \\ &\quad + \frac{1}{2}\left(\frac{\alpha_\gamma}{2\pi}\, t\right)^2 \left[\frac{9}{4}\delta(1-x) + 3P_{ff}^V(x) + I_{fVVf}(x) + I_{ffff}(x)\right] \,, \\ f_{\ell_{\rm sea}}^{(\alpha^2)}(x,t) &= \frac{1}{2}\left(\frac{\alpha_\gamma}{2\pi}\, t\right)^2 I_{fVVf}(x) \,, \\ f_\gamma^{(\alpha^2)}(x,t) &= \frac{\alpha_\gamma}{2\pi}\, t\, P_{Vf}^f(x) + \frac{1}{2}\left(\frac{\alpha_\gamma}{2\pi}\, t\right)^2 \left[\left(\frac{3}{2} - \frac{2}{3}N_f^{\rm QED}\right) P_{Vf}^f(x) + I_{Vfff}(x)\right] \,, \end{aligned} \tag{3.6}$$

where the $I_{ABBC}(x) \equiv \int_x^1 \frac{dz}{z} P_{AB}^X(z) P_{BC}^Y(x/z)$ integrals are collected in Eq. (A.7). We report the comparison between these expressions and our numerical results in Figure 3.2: for the photon we find excellent agreement already at LO, while going up to $\mathcal{O}(\alpha^2 t^2)$ is required in order to describe the low-x behavior of valence and sea lepton PDFs, that is dominated by the $\gamma \to \ell^+\ell^-$ splitting (i.e. the $I_{fVVf}(x)$ term above).

Gluon PDF starts formally at $\mathcal{O}(\alpha_\gamma^2 \alpha_s t^3)$. However, due to the large value of α_s at low energies and the importance of a careful treatment of the matching at $Q_{\rm QCD}$, a fixed-order solution would not be a good approximation for the correct result. For the same reason we do not consider here quark PDFs, even if they formally arise already at $\mathcal{O}(\alpha_\gamma^2 t^2)$, since they receive a large QCD contribution from gluon splitting into $q\bar{q}$. A correct description of the quark and gluon PDFs in a lepton therefore motivates a complete numerical solution of the DGLAP equations.

3.2 DGLAP evolution in the SM

For energies above the EW scale, the splitting processes in the initial states can involve all SM interactions and fields, which must then be included in the DGLAP equations. The

Leptons	$e_{L,R}$	$\mu_{L,R}$	$\tau_{L,R}$	ν_e	ν_μ	ν_τ	$\bar{\ell}_{L,R}$	$\bar{\tau}_{L,R}$	$\bar{\nu}_\ell$	$\bar{\nu}_\tau$
Quarks	$u_{L,R}$	$d_{L,R}$	$c_{L,R}$	s_L	$t_{L,R}$	$b_{L,R}$	+ h.c.			
Gauge Bosons	$\gamma_\pm$	$Z_\pm$	$Z/\gamma_\pm$	$W^\pm_\pm$	$g_\pm$					
Scalars	h	Z_L	h/Z_L	$W^\pm_L$						

Table 3.1: Independent degrees of freedom for our DGLAP evolution above the EW scale.

chiral nature of EW interactions induces polarization effects on PDFs, so in this region all gauge bosons and fermions polarizations are treated separately. Splitting functions for SM interactions in the unbroken phase have been computed in Refs. [33, 46, 55, 56, 75], with which we agree. Another well known effect in EW PDFs is the interference between photon and transverse Z_T, which must be described with a Z/γ mixed PDF, as well as between the Higgs boson and the longitudinal Z_L, which induces a h/Z_L mixed PDF [33, 46, 55]. Also, the non-abelian nature of EW interactions induces Sudakov double logarithms, which must be resummed when one is interested in high energies [52–54].

Due to the fermion thresholds, only a few PDFs are related:

$$\begin{aligned} f_{\bar{\ell}_L} &\equiv f_{\bar{e}_L} = f_{\bar{\mu}_L} \ , \\ f_{\bar{\ell}_R} &\equiv f_{\bar{e}_R} = f_{\bar{\mu}_R} \ , \\ f_{\bar{\nu}_\ell} &\equiv f_{\bar{\nu}_e} = f_{\bar{\nu}_\mu} \ , \\ f_{d_R} &= f_{s_R} \ , \quad f_{\bar{d}_R} = f_{\bar{s}_R} \ . \end{aligned} \tag{3.7}$$

The fact that PDFs for right-handed fermions and their conjugate are different is due to the induced polarization effects in the gluon, photon, and Z boson PDFs. The independent degrees of freedom are given in Table 3.1, the final count is 54 independent PDFs. Note that, differently from the first phase of the evolution and from the right-handed counterparts, $f_{s_L} \neq f_{d_L}$ due to charged current interaction $s_L c_L W$. Regarding the mass thresholds, we include each degrees of freedom (W, Z and h) right at the corresponding mass scale.

3.2.1 Electroweak symmetry breaking effects

EW symmetry breaking effects can be classified as either due to non-vanishing parton masses or as new contributions to the splitting functions that vanish in the limit of unbroken symmetry [55]. The latter are the so-called ultra-collinear splittings, which are particularly relevant for the longitudinal polarizations of EW gauge bosons [42, 55], providing the leading contributions for their PDFs even when $Q \gg Q_{\rm EW}$. In order to easily keep track of all these effects near the EW scale it is convenient to work in the broken phase and with the mass eigenstates. Then, as the DGLAP equations remain the same also for higher energies, we remain in the broken phase for any $Q > Q_{\rm EW}$.

In case any of the particles involved in the splitting $A \to B{+}C$ is massive, the kinematics of the process and the ensuing splitting functions are modified. As shown in Eq. (2.47),

the relation between the p_T and the virtuality of the parton B entering the hard scattering process becomes

$$\widetilde{p}_T^2 \equiv \bar{z}(m_B^2 - p_B^2) = p_T^2 + z m_C^2 + \bar{z} m_B^2 - z\bar{z} m_A^2 + \mathcal{O}\left(\frac{m^2}{E^2}, \frac{p_T^2}{E^2}\right) , \tag{3.8}$$

and m^2/E^2 or p_T^2/E^2 terms can be neglected in the regime where factorization can be applied. In the DGLAP equations, this modified propagator of the virtual parton B effectively corresponds to a rescaling of the splitting functions as [55]

$$P_{BA}^C(z) \quad \to \quad \widetilde{P}_{BA}^C(z, p_T^2) = \left(\frac{p_T^2}{\widetilde{p}_T^2}\right)^2 P_{BA}^C(z) \ . \tag{3.9}$$

Mass effects in matrix elements that are also present in the unbroken (i.e. massless) theory are instead suppressed by powers of m/E, therefore negligible.

Regarding the ultra-collinear splitting functions, the main feature of these contributions is that they do not scale logarithmically with Q^2 but at large factorization scales are suppressed as v^2/Q^2 . Nevertheless, they provide important contributions that accumulate during the DGLAP evolution in the region $Q \sim Q_{\rm EW}$ and then remain almost constant at higher scales, see for instance the W_L PDF in the right panel of Figure 3.3. We report the full set of splitting functions in Appendix A.2[5], while the list of SM DGLAP equations can be found in Appendix A.3.

In principle, with massive partons we should care of kinematics bounds: the splittings described by DGLAP equations involve partons A, B and C with energies zE, xE and $(z-x)E$ respectively, all fractions of the energy of the beam E. Since the particle C is emitted on-shell, we need $E_C \geq m_C$, that is $z \geq x + \frac{m_C}{E}$. This means that the lower extreme of integration in Eq. (2.61) should be modified. However, as in Eq. (3.8), m/E terms can be neglected and we can safely start the integration from x.

3.2.2 Electroweak double logarithms

The fact that the initial and final states are EW non-singlets has important implications, even for inclusive processes. The Bloch-Nordsieck theorem [76], that guarantees cancellation of IR divergencies between real emission and virtual corrections in such processes, is violated for non-abelian symmetries, implying the presence of Sudakov double logarithms. While in the QCD case this effect vanishes upon averaging over color of the initial states, for $SU(2)_L$ we do not take such average and the initial state breaks explicitly the symmetry, hence double logs do appear also in inclusive processes [52–54, 77, 78]. In our context they can be seen appearing in the terms of the DGLAP equations containing a $1/(1-z)$

[5]The ultra-collinear splitting functions have been calculated in Refs. [55] and [42]. The former used the Goldstone equivalence gauge, while in the latter the theory is formulated in a standard R_ξ-gauge, with 5-dimensional polarization vectors of the gauge bosons to take into account the Goldstone contribution to the longitudinal component. We checked the results with both methods and we agree with them.

pole and can be made explicit by introducing an IR cutoff in the integral, which allows also to resum the Sudakov double logs related to ISR [33, 75, 79–81].[6] We implement this following Ref. [33], by modifying the boundaries of the integral in Eq. (2.61) as

$$\frac{\alpha_{ABC}(Q)}{2\pi}\int_x^1 \frac{dz}{z} P_{BA}^C(z) f_A\left(\frac{x}{z},Q^2\right) \quad \to \quad \frac{\alpha_{ABC}(Q)}{2\pi}\int_x^{z_{\max}^{ABC}(Q)} \frac{dz}{z} P_{BA}^C(z) f_A\left(\frac{x}{z},Q^2\right) \ , \tag{3.10}$$

where $z_{\max}^{ABC}(Q)$ plays the role of an explicit IR cutoff for the $1/(1-z)$ poles, and is set equal to $1 - Q_{\rm EW}/Q$ for the cases where the soft divergence is not cancelled between real emission and virtual corrections. This modifies the computation of the virtual corrections, that becomes

$$P_A^v(Q) \supset -\sum_{B,C}\frac{\alpha_{ABC}(Q)}{2\pi}\int_0^{z_{\max}^{ABC}(Q)} dz\, z\, \widetilde{P}_{BA}^C(z) + \text{ultra-collinear} \ . \tag{3.11}$$

The mismatch of IR divergencies between real and virtual contributions takes place in processes where the emitted radiation (e.g. a $W^\pm$ boson) changes the $SU(2)_L$ component of the initial state, and is always proportional to the amount of explicit breaking of the $SU(2)_L$ symmetry. In fact, the physical effect of these double logs is to restore $SU(2)_L$ invariance at high scales. As an explicit example for leptons, let us consider the DGLAP equations for the μ_L and the corresponding $SU(2)_L$ partner ν_μ

$$\begin{aligned}
\frac{df_{\mu_L}}{d\log Q^2} &= \frac{\alpha_2}{2\pi}\frac{1}{2}\int_0^{z_{\max}(Q)} dz P_{ff}^V(z)\left(\frac{1}{z}f_{\nu_\mu}\left(\frac{x}{z},Q^2\right) - z f_{\mu_L}(x,Q^2)\right) + \dots \ , \\
\frac{df_{\nu_\mu}}{d\log Q^2} &= \frac{\alpha_2}{2\pi}\frac{1}{2}\int_0^{z_{\max}(Q)} dz P_{ff}^V(z)\left(\frac{1}{z}f_{\mu_L}\left(\frac{x}{z},Q^2\right) - z f_{\nu_\mu}(x,Q^2)\right) + \dots \ ,
\end{aligned} \tag{3.12}$$

where the ellipses include other finite contributions to the integral, as well as other interactions. The first term in brackets is due to real emission of a transverse W boson, while the second one is the corresponding virtual correction. The fact that the muon and neutrino PDFs are different is an explicit breaking of $SU(2)_L$ and implies a non-cancellation of the pole for $z \to 1$ inside $P_{ff}^V(z)$, which in turn generates the double log. To see this explicitly, let us isolate on the right-hand side only the terms that are singular in $z \to 1$, fixing $z = 1$ everywhere else:

$$\begin{aligned}
\frac{df_{\mu_L}}{d\log Q^2} &\approx -\frac{\alpha_2}{4\pi}\Delta f_{L_2}(x)\int_0^{z_{\max}(Q)} dz\frac{2}{1-z} + \dots \approx -\frac{\alpha_2}{4\pi}\log\frac{Q^2}{Q_{\rm EW}^2}\Delta f_{L_2}(x) + \dots \ , \\
\frac{df_{\nu_\mu}}{d\log Q^2} &\approx \frac{\alpha_2}{4\pi}\Delta f_{L_2}(x)\int_0^{z_{\max}(Q)} dz\frac{2}{1-z} + \dots \approx \frac{\alpha_2}{4\pi}\log\frac{Q^2}{Q_{\rm EW}^2}\Delta f_{L_2}(x) + \dots \ ,
\end{aligned} \tag{3.13}$$

where $\Delta f_{L_2} \equiv f_{\mu_L} - f_{\nu_\mu}$. Upon integration in Q^2, a $\log^2 Q^2/Q_{\rm EW}^2$ contribution is generated, that tends to deplete the muon PDF and enhance the neutrino one. This example also

[6] A complete description of all double logarithms in a full process requires, however, the inclusion of further contributions (e.g. virtual corrections, soft radiation, fragmentation, etc.), see for instance [52, 81–86].

clearly shows how no such double log is generated for photon or Z_T emission from a fermion or W, since the real and virtual contribution would be proportional to the PDF of the same parton. A Sudakov double log is instead expected for splittings such that the splitting function is divergent in the soft limit, $z \to 1$, and the A and B partons are different:

$$z_{\max}^{ABC}(Q) = 1 - \frac{Q_{\rm EW}}{Q} \qquad \text{if} \quad P_{BA}^{C},\ U_{BA}^{C} \propto \frac{1}{1-z} \text{ and } A \neq B\ , \tag{3.14}$$

otherwise we put $z_{\max} = 1$ and employ the + distribution, Eq. (2.65), to regulate the $z \to 1$ divergence, for a more stable numerical evaluation of the DGLAP equations.

In practice, this happens for $W_T^{\pm}$ emission off any parton (in correspondence to the poles in the P_{ff}^V, P_{VV}^V, and P_{hh}^V splittings) and for Z_T boson emission from an initial longitudinal Z_L or Higgs (due to the P_{hh}^V splitting), since Z emission changes $Z_L \longleftrightarrow h$. Analogously, for ultra-collinear splittings this takes place for any W_L emission and for Z_L emission off an initial Higgs or Z_L.

This procedure amounts to a double-logarithmic (DL) approximation to the Sudakov factor for initial-state radiation. This could be further improved to LL or NLL resummation by suitably modifying the scale at which the coupling constant $\alpha_2(Q)$ is evaluated, as discussed in Refs. [56, 87]. Since we are interested in energies where $\alpha_2 \log^2 Q^2/Q_{\rm EW}^2 \sim \mathcal{O}(1)$ but $\alpha_2 \log Q^2/Q_{\rm EW}^2 \ll 1$, we limit ourselves to the DL approximation for electroweak corrections in the present work.

3.2.3 Top quark as parton

When the energy of the hard process Q is much larger than the top mass, processes with a collinearly emitted top quark can develop a logarithmic enhancement proportional to $\log Q^2/m_t^2$. It can therefore become useful to resum these logarithms by including the top quark among the other partons [88, 89]. The question of whether or not one should include it as a parton depends on the process considered and on the optimal way to rearrange the perturbative series [90, 91]. With this in mind, we provide two versions of our PDFs of leptons, one in the 5-flavor-scheme (5FS) and one in a 6FS, where the top quark is added in the DGLAP evolution for scales above m_t. While codes that include the top quark in proton PDFs assume it is massless, in our approach we keep a finite top mass in the same spirit in which we keep finite W and Z masses for the weak bosons PDFs. This is justified by the fact that in our case, contrary to proton PDFs, EW interactions and EW symmetry breaking effects are crucial, and the top mass is one of such effects. For a detailed discussion of different schemes for the top mass in the computation of hadron collider observables with a top quark PDF see [91].

The DGLAP equations for the t_L, $\bar{t}_L$, t_R, $\bar{t}_R$ are reported explicitly in Eqs. (A.41, A.42, A.49, A.50). We checked numerically that the dominant contributions are those from initial transverse gauge bosons, with electroweak bosons, photon and gluon terms being approximately of similar size. Instead, ultra-collinear contributions are practically

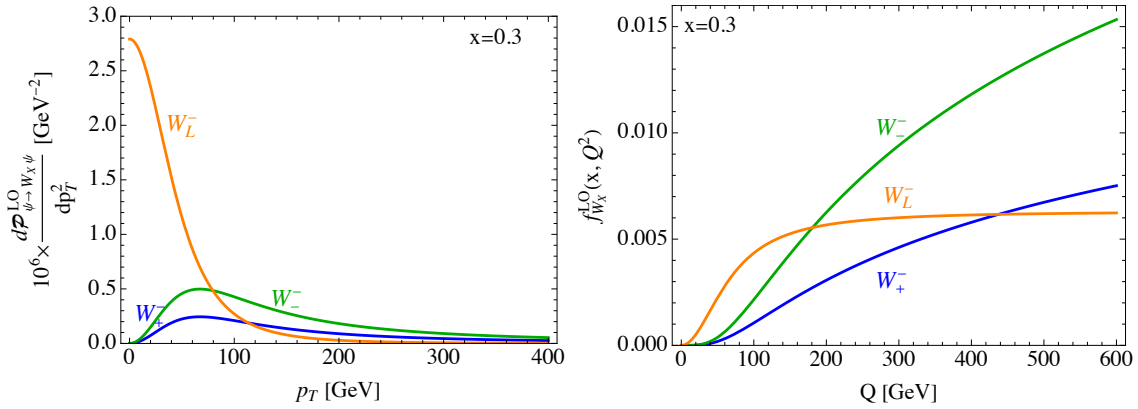

Figure 3.3: Integrand functions (left) and resulting PDFs (right) for the computation of the EW PDFs for transverse and longitudinal W boson of Eqs. (3.15, 3.16).

negligible. Nevertheless, in our numerical evaluation we keep all terms.

3.2.4 Effective Vector Boson Approximation

The EPA has been generalized to describe EW gauge bosons in high-energy collisions since the '80s [92–95], in what is now known as the Effective Vector Boson Approximation [18, 64, 65, 96–98].

One can compute the EW gauge bosons PDFs by evaluating the DGLAP equations at fixed order, similarly to what we did in Section 3.1 for QED, using $f^{(0)}_{\mu_L}(x) = f^{(0)}_{\mu_R}(x) = \frac{1}{2}\delta(1-x)$ for the muon PDF. Taking the DGLAP equations for the transverse and longitudinal W^- boson, Eqs. (A.63, A.64, A.68), one gets the leading order results

$$\begin{aligned} f^{(\alpha)}_{W^-_\pm}(x,Q^2) &= \int_{m_\mu^2}^{Q^2} dp_T^2 \frac{1}{2}\frac{d\mathcal{P}_{\psi\to W_T\psi}}{dp_T^2}(x,p_T^2) = \int_{m_\mu^2}^{Q^2} dp_T^2 \frac{\alpha_2}{8\pi}\frac{p_T^2}{(p_T^2+(1-x)m_W^2)^2} P^f_{V_\pm f_L}(x) = \\ &= \frac{\alpha_2}{8\pi} P^f_{V_\pm f_L}(x)\left(\log\frac{Q^2+(1-x)m_W^2}{m_\mu^2+(1-x)m_W^2} - \frac{Q^2}{Q^2+(1-x)m_W^2}\right) = \\ &\approx \frac{\alpha_2}{8\pi} P^f_{V_\pm f_L}(x)\left(\log\frac{Q^2}{m_W^2} - \log(1-x) - 1\right) + \mathcal{O}\left(\frac{m_W^2}{Q^2}\right) , \end{aligned} \tag{3.15}$$

$$\begin{aligned} f^{(\alpha)}_{W^-_L}(x,Q^2) &= \int_0^{Q^2} dp_T^2 \frac{1}{2}\frac{d\mathcal{P}_{\psi\to W_L\psi}}{dp_T^2}(x,p_T^2) = \int_0^{Q^2} dp_T^2 \frac{\alpha_2}{4\pi}\frac{m_W^2}{(p_T^2+(1-x)m_W^2)^2}\frac{(1-x)^2}{x} = \\ &= \frac{\alpha_2}{4\pi}\frac{1-x}{x}\frac{Q^2}{Q^2+(1-x)m_W^2} \approx \frac{\alpha_2}{4\pi}\frac{1-x}{x} + \mathcal{O}\left(\frac{m_W^2}{Q^2}\right) , \end{aligned} \tag{3.16}$$

and analogously for the Z and Z/γ PDFs:

$$f^{(\alpha)}_{Z_\pm}(x,Q^2) = \frac{\alpha_2}{4\pi c_W^2}\left(P^f_{V_\pm f_L}(x)(Q^Z_{\mu_L})^2 + P^f_{V_\pm f_R}(x)(Q^Z_{\mu_R})^2\right) \left(\log\frac{Q^2+(1-x)m_Z^2}{m_\mu^2+(1-x)m_Z^2} - \frac{Q^2}{Q^2+(1-x)m_Z^2}\right) , \tag{3.17}$$

$$f^{(\alpha)}_{Z/\gamma_\pm}(x,Q^2) = -\frac{\sqrt{\alpha_\gamma\alpha_2}}{2\pi c_W}\left(P^f_{V_\pm f_L}(x)Q^Z_{\mu_L} + P^f_{V_\pm f_R}(x)Q^Z_{\mu_R}\right)\log\frac{Q^2+(1-x)m_Z^2}{m_\mu^2+(1-x)m_Z^2} , \tag{3.18}$$

$$f^{(\alpha)}_{Z_L}(x,Q^2) = \frac{\alpha_2}{2\pi c_W^2}\frac{1-x}{x}\left((Q^Z_{\mu_L})^2+(Q^Z_{\mu_R})^2\right)\frac{Q^2}{Q^2+(1-x)m_Z^2} , \tag{3.19}$$

The muon mass here serves as an IR cutoff for the logarithm in the transverse case to cure the $x \to 1$ limit, while we neglect it in the other terms. Notably, the W^+ has no contribution at this order.

In Figure 3.3 we show the dependence in $\sqrt{p_T^2}$ of the integrands (left), and the resulting PDFs (right), fixing a value $x = 0.3$ and showing separately the two polarization of the transverse W^-. One can see that the integrands are peaked before the EW scale and, while in the case of W_T it decreases as $\sim 1/p_T^2$ inducing the logarithmic growth of the PDF, for the longitudinal W polarization the contribution to the integral is localised in p_T^2 before the EW scale and the PDF tends to a constant at large scales.

In our numerical integration of DGLAP equations, the effects due to EW interactions are introduced only above the $Q_{\rm EW}$ matching scale. Since we employ p_T as factorization scale, this effectively corresponds to performing the integration in Eqs. (3.15, 3.16) only for $p_T^2 > Q^2_{\rm EW}$, missing the region $0 < p_T^2 < Q^2_{\rm EW}$. To address this issue we match the gauge bosons PDFs at $Q_{\rm EW}$ to the analytically computed one for the same scale and use it as boundary conditions:

$$f_A(x,Q^2_{\rm EW}) \equiv f_A^{(\alpha)}(x,Q^2_{\rm EW}) \quad \text{for} \quad A = W^-_{L,\pm},\ Z_{L,\pm},\ Z/\gamma_\pm , \tag{3.20}$$

and then continue the integration numerically to higher scales. The boundary conditions for the PDFs of other heavy states (h, h/Z_L, top quark) are instead set to zero at the corresponding mass scales.

3.3 Results

Here we discuss several aspects of our LePDFs. The details of our numerical implementation of the DGLAP equations are reported in Appendix B.

Figure 3.4 (left panel) collects, as an example, a set of PDFs evaluated at a scale $Q = 3$ TeV. One first thing to notice is that, as expected, for $x \gtrsim 0.5$ the muon PDF dominates, while for smaller x the largest PDF is the photon one. However, the transverse W_T^- PDF is only a factor ~ 2 smaller and the transverse Z_T boson is another factor of 2 smaller than that: they both receive contributions from the emission off an initial muon.

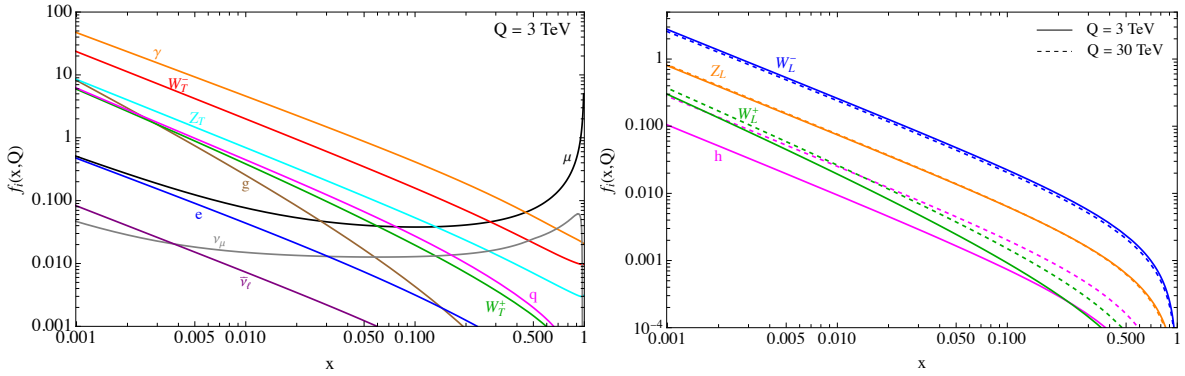

Figure 3.4: (Left panel): Sample of PDFs evaluated at a scale $Q = 3$ TeV for a muon. For this plot we sum over polarizations and q represents the sum of all quark PDFs except for the top. (Right panel): PDFs for the scalar degrees of freedom in the SM. Solid (dashed) lines are evaluated at a scale of $Q = 3\,(30)$ TeV.

Analogously, the muon neutrino ν_μ has a large PDF at large x values due to the emission off a μ_L^-, which has also a Sudakov double-log enhancement. The transverse W_T^+ PDF is instead more suppressed because its leading contribution arises from the emission off the muon neutrino and off another gauge boson. The importance of EW gauge bosons PDFs reflects the common lore that *a high-energy lepton collider is also a weak boson collider*.

In the right panel of Figure 3.4 we show the PDFs for the longitudinal polarizations of EW gauge bosons and the Higgs, evaluated at scales of 3 TeV (solid lines) and 30 TeV (dashed lines). The PDFs for W_L^- and Z_L are mostly scale independent, since they receive the dominant contribution from the ultra-collinear splitting off a muon. On the other hand, the ultra-collinear contribution to the W_L^+ PDF comes mostly from the muon neutrino, which has a PDF suppressed with respect to the muon one. Therefore, other contributions from standard splitting functions (e.g. from P_{hV}^h and P_{hh}^V) are sizeable and induce a scale dependence. In case of the Higgs boson there is no ultra-collinear contribution from massless fermions, so one does not expect ultra-collinear terms to dominate and indeed its PDF shows a large scale dependence.

The fraction of the momentum carried by each of the partonic components is given by the $n = 2$ Mellin transform of the PDF, Eq. (2.62), and it can be used to evaluate the relevant role of the various individual components at different scales. To this end, in Table 3.2 we give three examples at scales 3 TeV, 10 TeV, and 30 TeV.[7] We observe that as the energy of the hard process is increased the percentages of both the left- and right-handed muon components are decreased and those of all other partons increased, which illustrates the importance of electroweak interactions at higher energies.

In Figure 3.5 we show some examples of parton luminosities for a 3 and 10 TeV muon

[7]The numerical integrals needed for the Mellin transform are performed with the rectangles method. Due to the rapid growth of the muon PDF for $x \to 1$, numerical routines such as NIntegrate on Mathematica fail to reproduce the correct result, see Appendix B for details.

field	$Q = 3$ TeV	$Q = 10$ TeV	$Q = 30$ TeV
μ_L	48.03%	47.78%	47.26%
μ_R	45.54%	43.15%	40.57%
ν_μ	1.75%	3.58%	5.89%
ν_{sea}	0.0075%	0.015%	0.024%
ℓ_{sea}	0.073%	0.096%	0.119%
q	0.125%	0.18%	0.24%
t	0.026%	0.0401%	0.054%
γ	3%	3.22%	3.39%
W^-	1.28%	1.61%	1.89%
W^+	0.096%	0.201%	0.339%
Z	0.416%	0.57%	0.724%
g	0.019%	0.027%	0.036%
h	0.003%	0.006%	0.009%
Total	100.37%	100.47%	100.54%

Table 3.2: Fraction of the momentum carried by each parton at $Q = 3, 10, 30$ TeV. The muon is the valence lepton.

colliders where, unless specified, we sum over polarizations. Parton luminosities can be useful for computing cross sections integrated over angular variables. In case of a muon collider they are defined from the convolution of the PDFs of parton i from the muon and parton j from the anti-muon, as follows:

$$\mathcal{L}_{ij}(\hat{s}, s_0) \equiv \int_{\hat{s}/s_0}^{1} \frac{dx}{x} f_i^{(\mu)}\left(x, \frac{\sqrt{\hat{s}}}{2}\right) f_j^{(\bar{\mu})}\left(\frac{\hat{s}}{x s_0}, \frac{\sqrt{\hat{s}}}{2}\right) , \tag{3.21}$$

where $\sqrt{s_0}$ is the collider center of mass energy and $\sqrt{\hat{s}}$ is the invariant mass of the two-parton system. From Figure 3.5 we can notice that, even at small invariant masses, the $\mu\bar{\mu}$ luminosity is much larger than the W^+W^- luminosity (also the charged-current $\mu_L\bar{\nu}_\mu$ luminosity is sizeable). The impact of this channel in VBF studies at muon colliders should therefore be studied in more details. It is also interesting to point out that the QCD-related luminosities (gluons and quarks) are very small, and therefore QCD-induced backgrounds in electroweak processes are strongly suppressed.

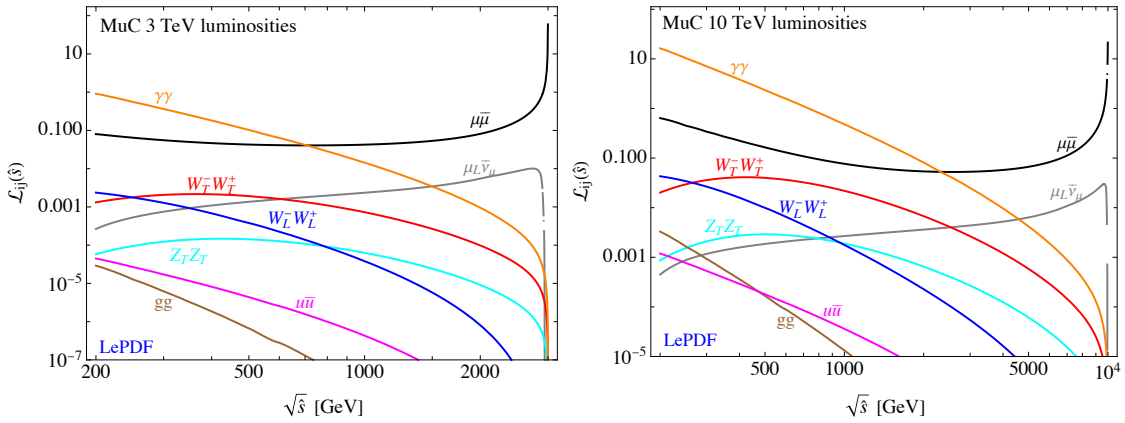

Figure 3.5: Examples of parton luminosities at a 3 TeV (left) and 10 TeV (right) MuC. Unless specified, for this plot we sum over polarizations.

3.3.1 Threshold effects

Removing the fermion mass thresholds, the number of independent degrees of freedom is reduced. Concerning the first phase of the evolution, Eq. (3.1) becomes

$$\begin{aligned} f_{\ell_{\text{sea}}} \equiv f_e = f_{\bar{e}} = f_{\bar{\mu}} = f_\tau = f_{\bar{\tau}} \ , \\ f_u = f_{\bar{u}} = f_c = f_{\bar{c}} \ , \\ f_d = f_{\bar{d}} = f_s = f_{\bar{s}} = f_b = f_{\bar{b}} \ , \end{aligned} \tag{3.22}$$

since now all fermions of the same kind, except the muon, have the same PDF evolution equations and initial conditions at $Q = m_\mu$. Analogously, PDFs for the particles in Table 3.1 are related as follows:

$$\begin{aligned} f_{e_{L,R}} &= f_{\tau_{L,R}} \ , \\ f_{\bar{e}_{L,R}} &= f_{\bar{\mu}_{L,R}} = f_{\bar{\tau}_{L,R}} \ , \\ f_{\nu_e} &= f_{\nu_\tau} \ , \\ f_{\bar{\nu}_e} &= f_{\bar{\nu}_\mu} = f_{\bar{\nu}_\tau} \ , \\ f_{u_{L,R}} &= f_{c_{L,R}} \ , \\ f_{\bar{u}_{L,R}} &= f_{\bar{c}_{L,R}} \ , \\ f_{d_L} &= f_{s_L} \ , \\ f_{\bar{d}_L} &= f_{\bar{s}_L} \ , \\ f_{d_R} &= f_{s_R} = f_{b_R} \ , \\ f_{\bar{d}_R} &= f_{\bar{s}_R} = f_{\bar{b}_R} \ . \end{aligned} \tag{3.23}$$

The final count is therefore 6 independent PDFs in the first phase and 40 in the second one.

In Figure 3.6 we report the differences between the PDFs computed with and without thresholds, normalized with the latter. While many PDFs are practically unaffected by the

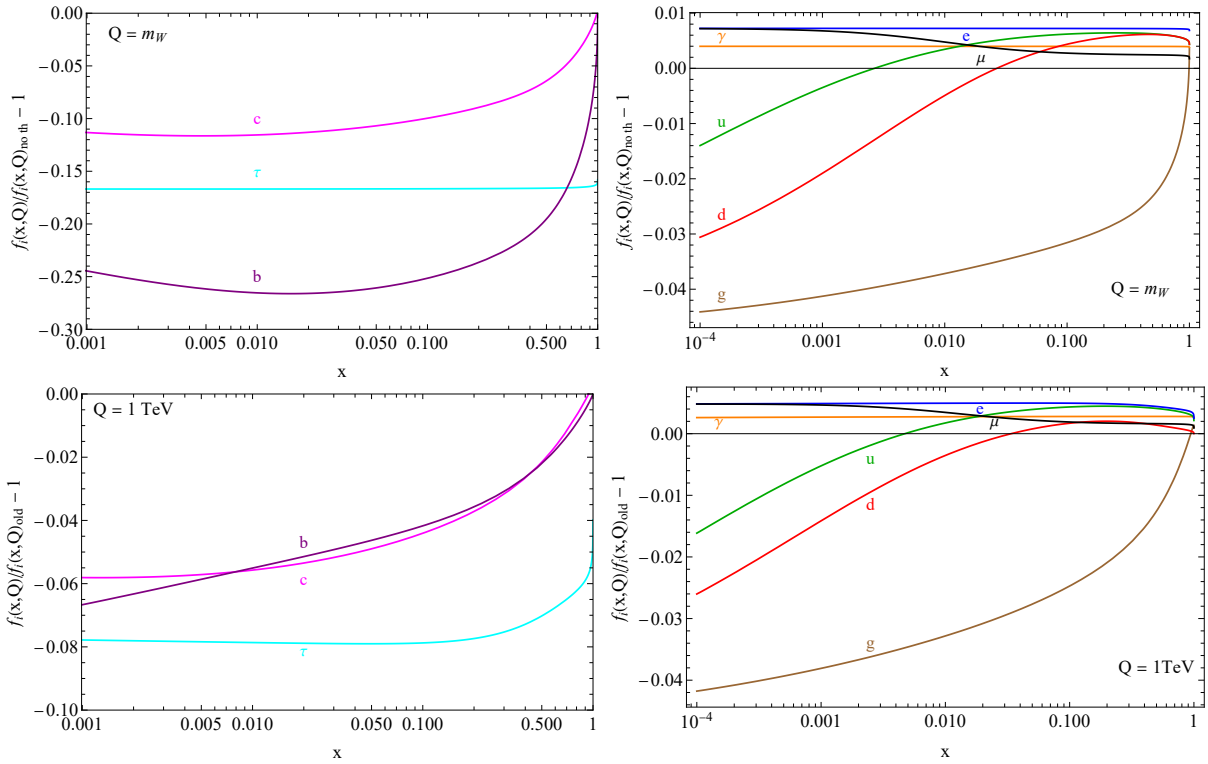

Figure 3.6: Difference between PDFs computed with and without mass thresholds at the scale $Q = m_W$ (top) and $Q = 1\,\text{TeV}$ (bottom).

thresholds, with differences of $\mathcal{O}(1\%)$ at most (right panels), the effect becomes significant for c, τ and b. This is due to the smaller amount of *time* of evolution in presence of the thresholds, with differences of $\mathcal{O}(10\%)$ at the EW scale. The effect is progressively washed out increasing the scale, since at high energies the c, τ and b mass scales become negligible.

3.3.2 Polarizations

The chiral structure of SM interactions above the EW scale induces polarization effects for the PDFs [56]. In Figure 3.7 we show polarization ratios for several PDFs at a scale $Q = 3$ TeV. The observed behavior can be easily understood as follows. The W_T^-, W_T^+, and Z_T PDFs receive the dominant contribution from the emission off $\mu_{L,R}^-$ or ν_μ. Since the $P^f_{V_+ f_L}$ splitting function goes to zero for $z \to 1$, while $P^f_{V_- f_L}$ tends to a constant, the positive helicity of the EW gauge bosons will be suppressed for $x \to 1$. In case of the photon, the leading contribution comes from the muon splitting and it is vector-like at leading order, so the polarization effect will be suppressed.

In case of fermions, left-handed chiralities (and their conjugate) receive contributions from W bosons splitting to $\psi_L \bar{\psi}'_L$, therefore their PDF is expected to be larger than the right-handed counterparts. The tendency increases with x in the case of the leptons (except for the muon) and down-type quarks as opposed to antileptons and up-type quarks, since the left-handed parts of the former receive contributions from W_T^-, while the latter from

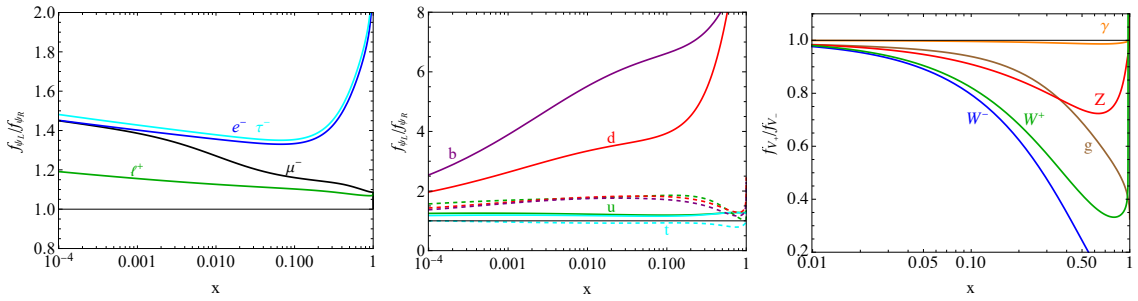

Figure 3.7: Polarization ratios for the PDFs of leptons (left), quarks (center), and gauge bosons (right) at a scale $Q = 3$ TeV. Dashed lines in the central panel are for the corresponding anti-quarks.

W_T^+, and the W_T^+ PDF falls faster than the W_T^- PDF at high x (see Figure 3.4) This effect can be of $\mathcal{O}(1)$, since the W^- PDF is comparable in size to the photon one. The b_L PDF is further enhanced compared to b_R due to the $W_L^- \to b_L \bar{t}_R$ splitting proportional to y_t.

3.3.3 Comparison with the Effective Vector Boson Approximation

In Figure 3.8 we show our results for EW gauge bosons PDFs, compared with the LO EVA discussed in Section 3.2.4. We use the non approximated results in Eqs. (3.15-3.19) and we show the sum of transverse polarizations, to reduce the number of lines plotted. Several things can be noticed.

For Z/γ, the EVA result is two orders of magnitude smaller than what we find with the numerical evolution. This is due to the fact that $Q^Z_{\mu_L} + Q^Z_{\mu_R} = -\frac{1}{2} + 2s^2_W \ll 1$ is accidentally suppressed (indeed, it becomes zero when evolving the Weinberg angle at a scale of about 3.6 TeV). This cancellation takes place because in EVA it is assumed that the initial-state muon is not polarized. However, in the evolution from the EW scale upward, electroweak interactions induce a polarization of the muon PDF, which becomes up to $\sim 40\%$ at a scale of 3 TeV, as can be seen in Figure 3.7 (left panel). Therefore, in the full numerical evolution there is no such tuned cancellation in the Z/γ PDF. This clearly shows that the EVA result is not reliable for this PDF.

For the longitudinal polarizations, the EVA provides a good description of the PDFs, to within $\sim 10\%$ accuracy. In case of the transverse W and Z polarizations, instead, there is a noticeable discrepancy which grows even up to $\mathcal{O}(50\%)$ at multi-TeV scales for small x values. This is dominantly due to the missing contributions from $V \to VV$ splittings, that start at NLO. Such contributions become important due to two effects: the PDF of the initial-state gauge boson at small x is much larger than the muon PDF and they include IR Sudakov corrections. We perform two checks to verify this. First, we do a run of our numerical code setting to zero the P_{VV} splitting functions (both in real emission and radiative corrections): the resulting EW gauge bosons PDFs agree well with

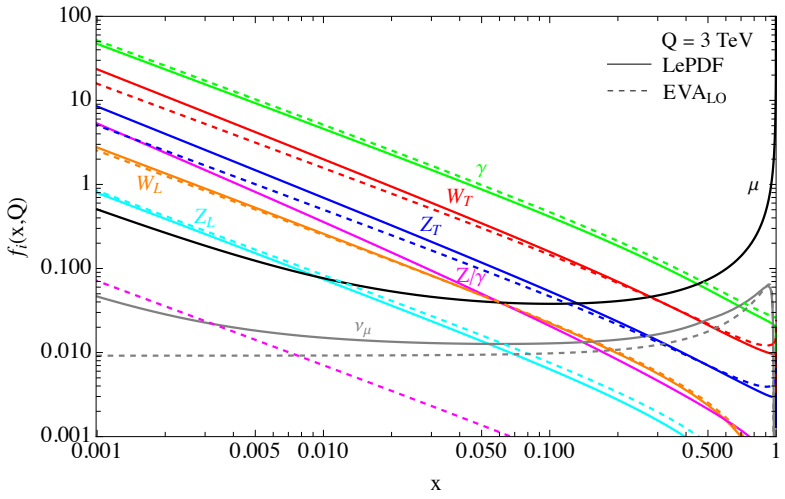

Figure 3.8: PDFs for EW gauge bosons (plus muon and muon neutrino) at a scale $Q = 3$ TeV. Solid lines are from the numerical solution of DGLAP equations while dashed ones are from the LO EVA expressions in Eqs. (3.15)-(3.19).

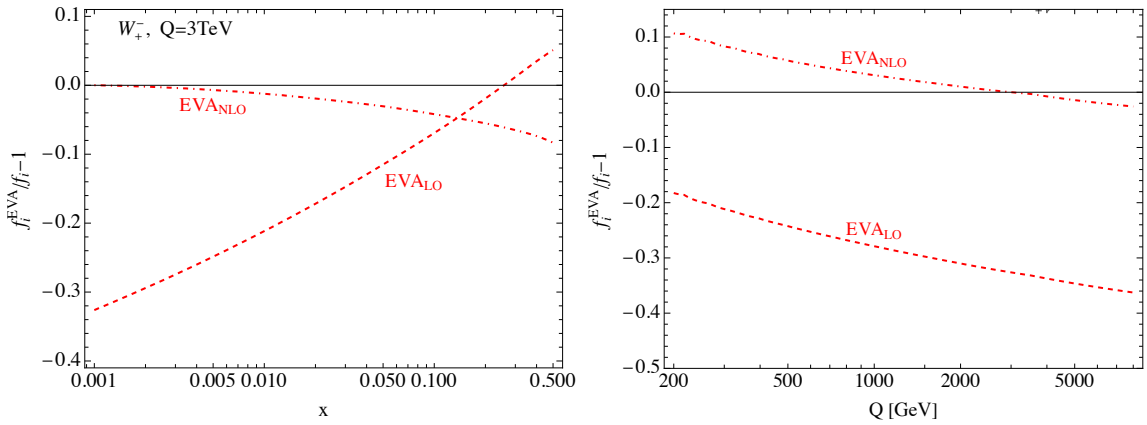

Figure 3.9: Relative difference between the numerical result for the W_+^- PDF and the LO (dashed) or NLO (dot-dashed) EVA expression for a fixed scale $Q = 3$ TeV (left) and for fixed $x = 0.001$ (right).

LO EVA. Second, focusing only on the W_+^- PDF for simplicity, we compute iteratively the $\mathcal{O}(\alpha^2)$ contributions to the weak bosons PDFs, adding the real emissions from P_{VV}^V and P_{Vf}^f splittings, and the corresponding virtual corrections. In practice, we take the DGLAP equations for transverse EW gauge bosons in Section A.3.3 and use the $\mathcal{O}(\alpha)$ results for the gauge bosons PDFs of Eqs. (3.15-3.19) and the muon. For simplicity, at this step we use approximate expressions for the LO EVA by keeping only the $\log \frac{Q^2}{m_{W,Z}^2}$ term, which makes our NLO EVA result reliable only for $Q \gg m_W$ and $x \ll 1$. We also neglect contributions from longitudinal modes and ultra-collinear ones. We then perform analytically the convolution with the splitting functions and finally the integral from m_W

up to the factorization scale Q:

$$f^{(\alpha)}_{\mu_L}(x,t) \simeq \int_{t_{m_W}}^{t} dt' \left(\frac{1}{2} P^{v}_{\mu_L}(t') \delta(1-x) + \frac{\alpha_\gamma}{4\pi} P^{V}_{ff}(x) + \frac{\alpha_2}{4\pi c_W^2} (Q^Z_{\mu_L})^2 P^{V}_{ff}(x) \right) ,$$

$$f^{(\alpha^2)}_{W^-_+}(x,t) \simeq \int_{t_{m_W}}^{t} dt' \left(P^{v}_{W^-_+} f^{(\alpha)}_{W^-_+} + \frac{\alpha_2}{4\pi} P^{f}_{V_+ f_L} \otimes f^{(\alpha)}_{\mu_L} + \frac{\alpha_2}{2\pi} c_W^2 P_{V_+ V_s} \otimes (f^{(\alpha)}_{W^-_s} + f^{(\alpha)}_{Z_s}) + \right. \quad (3.24)$$

$$\left. + \frac{\alpha_\gamma}{2\pi} P_{V_+ V_s} \otimes (f^{(\alpha)}_{W^-_s} + f^{(\alpha)}_{\gamma_s}) + \frac{\sqrt{\alpha_\gamma \alpha_2}}{2\pi} c_W P_{V_+ V_s} \otimes f^{(\alpha)}_{Z/\gamma_s} \right) .$$

It can be noted that Sudakov double logs appear here in the virtual contributions to $f^{(\alpha)}_{\mu_L}$ and to $f^{(\alpha^2)}_{W^-_+}$, as well as in the $P_{V_+V_+}$ terms from the neutral gauge bosons.
In Figure 3.9 we show the relative deviation of the LO (dashed) and NLO (dot-dashed) EVA results from the complete numerical PDF as function of x (left panel) and as function of the scale (right panel). We observe that the NLO EVA result improves substantially the agreement with the full numerical result, while the LO EVA has large deviations at small x. The missing terms in the LO EVA become more and more important with larger scales, confirming the argument made above.

In Figure 3.10, instead, we plot the $W^-_+W^+_-$ (left panel) and $W^-_L W^+_L$ (right panel) parton luminosities for a 10 TeV MuC. We show a comparison between the LePDF result (solid lines) and the LO EVA expression in the $Q \gg m_W$ approximation[8] (dot-dashed), or with the complete W mass dependence as in Eq. (3.15) (dashed). We see that, at the level of luminosity, the LO EVA with the complete mass dependence provides a good approximation of the resummed LePDF result up to $\sim 15\%$ deviations for the transverse modes. This means that the much larger deviations we observe at the PDF level for small x are diluted when the luminosities are calculated. On the other hand, the massless approximation deviates up to $\mathcal{O}(1)$ even at the luminosity level and in particular at partonic center of mass energies of few hundreds of GeV, where the weak-boson fusion process cross sections are the largest.

3.3.4 Muon neutrino PDF

The leading contribution to the muon neutrino PDF arises already at $\mathcal{O}(\alpha_2)$ from the $\mu_L \to W^-\nu_\mu$ splitting, which presents an IR soft divergence that is cutoff by the W mass. As already discussed in Sec. 3.2.2, the missing counterpart of this divergence in the virtual correction is at the origin of the Sudakov double log. In the same spirit as done for the EVA, we can compute the neutrino PDF by iteratively solving the DGLAP equations up

[8]For transverse polarizations we also neglect the Q-independent terms of Eq. (3.15), keeping only $\log(Q^2/m_V^2)$. This corresponds effectively to use the virtuality of the parton as factorization scale, see Ref. [65] for details.

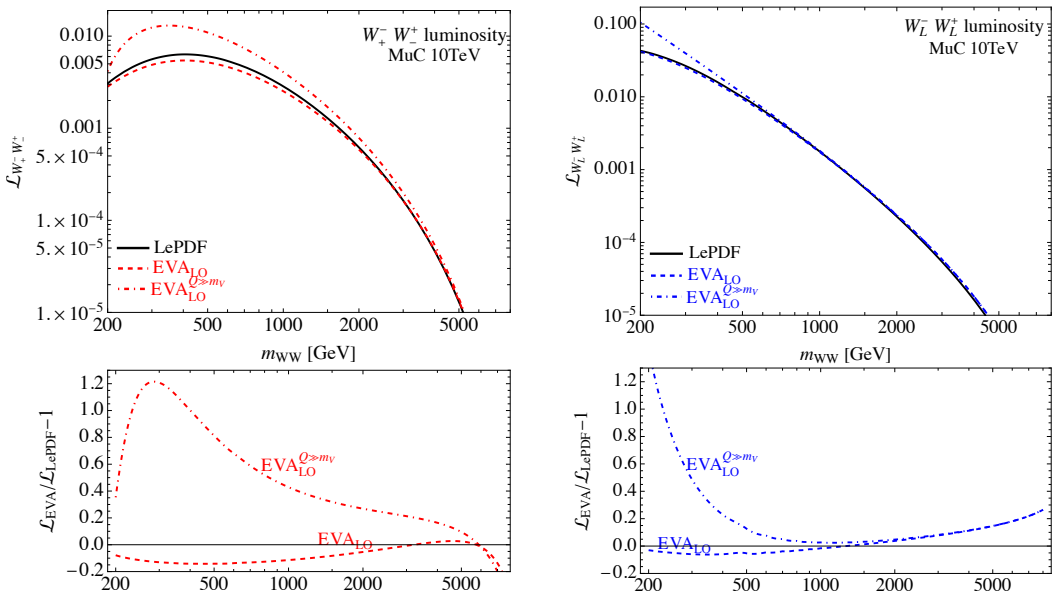

Figure 3.10: Parton luminosities for $W_+^- W_-^+$ (left) and $W_L^- W_L^+$ (right) at a 10 TeV muon collider. We show a comparison with luminosities obtained with the LO EVA result in Eq. (3.15) (dashed) and with the $Q \gg m_W$ approximation, implemented in [65] (dot-dashed).

to $\mathcal{O}(\alpha)$, using the zeroth-order expression for the μ_L PDF:

$$\begin{aligned}\frac{df_{\nu_\mu}^{(\alpha)}}{d\log Q^2} &= \int_x^{1-m_W/Q} \frac{dz}{z}\frac{Q^4}{(Q^2+zm_W^2)^2}\left[\frac{\alpha_2}{4\pi}P_{ff}^V(z)+\frac{v^2}{16\pi^2Q^2}U_{\nu\mu_L}^{W_L^-}(z)\right]\frac{1}{2}\delta\left(1-\frac{x}{z}\right)\\ &= \frac{Q^4}{(Q^2+xm_W^2)^2}\theta\left(1-\frac{m_W}{Q}-x\right)\left(\frac{\alpha_2}{8\pi}P_{ff}^V(x)+\frac{v^2}{32\pi^2Q^2}U_{\nu\mu_L}^{W_L^-}(x)\right)\,.\end{aligned} \tag{3.25}$$

The Heaviside theta is the result of the IR cutoff $z_{\max} = 1-\frac{m_W}{Q}$ in the integral. Integrating this differential equation from m_W^2 up to Q^2 we get:

$$\begin{aligned}f_{\nu_\mu}^{(\alpha)}(x,Q^2) = \frac{\alpha_2}{8\pi}\,\theta\left(Q^2-\frac{m_W^2}{(1-x)^2}\right)\Bigg[P_{ff}^V(x)\Bigg(&\log\frac{Q^2+xm_W^2}{m_W^2}+\\ &+\log\frac{(1-x)^2}{1+x(1-x)^2}+\frac{xm_W^2}{Q^2+xm_W^2}-\frac{x(1-x)^2}{1+x(1-x)^2}\Bigg)\\ &+\frac{2x^2}{1-x}\frac{(1-x)^2Q^2-m_W^2}{(1+x(1-x)^2)(Q^2+xm_W^2)}\Bigg]\,.\end{aligned} \tag{3.26}$$

We observe here the single logarithm due to the standard collinear divergence, while the Sudakov log is absent because the initial muon PDF at zeroth order is just a delta function. It will appear, however, in the computation of an inclusive cross section upon integration of the PDF, due to the $x \to 1$ divergence inside $P_{ff}^V(x)$, that is not cancelled by a virtual correction at the same order but is instead cut off at the W mass by the theta function.

In Figure 3.8 we show a comparison between this $\mathcal{O}(\alpha)$ approximation of the muon neutrino PDF (dashed gray line) with the one from LePDF (solid gray), at a scale $Q =$

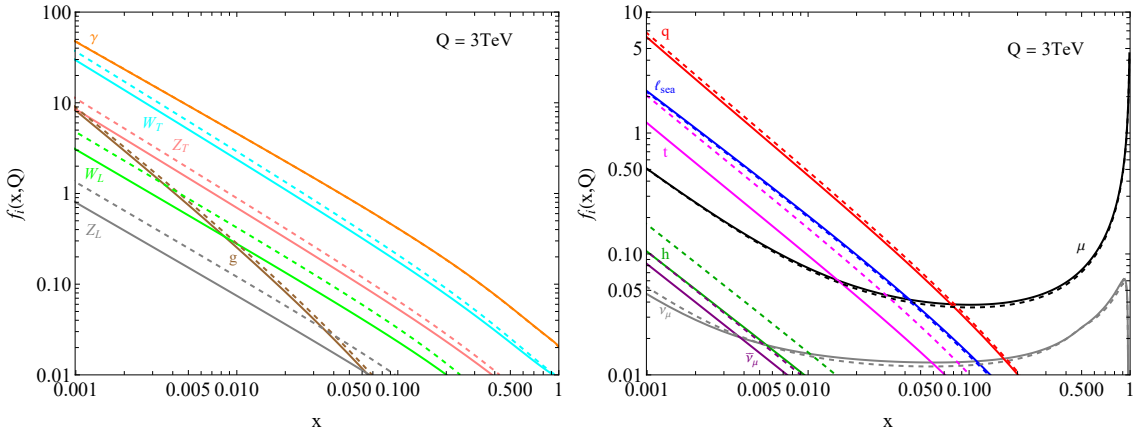

Figure 3.11: PDFs for gauge bosons (left), fermions and Higgs (right) at a scale $Q = 3$ TeV. Solid lines are the full result while dashed ones are obtained neglecting the masses in the propagators. For simplicity in this plot we sum over polarizations.

3 TeV. We observe a very good agreement at large x values, i.e. where the $\mu_L \to W^- \nu_\mu$ splitting dominates. At smaller x values the $\mathcal{O}(\alpha^2)$ contribution from $Z \to \nu_\mu \bar{\nu}_\mu$ will instead dominate. Comparing to the results of Refs. [62, 63], we observe a different behavior of the ν_μ PDF for $x \to 1$: while both our analytic result described above and LePDF show a cutoff (due to the IR m_W cutoff) at $x \lesssim 1$, in their result the ν_μ PDF increases similarly to the muon PDF up to $x = 1$.

3.3.5 Mass effects

We showed in Section 3.2.1 that massive particles modify the virtuality of the particle B as in Eq. (3.8). As already discussed in [55, 64], the impact of the latter effect is important since, due to the presence of the masses in the denominators of the DGLAP equations, the PDFs are lowered or enhanced when $m_{B,C} \neq 0$ and $m_A \neq 0$ respectively. In Figure 3.11 we show the PDFs computed keeping and neglecting the masses in $\widetilde{p}_T$, still starting the evolution of a given massive parton at the scale corresponding to its mass.

For instance, in case of EW gauge bosons (both transverse and longitudinal) one can expect that mass effects lower their PDFs, with the biggest effects at small x due to the $(1-x)$ factor appearing in front of the mass corrections. This can also be verified from the LO EVA in Eqs. (3.15-3.19). In case of the Higgs, its interactions have the form $A \to h + A$, with $A = W, Z, t$, which implies $\delta^2_{p_T} = x^2 m_A^2 + (1-x) m_h^2 > 0$, which explains why the Higgs PDF is bigger when masses are neglected.

3.3.6 Top quark PDF

In Figure 3.12 we compare the results between the 5FS and the 6FS showing the top PDFs together with the PDFs mostly affected by the inclusion of the top. As already mentioned in Section 3.2.3 the top PDFs are mainly driven by the collinear emission off

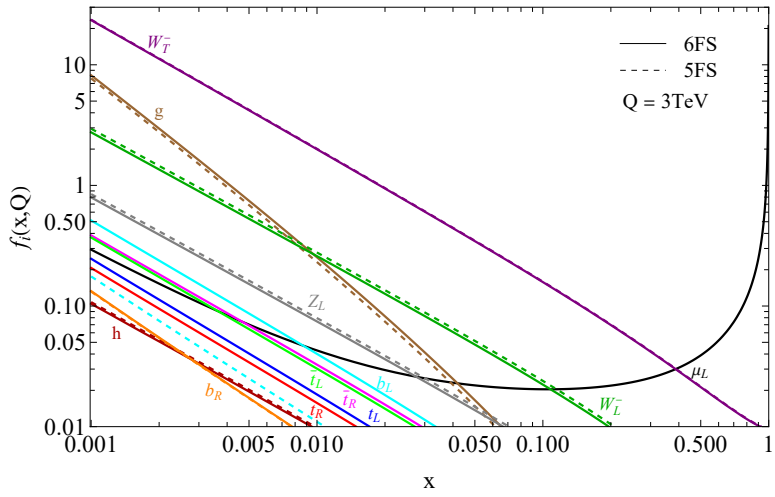

Figure 3.12: Comparison between 5-flavor-scheme (dashed) and 6-flavor-schemes (solid) at a scale $Q = 3$ TeV.

the transverse gauge bosons and the differences are more noticeable in high energies (we use the benchmark $Q = 3$ TeV). Since the PDFs of W_T^- and W_L^- are large compared to the Z and W_T^+, we expect a larger PDF for $\bar{t}_L$ and $\bar{t}_R$ than t_L or t_R. Also, the same splittings $W_T^- \to b_L \bar{t}_L$ and $W_L^- \to b_L \bar{t}_R$ will induce a large enhancement of the b_L PDF compared to b_R in the 6FS.

Additionally, we observe that the PDFs of the EW transverse gauge bosons themselves are almost unaffected, since they are dominated by splitting off a muon. The gluon PDF, instead, receives a noticeable further contribution. Shifts of comparable size are also induced in the PDFs of the longitudinal gauge bosons (and even smaller for the Higgs), but in this case the PDFs are decreased due to a mass effect similar to the ones discussed in the previous Section 3.3.5.

3.3.7 Uncertainties

Here we discuss several sources of uncertainties in our computation. Some are physical, such as the choice of $Q_{\rm QCD}$ or missing higher orders, while others are intrinsic in the numerical implementation of the DGLAP equations and can be improved simply by dedicating more computational time to the task.

QCD matching scale

As already discussed in Section 3.1 the QCD scale $Q_{\rm QCD}$ is not clearly determined and different choices of this parameter can have a non negligible impact on the PDF, in particular for the colored particles. To study the dependence of our results on $Q_{\rm QCD}$ we repeat the evolution for $Q_{\rm QCD} = 0.52$ GeV and $Q_{\rm QCD} = 1$ GeV and we compute the relative

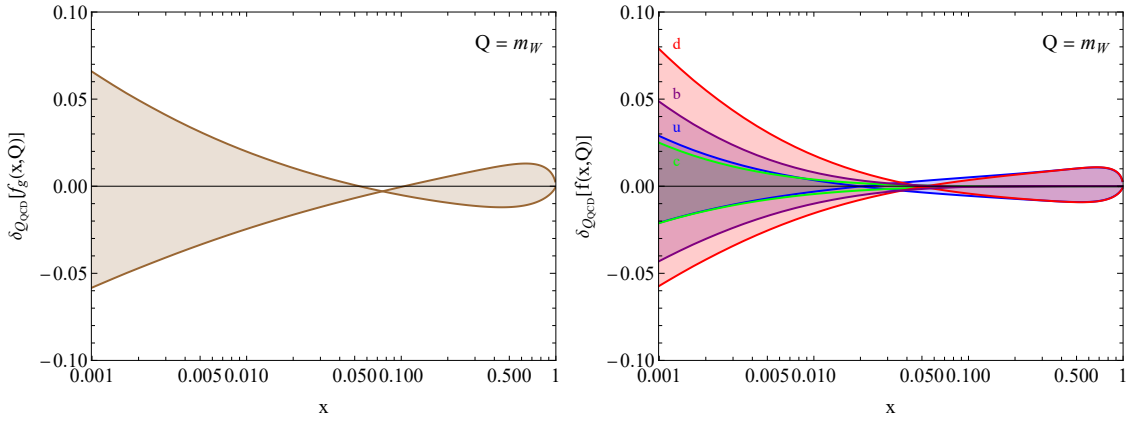

Figure 3.13: Effects of the choice of $Q_{\rm QCD}$ on the PDFs of gluon (left) and quarks (right) at the EW scale $Q = m_W$.

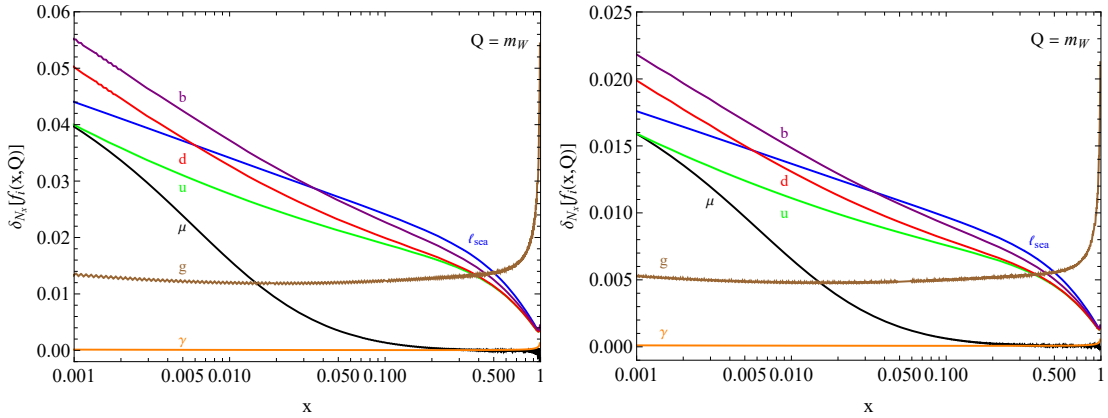

Figure 3.14: Effects of N_x on the PDFs at the EW scale $Q = m_W$. The relative differences correspond to $N_x = \{300; 600\}$ (left) and to $N_x = \{600; 1000\}$ (right).

differences with respect to the chosen value of 0.7 GeV

$$\delta_{Q_{\rm QCD}}\left[f_A(x,Q)\right] = \frac{f_A(x,Q)|_{Q_{\rm QCD}} - f_A(x,Q)|_{0.7\ \rm GeV}}{f_A(x,Q)|_{0.7\ \rm GeV}}, \quad Q_{\rm QCD} = \{0.52\ \text{GeV}, 1\ \text{GeV}\}\,. \tag{3.27}$$

In Figure 3.13 we show the results for the colored particles, which are the most affected by the choice of the QCD scale, while for the photon and the leptons the relative differences are smaller than 10^{-5}. We report the results at $Q = m_W$ after the QED+QCD evolution, since this is the phase in which these effects are stronger.

Discretization

The second source of uncertainty we take into account is the discretization, that is the number of grid bins N_x. Again we focus for simplicity on the first phase of the evolution, since these effects do not change much with the energy scale[9]. As for $Q_{\rm QCD}$ we repeat

[9]We checked that this is actually the case computing the PDFs in the full SM both with $N_x = 600$ and $N_x = 1000$: for instance at a scale $Q = 3$TeV the relative differences are smaller than 2%.

the evolution for different values of N_x and compute the relative differences of the PDFs obtained. The results at the EW scale m_W, obtained varying N_x from 300 to 600 and then to 1000, are reported in Figure 3.14: it is clear that as we increase N_x the relative differences are reduced, as expected since in this way we are approaching the continuum limit. Being the relative difference between $N_x = 600$ and $N_x = 1000$ already of $\mathcal{O}(10^{-2})$, we take the latter as reference value, since a further increase will introduce even smaller corrections.

Integration step

Numerical uncertainties also arise due to the discretization in t, depending on the choice of the integration step dt, as shown in Eq. (B.3). As for the previous cases, we compute the relative differences of the PDFs obtained for two different values of dt, in particular we choose $dt = t(m_W)/N_t$, with $N_t = \{100; 200\}$: this means that we consider N_t steps in the first phase of the evolution. We do not report any plot, since we checked that the relative differences are at most of $\mathcal{O}(10^{-3})$, both at $Q = m_W$ and at higher scales.

Higher orders

The largest theoretical uncertainties in our results originate from neglecting higher order corrections. In particular, in the DL approximation terms of $\mathcal{O}(\alpha_2 \log(Q/Q_{\rm EW}))$ are not consistently resummed [87]. For example, at $Q = 3$ TeV, these terms already amount to 10%, while at $Q = 10$ TeV to 14%. We notice that promoting our approximation to the full LL result does not improve the situation [87], since single-log terms of the same size from the NLL expansion are still present. However, performing the NLO matching as prescribed in Refs. [80] can reduce the uncertainties to 4% for $Q = 3$ TeV. Extending our formalism to NLL order would eventually correspond to $< 3\%$ accuracy regardless of the energy scale.

An estimate of the PDF uncertainties due to missing higher orders is typically obtained by varying the factorization scale. In Figure 3.15 we show with colored bands the envelope, for each PDF, obtained by varying the factorization scale Q by a factor of 1/2 and 2 around the central value of 500 GeV. We see that these uncertainties are small for the photon, the muon and the longitudinal polarization of EW bosons, while they are much larger for the transverse polarizations of W and Z, and for the muon neutrino. This can be understood as follows. The longitudinal W_L and Z_L PDFs receive the dominant contribution from ultra-collinear emission off the valence muon. As discussed in Section 3.2.1, such terms have no logarithmic scaling with Q and approach instead a constant value at large scales, hence the very small scale dependence. The different scale dependence between the photon and muon on the one hand, and W_T, Z_T, and muon neutrino on the other, is due to the fact that the former have a leading contribution from QED interactions starting from the m_μ scale, i.e. scaling as $\log Q^2/m_\mu^2$, while the latter evolve approximately as $\log Q^2/m_W^2$.

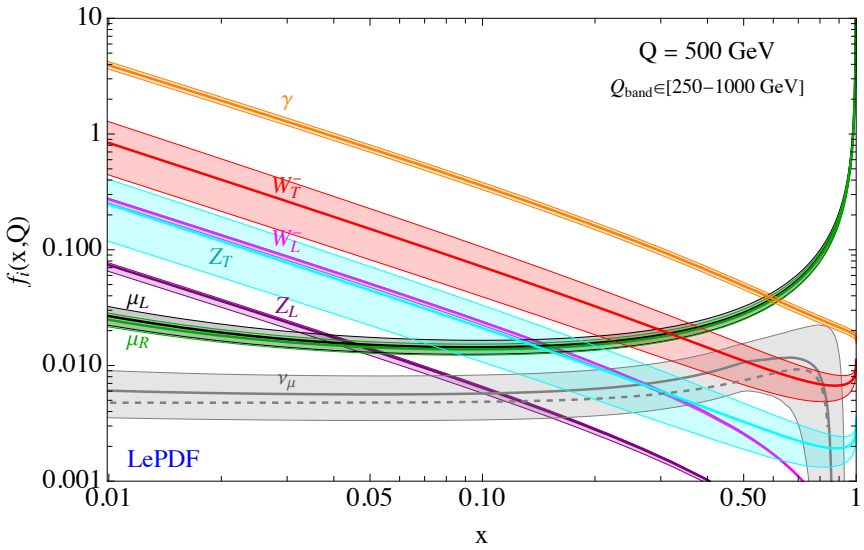

Figure 3.15: PDFs of a muon for a factorization scale $Q = 500\,\text{GeV}$. The uncertainty bands correspond to the envelope obtained changing the factorization scale by a factor of 1/2 and 2. The dashed gray line is the result for the muon neutrino PDF obtained with the $\mathcal{O}(\alpha)$ expression in Eq. (3.26).

A variation of scale by a factor of 2 around 500 GeV gives a relative $\sim 8\%$ effect in the case of QED contributions, compared to a $\sim 38\%$ change for EW ones. It is clear that in order to obtain precise SM predictions such uncertainties should be reduced by deriving higher order EW PDFs. Some discussions on possible extensions to NLL and NNLL can be found in Ref. [56].

3.3.8 PDFs for electron beams

Our numerical code, with obvious substitutions, can also be used to derive LePDFs for electron beams. While most future projects for e^+e^- colliders are focused on EW-scale energies to perform high-precision studies of EW gauge bosons, the Higgs, and top quark, linear collider projects also envisage later stages with TeV-scale center of mass energies. In this case our SM PDFs can provide a useful tool. We therefore provide public PDFs for electron/positron beams alongside those for muons and anti-muons. In Figure 3.16 we show only an example plot for some PDFs of an electron. As for the muon case, in case of EW gauge bosons PDFs we did a comparison with the EVA approximation at LO and NLO, obtaining similar results as shown above for the muon. The main difference in the PDFs of an electron compared to those of a muon is that photon, charged leptons and quarks PDFs are larger. This is due to the longer QED evolution from m_e to m_μ. A consequence of larger quarks PDF is also a larger gluon one, even if $Q_{\text{QCD}} > m_\mu$. On the other hand, EW gauge boson PDFs are very similar since, at first order, their PDF is insensitive on physics at scales below the EW one.

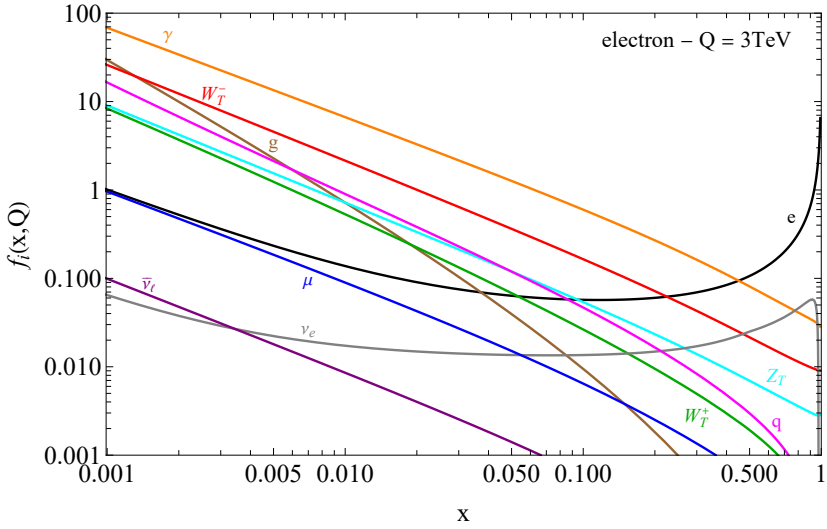

Figure 3.16: In this plot we show some PDFs evaluated at a scale $Q = 3$ TeV for an electron beam. For this plot we sum over polarizations and q represents the sum of all quark PDFs except for the top.

3.4 Assessing the neutrino PDF at a Muon Colliders

In this Section we study processes that show a strong dependence of the neutrino PDF. They could be used as an experimental probe for this contribution, under the assumption that new physics does not introduce a sizeable effect. Specifically, we study $\mu\bar{\mu} \to e^-\bar{\nu}_e$ and $\mu\bar{\mu} \to W^-\gamma$, emphasizing the influence of the ν-induced contribution. These straightforward cases enable us to demonstrate qualitatively and quantitatively the significance of the neutrino PDF.

3.4.1 Single electron production

The main process which could be used as a probe of the muon neutrino PDF is $\mu\bar{\mu} \to e^-\bar{\nu}_e$, where the partonic process we are interested in is

$$\mu^-\bar{\nu}_\mu \to e^-\bar{\nu}_e, \tag{3.28}$$

which proceeds via s-channel W exchange. We refer to this as the signal. The irreducible background arises via vector boson fusion:

$$\begin{aligned} W^-\gamma &\to e^-\bar{\nu}_e, \\ W^-Z &\to e^-\bar{\nu}_e. \end{aligned} \tag{3.29}$$

The Feynman diagrams for these processes are depicted in Figure 3.17. The calculation of the background cross section includes the effect of interference between the photon and transverse Z processes, which is then convoluted with the mixed Z/γ PDF.[10] We neglect

[10] A dedicated study on the effects due to to the $Z\gamma$ PDF at muon colliders is the focus on an upcoming paper [99].

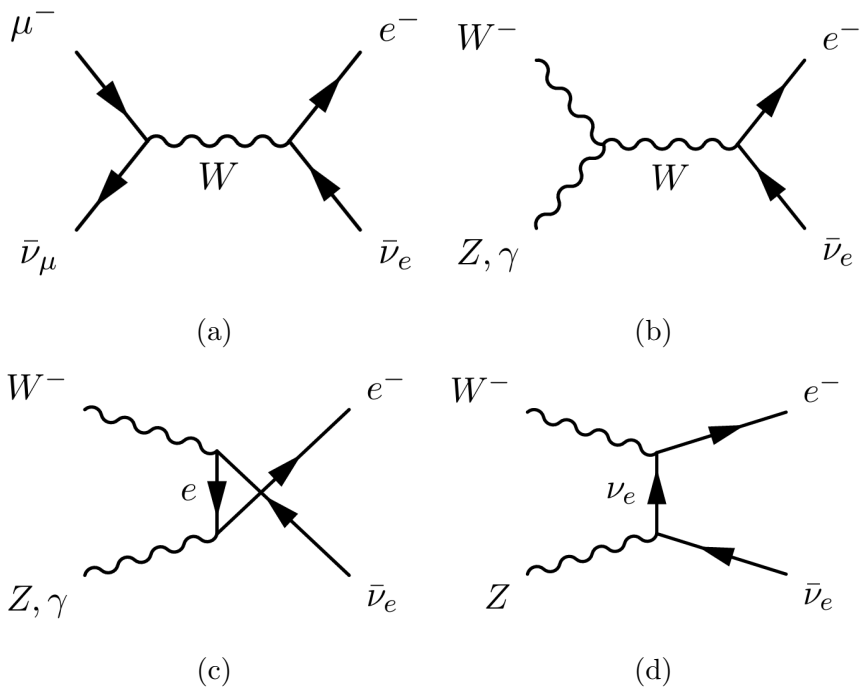

Figure 3.17: Leading partonic diagrams, in the unitary gauge, contributing to $e^-\bar{\nu}_e$ production at a muon collider. (a) is the signal, the others represent the background.

other background processes such as $e^-\bar{\nu}_e \to e^-\bar{\nu}_e$, $\tau^-\bar{\nu}_\tau \to e^-\bar{\nu}_e$, and $d_i\bar{u}_j \to e^-\bar{\nu}_e$, since their effects are further suppressed by small parton luminosities, as discussed in Section 3.3.

As stated above, in order to employ this process to study the neutrino PDF one must assume that new physics is not introducing large effects. A complete evaluation of this question goes beyond our purpose, however we can provide some arguments for why this assumption is reasonable. Possible new physics affecting the signal would also enter the muon decay and leptonic W decays, both of which are tested at the per-mil level or better. The background, on the other hand, could be affected by anomalous triple gauge couplings of EW bosons, which at present are constrained at the percent level [28].

We can start to understand the relative weights of signal and background processes with simple estimates. The partonic cross section of both processes, for partonic invariant masses above the EW scale $\hat{s} \gg m_W$, follows the same scaling $\hat{\sigma}_{\mu\bar{\nu}} \sim \hat{\sigma}_{\rm VBF} \sim \alpha_{\rm EW}^2/\hat{s}$. The physical cross section is obtained by convoluting these with the corresponding parton luminosities in Figure 3.15. Since the $\mu\bar{\nu}_\mu$ luminosity dominates over the VV ones at large invariant masses, we can expect that the signal will dominate the cross section in the high-energy region. This makes the $e^-\bar{\nu}_e$ process particularly sensitive to the neutrino PDF.

The physical triple differential cross sections for both the signal and backgrounds are

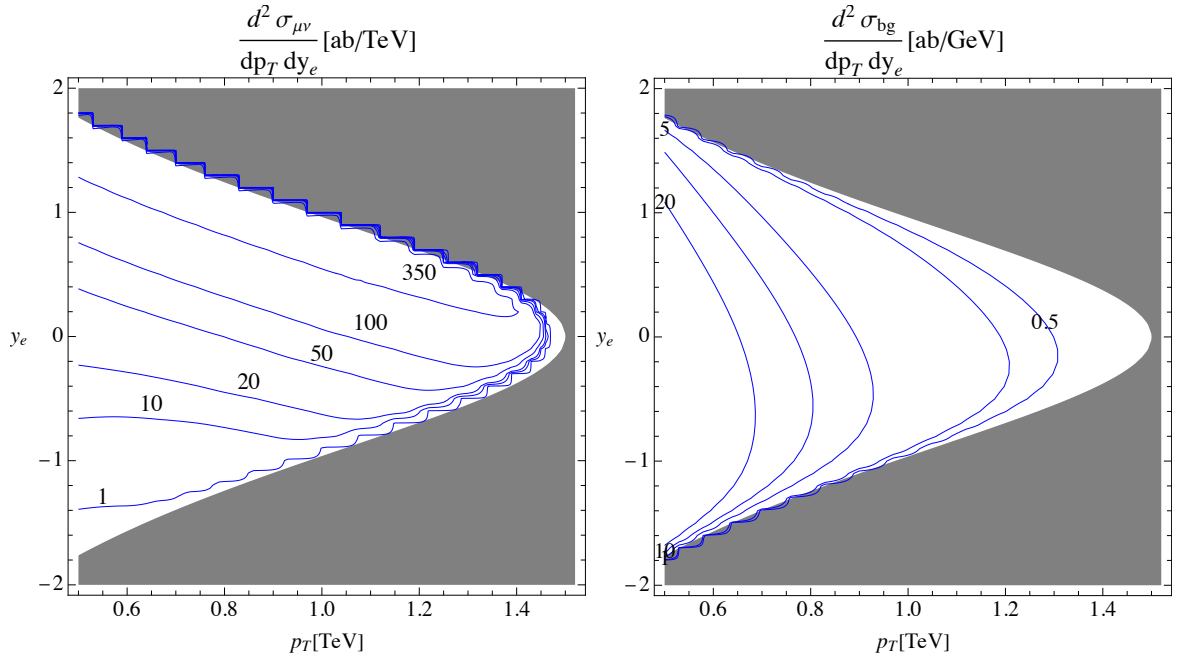

Figure 3.18: Single electron production differential distributions in p_T and y_e for the signal (left) and the background (right) at $\sqrt{s_0} = 3\,\text{TeV}$. The gray regions are kinematically forbidden, see Eq. (C.7).

obtained by convoluting the partonic ones with the PDFs of the initial-state partons:[11]

$$\frac{d^3\sigma(\mu\bar{\mu} \to e^-\bar{\nu}_e + X)}{dy_e dy_\nu dp_T} = \sum_{i,j} f_i^{\mu}(x_1) f_j^{\bar{\mu}}(x_2) \left(\frac{2p_T\hat{s}}{s_0}\right) \frac{d\hat{\sigma}}{d\hat{t}}(ij \to e^-\bar{\nu}_e)(\hat{s},\hat{t}) \ . \tag{3.30}$$

We refer to Appendix C.1 for the expressions of the kinematical variables in terms of the rapidities $y_{e,\nu}$ of the final-state particles and their p_T. Since the neutrino cannot be detected, we integrate in y_ν to obtain the double differential cross section in y_e and p_T. In Figure 3.18 we show the results for the signal and the background for a 3 TeV muon collider. We limit the p_T of the electron to values bigger than 500 GeV in order to ensure the validity of the collinear approximation for EW PDFs: $m_{\text{EW}} \ll E_{\text{hard}} \sim p_T^e$. Electron rapidity is considered in the [-2,2] interval, motivated by the geometrical acceptance of the detector [100].

To get quantitative information on the impact of neutrino PDF on this process, we bin p_T and y_e and integrate to obtain the total cross section in each bin, for both the signal and the background. We also define the following ratio

$$R_{\text{bg}}^{e\nu} = \frac{\sigma(\mu^-\bar{\nu}_\mu \to e\bar{\nu}_e)}{\sigma_{\text{bg}}^{e\nu}}, \tag{3.31}$$

where $\sigma_{\text{bg}}^{e\nu}$ is the background cross section. This ratio quantifies in each bin how much the neutrino induced partonic process contributes to the total cross section and it can be used

[11] The formula is exact when the two partons and the final states are all massless. The generalization to massive partons, which is the case for the background, is straightforward and we checked that differences are negligible in the kinematical regime when collinear factorization can be applied, i.e. $p_T \gg m_W$.

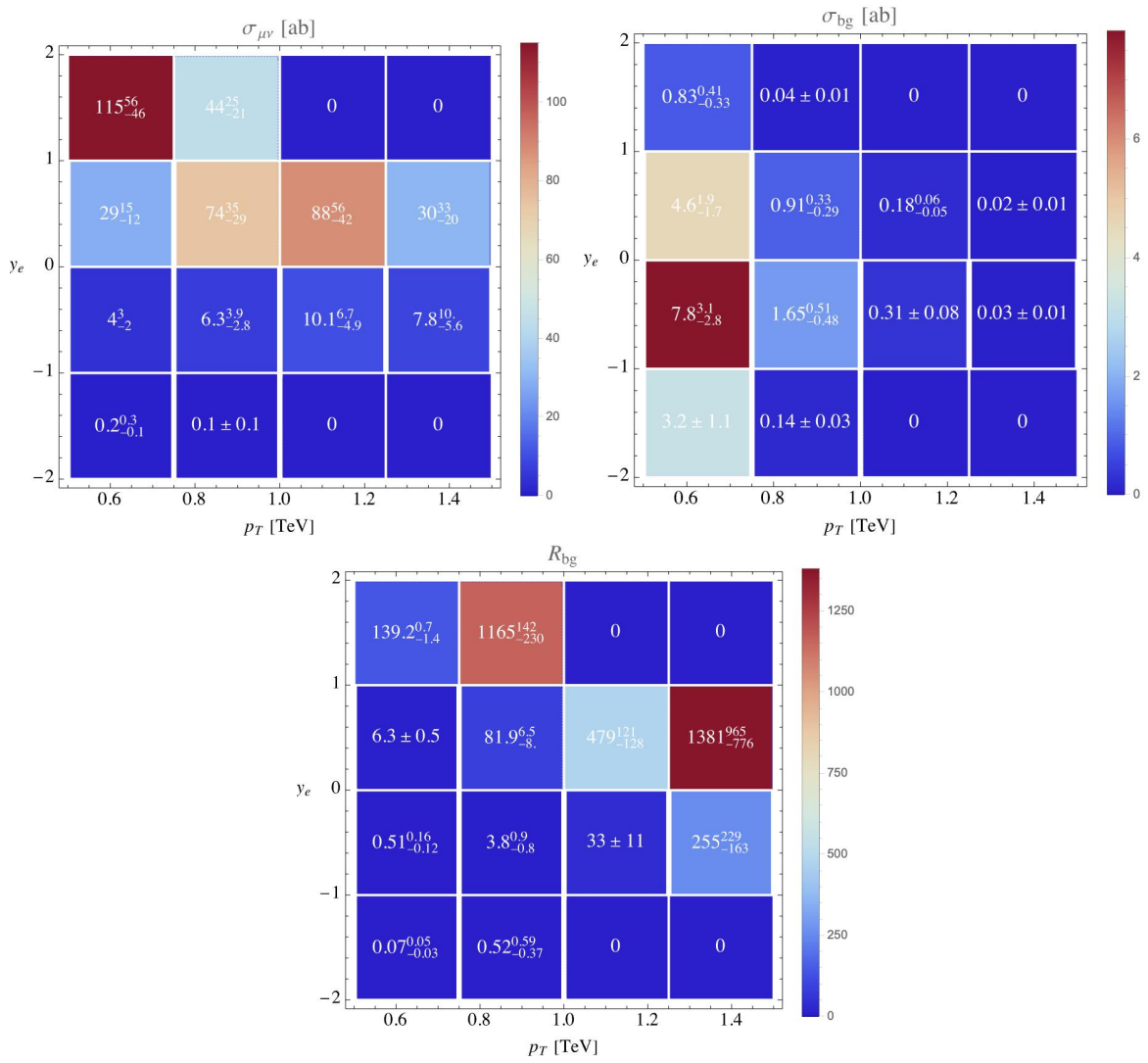

Figure 3.19: Top: Binned cross section for $\mu\bar{\mu} \to e^{-}\bar{\nu}_e$ at a 3 TeV Muon Collider, showing only the signal (left panel) or the background cross section (right panel). Bottom: Ratio of the signal cross section over the VBF background.

to establish the ideal place to look for neutrino PDF contributions, i.e. in bins where both the R_{bg} and the signal cross section are big enough. The results are shown in Figure 3.19. We observe that for the central y_e bins the signal cross section increases with the p_T of the electron, while it decreases in the last bin, meaning that the $1/\hat{s}$ suppression of the partonic process starts dominating over the luminosity enhancement[12]. The background cross section instead always decreases with p_T and, as a result, the ratio $R^{e\nu}_{\text{bg}}$ largely increases. The growth of the signal with y_e is instead due to the form of the partonic cross section, $d\hat{\sigma}/dcos\theta \sim (1 + \cos\theta)^2$, which favors the emission of forward electrons.

[12]In the highest and lowest y_e bins the behaviour is different due to the kinematically suppressed regions.

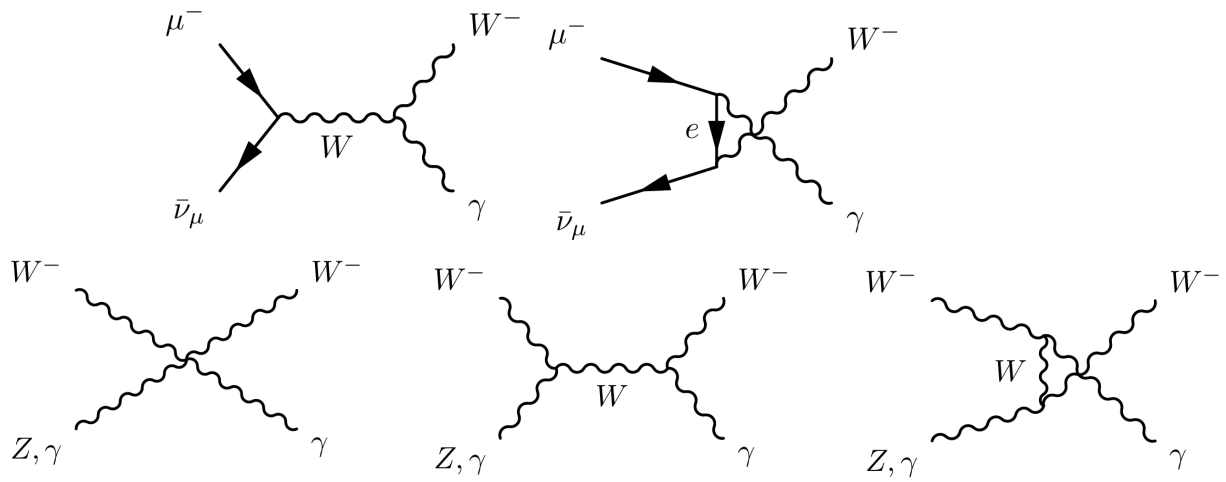

Figure 3.20: Leading partonic diagrams, in the unitary gauge, contributing to $W\gamma$ production at a muon collider, for both the signal (upper line) and the background (lower line).

3.4.2 $W\gamma$ production

The associated production of a photon and a W, $\mu\bar{\mu} \to W^-\gamma$, follows the same lines as the single electron production: at the parton level we have a neutrino induced signal and the background proceeding via vector boson fusion:

$$\begin{aligned} &\mu^-\bar{\nu}_\mu \to W^-\gamma, \\ &W^-\gamma \to W^-\gamma, \\ &W^-Z \to W^-\gamma. \end{aligned} \tag{3.32}$$

The relevant Feynman diagrams are reported in Figure 3.20. As for single electron production, we neglect electron, tau and quark induced background processes due to parton luminosity suppression.

For the same reasons discussed in Section 3.4.1, we assume negligible new physics contribution and we employ this process to study the impact of neutrino PDF. Note that this process is less sensitive to neutrino PDF, since the background partonic cross section $\hat{\sigma}_{\rm VBF}$ is constant at large energies, while as before $\hat{\sigma}_{\mu\bar{\nu}} \sim \alpha_{\rm EW}^2/\hat{s}$.

The analysis is similar to the previous one, but this time, being also the rapidity of the W measurable, we can study distributions at the level of the triple differential cross section. We use again the formula in Eq. (C.1), since factorization holds when the invariant mass of the hard scattering is much bigger than the electroweak scale and we can therefore neglect the masses in our analysis.

We define $R_3^{W\gamma}$ as the ratio between the contribution to the triple differential cross section due to the muon neutrino PDF and the total:

$$R_3^{W\gamma} \equiv \frac{d^3\sigma(\mu^-\bar{\nu}_\mu \to W^-\gamma)}{dy_W dy_\gamma dp_T} \left(\frac{d^3\sigma(\mu\bar{\mu} \to W^-\gamma)}{dy_W dy_\gamma dp_T}\right)^{-1} . \tag{3.33}$$

Iso-lines of the $R_3^{W\gamma}$ are reported in Figure 3.21 for a 3 TeV muon collider.

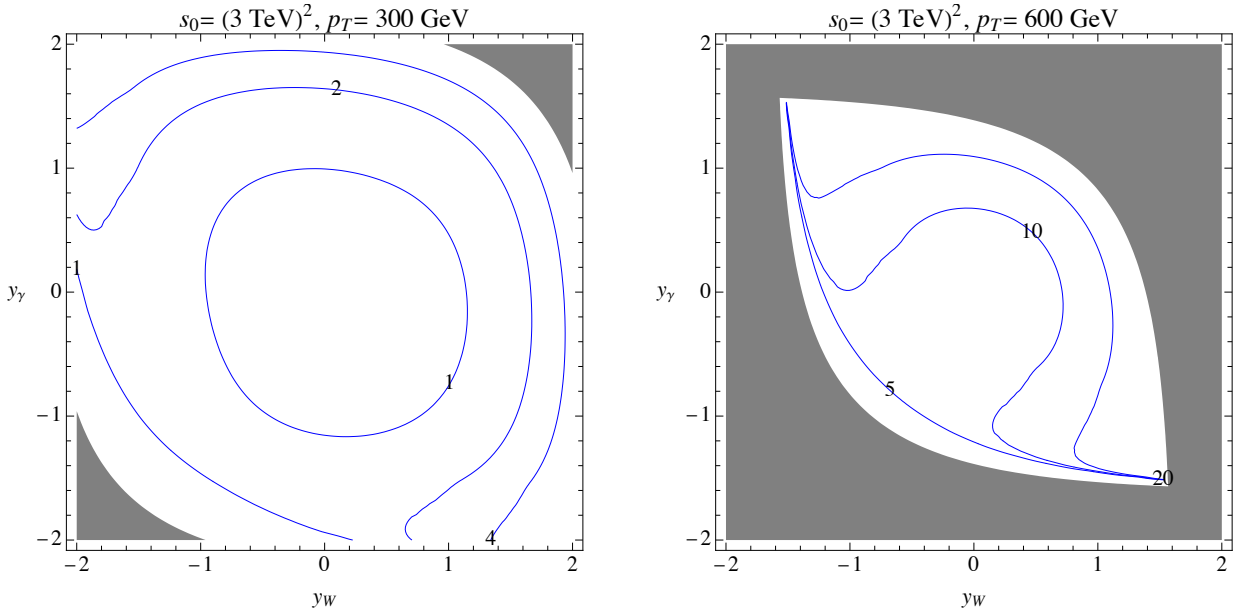

Figure 3.21: Iso-lines of the $R_3^{W\gamma}$ ratio, in percent, as function of the W and photon rapidities, for p_T = 300 GeV (left) and 600 GeV (right), at a 3 TeV muon collider. The gray regions are kinematically forbidden, see Eq. (C.6).

Finally, as we did for the single electron production, we integrate over the W rapidity and then compute the total cross sections in bins of y_γ and p_T[13]. The results are reported in Figure 3.22, where R_{bg} is defined as in Eq. (3.31). The behaviour in p_T is analogous to the case of single electron production, both for the signal and the background cross sections. However, as expected, the latter decreases less rapidly due to the constant partonic cross section and therefore the ratio R_{bg} takes smaller values wrt the previous case, making this process less efficient to measure the impact of muon neutrino PDF.

3.5 Impact of neutrino PDF on Higgs physics at muon colliders

A MuC has the capability to reach very high energies and luminosities, functioning as a Higgs factory [14, 16, 17, 64, 101]. It has been shown that a 3 TeV MuC could reach a precision of $\mathcal{O}(1\%)$ on several Higgs couplings, while a 10 TeV MuC could improve this to $\mathcal{O}(.1\%)$ [102–104]. At this level of precision it will be crucial to provide accurate SM predictions. In this Section we study the impact of the neutrino PDF on the most relevant Higgs production channel at a MuC, that is single Higgs production, occurring through vector boson fusion as shown in Figure 3.23.

If ISR is not considered, the only processes are with initial state $\mu^-\mu^+$. The dominant

[13]We choose to use the photon rapidity being it easier to measure, without the need to reconstruct the W from the decay products.

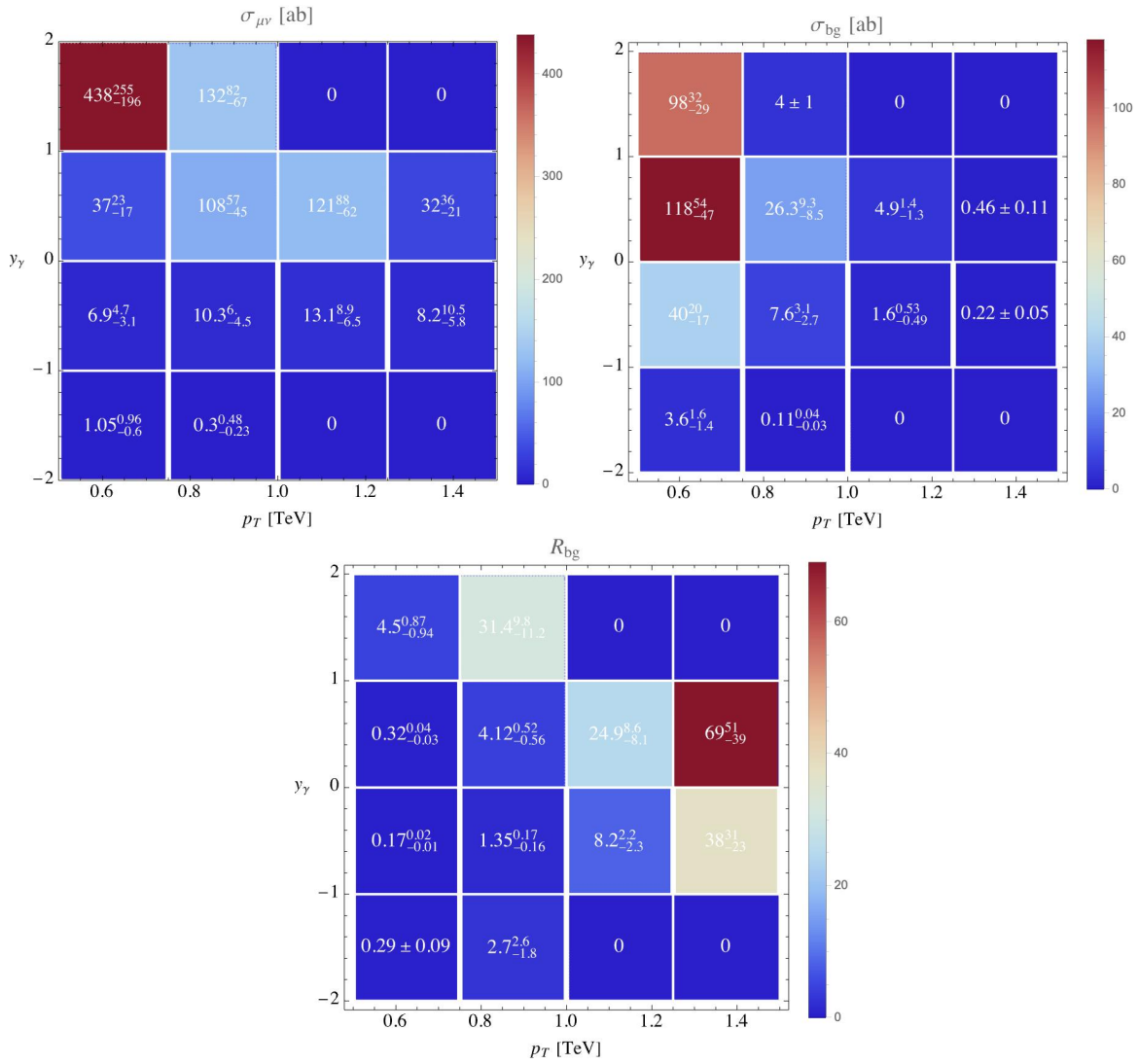

Figure 3.22: Top: Binned cross section for $\mu\bar{\mu} \to W^-\gamma$ at a 3 TeV Muon Collider, showing only the signal (left panel) or the background (right panel). Bottom: Ratio of the signal cross section over the VBF background.

contribution comes from the charged current (CC) channel, $\mu^-\mu^+ \to \nu_\mu\bar{\nu}_\mu H$, followed by the neutral current (NC) one, $\mu^-\mu^+ \to \mu^-\mu^+ H$, which is approximately ten times smaller in magnitude:

$$\begin{aligned} \sigma(\mu^-\mu^+ \to \nu_\mu\bar{\nu}_\mu H)(s) &\approx 498\,\text{fb}|_{\sqrt{s}=3\text{TeV}} \;, \quad 843\,\text{fb}|_{\sqrt{s}=10\text{TeV}} \;, \\ \sigma(\mu^-\mu^+ \to \mu^-\mu^+ H)(s) &\approx 50.8\,\text{fb}|_{\sqrt{s}=3\text{TeV}} \;, \quad 87.4\,\text{fb}|_{\sqrt{s}=10\text{TeV}} \;. \end{aligned} \tag{3.34}$$

As can be seen, the event rate of these two hard scattering processes increases with the total invariant mass. As this is much above the EW scale we are justified in employing the PDF approach to describe the effect of collinear ISR.

Since the partonic hard cross section for single Higgs production increases with the energy, the only relevant partons are the muon and muon neutrino for the muon beam, and their corresponding antiparticles for the anti-muon beam. Being the muon neutrino

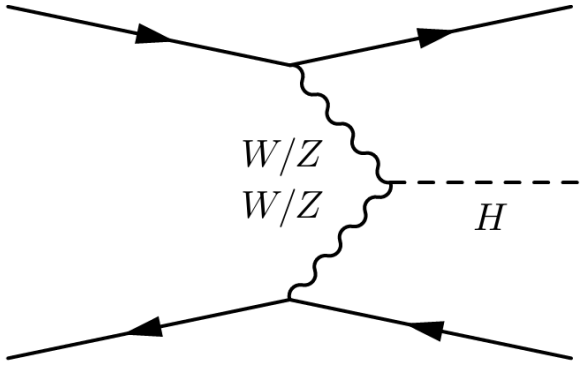

Figure 3.23: Leading partonic diagrams contributing to single Higgs production at a muon collider.

Partonic process	Channel	σ(3TeV) [fb]	σ(10TeV) [fb]
$\mu^-\mu^+ \to \nu_\mu\bar{\nu}_\mu H$	CC	$480.3^{+0.8}_{-0.7}$	$820.9^{+0.6}_{-0.2}$
$\mu^-\mu^+ \to \mu^-\mu^+ H$	NC	$47.7^{+0.6}_{-0.8}$	$80.5^{+1.5}_{-1.7}$
$\mu^-\bar{\nu}_\mu \to \mu^-\bar{\nu}_\mu H$	NC	$2.4^{+1.6}_{-1.2}$	10^{+4}_{-3}
$\nu_\mu\bar{\nu}_\mu \to \mu^-\mu^+ H$	CC	$0.19^{+0.45}_{-0.15}$	$2.4^{+3.0}_{-1.5}$
$\nu_\mu\bar{\nu}_\mu \to \nu_\mu\bar{\nu}_\mu H$	NC	$0.08^{+0.17}_{-0.06}$	$1^{+1.2}_{-0.6}$

Table 3.3: Contributions of the main partonic processes to single Higgs production total cross sections at 3 and 10 TeV MuCs. Uncertainties are obtained varying the factorization scale from $\hat{s}/2$ to $\hat{s}$ and $\hat{s}/4$.

PDF always smaller than the muon one, see Figure 3.4, we expect that processes initiated by $\mu^-\mu^+$ dominate, followed by those induced by $\mu^-\bar{\nu}_\mu$ and $\nu_\mu\mu^+$, while the ones induced by $\nu_\mu\bar{\nu}_\mu$ will be further suppressed. This is confirmed by our numerical results, which include the effects of PDFs by convoluting the partonic total cross sections for single Higgs production with the corresponding PDF pairs, as in Eq. (C.9). Final results for each channel are shown in Table 3.3, for a collider invariant mass of either 3 or 10 TeV. We also report an uncertainty obtained by varying the PDF factorization scales, as discussed in Section 3.3.7.

When using such Higgs production processes to set constraints on Higgs couplings, a framework commonly employed is the one of kappa-factors, that corresponds to multiplying the tree-level Higgs coupling to Z and W bosons by a κ_Z and κ_W factor respectively. The SM prediction is recovered, by definition, for $\kappa_Z = \kappa_W = 1$. Using this framework we can put together the various contributions to the single Higgs production cross section for 3

Cross sections [fb]	No PDFs	Only μ PDF	Both μ and ν_μ PDF
$\sigma^{3\text{TeV}}_{\kappa_W^2}$	498	480 (-3.6%)	480 (+0.04%)
$\sigma^{3\text{TeV}}_{\kappa_Z^2}$	50.8	47.7 (-6.1%)	52.6 (+10%)
$\sigma^{10\text{TeV}}_{\kappa_W^2}$	842	821 (-2.6%)	823 (+0.3%)
$\sigma^{10\text{TeV}}_{\kappa_Z^2}$	87.4	80.5 (-7.9%)	102 (+27%)

Table 3.4: Coefficients of κ_W^2 and κ_Z^2 in single Higgs production cross sections at 3 and 10 TeV MuC. The second column shows the result obtained without considering ISR effects. The third column includes the muon PDF while the fourth column also adds the muon neutrino PDF. In parenthesis we show the relative change from the previous column.

and 10 TeV muon colliders. The results, in fb, are shown in Table 3.4, where we separate the coefficients multiplying κ_W^2 and κ_Z^2:

$$\sigma^{\text{N TeV}}_{\mu\bar{\mu}\to H} = \sigma^{\text{N TeV}}_{\kappa_W^2}\kappa_W^2 + \sigma^{\text{N TeV}}_{\kappa_Z^2}\kappa_Z^2 \ . \tag{3.35}$$

We observe that the coefficient of κ_W^2 is affected mainly by the muon PDF. The change is negative since collinear radiation takes energy away from the valence muon, amounting to a reduction in cross section since the partonic cross section grows with the energy. The effect is approximately 3% at both 3 and 10 TeV muon colliders. The neutrino PDF instead has negligible impact, since the only contribution to $\sigma^{\text{N TeV}}_{\kappa_W^2}$ requires neutrino PDFs in both initial legs, amounting to a large suppression. In case of κ_Z^2 we see a similar depletion due to the muon PDF, now of about 6% (8%) at 3 (10) TeV MuC. The neutrino PDF, that in this case can enter only in one of the two initial legs (via $\mu\bar{\nu}_\mu \to \mu\bar{\nu}_\mu H$ plus the conjugate process), gives a large and positive contribution of about 10% (27%) at 3 (10) TeV MuC.

We can conclude that a proper inclusion of both ISR from the valence muon and the contributions arising from muon neutrino PDF should be included in the SM prediction since the corresponding effects are much larger than the expected statistical precision attainable in these measurements [104].

3.6 Summary

In this Chapter we showed our solution for the set of DGLAP equations for an initial-state lepton, evolving the complete set of PDFs from the infrared up to multi-TeV scales. Our computation is performed with LO splitting functions, keeping into account all relevant mass thresholds, EW symmetry breaking terms, masses of all EW states, and resumming EW Sudakov logs at the double-logarithmic level. The residual uncertainty is dominated by the incomplete single-log EW resummation and can be estimated to be of $\mathcal{O}(10\%)$, while we show that other systematic uncertainties are fully under control.

Polarization effects, due to the chiral nature of SM interactions, are shown to be of $\mathcal{O}(1)$ in Figure 3.7, or even larger than that in case of the b quark. This last effect is due to

the interaction with the top quark via the large top Yukawa coupling, and becomes much smaller in the 5FS, where the top is not included in the evolution. As already observed in previous studies, we confirm that the inclusion of EW states' masses in the propagators gives sizeable correction to the PDFs, even for large factorization scales.

Furthermore, we performed a detailed comparison of our results for the EW gauge bosons PDFs with the widely used Effective Vector Approximation. This comparison, presented in Figure 3.8, illustrates how the EVA fails to describe correctly the transverse EW gauge bosons PDFs at small x values, with deviations reaching even $\mathcal{O}(50\%)$ for $W_T^{\pm}$ and Z_T at large scales, or even missing the target by more than one order of magnitude in case of the off-diagonal Z/γ PDF. The cause of the latter large deviation is the well-known accidental cancellation in the vector-like coupling of a lepton to the Z boson, which does not take place in the full result since the muon gains a strong polarization. The smaller, but still substantial deviations in the PDFs of transverse EW gauge bosons are due to the fact that the EVA, treated at LO, does not include contributions from gauge boson splitting off an initial gauge boson. Such terms, while being formally of higher order, become enhanced due to the large γ, W, Z PDFs and the fact that these splittings come with associated Sudakov double logs. In fact, by extending iteratively the EVA up to $\mathcal{O}(\alpha^2)$ we obtain a much better agreement with the complete numerical result, as shown in Figure 3.9. In light of this, we recommend the use of LePDF to derive precision predictions for SM and BSM processes at high-energy electron or muon colliders (they could also be used for lepton-hadron collisions), when one is interested in being inclusive on radiation emitted at small p_T compared to the typical energy of the hard scattering, $E \gg p_T^{\text{coll.rad.}}$, and when $E \gg m_W$, which are the conditions for factorization to be valid.

As a direct application, we studied the impact of muon neutrino PDF at muon colliders. In particular we showed how it contributes to the two processes $\mu\bar{\mu} \to e^-\bar{\nu}_e$ and $\mu\bar{\mu} \to W^-\gamma$, identifying the kinematical regions in which it is more relevant. Finally the analysis of single Higgs production showed that both muon and neutrino PDFs have to be taken into account in the SM predictions, since its contribution exceeds the expected sensitivity of muon colliders, especially in processes mediated by the Z boson.

Chapter 4

New physics in $b \to s\mu\mu$: MuC vs FCC-hh

In this Chapter we explore a few motivated new physics scenarios relevant for (semi)leptonic B-meson decays. We will assess and compare the prospects at the colliders listed in Table 4.1. The main goal is to compare FCC-hh versus the MuC in the leftover parameter space. The reason for choosing diverse benchmark models is to broadly cover the BSM space. There have already been several prospect studies for some of these models at the FCC-hh [105–111], MuC [111–118], and HL(HE)-LHC [105, 106, 119, 120]. Throughout the Chapter we comment on the similarities and differences between our study and some of the previous ones, being the use of LePDFs one of the main novelties of our analysis.

We start in Section 4.1 with a brief recap on flavor anomalies, showing the status before and after the LHCb update of December 2022, and discussing possible new physics explanations. The relevant physics at the MuC is discussed in Section 4.2 and Section 4.3 reviews the complementary signatures at hadron colliders. In Section 4.4 we consider the most pessimistic scenario, where the new physics states are too massive to be produced on-shell, and then look for the correlated effect of the new semileptonic contact interactions in the high-energy tails. Then we study explicit mediator models, focusing only on tree-level mediators. In Section 4.5 we study two representative examples of the Z' models, where the mediator is a massive gauge boson of a spontaneously broken $U(1)$ gauge symmetry, while in Section 4.6 we consider separately two single-leptoquark simplified models: a scalar weak triplet S_3 and a vector weak singlet U_1, where we use the nomenclature of Ref. [121]. In all the cases we examine scenarios in which the flavor anomalies are either neglected or addressed. Conclusions are given in Section 4.7. In Appendices C.2 and D we report some analytic results for cross sections at MuC and details of our analysis.

Collider	C.o.m. Energy	Luminosity	Label
LHC Run-2	13 TeV	140 fb^{-1}	LHC
HL-LHC	14 TeV	6 ab^{-1}	HL-LHC
FCC-hh	100 TeV	30 ab^{-1}	FCC-hh
Muon Collider	3 TeV	1 ab^{-1}	MuC3
Muon Collider	10 TeV	10 ab^{-1}	MuC10
Muon Collider	14 TeV	20 ab^{-1}	MuC14

Table 4.1: The energy and the luminosity of benchmark colliders. The detector specifications for FCC-hh and MuC are discussed in Appendix D.2. The last column shows the short-hand label for each collider, used for all the sensitivity plots in the Chapter.

4.1 Flavor anomalies

Here we recall the past status of flavor anomalies, i.e. the discrepancies between the SM predictions and the experimental measures in some observables related to $B-$meson decays. These include many angular distributions and branching ratios [122–133] in channels as $B \to K\ell\ell$, $B_s \to \ell\ell$ and $B_s \to \phi\ell\ell$, and two lepton flavor universality violating ratios $R_{K^{(*)}}$ [19, 20, 134–136] and $R_{D^{(*)}}$ [137], defined as

$$R_{K^{(*)}} = \frac{\mathcal{B}(B \to K^{(*)}\mu^+\mu^-)}{\mathcal{B}(B \to K^{(*)}e^+e^-)}, \tag{4.1}$$

$$R_{D^{(*)}} = \frac{\mathcal{B}(B \to D^{(*)}\tau\nu)}{\mathcal{B}(B \to D^{(*)}\ell\nu)}. \tag{4.2}$$

In the following we will focus on $R_{K^{(*)}}$[1]. They are measured for GeV-scale invariant mass of the lepton pairs, $q^2 \in [1.1, 6]\,\text{GeV}^2$, allowing for an extremely clean theoretical prediction: QCD resonances, like the ρ and the J/ψ, lie outside the considered q^2 bin and the branching ratios are therefore dominated by short-distance contributions. The SM result is very simple, $R_{K^{(*)}} = 1$, since interactions are flavor universal and both electrons and muons are effectively massless at these energy scales. The uncertainty is $\mathcal{O}(1\%)$ and it is due to QED [138], while the QCD background is cancelled in the ratio. Any deviation from unity is then a measurement of LFU violation. At the time of our work [139], the measured values [20]

$$R_K^{\text{old}} = 0.846^{+0.044}_{-0.041}, \qquad R_{K^*}^{\text{old}} = 0.69^{+0.12}_{-0.09}, \tag{4.3}$$

combined with the other observables, showed a deviation from the SM. The global significance of the new physics hypothesis, including the look-elsewhere effect, was conservatively estimated to be $4.3\,\sigma$ [140].

[1]The combined measure from BaBar, Belle and LHCb for $R_{D^{(*)}}$ show a discrepancy of $\sim 3\sigma$ with the SM.

As already stated, the discrepancies were due to systematics effects, and the values after the recent LHCb update are [21]

$$R_K = 0.949 \pm 0.047, \qquad R_{K^*}^{\text{old}} = 1.027^{+0.077}_{-0.073}. \tag{4.4}$$

In the rest of the Chapter we will report anyway the analyses performed with the wrong old values in Eq. (4.3): even though the results are now meaningless, they still represent a good example of analysis at future colliders and similar strategies may be adopted in the future if new discrepancies with the SM will show up.

4.1.1 Mediators for R_K

The anomalies could be coherently explained by a short-distance new physics contribution in the underlying quark-level transition $b \to s\mu^+\mu^-$ (we refer to this as $bs\mu\mu$ anomalies in what follows), leading to the existence of a new super-weak Fermi force of $\mathcal{O}(10^{-5})\, G_F$. In analogy with the prediction of the weak scale from G_F, this gave us information about the scale where new mediator states are integrated out. The violation of perturbative unitarity in $2 \to 2$ scattering implied a new state with mass below (roughly) 100 TeV [141]. In other words, there was empirical evidence for a new mass threshold in the vicinity of our present and planned colliders.

When interpreting all of the data in a low-energy effective field theory, a consistent picture of new physics emerged. Using the following effective Hamiltonian [61]

$$\mathcal{H}_{\text{eff}}^{\text{NP}} \supset -\frac{4G_F}{\sqrt{2}} V_{tb} V_{ts}^* \frac{\alpha}{4\pi} \left[\Delta C_9^\mu (\bar{s}_L \gamma_\alpha b_L)(\mu \gamma^\alpha \mu) + \Delta C_{10}^\mu (\bar{s}_L \gamma_\alpha b_L)(\mu \gamma^\alpha \gamma_5 \mu) \right] + \text{h.c.}\,, \tag{4.5}$$

the global fits identified two preferred scenarios: $\Delta C_9^\mu = -0.73 \pm 0.15$ (vectorial muon current), or $\Delta C_9^\mu = -\Delta C_{10}^\mu = -0.39 \pm 0.07$ (left-handed muon current).

There is a finite number of tree-level mediators that can produce a semileptonic four-fermion interaction at low energies. These are bosons, either color singlets or triplets. We restrict our discussion to the Z' (color-singlet vectors) and leptoquarks (color-triplet scalars or vectors).

Heavy neutral vectors are obvious candidates for mediating $b \to s\mu\mu$ transitions at the tree-level [142–164]. The relevant couplings are the ones to the muon current, $g_{\mu\mu}$, and to the flavor-violating sb current, g_{sb}, since the contribution to $b \to s\mu\mu$ transitions is proportional to the product $g_{sb} g_{\mu\mu}$. The same heavy vector mediates also $B_s - \overline{B}_s$ mixing, proportional to g_{sb}^2, thus $g_{sb} \ll g_{\mu\mu}$ was needed for phenomenologically viable models aiming at addressing the flavor anomalies. Furthermore there is a contribution to neutrino trident processes, which gives an upper bound on $g_{\mu\mu}$. As shown in Section 2.3.2, integrating out the Z' we recover the vectorial muon current scenario.

On the other hand, leptoquarks [121] are hypothetical particles that can couple quarks to leptons at the renormalizable level. They are motivated by the idea of quark-lepton unification hinted by the hypercharge quantization in the SM. Interesting examples are

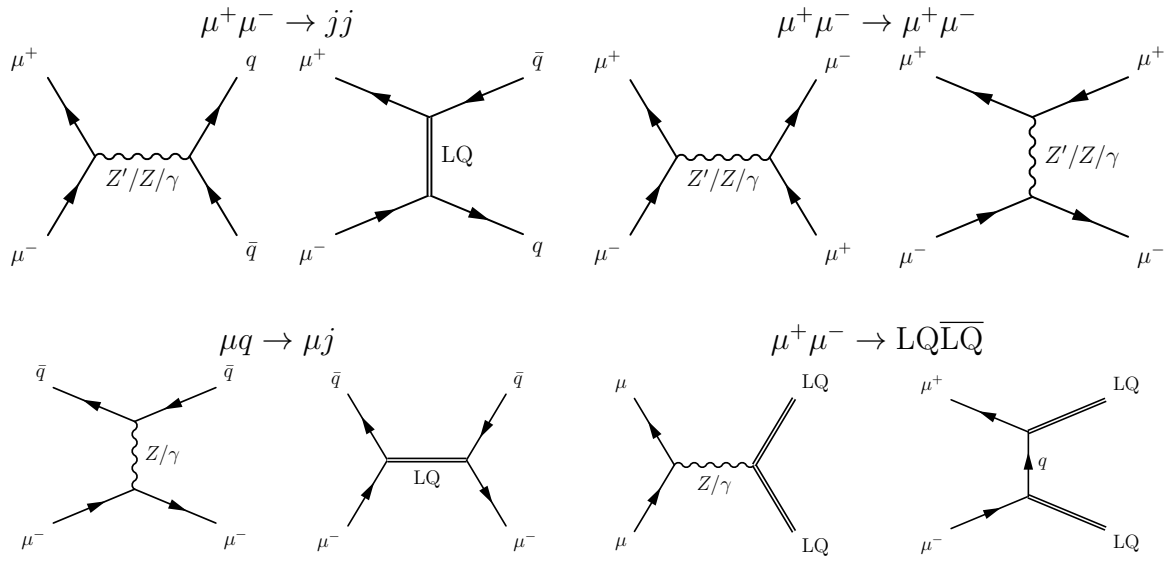

Figure 4.1: Feynman diagrams for the partonic processes relevant for our MuC phenomenology. For the scalar leptoquark S_3 one should exchange $q \leftrightarrow \bar{q}$.

the scalar S_3, with SM quantum numbers $(\bar{\mathbf{3}}, \mathbf{3}, 1/3)$, and the vector $U_1 \sim (\mathbf{3}, \mathbf{1}, 2/3)$, that represented a viable single-mediator solution of the $bs\mu\mu$ anomalies [165]. They reproduce the left-hand muon current scenario once integrated out.

4.2 Signatures at a muon collider

Muon colliders combine the advantages of both proton-proton and electron-positron colliders: high energy reach, where all the collider energy is accessible in $\mu^+\mu^-$ collisions, with high precision measurements, thanks to the low QCD background and clean initial state [14, 15, 64, 166].

In the evaluation of the physics potential of MuC we take into account LePDF of muons, and again we denote the muon (anti-muon) beam as μ ($\bar{\mu}$), while the individual partons are $\mu^\pm, \ell^\pm, \nu_i, q_i, \bar{q}_i, \gamma, W, Z$, etc.

For the Z' and leptoquark benchmark models, the relevant MuC processes are: di-jet and di-tau production from muon annihilation ($\mu^+\mu^- \to jj, \tau^+\tau^-$), Bhabha scattering of muons ($\mu^+\mu^- \to \mu^+\mu^-$), muon-quark scattering ($\mu^\pm q \to \mu^\pm q$, that includes single production of leptoquark), and pair production of leptoquarks ($\mu^+\mu^- \to \mathrm{LQ}\overline{\mathrm{LQ}}$). Except for $\mu q \to \mu q$, all the other processes we study are initiated by $\mu^-\mu^+$, i.e. the valence partons inside the muonic and anti-muonic beam, respectively. As shown in the left panel of Figure 4.2, the $\mu^-\mu^+$ luminosity $\mathcal{L}_{\mu\mu}(m_{\mu\mu})$ grows when $m_{\mu\mu} \to 0$ due to the contribution arising from the splitting of photons and EW gauge bosons, as well as when going closer to the collider energy $m_{\mu\mu} \to \sqrt{s_0}$, with a minimum in the intermediate energies. This behavior is completely different than $q - \bar{q}$ luminosities in proton-proton colliders, where the luminosity monotonously decreases going to higher energies and becomes negligible

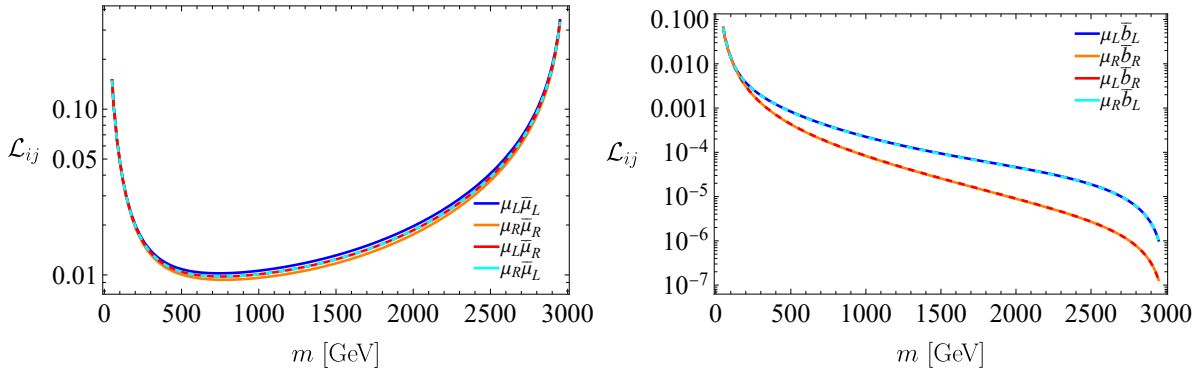

Figure 4.2: Parton luminosities, for $\sqrt{s_0} = 3$ TeV, involving two muons (left) or a muon and a $\bar{b}$ (right).

well before the kinematical limit of the collider. This difference is important to understand our numerical results. In a MuC, if the new physics has a mass below the collider energy one can look for its effect both in the shape of the cross section (a resonance peak or a $t(u)$-channel exchange) for $m_{\mu\mu} < \sqrt{s_0}$ as well as in the very precise measurement of the cross section at the highest invariant mass bin, $m_{\mu\mu} \approx \sqrt{s_0}$. The latter method works much better at MuC compared to similar methods at hadron colliders, see e.g. [167, 168], thanks to the large parton luminosity, lower theory uncertainties, and cleaner collider environment. For new physics states heavier than $\sqrt{s_0}$, instead, the sensitivity arises only from the latter strategy.

In the following we provide more details for each of the MuC processes we studied. The differential cross sections are derived after computing analytically the partonic cross sections of the $2 \to 2$ processes (see Appendix C.2) and convoluting them with the parton luminosities of the initial state.

4.2.1 Di-jet

This process is dominated by the inverted Drell-Yan (IDY) channel $\mu^+\mu^- \to jj$ shown in Figure 4.1. Due to the non-negligible muon neutrino PDF in the muon beam (see Figure 3.4), a sub-leading but relevant contribution is induced by the charged-current channel $\nu_\mu\mu^+ \to jj$ and its conjugate, while the purely neutrino-induced channel $\nu_\mu\bar{\nu}_\mu \to jj$ is suppressed by the $\nu_\mu\bar{\nu}_\mu$ luminosity, that is always a factor of at least ~ 10 smaller than the $\mu^+\mu^-$ one. In light of this, in our analysis of the di-jet channel we include both $\mu\mu \to jj$ and $\nu_\mu\mu \to jj$, but neglect the purely neutrino-induced process. On the other hand, the QCD contribution $q(g)\bar{q}(g) \to jj$ is always negligible due to the quark and gluon PDF suppression.

Muonic IDY is very sensitive to new physics coupled to muons and quarks, as in our benchmark models. After integrating over angular distributions, we construct the di-jet invariant mass bins following the hadronic calorimeter resolution described in Appendix D.2. In Figure 4.3 (left) we show the SM IDY cross section for a 3 TeV MuC (orange)

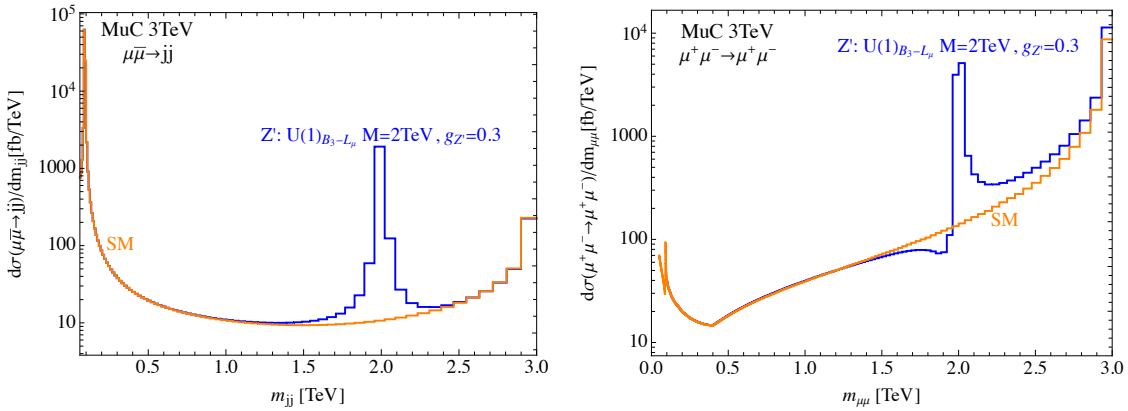

Figure 4.3: Differential cross sections for inclusive IDY $\mu\bar{\mu} \to jj$ (left) and $\mu^+\mu^- \to \mu^+\mu^-$ (right) for a 3 TeV MuC, taking into account muon PDFs. The SM cross section is shown in orange, while the prediction for a Z' resonance in the $U(1)_{B_3-L_\mu}$ model with $m_{Z'} = 2$ TeV and coupling $g_{Z'} = 0.3$ is shown in blue.

as well as the contribution from a Z' resonance (blue) (for details on the specific model see Section 4.5). We observe that, due to the $\mu^+\mu^-$ PDF luminosity and the shape of the SM partonic cross section, the convoluted SM cross section decreases above the Z boson invariant mass, to then increase again when the m_{jj} invariant mass approaches the collider energy $\sqrt{s_0}$. This behaviour of the SM cross section has important implications for the new physics searches. In case of a four-fermion contact interaction, the strongest sensitivity is obtained from the last few bins, where both the cross section and the energy are largest. For s-channel resonance searches, instead, the peak typically provides the dominant sensitivity. In particular, the bulk of the sensitivity is given not so much from the shape of the (possibly narrow) peak as from its integrated contribution to the cross section. Finally, a non-negligible contribution comes from the precision measurement of the cross section in the highest-energy bin. In Figure 4.4 we compare the constraints on a Z' resonance from a gauged $U(1)_{B_3-L_\mu}$ model (see Section 4.5.1 for details) at MuC3 from $\mu\bar{\mu} \to jj$. The solid red line is obtained employing the full calorimeter resolution, the dot-dashed green prospect instead uses a few bins much larger than the resonance width ([0.15-0.3-0.7-2-3] TeV), and finally the dashed blue prospect is obtained by considering only the very last invariant mass bin ([2.9-3] TeV). This also shows that the specific choice we employ for the calorimeter resolution does not affect much our results.

In case of leptoquark exchanged in the t-channel, since no sharp resonance or feature is present, as can be seen from the differential cross section in Figure 4.5 (left), the dominant contribution to the sensitivity comes from the precise cross section measurement in the last bins. In Ref. [115] it was shown that studying the rapidity distribution of the final state jets could provide additional handles to increase the signal to background ratio for leptoquarks.

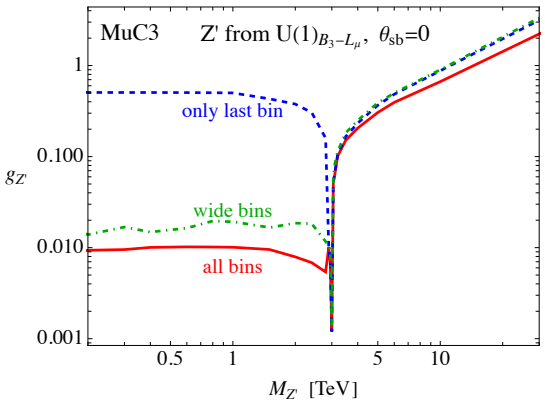

Figure 4.4: Comparison of 5σ discovery prospects for a Z' in a gauged $U(1)_{B_3-L_\mu}$ model (see Section 4.5.1) at MuC3 from $\mu\bar{\mu} \to jj$ using the full di-jet resolution (solid red), a few large bins (dot-dashed green), and only the last invariant mass bin (dashed blue).

4.2.2 Di-tau

This process is sensitive to the s-channel exchange of a Z' vector boson coupled to both muon and tau leptons. It is particularly relevant for the baryophobic models such as the $U(1)_{L_\mu - L_\tau}$ detailed in Section 4.5.2. A proper analysis of this channel is complicated by the fact that tau leptons decay into neutrinos, implying that the total invariant mass can not be properly reconstructed. Other kinematical variables, such as the transverse mass m_T, are therefore typically considered. These, however, can only be obtained by letting the tau leptons decay and performing a full-fledged collider analysis (see e.g. [169]). This is well beyond our scope. Instead, to estimate conservatively the reach in this channel we consider directly the di-tau invariant mass as our kinematical variable but, to take into account the reconstruction issues due to the neutrinos in the final state, we consider only very wide $m_{\tau\tau}$ bins: [0.15-0.5-2-3] TeV and [0.15-0.5-2-5-10] TeV for the MuC3 and MuC10, respectively. We checked that modifying these bins does not affect substantially the result, as expected in light of the result shown in Figure 4.4 for $\mu^+\mu^- \to jj$. Furthermore, we assume conservatively the efficiency for the di-tau detection to be 70%, see [113].

4.2.3 Di-muon

The partonic-level process which by far dominates the di-muon production cross section is the Bhabha scattering $\mu^+\mu^- \to \mu^+\mu^-$, see Figure 4.1. This signature is employed in the context of our $U(1)_{L_\mu - L_\tau}$ detailed in Section 4.5.2. The SM differential cross section (orange) as well as a benchmark Z' contribution (blue) are shown in Figure 4.3 (right). We impose a cut on the lab-frame rapidity $|y_{\mu^\pm}| < 2$ by integrating numerically the triple differential cross section from Eq. (C.8). The di-muon invariant mass bins are constructed following the muon p_T resolution described in Appendix D.2.

As in the IDY channel, the SM cross section first decreases and then increases again

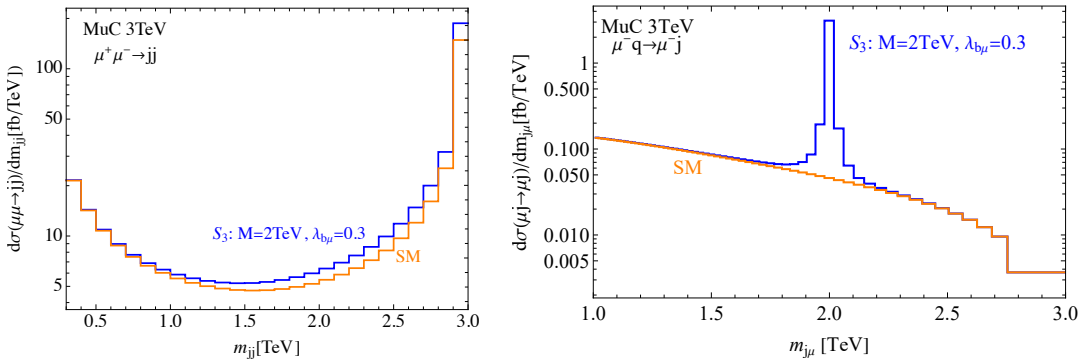

Figure 4.5: Differential cross sections for inclusive $\mu^+\mu^- \to jj$ (left) and $\mu^- q \to \mu^- j$ (right) for a 3 TeV MuC. The SM cross section is shown in orange, while the prediction for the S_3 resonance with $m_{S_3} = 2$ TeV and coupling $\lambda_{b\mu} = 0.3$ is shown in blue.

when approaching the collider energy. Similarly to the exchange of the SM neutral electroweak bosons, a Z' can be exchanged both in the s and t channels, inducing the typical interference pattern exhibited in Figure 4.3. For masses $M < \sqrt{s_0}$, the sensitivity is obtained by a combination of the resonance peak and the precise measurement of the cross section in the last bin, similarly to what is seen in the di-jet channel. We note that, if the Z' mass is sufficiently small ($M \ll \sqrt{s_0}$), the cross section measurement in the last bin depends only on the resonance coupling $g_{Z'}$. On the other hand, if $M \gg \sqrt{s_0}$ then the new physics effect can be described as a four-muon contact interaction and the sensitivity is dominated by the precision measurement of the cross section in the highest invariant mass bins.

This final state, as well as the $\tau^+\tau^-$ one, have been already studied in Refs. [113, 116, 170] in the context of a $U(1)_{L_\mu - L_\tau}$ model. However, the previous literature does not employ muon PDFs. Instead, the PDF effect is approximated by the real soft photon emission process $\mu^+\mu^- \to \ell^+\ell^-\gamma$, where the photon is not detected. On the other hand, the production process of a Z' in association with a hard photon improves the sensitivity for low masses and could offer additional handles to detect the resonance. Since, as we will see, $\mu\mu \to \mu\mu$ covers a large portions of the parameter space already at the 3 TeV MuC, we will not consider the $Z'\gamma$ processes in this work.

4.2.4 Mono-lepton plus jet

This channel offers the unique possibility of producing, in a $2 \to 2$ process, an s-channel resonance that couples directly to quarks and leptons, i.e. a leptoquark. See the relevant diagrams in Figure 4.1 for the partonic process $\mu q \to \mu q$. When the mass of a leptoquark is lower than $\sqrt{s_0}$ of the MuC, the dominant signal would appear as a peak in the invariant μj mass distribution, $m_{\mu j}$. As an example, we show in Figure 4.5 (right) the S_3 leptoquark resonance (blue) over the SM background for a 3 TeV MuC (orange). An analogous peak

appears in the U_1 leptoquark s-channel exchange. For more details about the leptoquark models see Section 4.6. Due to the absence of additional hard leptons or jets in the final state, this process is different than the more typical on-shell single-production of leptoquarks (see e.g. Ref. [115]).

Notice that the parton luminosities involving a muon and a quark are rapidly decreasing for higher $m_{\mu j}$ (see Figure 4.2), because the quark content of the lepton vanishes in the limit $x \to 1$. As a result, the sensitivity to the resonance peak is stronger at values of $m_{\mu j}$ lower than the collider energy $\sqrt{s_0}$.

Lastly, if the mass of a new physics mediator is larger than the collider energy, the induced contact interaction mostly manifests in the highest energy bins available, compatibly with the luminosity decrease. Yet, the sensitivity reach in this case is considerably weaker than in the case of the t-channel exchange in $\mu^+\mu^- \to jj$, as it can be seen from the derived limits in Section 4.6.

4.2.5 Leptoquark pair production

This channel is dominated by the partonic process $\mu^+\mu^- \to \mathrm{LQ}\,\overline{\mathrm{LQ}}$ for M_{LQ} close to $\sqrt{s_0}/2$, where all the PDFs except the muon one (and muon neutrino, to a lesser extent) are completely negligible. We thus compute analytically the partonic cross section considering the Z/γ exchange in the s-channel, the quark exchange in u-channel and their interference, see the diagrams in Figure 4.1, and then convolute with muon PDFs to obtain the total cross section. We consider only the case of on-shell leptoquarks. In order to estimate the MuC reach on this channel we requiring that at least 100 events of pair-produced leptoquarks are generated. This number is compatible with the one obtained by the more detailed analysis of [112, 115], assuming a $\mathrm{Br}(LQ \to b\mu) \sim \mathcal{O}(1)$. As one might expect, we find that the leptoquark mass reach from pair production is approximately given by $M_{\mathrm{LQ}}^{\mathrm{reach}} \approx \sqrt{s_0}/2$, and this is fairly independent on the precise number of events required.

A full collider simulation of this process and its backgrounds is beyond the purpose of this paper, and we refer to [112, 115] for a more detailed study of both leptoquark pair and single production at muon colliders.

4.3 Signatures at a hadron collider

In this Section, we highlight the processes at hadron colliders subject to our numerical studies. We use the current LHC data from CMS and ATLAS collaborations to set the 95% CL limits that define the targeted parameter space for all considered models to be explored at future colliders.

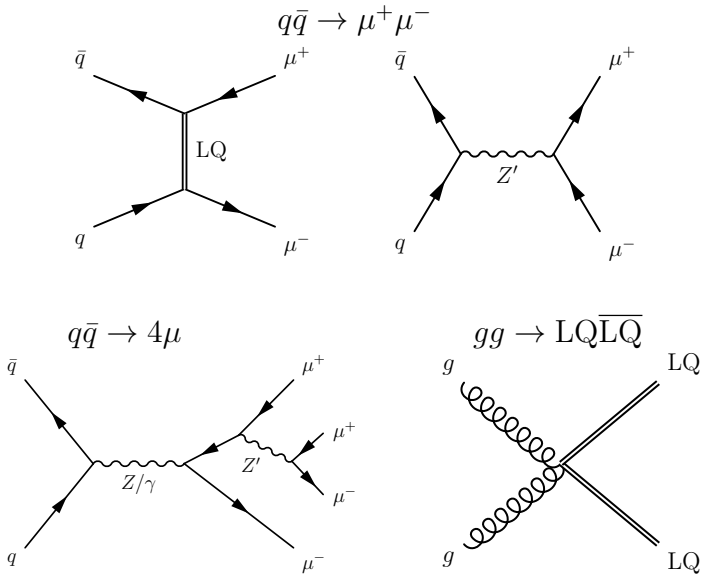

Figure 4.6: Sample Feynman diagrams for the partonic processes relevant at hadron colliders. For the scalar leptoquark S_3 one should exchange $q \leftrightarrow \bar{q}$.

4.3.1 Di-muon

Following Ref. [171], a short-distance new physics above the electroweak scale contributing to the (semi)leptonic B-meson decays generically predicts a correlated effect in the Drell–Yan (DY) process ($pp \to \mu^+\mu^-$). In particular, a Z' would show up as an s-channel resonance, while a leptoquark would lead to a non-resonant effect via a t-channel contribution, see Figure 4.6 for the respective Feynman diagrams. Should the mass of these mediators be above the accessible di-muon invariant mass spectrum, their impact would be described by a four-fermion quark-lepton interaction considered in Section 4.4. Such interactions modify the high-invariant mass tails of the DY process [169, 171–196]. After specifying the quark flavor structure for a given operator, the sensitivity in the tails can be compared to those from the low-energy flavor physics.

The production cross section depends crucially on the quark flavors involved in the initial state. For example, quark-flavor universal Z' models with $B/L_\mu \sim \mathcal{O}(1)$ and MFV in the quark sector are already very well tested by current DY data at LHC. The dominant production channel in these models is due to the valence quarks, and it is enhanced because of their large PDFs. Here, we only consider models in which the dominant couplings are with the heavy flavors, so that they can evade LHC searches thanks to the suppression from the sea quark PDFs. In Section 4.5.1 we investigate the $U(1)_{B_3-L_\mu}$ gauge extension of the SM where the Z' primarily interacts with the third generation of quarks and second generation of leptons. The dominant DY channel in this model is the $b\bar{b}$ fusion. In Section 4.6, we derive the DY limits on the leptoquark models. While the main results are summarised in the aforementioned sections, the technical details of the numerical studies are discussed in Appendix D.3.

4.3.2 Multilepton

The multilepton production at hadron colliders is relevant for a class of Z' models in which the coupling to leptons is considerably larger than the coupling to quarks. The case study example is the $U(1)_{L_\mu - L_\tau}$ gauge model considered in Section 4.5.2. The Drell-Yan channels correlated with the $b \to s\mu^+\mu^-$ decays ($b\bar{b}$, $s\bar{s}$, $s\bar{b}$ and $b\bar{s}$) are not only PDF-suppressed but are induced from a relatively small coupling in comparison with the muonic coupling. As we will show later, even the FCC-hh will have difficulties discovering such a scenario in $pp \to \mu^+\mu^-$. On the other hand, a Z' can be emitted from a muon in the charged or neutral current Drell-Yan leading to three or four muons in the final state after Z' decays. A representative Feynman diagram for $pp \to \mu^+\mu^- Z' \to 4\mu$ is shown in Figure 4.6. In this work, we calculate the HL-LHC and the FCC-hh discovery projections (the technical details are left for the Appendix D.3). A qualitative comparison is made with Ref. [170] which derives the 95% CL limits at the HL-LHC setting up a different analysis strategy.

4.3.3 Leptoquark pair production

Leptoquarks are colored particles and therefore they can be easily produced in hadron colliders thanks to the QCD interactions [197–204]. The representative Feynman diagram is shown in Figure 4.6. The production cross section is set by α_s and by the leptoquark mass and its spin.[2] When a leptoquark coupling to a quark and a lepton ($q\ell$-LQ) is large, there is an additional contribution to the pair production coming from the t-channel lepton exchange [203]. This contribution is numerically relevant only in the parameter space where the Drell-Yan already provides better constraints.

While the $q\ell$-LQ coupling can be neglected in the production of leptoquark pairs which is mainly due to QCD, it is very important for the decay channels. In our model examples, a leptoquark decay to μj has a sizeable branching ratio, see Section 4.6. The FCC-hh projections for the scalar leptoquark pair production in $\mu^+\mu^- jj$ final state have been derived in Ref. [107]. We translate these bounds for the vector leptoquark using the toolbox of Ref. [201] based only on the total cross section and neglecting the differences in the kinematics. Other on-shell leptoquark production mechanisms at hadron colliders, such as the single [201, 205, 206] and the resonant [51, 207–209] production, are left for future studies. A common expectation is that for leptoquarks dominantly coupled to heavy quarks, the phenomenology at hadron colliders is charted mainly by the pair production and the non-resonant contributions to the Drell-Yan, see [182, 201, 208].

[2]The cross section for the vector leptoquark U_1 also depends on another model-dependent coupling, see Eq. (4.26). For concreteness, we will assume that U_1 is a massive gauge boson of a Yang-Mills theory.

4.4 Contact interactions

New physics states heavier than the energies accessible for on-shell production can still leave a trace in higher-dimensional operators of the SMEFT. Discovering a new contact interaction, albeit at high energies, would still provide a valuable piece of information about the new physics. In particular, two effective operators in the SMEFT that match at tree-level to the low-energy operators relevant for $bs\mu\mu$ anomalies (and semileptonic decays in general) are

$$\mathcal{L}_{\rm SMEFT} \supset [C_{\ell q}^{(1)}]_{22ij}(\bar{l}^2\gamma_\alpha l^2)(\bar{q}^i\gamma^\alpha q^j) + [C_{\ell q}^{(3)}]_{22ij}(\bar{l}^2\gamma_\alpha \sigma^a l^2)(\bar{q}^i\gamma^\alpha \sigma^a q^j) \ , \tag{4.6}$$

where q^i and l^i are the SM left-handed quark and lepton weak doublets and $i,j = 1,2,3$ are flavor indices. The flavor alignment is to the down-quark mass basis, $q^i = (V_{ji}^* u_L^j, d_L^i)^T$, $l^i = (\nu_L^i, e_L^i)^T$, where u_L^i, d_L^i, e_L^i fields are already the mass-eigenstates and the neutrinos are assumed to be massless.

At the LHC and the FCC-hh, these operators give a correction to the high invariant mass neutral-current DY tails $pp \to \mu^+\mu^-$ [171] as well as to charged-current DY $pp \to \mu\nu$. For the latter we adapt the prospects derived in Ref. [179].[3] At muon colliders these operators contribute to the high invariant mass di-jet production from both the neutral-current ($\mu^+\mu^- \to jj$) and charged-current processes ($\mu^+\nu_\mu \to jj + h.c.$).

4.4.1 MFV scenario

To begin with, we first study the MFV scenario (see Section 2.3.1 for details) in the quark sector. We assume the $U(3)_Q$ flavor symmetry in Eq. (4.6), leaving us with two universal and real parameters: $[C_{lq}^{(1)}]_{22ij} = C_{lq}^{(1)}\delta_{ij}$ and $[C_{lq}^{(3)}]_{22ij} = C_{lq}^{(3)}\delta_{ij}$. Breaking the symmetry by the insertions of the quark Yukawa matrices does not impact the Drell-Yan bound, however it induces contributions to mesonic decays [171].

In Figure 4.7 we show the projected 95% CL limits for various future colliders, compared with the present exclusion from the recast of the CMS search [211] (solid black line), see Appendix D.3 for details. Shown in the right plot is a zoom-in view around the origin of the left plot.

Interestingly, MuC and FCC-hh probe complementary directions in the parameter space. While the MuC3 shows just slightly better sensitivity than the HL-LHC, the MuC10 is comparable with the FCC-hh. One of the reason for this is that at hadron colliders the production cross section is enhanced by the valence quarks. As we show in the next Section, when the dominant interaction is to heavy quark flavors, already MuC3 is comparable with the FCC-hh.

[3] We translate $[C_{\ell q}^{(3)}]_{ijkl} = W/(2v^2)\delta_{ij}\delta_{kl}$, where W is the oblique EW parameter defined in Ref. [210], and rescale the bound by factor $1/\sqrt{2}$ to account for the fact that we have no contribution to the electron channel.

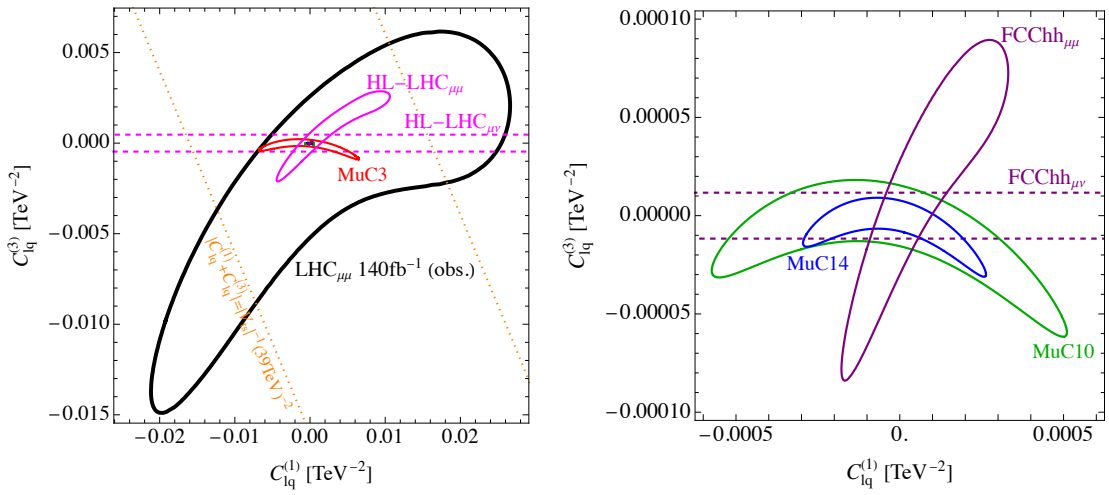

Figure 4.7: Sensitivity reach (95% CL) for the quark flavor-universal scenario on the two EFT coefficients $C_{lq}^{(1)}$ and $C_{lq}^{(3)}$, in TeV^{-2}, for different colliders. The right plot is a zoomed-in version near the origin of the left plot. For the future prospects at hadron colliders, we also include the sensitivity on $C_{lq}^{(3)}$ from the charged-current channel $pp \to \mu\nu$ (dashed lines), adapting the bound from Ref. [179]. The dotted orange lines are the solutions of $|C_{lq}^{(1)} + C_{lq}^{(3)}| = |V_{ts}^{-1}|\,(39\text{TeV})^{-2}$ and illustrate an expectation from the $bs\mu\mu$ anomalies assuming MFV, see Eq. (4.9).

4.4.2 Addressing b anomalies

Matching Eq. (4.6) to the low-energy EFT at tree-level gives the relevant operator controlling the $b \to s\mu^+\mu^-$ decays,

$$C_{sb\mu\mu} = \left([C_{\ell q}^{(1)}]_{2223} + [C_{\ell q}^{(3)}]_{2223}\right) \ . \tag{4.7}$$

In realistic models the $sb\mu\mu$ interaction is rarely generated alone: it comes along with the flavor-diagonal interactions, such as $bb\mu\mu$. In motivated flavor scenarios that aim at addressing the flavor puzzle and providing sufficient protection for approximate accidental symmetries, such as the $U(2)^3$ flavor symmetry in the quark sector (see Section 2.1.3), the $bb\mu\mu$ contact interaction is expected to be enhanced with respect to the $sb\mu\mu$. For this reason, in the following we consider two scenarios: only $sb\mu\mu$ contact interaction and only the $bb\mu\mu$ one (where $sb\mu\mu$ is assumed to be $\sim |V_{ts}|$ suppressed with respect to the flavor diagonal one and thus negligible). Assuming the $C_{\ell q}^{(1)} = C_{\ell q}^{(3)}$ alignment, we study high-energy constraints on the following effective Lagrangian:

$$\mathcal{L}_{\text{EFT}} = C_{bb\mu\mu}\ (\bar{b}_L\gamma_\alpha b_L)(\bar{\mu}_L\gamma^\alpha\mu_L) + (C_{sb\mu\mu}\ (\bar{s}_L\gamma_\alpha b_L)(\bar{\mu}_L\gamma^\alpha\mu_L) + \text{h.c.}) \ . \tag{4.8}$$

This choice of contact interactions is just the left-handed muon current scenario described in Section 4.1.1. The best-fit point from [61] corresponds to

$$C_{sb\mu\mu}|_{\text{best-fit}} \approx (39\,\text{TeV})^{-2} \ . \tag{4.9}$$

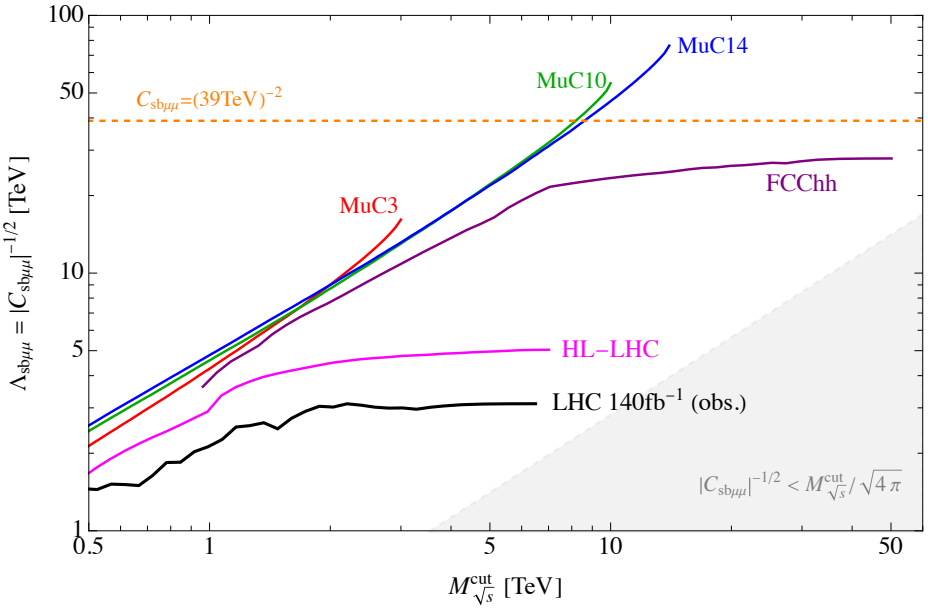

Figure 4.8: Sensitivity reach (95%CL) for the $(\bar{s}_L\gamma_\alpha b_L)(\bar{\mu}_L\gamma^\alpha\mu_L)$ contact interaction as function of the upper cut on the final-state invariant mass, compared to the value required to fit $bs\mu\mu$ anomalies (dashed orange line).

Since at high energies (in the massless limit), the amplitudes with different muon chiralities do not interfere, we do not expect a big difference between this scenario and the one with the vectorial muon current. Therefore we consider only the left-handed muon current, while the effective operator with the vectorial muon current is instead explicitly realized in the two Z' models studied in the next section.

In Figures 4.8 and 4.9 we show the expected 95% CL sensitivity on the EFT coefficients in Eq. (4.8) for the future colliders listed in Table 4.1, as well as the observed bound from the recast of the CMS search [211]. The constraints are shown as lower limits on the effective scale $\Lambda_X = |C_X|^{-1/2}$ in TeV, as a function of the upper cut on the invariant mass of the final state, $M^{\rm cut}_{\sqrt{s}}$. We recall that in order for the EFT to be valid, the new physics scale should be higher than the maximal experimental energy, in this case $M^{\rm cut}_{\sqrt{s}}$, hence: $M_{\rm NP} > M^{\rm cut}_{\sqrt{s}}$. Parametrising the EFT coefficients as $C = g_*^2/M^2_{\rm NP}$, where g_* describes the interaction strength between the new physics and the SM, the loosest EFT validity constraint is derived for strongly coupled theories, $g_*^2 \sim 4\pi$, from which we get the bound $|C|^{-1/2} > M^{\rm cut}_{\sqrt{s}}/\sqrt{4\pi}$. The region that does not satisfy this condition is shaded in gray. This approximates the perturbative unitarity bound on $M_{\rm NP}$ for a given value of the coefficient C [141].

As shown in Figures 4.8 and 4.9, the FCC-hh comes close to the minimal scenario $C_{sb\mu\mu} = (39\,\text{TeV})^{-2}$ and can easily cover the more realistic scenario, in which $C_{bb\mu\mu} = \pm|V_{ts}|^{-1}(39\,\text{TeV})^{-2}$.[4] The interference with the SM is negligible in the former case, while

[4]We neglect the RG effects for the purpose of this comparison since the chosen operators do not renormalize under QCD [212, 213].

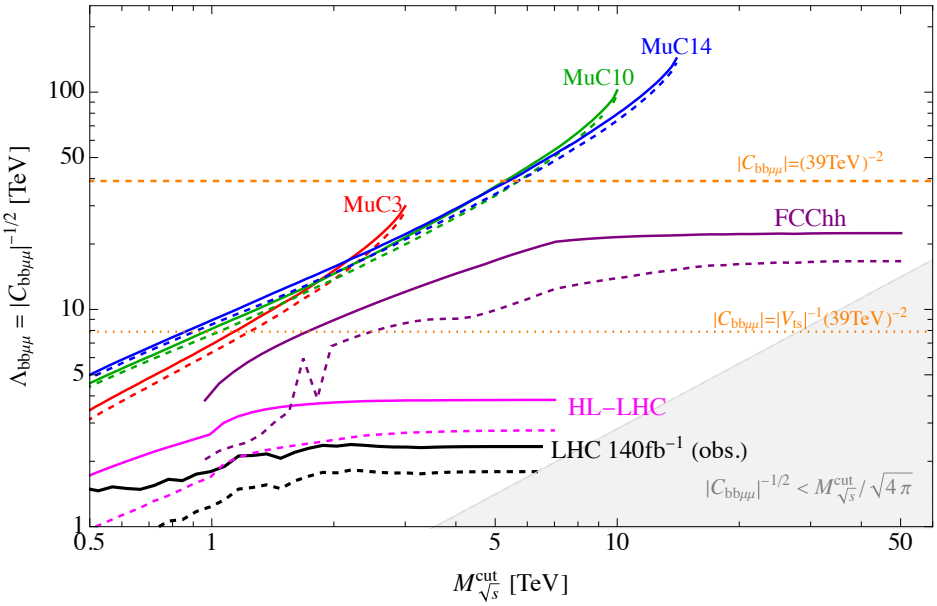

Figure 4.9: Sensitivity reach (95%CL) for the $(\bar{b}_L\gamma_\alpha b_L)(\bar{\mu}_L\gamma^\alpha\mu_L)$ contact interaction as function of the upper cut on the final-state invariant mass. Solid (dashed) lines represent the limit for positive (negative) values of $C_{bb\mu\mu}$. The orange dotted and dashed lines shows reference values in relation to the $bs\mu\mu$ anomalies fit, with or without a $1/V_{ts}$ enhancement of the bb operator compared to the bs one, respectively.

in the latter case it dominates the limit. The solid and the dashed lines in Figure 4.9 stand for the positive and the negative sign of $C_{bb\mu\mu}$, respectively. Finally, our projections agree with the previous studies for the HL-LHC [171] and for the FCC-hh [108]. The latter reference also considers the effect of subleading backgrounds.

Similarly to the FCC-hh, the 3 TeV MuC also comes close to the minimal scenario and can easily cover the more realistic scenario, as already anticipated for the case involving heavy flavors and suppressed production at hadron colliders (see also Ref. [114] for similar results). Both MuC10 and MuC14, instead, are able to completely test both scenarios.

At the MuC, the EFT limits for the highest invariant mass cut $= \sqrt{s_0}$, can be easily estimated by looking just at the partonic cross section $\hat{\sigma}(\mu^+\mu^- \to jj)(m_{\mu\mu})$. For energies $m_{\mu\mu} \gg m_Z$ we have:

$$\begin{aligned}
&\hat{\sigma}(\mu^+\mu^- \to jj)(m_{\mu\mu}) = \\
&\approx \frac{N_c}{48\pi m_{\mu\mu}^2}\left(\sum_{q_X}\sum_{Y=L,R}\left|g_Z^{q_X}g_Z^{\mu_Y} - e^2Q^{q_X} + m_{\mu\mu}^2 C_{q_Xq_X\mu\mu}\right|^2 + 2m_{\mu\mu}^4|C_{sb\mu\mu}|^2\right) \approx \\
&\approx \frac{624\,\text{fb}}{(m_{\mu\mu}/\text{TeV})^2}\left(1 + 2.35C_{bb\mu\mu}m_{\mu\mu}^2 + 12.4C_{bb\mu\mu}^2m_{\mu\mu}^4 + 24.8|C_{sb\mu\mu}|^2m_{\mu\mu}^4\right), \qquad (4.10)
\end{aligned}$$

up to relative corrections of $\mathcal{O}\left(m_Z^2/m_{\mu\mu}^2\right)$, where the sum over q_X runs on all quarks with both left and right chiralities, except for the top. For instance, assuming 1 ab^{-1} of luminosity and a 2% systematic uncertainty, for the 3 TeV muon collider one gets a

95% CL bound $|C_{sb\mu\mu}| \lesssim (15\,\text{TeV})^{-2}$, very similar to the one shown in Figure 4.8 following from a full numerical study detailed in the Appendices. In case of the flavor-diagonal $C_{bb\mu\mu}$ contact interaction in Figure 4.9, given the energy and precision of the measurements, the MuC limits are dominated by the interference with the SM, as can be quickly derived from Eq. (4.10), hence the limits are essentially symmetric between positive and negative values.

4.5 Z' models

In this Section we discuss explicit Z' models. We consider couplings to the muon current, $g_{\mu\mu}$, to flavor-conserving quark currents, g_{qq}, and to the flavor-violating sb current, g_{sb}, with $g_{sb} << g_{\mu\mu}$. The effect of flavor diagonal couplings g_{qq} is typically the most relevant in the high-p_T processes, due to the interference with the SM amplitude. In the case of a hadron collider, it is particularly important to identify the size of g_{qq} for each quark flavor q, since couplings to the first generation induce larger signals due to the PDF enhancement of valence quarks. There is no such distinction at a MuC in the inclusive di-jet searches, however, employing b-tagging would enhance the sensitivity to g_{bb} with respect to other light flavors.

The quark flavor-universal case with $g_{qq} \sim g_{\mu\mu}$ was explored in Ref. [171], which concluded that the current LHC data already provide stringent constraints. Therefore, we expect future hadron colliders to perform better compared to MuCs in such scenarios. In light of this, we consider models in which the dominant quark coupling is to heavy flavors. There are two qualitatively different scenarios that still need to be studied. Either $g_{sb} \ll g_{bb} \sim g_{\mu\mu}$, in which case the flavor-conserving couplings to quarks and to muons are of the same order and the flavor symmetry protects against excessive flavor violation, or $g_{sb} \sim g_{bb} \ll g_{\mu\mu}$, in which case all couplings to quarks are suppressed with respect to couplings to leptons. These two setups predict different phenomenologies and are therefore worth studying separately. The first scenario is naturally realised, for instance, by gauging $X = B_3 - L_\mu$ (Section 4.5.1). The second scenario instead can be obtained by gauging $X = L_\mu - L_\tau$ (Section 4.5.2). Both models are free of chiral anomalies with the fermionic content minimally extended to include right-handed neutrinos. In the following we consider the two models separately. In both cases, the Z' coupling to sb can be generated, for instance, via quark mixing with some vectorlike fermions after spontaneous breaking of the $U(1)_X$ gauge symmetry.

4.5.1 $U(1)_{B_3-L_\mu}$ model

Let us consider an extension of the SM gauge symmetry where the anomaly-free charge $X = B_3 - L_\mu$ is gauged. Similar models have been proposed as a way to address the past $bs\mu\mu$ anomalies in Refs. [151, 156, 161], to which we refer for more details. In the unbroken phase, the $U(1)_{B_3-L_\mu}$ gauge boson Z' has a vectorial coupling to third-generation

quarks and second-generations leptons. A small coupling to the second-generation quark doublet is induced after spontaneous symmetry breaking with a scalar field ϕ, charged only under $U(1)_{B_3-L_\mu}$. The gauge-invariant operators $(\phi^\dagger D_\mu \phi)(\bar{q}^2\gamma^\mu q^3)$ and $\bar{q}^2 H \phi b_R$ get generated after integrating out, for example, heavy vectorlike quarks. In particular, the latter operator is anyhow required by the CKM elements V_{td} and V_{ts} which are absent in the renormalizable model with the minimal matter content. The smallness of the 1-3 and 2-3 mixing in the quark sector is explained by the higher-dimensional operator breaking the accidental flavor symmetry of the renormalizable Lagrangian. In addition, the same operator indirectly induces the $Z'sb$ coupling in the broken phase after the rotation to the mass basis of the left-handed down quarks by a small angle θ_{sb}. Thus, the model naturally predicts an approximate $U(2)^3$ flavor symmetry allowing for a TeV-scale new physics compatible with flavor bounds.

Assuming only the rotations for left-handed fermions and $\theta_{sb} \ll 1$, the leading Z' couplings to SM fermions are

$$\begin{aligned}\mathcal{L}^{\rm int}_{Z'_{B_3-L_\mu}} = &- g_{Z'} Z'_\alpha \left[\frac{1}{3}\bar{q}^3\gamma^\alpha q^3 + \frac{1}{3}\bar{b}_R\gamma^\alpha b_R + \frac{1}{3}\bar{t}_R\gamma^\alpha t_R - \bar{l}^2\gamma^\alpha l^2 - \bar{\mu}_R\gamma^\alpha \mu_R + \right. \\ &\left. + \left(\frac{1}{3}\epsilon_{sb}\bar{q}^2\gamma^\alpha q^3 + \text{h.c.} \right) + \mathcal{O}(\epsilon_{sb}^2) \right] \ ,\end{aligned} \tag{4.11}$$

where for convenience we introduced $\epsilon_{sb} \equiv \frac{1}{2}\sin 2\theta_{sb}$. Thus, the total decay width to the SM fermions for the Z' is

$$\Gamma_{Z'_{B_3-L_\mu}} \approx \frac{M_{Z'} g_{Z'}^2}{24\pi} \left[3 + \frac{1}{3}\left(4 + 4|\epsilon_{sb}|^2\right) \right] \ , \tag{4.12}$$

where the top mass is neglected (in the numerical study we keep finite m_t effects). We consider $\Gamma_{Z'}/M_{Z'} < 0.25$ as a qualitative perturbative criterion for the model.[5] We neglect the muon-flavored right-handed neutrino assuming $m_N > m_{Z'}/2$. Otherwise, it would contribute to the total Z' decay width slightly changing the numerical results.

The measurement of neutrino trident production cross section sets an upper limit on the coupling to muons as a function of the mass [143],

$$g_{Z'} < 2.0 \, \frac{M_{Z'}}{\text{TeV}} \ . \tag{4.13}$$

No-mixing scenario

By assuming $\epsilon_{sb} = 0$ in Eq. (4.11) we study the discovery potential of future machines for a Z' coupled only to muons (and muon neutrinos) and third generation quarks. We consider the signatures discussed in Section 4.2 (for a MuC) and in Section 4.3 (for a hadron

[5]By the optical theorem, the decay width of the resonance is related to the imaginary part of the two-point function starting at the one-loop level. Therefore, when the width becomes of the order of the mass, the loop corrections are comparable with the tree level, which indicates a loss of perturbativity.

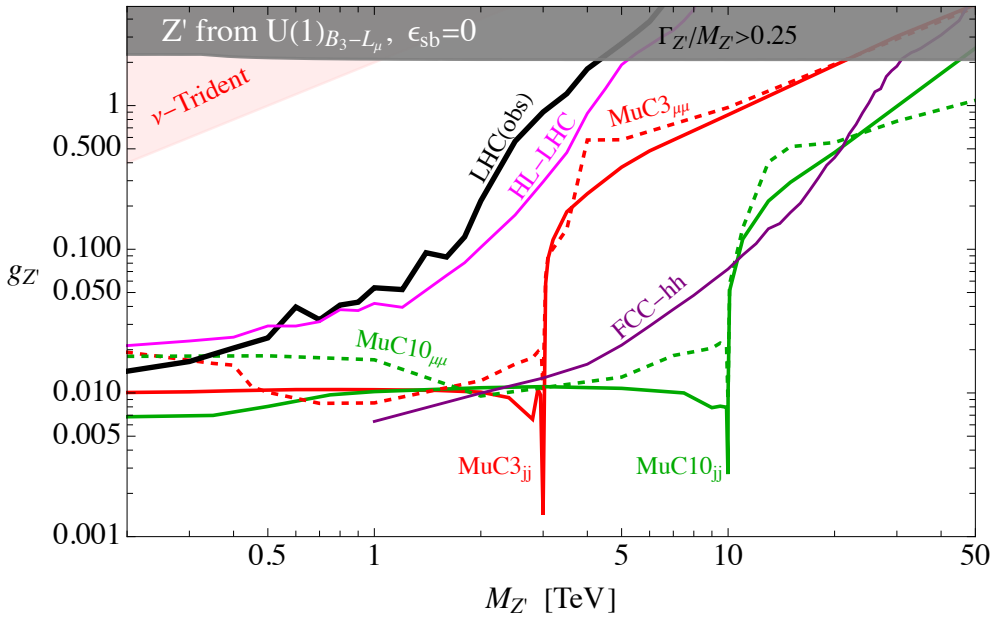

Figure 4.10: Discovery reach at 5σ for the $B_3 - L_\mu$ model with $\epsilon_{sb} = 0$, for different final states at each collider (as indicated by the labels). The region excluded at 95% CL by LHC [211] is above the black line while in the dark gray region the Z' has a large width, signaling a loss of perturbativity.

collider). Shown in Figure 4.10 are the present 95% CL exclusion bounds from the recast of the CMS Drell-Yan analysis [211] (thick black line) and neutrino trident production (red region), as well as the 5σ discovery prospects for various future colliders. The dark gray region corresponds to $\Gamma_{Z'}/M_{Z'} > 0.25$, which signals a loss of perturbativity.

We observe that MuC3 improves substantially from the HL-LHC prospects for all masses and MuC10 provides the best potential sensitivity (MuC14 would further improve on this). In this model FCC-hh shows a sensitivity comparable, albeit somewhat weaker, than MuC10.

Addressing $bs\mu\mu$ anomalies

Now we turn to a more specific study for $bs\mu\mu$ anomalies. For given values of $g_{Z'}$ and $M_{Z'}$, the mixing parameter required to fit the $bs\mu\mu$ anomalies is

$$\epsilon_{sb} = -1.7 \times 10^{-3} \left(\frac{M_{Z'}}{g_{Z'}\,\text{TeV}}\right)^2 \left(\frac{\Delta C_9^\mu}{-0.73}\right) \,. \tag{4.14}$$

The same coupling ($Z'sb$) induces $B_s - \overline{B}_s$ mixing:

$$C_{B_s}^1 = \frac{\left(g_{Z'}\frac{1}{3}\epsilon_{sb}\right)^2}{M_{Z'}^2} \,, \tag{4.15}$$

which is constrained by $|C_{B_s}^1| < |V_{tb}V_{ts}^*|^2/(9.2\,\text{TeV})^2$ [214, 215], implying a lower value for $g_{Z'} \geq 0.125\,\Delta C_9^\mu/(-0.73)(M_{Z'}/\text{TeV})$, if Eq. (4.14) is imposed. This also ensures that the

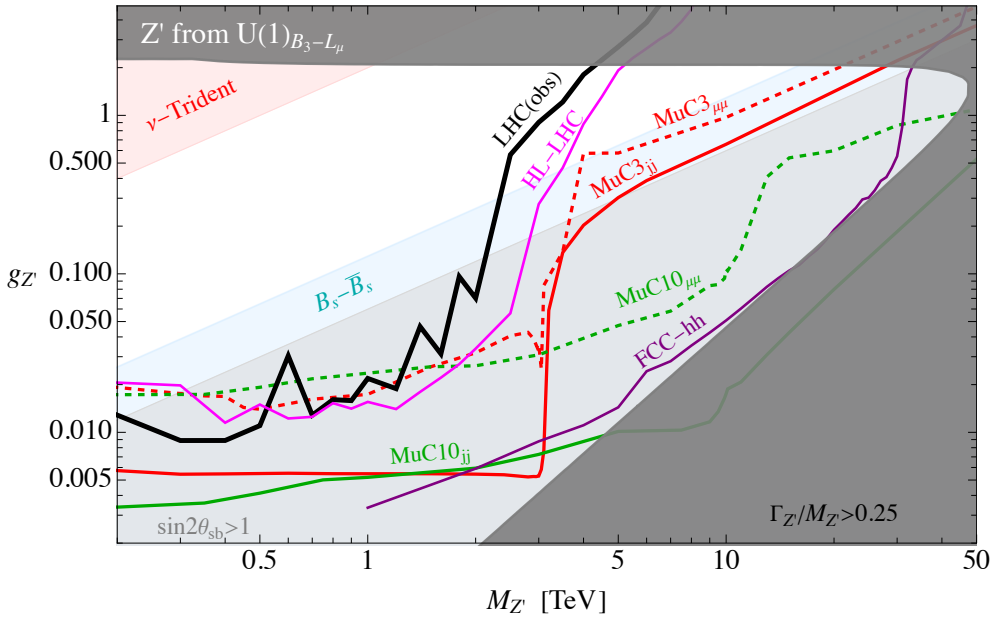

Figure 4.11: Discovery reach at 5σ for the $B_3 - L_\mu$ model. The fit to $bs\mu\mu$ anomalies is imposed everywhere, Eq. (4.14). The region excluded at 95% CL by LHC [211] is above the black line, while the one excluded by B_s mixing is colored in light blue. The light gray region cannot provide a successful fit to $b \to s\mu\mu$ anomalies for values of $\sin 2\theta_{sb} < 1$, while in the dark gray region the Z' has a large width, signaling a loss of perturbativity. The discoverable region at future colliders is the one on the side of the line where the corresponding label has been drawn.

condition $\theta_{sb} \ll 1$ is always satisfied in the acceptable region. In this model the contributions to D^0-mixing is suppressed by $(\epsilon_{sb} V_{cs} V_{ub})^2$ or $(\epsilon_{sb}^2 V_{cs} V_{us})^2$, making the corresponding bound much less stringent than the B_s-mixing one.

We impose Eq. (4.14) assuming the best fit value for ΔC_9^μ in order to address the $bs\mu\mu$ anomalies in every point of the $(M_{Z'}, g_{Z'})$ plane shown in Figure 4.11. The difference with the previous result is that, for a given mass, decreasing $g_{Z'}$ requires larger values of ϵ_{sb} (i.e. θ_{sb}). The $B_s - \overline{B}_s$ constraint is shown as a light-blue region. The light gray region corresponds to values of masses and coupling that would require $\sin 2\theta_{sb} > 1$ in order to fit the $bs\mu\mu$ anomalies.[6]

Our recast of the present CMS Drell-Yan search excludes at 95% CL the region above the thick black line, which includes all viable couplings in the mass range $200\,\text{GeV} < M_{Z'} \lesssim 2\,\text{TeV}$ (we do not study the model for masses below 200 GeV). Instead, for the future colliders listed in Table 4.1, we show the 5σ discovery reach, where the region in parameter space above the corresponding line is discoverable. Regarding hadron colliders, the HL-LHC projected bounds will only be slightly improved, while the FCC-hh will be

[6]While this is not possible in the model of Ref. [161], it could in principle be achieved by having some vectorlike quarks with large charges. However, it is likely that in this case couplings to b and t quarks also receive $\mathcal{O}(1)$ corrections from the mixing. In any case, this region is excluded by B_s-mixing.

able to completely test this scenario via resonance searches in $pp \to \mu^+\mu^-$. The 3 TeV MuC is also able to completely cover the viable parameter space not already excluded by the existing constraints. For masses below 3 TeV, a resonance could be observed directly in both di-muon (dashed red) and di-jet channels (solid red), while a heavier Z' would show-up as a smooth deviation from the SM in the highest invariant mass bins. A 10 TeV MuC would further improve the sensitivity allowing for resonance searches even for a heavier Z', up to the region allowed by perturbativity and meson mixing.

4.5.2 $U(1)_{L_\mu - L_\tau}$ model

We next consider a heavy Z' arising from a spontaneously broken $U(1)_{L_\mu - L_\tau}$ gauge symmetry. In the limit of a vanishing kinetic mixing with the hypercharge ($X_{\mu\nu}B^{\mu\nu}$), the Z' does not couple to quarks at the renormalizable level when only the minimal matter content is present. For instance, those couplings can be generated, after the spontaneous symmetry breaking, via mixing with heavy vectorlike quarks charged under $L_\mu - L_\tau$. Therefore, the quark couplings (including b quarks) are expected to be much smaller than couplings to muons and taus. Let ϵ_b and ϵ_s be some small mixings with vectorlike quarks of the corresponding left-handed quark doublets in the down-quark mass basis of third and second generation, respectively. The relevant $SU(2)_L$ invariant Z' interactions are

$$\begin{aligned}\mathcal{L}^{\rm int}_{Z'_{L_\mu - L_\tau}} = &- g_{Z'} Z'_\alpha \left[\bar{l}^2\gamma^\alpha l^2 + \bar{\mu}_R\gamma^\alpha\mu_R - \bar{l}^3\gamma^\alpha l^3 - \bar{\tau}_R\gamma^\alpha\tau_R + \right. \\ &\left. + |\epsilon_b|^2\bar{q}^3\gamma^\alpha q^3 + |\epsilon_s|^2\bar{q}^2\gamma^\alpha q^2 + \left(\epsilon_b\epsilon_s^*\bar{q}^2\gamma^\alpha q^3 + \text{h.c.}\right) + \ldots\right] \ .\end{aligned} \tag{4.16}$$

The total decay width of the Z' is

$$\Gamma_{Z'_{L_\mu - L_\tau}} \approx \frac{M_{Z'} g_{Z'}^2}{24\pi}\left[6 + 3\left(2|\epsilon_s|^4 + 4|\epsilon_s|^2|\epsilon_b|^2 + 2|\epsilon_b|^4\right)\right] \ , \tag{4.17}$$

where the top mass is neglected (in the numerical study we keep the physical m_t). Similarly to Section 4.5.1, we impose $\Gamma/M < 0.25$ as the perturbative limit and neglect the right-handed neutrinos in Z' decays. The constraint on $g_{Z'}$ from neutrino trident production is the same as in Eq. (4.13).

Quark-phobic Z'

We first focus on a scenario where the Z' is quark-phobic ($\epsilon_s = \epsilon_b = 0$) and derive the present 95% CL exclusion bounds as well as the future discovery projections. The results are reported in Figure 4.12, where we show the 5σ sensitivity reach for various future colliders. The shaded regions are analogous to the ones from the previous Section.

This case (not surprisingly) illustrates a situation in which even the MuC3 outperforms the FCC-hh, since the Z' is both quark-phobic and leptophilic. Our limits for MuC3 agree well with those obtained in Ref. [113].

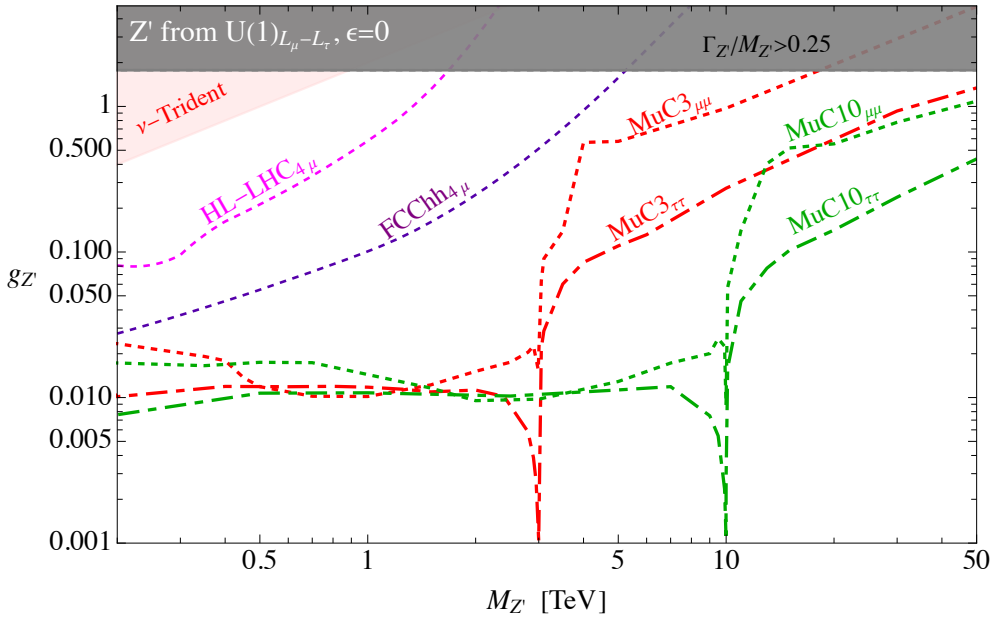

Figure 4.12: Discovery reach at 5σ for the $L_\mu - L_\tau$ model with $\epsilon_s = \epsilon_b = 0$ in Eq. (4.16). In the dark gray region the Z' has a large width, signaling a loss of perturbativity.

Addressing $bs\mu\mu$ anomalies

In order to address the $bs\mu\mu$ anomalies, the product of the mixing parameters is set to

$$\epsilon_b \epsilon_s^* = -5.7 \times 10^{-4} \left(\frac{M_{Z'}}{g_{Z'}\,\text{TeV}} \right)^2 \left(\frac{\Delta C_9^\mu}{-0.73} \right) . \tag{4.18}$$

Even after imposing $\Delta C_9^\mu = -0.73$, we are left with other free parameters besides $M_{Z'}$ and $g_{Z'}$. Our goal here is to study the case where $|\epsilon_s/\epsilon_b| \sim \mathcal{O}(1)$ which is qualitatively different from the model in Section 4.5.1. For concreteness, in our numerical analysis we assume $\epsilon_b = -\epsilon_s$ and $\text{Im}\epsilon_b = 0$. With this simplification, we are able to plot our results in the $(M_{Z'}, g_{Z'})$ plane.

Analogously to Section 4.5.1, the B_s mixing, $C^1_{B_s} = -(g_{Z'}\epsilon_s^*\epsilon_b)^2/M^2_{Z'}$, together with Eq. (4.18), imply the lower limit $g_{Z'} > 0.125 M_{Z'}/\text{TeV}$. The $D^0 - \overline{D}^0$ mixing gives another constraint on the parameters: $C^1_{D^0} = (g_{Z'} V_{us}^* V_{cs} |\epsilon_s|^2)^2/M^2_{Z'} < 2.5 \times 10^{-13}\text{GeV}^{-2}$ [214, 215], corresponding to $g_{Z'} > 0.25 M_{Z'}/\text{TeV}$. Interestingly, D^0 mixing provides stronger constraints than B_s-mixing in this model.

Our main results are shown in Figure 4.13. The present CMS $pp \to \mu^+\mu^-$ data [211] exclude at 95% CL the region inside the thick black lines. For the future colliders listed in Table 4.1, the parameter space discoverable at 5σ is the one on the side of the corresponding line where the label is shown. Note that, in the case of $pp \to \mu^+\mu^-$ at hadron colliders or $\mu^+\mu^- \to jj$ at MuCs, the only accessible region is for intermediate values of $g_{Z'}$. According to Eq. (4.18), for a given Z' mass the couplings to quarks are inversely proportional to $g_{Z'}$. Since too large $g_{Z'}$ values imply too small couplings to quarks, and vice versa, there is always a suppression in $\sigma \times \mathcal{B}$ for the two processes. The di-muon searches at FCC-hh

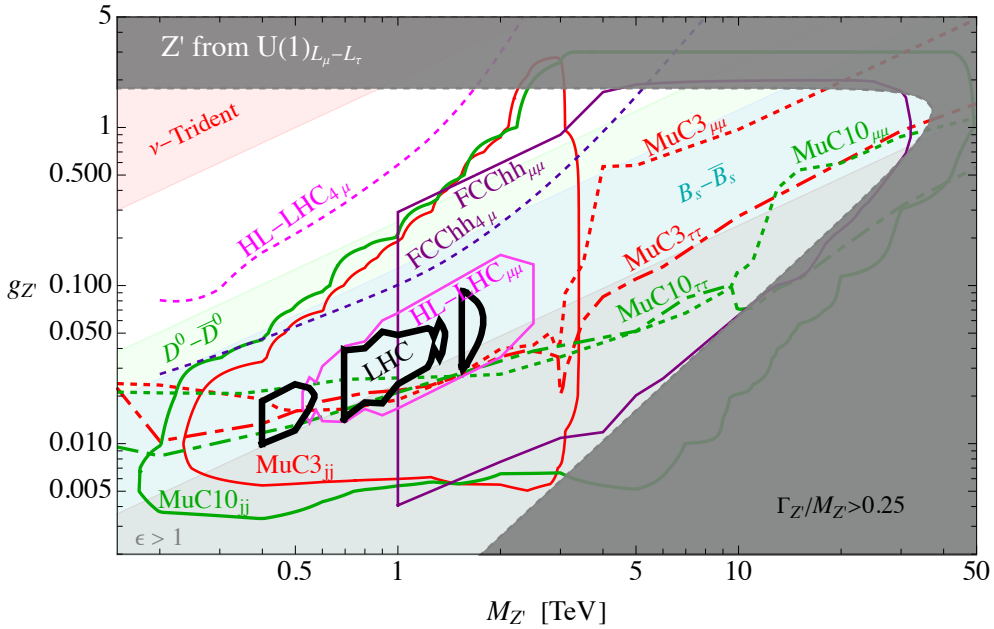

Figure 4.13: Discovery reach at 5σ for the $L_\mu - L_\tau$ model. The fit to $bs\mu\mu$ anomalies is imposed, Eq. (4.18). The regions excluded by B_s and D^0 mixings and neutrino trident production are colored in light blue, green and red, respectively. The light gray region requires $\epsilon > 1$ to fit $b \to s\mu\mu$ anomalies, while the dark gray region has $\Gamma_{Z'}/M_{Z'} > 0.25$. Our recast of the present LHC search [211] excludes at 95% CL the region inside the thick black lines. The discoverable region at future colliders is the one on the side of the line where the corresponding label has been drawn.

and the di-jet searches at MuC can cover a much larger parameter space than the one accessible at (HL-)LHC but are still unable to cover the viable parameter space for the $bs\mu\mu$ anomalies. In this respect, the most optimal channels at MuCs are $\mu\mu \to \mu\mu$ and $\mu\mu \to \tau\tau$, that even at a 3 TeV MuC are enough to completely cover the leftover parameter space. At hadron colliders, the most promising channel is $pp \to 4\mu$. Let us emphasize that even the HL-LHC can make significant progress, while the FCC-hh would fully cover the viable parameter space.

4.6 Leptoquark models

In this Section, we investigate the discovery prospects at future colliders for the S_3 and U_1 leptoquarks introduced in Section 4.1.1. We extend the SM minimally with a single heavy field (ignoring the UV origin of its mass) and focus on the renormalizable interactions with the left-handed SM fermions. We consider two different cases regarding the flavor structure of such interactions. First, we assume an exact $U(2)_q$ quark-flavor symmetry under which the first two generations q^i $(i = 1, 2)$ form a doublet, while the third-generation q^3 is a singlet. In addition, we assume an exact $U(1)_{\mu-LQ}$ symmetry under which l^2 and the

leptoquark are oppositely charged. This can be achieved by gauging one out of many possible anomaly-free lepton flavor non-universal $U(1)$ extensions of the SM, see [216]. In this case, the only allowed coupling will be to q^3 and l^2. In the second scenario, we aim at addressing the $bs\mu\mu$ anomalies by minimally adding a direct leptoquark coupling to q^2.

4.6.1 Scalar leptoquark

We start with the leptoquark $S_3 \sim (\bar{\mathbf{3}}, \mathbf{3}, 1/3)$ [121]. The interaction Lagrangian reads

$$\mathcal{L}_{S_3}^{\text{int}} = \lambda_{i\mu}\, \bar{q}^{c\,i}\, \epsilon\, \sigma^a l^2 S_3^a + \text{h.c.}\ , \tag{4.19}$$

where $\epsilon = i\sigma_2$ and $q^c = C(\bar{q})^T$. We assume a real coupling matrix for simplicity. The leptoquark triplet can be written as

$$S_3^a \sigma^a \equiv \begin{pmatrix} S_3^{(1/3)} & \sqrt{2} S_3^{(4/3)} \\ \sqrt{2} S_3^{(-2/3)} & -S_3^{(1/3)} \end{pmatrix}\ , \tag{4.20}$$

where the superscript indicates the electric charge of each S_3 component. We assume a degenerate mass spectrum for the components, as expected from the $SU(2)_L$ gauge symmetry. In the mass basis of SM fermions, the interaction Lagrangian (4.19) becomes

$$\mathcal{L}_{S_3}^{\text{int}} = -\lambda_{i\mu} S_3^{(1/3)} (V_{ji}^* \bar{u}_L^{j\,c} \mu_L + \bar{d}_L^{j\,c} \nu_\mu) + \sqrt{2}\lambda_{i\mu} \left(V_{ji}^* S_3^{(-2/3)} \bar{u}_L^{j\,c} \nu_\mu - S_3^{(4/3)} \bar{d}_L^{j\,c} \mu_L \right) + \text{h.c.}\ . \tag{4.21}$$

The total decay width of S_3, in the limit of vanishing fermion masses, is given by

$$\Gamma_{S_3} = \frac{|\lambda_{b\mu}|^2 + |\lambda_{s\mu}|^2}{8\pi} M_{S_3}\ , \tag{4.22}$$

assuming only $\lambda_{b\mu}$ ($i = 3$) and $\lambda_{s\mu}$ ($i = 2$) different from zero. The perturbative limit $\Gamma_{S_3}/M_{S_3} < 0.25$ is considered, as previously.

$U(2)^3$ symmetric case

Imposing an unbroken $U(2)^3$ quark flavor symmetry, and assuming S_3 to be charged under the muon number, only the $\lambda_{b\mu}$ coupling is allowed. This symmetry is broken in the SM by light quark masses and by the mixing of third-generation quarks with the first two via the CKM matrix. This is an approximate symmetry of the SM Yukawa sector, where the largest symmetry-breaking term is $|V_{ts}| \approx 0.04$. Assuming the minimal $U(2)^3$ breaking and no breaking of $U(1)_\mu$ as in the SM, the expected sizes of other non-zero leptoquark couplings are $|\lambda_{s\mu}| \sim |V_{ts}\lambda_{b\mu}|$ and $|\lambda_{d\mu}| \sim |V_{td}\lambda_{b\mu}|$, see Refs. [217–220]. Those can be neglected in our collider study.

In Figure 4.14 we show the present 95% CL limits from LHC searches (thick black) and the 5σ discovery prospects for future colliders (various colored lines), considering only $\lambda_{b\mu} \neq 0$, as motivated by the aforementioned approximate flavor symmetry of the SM. The leptoquark pair production at the LHC sets a robust lower limit on the mass even for small

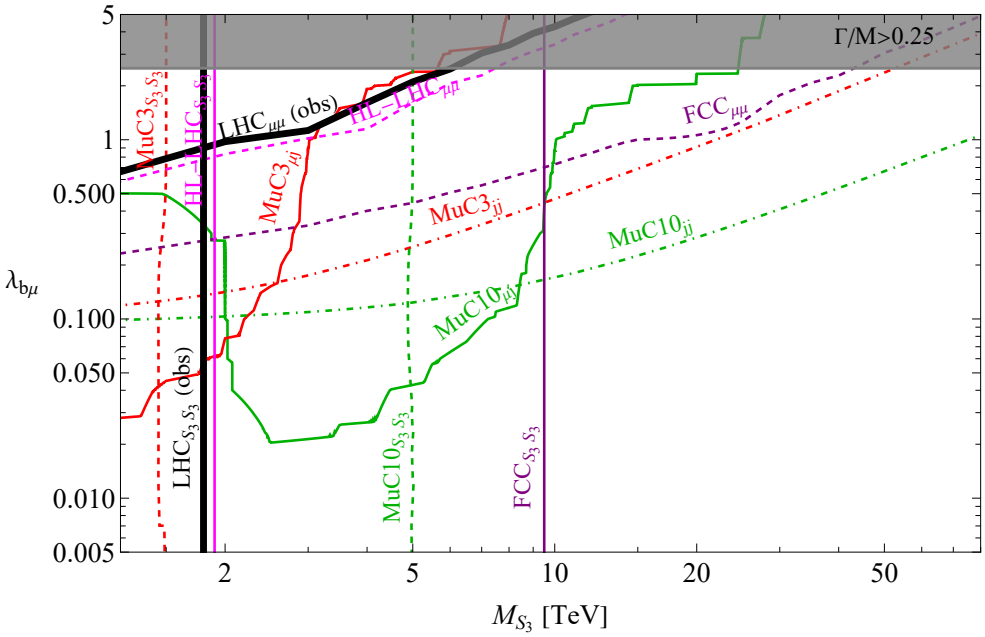

Figure 4.14: The 5σ discovery prospects at future colliders for the S_3 leptoquark assuming the $U(2)^3$ quark flavor symmetry and the exclusive leptoquark coupling to muons. The present LHC exclusions at 95% CL are shown as a thick black line. The perturbative limit $\Gamma_{S_3}/M_{S_3} < 0.25$ is violated in the grey region. The labels for various colliders and processes are on the discoverable side of a curve.

couplings, while the Drell-Yan process excludes a region with the large coupling even for higher masses. Interestingly, the HL-LHC 5σ discovery region is only marginally larger than the present 95% CL exclusions. Nevertheless, the FCC-hh will drastically improve both the Drell-Yan and the leptoquark pair production reach.

Regarding muon colliders, we find that a 3 TeV MuC would have a comparable reach from the IDY process as the FCC-hh from the DY, while the MuC10 would easily surpass the FCC-hh. On the other hand, the FCC-hh provides a far superior prospects on pair-production, being able to discover on-shell leptoquarks with masses of almost 10 TeV, compared to only 5 TeV for the MuC10. The resonant leptoquark production at the MuC10 could probe a unique region in the parameter space compared with other production mechanisms at muon colliders. However, this region can easily be covered at the FCC-hh.

Addressing the $bs\mu\mu$ anomalies

As shown by the extensive literature [165, 218, 220–237], S_3 is the only scalar leptoquark that can accommodate $bs\mu\mu$ anomalies at the tree level. After integrating out S_3, we find the following contribution to the relevant effective operators

$$\Delta C_9^\mu = -\Delta C_{10}^\mu = \frac{\pi}{\sqrt{2} G_F \alpha V_{ts}^* V_{tb}} \frac{\lambda_{b\mu}\lambda_{s\mu}}{M_{S_3}^2} \,. \tag{4.23}$$

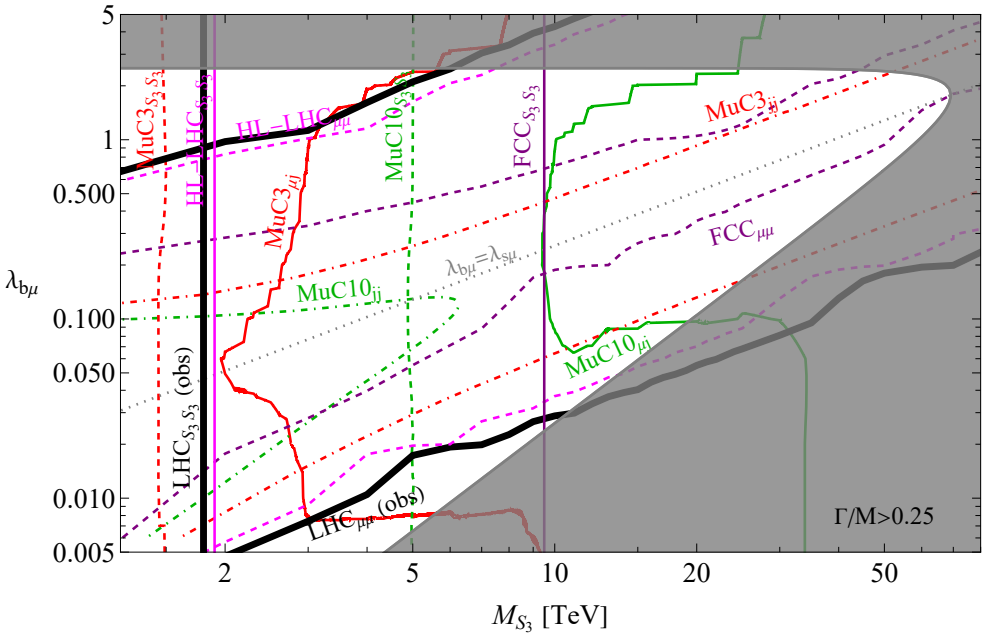

Figure 4.15: The 5σ discovery prospects for the S_3 leptoquark behind to $bs\mu\mu$ anomalies, i.e. imposing Eq. (4.24). The present LHC exclusions at 95% CL are shown as a thick black line. The dotted gray line corresponds to $\lambda_{b\mu} = \lambda_{s\mu}$. The perturbative limit $\Gamma_{S_3}/M_{S_3} < 0.25$ is violated in the grey region. For future colliders, the discoverable region is on the side of the line where the corresponding label is.

The fit to the $bs\mu\mu$ anomalies then implies

$$\lambda_{b\mu}\lambda_{s\mu} = 6.6 \times 10^{-4} \left(\frac{M_{S_3}}{\text{TeV}}\right)^2 \left(\frac{\Delta C_9^\mu}{-0.39}\right) \ . \tag{4.24}$$

In Figure 4.15 we perform the collider sensitivity study in the $M_{S_3} - \lambda_{b\mu}$ plane, while fixing $\lambda_{s\mu}$ by Eq. (4.24), where $\Delta C_9^\mu = -\Delta C_{10}^\mu = -0.39$. We do not show any complementary flavor physics constraints (such as the B_s mixing) since those are loop suppressed in the leptoquark models and do not put limits on the parameter space of interest to this analysis (for a global fit with the S_3 see Ref. [229] and with the U_1 see Ref. [238]).

The present LHC bounds at 95% CL from the DY process and the leptoquark pair production are shown with thick black lines. The 5σ discovery prospects for future colliders are depicted with various colored lines. The corresponding label for a collider and a process is always on the excluded (or discoverable) side. The HL-LHC can not discover much more of the parameter space that is not already excluded. However, the FCC-hh will explore all but a fraction of the parameter space in between the dashed purple (DY) lines and the vertical solid purple line (pair-production). This region of parameter space corresponds to $\lambda_{b\mu} \approx \lambda_{s\mu}$, which minimizes the contribution to $pp \to \mu\mu$ once Eq. (4.24) is imposed and is also beyond the pair production reach for higher masses. Note that this region of parameter space strongly violates the $U(2)^3$ flavor symmetry in the quark sector.

Moving on to muon colliders, a 3 TeV MuC discovery reach in the IDY channel is

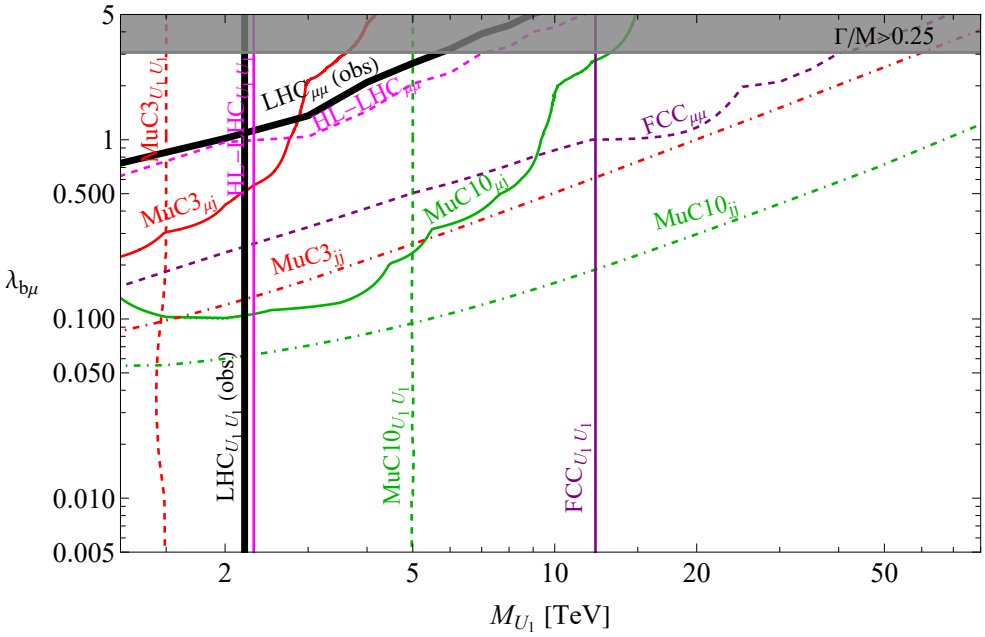

Figure 4.16: Discovery reach at 5σ for the U_1 leptoquark in the $U(2)^3$ symmetric case. The present 95%CL exclusion by LHC is shown as a thick black line. In the grey region, the perturbative limit $\Gamma_{U_1}/M_{U_1} < 0.25$ is violated.

comparable to the one of the FCC-hh. However, the leptoquark pair production prospects are substantially lower, stopping at $M_{S_3} \approx \sqrt{s_0}/2 = 1.5$ TeV which is even below the present LHC exclusion. On the other hand, the MuC10 will test the whole parameter space by combining different channels: IDY, pair production, and $\mu q \to \mu j$. Interestingly, both a 3 TeV and a 10 TeV MuC might directly observe an s-channel resonance in the $\mu q \to \mu j$ (see Section 4.2.4) for masses up to approximately $\sqrt{s_0}$. In other words, this seems to be the most promising on-shell process at muon colliders.

4.6.2 Vector leptoquark

Let us consider an extension of the SM with a heavy vector leptoquark $U_1 \sim (\mathbf{3}, \mathbf{1}, 2/3)$ [121]. Assuming only left-handed couplings, the interaction Lagrangian with fermions is

$$\mathcal{L}^{\text{int}}_{U_1} = \lambda_{i\mu} \bar{q}^i \gamma_\alpha l^2 U_1^\alpha + \text{h.c.} = \lambda_{i\mu} U_1^\alpha \left(V_{ji} \bar{u}^j_L \gamma_\alpha \nu_\mu + \bar{d}^i_L \gamma_\alpha \mu_L \right) + \text{h.c.} \,, \tag{4.25}$$

while interactions with the SM gauge bosons are described by

$$\mathcal{L}^{\text{gauge}}_{U_1} = -\frac{1}{2} U^\dagger_{\mu\nu} U^{\mu\nu} - i g_s \kappa_s U^\dagger_{1\mu} T^a U_{1\nu} G^{a\mu\nu} - i g' \frac{2}{3} \kappa_Y U^\dagger_{1\mu} U_{1\nu} B^{\mu\nu} \,, \tag{4.26}$$

where $U_{\mu\nu} = D_\mu U_{1\nu} - D_\nu U_{1\mu}$. The dimensionless parameters $\kappa_{s,Y}$ depend on the specific UV completion of the model. We assume that $U_{1\mu}$ arises from a spontaneously broken

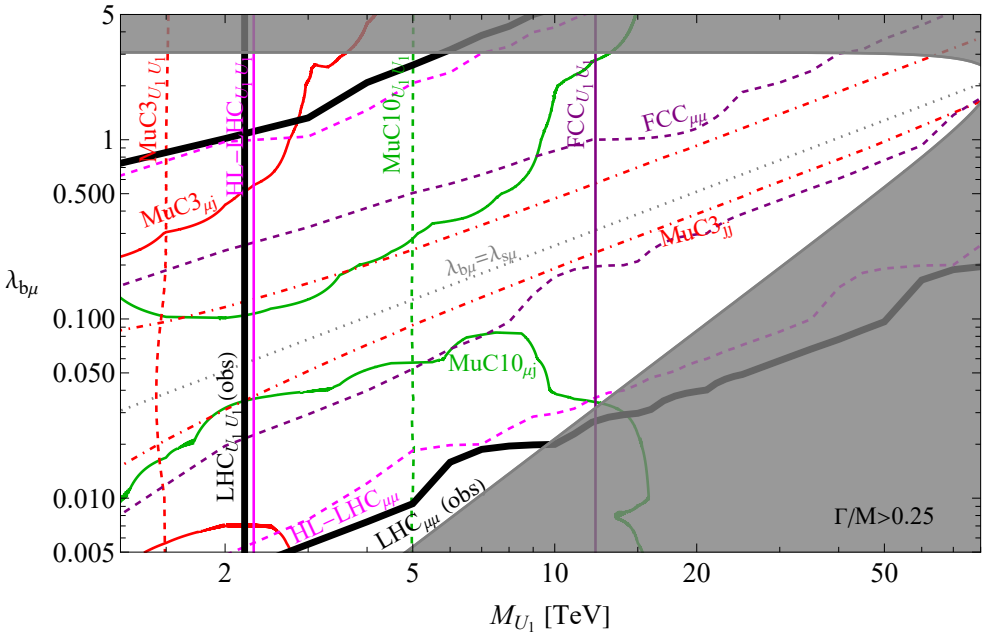

Figure 4.17: Discovery reach at 5σ for the U_1 leptoquark. The fit to $bs\mu\mu$ anomalies is imposed everywhere via Eq. (4.24). The present 95%CL exclusion by LHC is shown as a thick black line. The dotted gray line corresponds to $\lambda_{b\mu} = \lambda_{s\mu}$. In the grey region, the perturbative limit $\Gamma_{U_1}/M_{U_1} < 0.25$ is violated. The limit for the $\mu\bar{\mu} \to jj$ channel at 10 TeV MuC covers the whole plane. For future colliders, the discoverable region is the one on the side of the line where the corresponding label has been drawn.

Yang-Mills theory, that is $\kappa_{s,Y} = 1$.[7] The U_1 decay width is

$$\Gamma_{U_1} = \frac{|\lambda_{b\mu}|^2 + |\lambda_{s\mu}|^2}{12\pi} M_{U_1} \ , \tag{4.27}$$

where we take only $\lambda_{b\mu}$ $(i = 3)$ and $\lambda_{s\mu}$ $(i = 2)$ couplings to be non-zero. Analogously to the S_3 case, we consider two different scenarios for the $\lambda_{s\mu}$ coupling.

$U(2)^3$ symmetric case

The minimally broken $U(2)^3$ quark flavor symmetry predicts $|\lambda_{s\mu}| \sim |V_{ts}\lambda_{b\mu}|$ and even smaller $|\lambda_{d\mu}| \sim |V_{td}\lambda_{b\mu}|$, making all leptoquark couplings but $\lambda_{b\mu}$ irrelevant for high-p_T processes. On the leptonic side, we again assume an exclusive coupling to muons.

The present LHC constraints, as well as future 5σ discovery prospects are presented in the $M_{U_1} - \lambda_{b\mu}$ plane in Figure 4.16. The resulting picture is qualitatively similar to the one for the S_3 leptoquark in Section 4.6.1, to which we refer for a detailed discussion. The extra interaction term with gluons increases the reach at FCC-hh from the pair production

[7] We note that the for the benchmark $\kappa_Y = 0$ our phenomenological analysis remains identical, since the main production and decay channels are dominated by the QCD and $q\ell$-LQ couplings. Instead, $\kappa_s = 0$ lowers the pair production cross section, reducing the U_1U_1 limits from hadron colliders by about 30% on the mass, see e.g. [201].

up to $M_{U_1} \approx 12.9\,\text{TeV}$, while the reach at MuC is limited to $\sqrt{s_0}/2$ by kinematics. Note also the suppression in reach from the μj final state at MuC, compared to the scalar case. This is due to a factor of $1/2$ from the branching ratio of $U_1 \to d^i\mu$ and a factor of $\sqrt{2}$ less in the coupling to $d^i\mu$. As before, the MuC10 sensitivity prospect in the IDY channel is almost an order of magnitude better than at FCC-hh, while the MuC3 is comparable.

Addressing $bs\mu\mu$ anomalies

The U_1 vector leptoquark has attracted a great deal of attention in the context of the B-meson anomalies [165, 218, 239–258]. Regarding the contribution to $\Delta C_9^\mu = -\Delta C_{10}^\mu$, the expressions in Eqs. (4.23) and (4.24) hold identically with a replacement $M_{S_3} \to M_{U_1}$. In the following, we focus on the parameter space that can address the $bs\mu\mu$ anomalies. In particular, $\lambda_{s\mu}$ is fixed by the best-fit point from the $bs\mu\mu$ analysis, see Eq. (4.24), leaving only two input parameters M_{U_1} and $\lambda_{b\mu}$.

The results of our collider studies are summarised in Figure 4.17, where the color coding is the same as before. The prospects at the hadron colliders are similar to the S_3 case, see Section 4.6.1 for a detailed discussion. At MuCs, the IDY channel provides somewhat higher sensitivity, unlike the resonant production in $\mu q \to \mu j$. The MuC10 can discover at 5σ the entire viable parameter space by the IDY process alone, while the MuC3 can exclude it at 95% CL. However, it is important to stress that this is only an indirect effect: the leptoquark is exchanged in the t-channel and therefore a smooth distortion is predicted (see Figure 4.5). This is to be compared with FCC-hh, where the vector leptoquark can be discovered as an on-shell resonance in the pair production process up to $M_{U_1} \approx 12.9\,\text{TeV}$.

4.7 Summary

In this Chapter, we considered short-distance new physics relevant for rare (semi)leptonic B meson decays and investigated the complementary discovery prospects at the future colliders specified in Table 4.1. Our set of benchmarks includes heavy Z' and leptoquark mediators as well as semileptonic four-fermion interactions.

Our MuC studies focus on two-body final states sensitive to such new physics, the most relevant being di-jet, di-muon, di-tau, and muon plus jet (see Figure 4.1). For each topology we computed the leading SM background as well as the expected new physics signal. We identified an intriguing interplay between resonant and non-resonant signal shapes relevant to the discovery prospects (see Figure 4.4). The complementary processes considered at hadron colliders are summarised in Figure 4.6 and include di-muon and four-muon final states. Furthermore, for both muon and hadron colliders we also study the sensitivity from leptoquark pair production.

In our first analysis we assumed that the new mediators are too heavy for on-shell production even at future colliders and study the deviations in the high-energy tails due

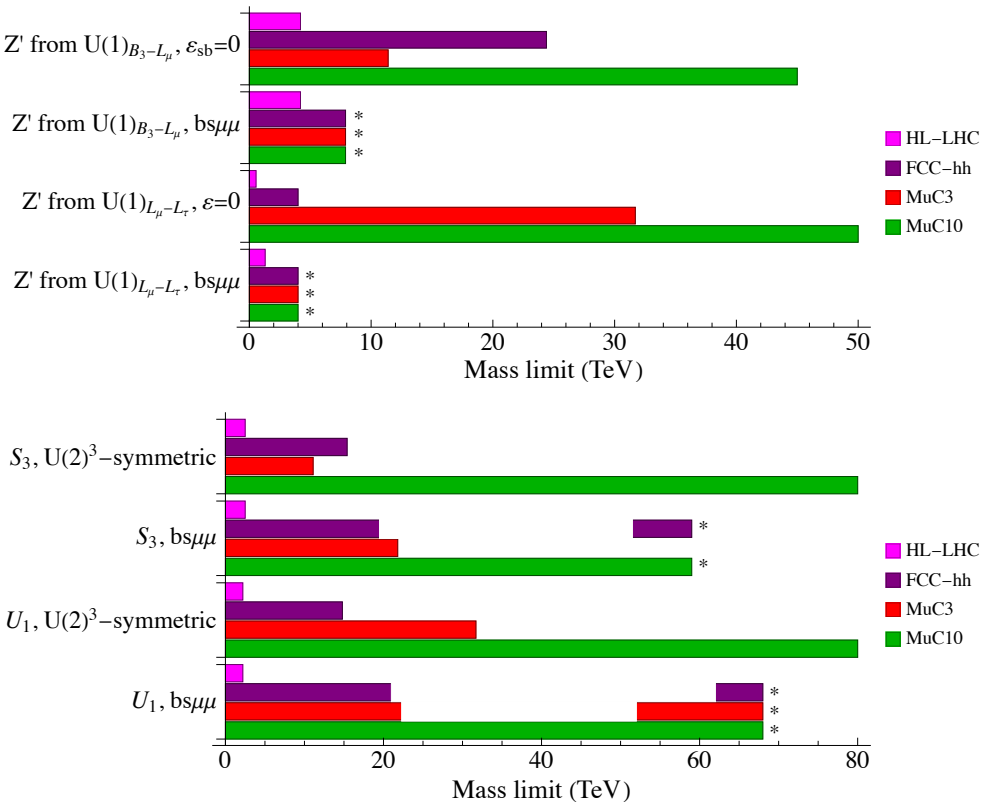

Figure 4.18: Comparison of the discovery reach of future colliders for the different models discussed in this Chapter. The corresponding couplings ($g_{Z'}$ or $\lambda_{b\mu}$) are set to 1. We denote with an asterisk cases where the reach exceeds the perturbative limit or meet any other relevant bound (e.g. from meson mixing).

to new semileptonic four-fermion interactions. For example, in Figure 4.7 we compare the projections from the di-jet final state at muon colliders to the di-muon and muon plus neutrino final states at hadron colliders, on operators involving left-handed doublets with different $SU(2)_L$ contractions, assuming flavor universality in the quark-sector. Interestingly, in this case a 3 TeV MuC only slightly improves upon the HL-LHC, while the FCC-hh probes substantially more parameter space, that can only be matched by a 14 TeV MuC. We then studied similar operators but with a different flavor structure: $bs\mu\mu$ and $bb\mu\mu$. The corresponding results are shown in Figures 4.8 and 4.9. In this case, even a 3 TeV MuC provides comparable sensitivity to the FCC-hh, while 10 TeV and 14 TeV MuCs are considerably better. This is due to the suppression from the sea quark parton distribution functions at hadron colliders.

Then we focused on models of Z' associated with the gauging of the $U(1)_{B_3-L_\mu}$ or the $U(1)_{L_\mu-L_\tau}$ group. For both models we considered two scenarios: *i*) the set of renormalizable couplings predicted by the corresponding $U(1)_X$ and *ii*) a minimal extension needed to address the $bs\mu\mu$ anomalies. Our main findings are presented in Figures 4.10 and 4.11 for $B_3 - L_\mu$ and Figures 4.12 and 4.13 for $L_\mu - L_\tau$. In the scenario *i*), the FCC-hh compares

to the MuC10 for the first model, while in the second model (which is quark-phobic), even a 3 TeV MuC is better than the FCC-hh. When the $bs\mu\mu$ anomalies are addressed, we found that the whole viable parameter space in both models can be fully explored at the MuC3 as well as the FCC-hh. Our results are also summarized in Figure 4.18, where one can directly compare the Z' mass reach of the future colliders for a benchmark value of the coupling $g_{Z'} = 1$.

Finally, we studied both scalar and vector leptoquarks, with couplings only to the second generation lepton doublet. In both cases, we considered two possible flavor structures for the couplings to quarks: *i*) one dictated by an exact $U(2)_q$ flavor symmetry and *ii*) a minimal scenario required to address the $bs\mu\mu$ anomalies. The main results are given in Figures 4.14 and 4.15 for the scalar, and Figures 4.16 and 4.17 for the vector, with similar conclusions. Moreover, Figure 4.18 offers again a simplified overview of the results for a choice of coupling $\lambda_{b\mu} = 1$. Both MuC3 and FCC-hh have the potential to cover large portions of the parameter space, with similar sensitivity on the leptoquark coupling while the FCC-hh has a much better prospect for on-shell leptoquark discovery via pair-production.

Chapter 5

Global analysis of top-quark SMEFT operators

In this Chapter we study the indirect constraints that can be obtained on the Wilson coefficients of effective operators involving the top quark by considering the effects they have on a large set of low energy observables, comparing these to the direct constraints that have been obtained by studying top quark processes at the LHC. Several groups studied indirect constraints on top anomalous interactions or top quark operators. Refs. [259–263] analyzed anomalous top couplings to W and Z bosons, and top-quark flavor violation, considering rare meson decays and electroweak precision data. Dipole and scalar SMEFT operators with top quarks have been considered in Refs. [264, 265], where indirect bounds from $b \to s\gamma$ and electric dipole moments have been derived after the RG evolution down to the low scale. More recently, Ref. [266] performed a more global analysis, where several top quark operators have been considered and the indirect constraints from B-meson observables and $Z \to b\bar{b}$ have been derived and compared with direct limits from LHC. In our work we go beyond these previous analyses by considering a much larger set of top quark operators (all the ones that involve top quarks) and by substantially enlarging the scope of the observables considered.

The Chapter is structured as follows. In Section 5.1 we discuss the special role of the top quark both in SM and for new physics, while in Section 5.2 we present the setup of our analysis, describing in general terms how we build the global likelihood. Section 5.3 contains an overview of all the observables we take into account, divided into different classes. In Section 5.4 we employ the global likelihood to derive fits in some simplified scenarios and discuss the results: one coefficient at a time, interesting pairs of coefficients, and a Gaussian fit with all coefficients except those of semileptonic operators. To showcase some other applications of this analysis, in Section 5.5 we study two specific UV models that we match to the SMEFT. The first contains a scalar leptoquark coupled only to the third generation quark and lepton doublets. The second simplified model, inspired by the Cabibbo anomaly, contains a scalar and a vector leptoquark. Finally, we conclude

in Section 5.6. Details on all the observables included in our analysis can be found in Appendix E.

5.1 Why the top quark

The top quark plays a special role both in the SM and beyond, due to its large mass or, in other terms, to its $\mathcal{O}(1)$ Yukawa coupling. In the SM, due to the GIM mechanism, it generates the dominant loop contribution in many low-energy flavor-changing neutral-current processes. It also induces some of the leading radiative corrections in the EW sector, it is the main driver of the RG evolution of the quartic Higgs coupling, and it is the main culprit of the (meta-)stability of the Higgs potential. The top quark also generates the largest corrections to the Higgs mass, therefore it is a crucial actor in all new physics scenarios that aim at addressing the naturalness problem of the EW scale. For instance, the so-called top partners are expected to be some of the lightest new particles in such scenarios, both in supersymmetric (stops) and in composite Higgs (vectorlike top partners) models. This expectation is reinforced by the fact that experimental constraints from direct searches of these particles are generally weaker than for the partners of the lighter quarks. Furthermore, due to the large top mass, its couplings to EW gauge bosons are still not so strongly constrained and large new physics effects could still hide there. Therefore, in many BSM scenarios the new states couple most strongly to the top quark. See Ref. [267] for a recent review.

Therefore, considering heavy new physics, it is reasonable to assume that at a UV scale Λ (we fix $\Lambda = 1\,\text{TeV}$ for concreteness) only effective operators involving the top quark are generated at the tree level.

5.2 Methodology

We assume that new physics is heavy, so that we can work in the SMEFT, which we introduced in Section 2.3. We choose the Warsaw basis of dimension-six operators, restricted to the ones that among quarks involve only the third generation quark doublet q^3 and right-handed top u^3, assuming that all the others vanish. The lepton sector is instead left completely general, since we want to consider also tests of lepton flavor universality. The set of SMEFT operators is then reduced to the list in Table 5.1[1]. In the rest of the Chapter, the superscripts '3' for quark indices in SMEFT coefficients are omitted, as they are in the Table. We work with the rescaled coefficients $C_i \equiv \frac{c_i^{(6)}}{\Lambda^2}$ in TeV^{-2} units. Since we want to describe also the mixing with light generations via the CKM matrix, we consider all quark masses. In this case, the flavor basis at the scale Λ is in general different than the quark mass basis, and we are forced to make a flavor assumption at the high scale. We

[1]We assume baryon and lepton number conservation at the scale Λ.

Semi-leptonic		Four quarks	
$\mathcal{O}_{lq}^{(1),\alpha\beta}$	$(\bar{l}^a\gamma_\mu l^\beta)(\bar{q}^3\gamma^\mu q^3)$	$\mathcal{O}_{qq}^{(1)}$	$(\bar{q}^3\gamma^\mu q^3)(\bar{q}^3\gamma_\mu q^3)$
$\mathcal{O}_{lq}^{(3),\alpha\beta}$	$(\bar{l}^a\gamma_\mu\tau^a l^\beta)(\bar{q}^3\gamma^\mu\tau^a q^3)$	$\mathcal{O}_{qq}^{(3)}$	$(\bar{q}^3\gamma^\mu\tau^a q^3)(\bar{q}^3\gamma_\mu\tau^a q^3)$
$\mathcal{O}_{lu}^{\alpha\beta}$	$(\bar{l}^\alpha\gamma^\mu l^\beta)(\bar{u}^3\gamma_\mu u^3)$	$\mathcal{O}_{uu}$	$(\bar{u}^3\gamma^\mu u^3)(\bar{u}^3\gamma_\mu u^3)$
$\mathcal{O}_{qe}^{\alpha\beta}$	$(\bar{q}^3\gamma^\mu q^3)(\bar{e}^\alpha\gamma_\mu e^\beta)$	$\mathcal{O}_{qu}^{(1)}$	$(\bar{q}^3\gamma^\mu q^3)(\bar{u}^3\gamma_\mu u^3)$
$\mathcal{O}_{eu}^{\alpha\beta}$	$(\bar{e}^\alpha\gamma^\mu e^\beta)(\bar{u}^3\gamma_\mu u^3)$	$\mathcal{O}_{qu}^{(8)}$	$(\bar{q}^3\gamma^\mu T^A q^3)(\bar{u}^3\gamma_\mu T^A u^3)$
$\mathcal{O}_{lequ}^{(1),\alpha\beta}$	$(\bar{l}^\alpha e^\beta)\epsilon(\bar{q}^3 u^3)$	Higgs-Top	
$\mathcal{O}_{lequ}^{(3),\alpha\beta}$	$(\bar{l}^\alpha\sigma_{\mu\nu}e^\beta)\epsilon(\bar{q}^3\sigma^{\mu\nu}u^3)$	$\mathcal{O}_{Hq}^{(1)}$	$(H^\dagger i\overleftrightarrow{\mathcal{D}}_\mu H)(\bar{q}^3\gamma^\mu q^3)$
Dipoles		$\mathcal{O}_{Hq}^{(3)}$	$(H^\dagger i\overleftrightarrow{\mathcal{D}}^a_\mu H)(\bar{q}^3\gamma^\mu\tau^a q^3)$
$\mathcal{O}_{uG}$	$(\bar{q}^3\sigma^{\mu\nu}T^A u^3)\tilde{H}G^A_{\mu\nu}$	$\mathcal{O}_{Hu}$	$(H^\dagger i\overleftrightarrow{\mathcal{D}}_\mu H)(\bar{u}^3\gamma^\mu u^3)$
$\mathcal{O}_{uW}$	$(\bar{q}^3\sigma^{\mu\nu}u^3)\tau^a\tilde{H}W^a_{\mu\nu}$	$\mathcal{O}_{uH}$	$(H^\dagger H)(\bar{q}^3 u^3\tilde{H})$
$\mathcal{O}_{uB}$	$(\bar{q}^3\sigma^{\mu\nu}u^3)\tilde{H}B_{\mu\nu}$		

Table 5.1: The 19 dimension-six operators considered in this work. They can be split in four classes, depending on the fields coupled to the top quark. We keep the lepton flavor structure arbitrary.

are assuming that new physics is mostly coupled to the top quark, so it is logical to work in the up-quark mass basis, Eq. (2.28), which corresponds to $q^i = (u_L^i,\, V_{ij}d_L^j)$. This will induce CKM-suppressed operators involving first and second generation left-handed down quarks. If only the operators listed in Table 5.1 are considered, then the results of the fit will of course depend on this choice.

The EFT approach represents a suitable framework to derive bounds on TeV-scale top-philic scenarios from a large set of low-energy observables, as it allows us to consistently study and keep track of the scale dependence of the operators in a multi-step procedure. In practice, renormalization group equations (RGEs) connect different energy scales within the range of validity of the EFT, while matching procedures allow us to integrate out heavy degrees of freedom, linking EFTs valid above or below the threshold.

The description of low energy observables below the electroweak scale relies on the LEFT Lagrangian [268]:

$$\mathcal{L}_{\text{LEFT}} = \mathcal{L}_{\text{QED+QCD}} + \sum_i L_i^{(5)} O_i^{(5)} + \sum_i L_i^{(6)} O_i^{(6)}\,, \tag{5.1}$$

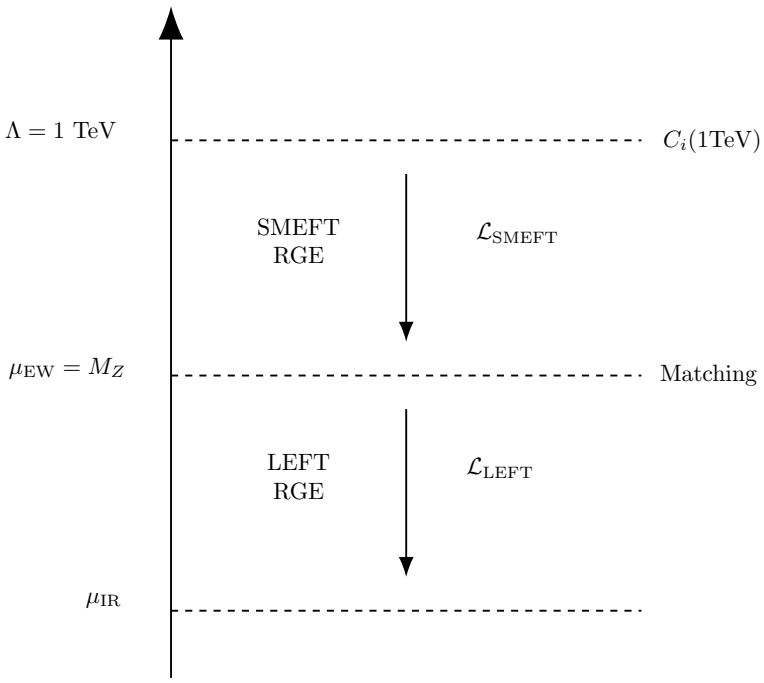

Figure 5.1: Sketch of the EFT analysis procedure. $\mu_{\rm IR}$ is the scale relevant to the low energy observable under consideration.

where the Higgs, W and Z bosons and the top quark have been integrated out, leaving the QCD sector with only two up-type quarks. Higher dimensional non-renormalizable operators are generated both by the SM heavy particles and by SMEFT contributions, again in a model-independent EFT framework. The complete list of LEFT operators is provided in Table E.3.

We consider a large set of low-energy observables in a global analysis, including rare B-meson and kaon decays, meson mixing observables, all the processes used to measure the Cabibbo angle, anomalous magnetic moments of the electron and muon, lepton flavor universality tests in charged-current lepton decays, charged lepton flavor-violating processes, and precision electroweak and Higgs measurements. To obtain the dependence of low-energy observables on our SMEFT coefficients, we perform the following steps.

- We evolve the SMEFT coefficients C_i from Λ down to the electroweak matching scale, that we fix to $\mu_{\rm EW} = m_Z \simeq 91.2$ GeV. We perform this running procedure numerically using the DSixTools package [269, 270], which implements the RGEs provided in [212, 271, 272].

- As discussed in Ref. [273], we combine the one-loop matching with one-loop RG evolution. For the matching between the SMEFT and the LEFT we use the results computed in Ref. [274] and refer to its ancillary files for the complete expressions (see also Ref. [275]).

- The LEFT coefficients [276] are then evolved from the electroweak scale down to the

energy scales $\mu_{\rm IR}$ relevant to the specific observable, e.g. $\mu_{\rm IR} = 4.2$ GeV for B decays, again using the DSixTools numerical routines.

- We express the low-energy observables in terms of the LEFT Wilson coefficients generated by the previous steps.

The whole process is sketched in Figure 5.1, where the main steps and the corresponding energy scales are outlined. QCD effects are known to be relevant, especially at low energies, and a resummation beyond the leading order is required. So, as an exception, we use the five-loop QCD correction for quark Yukawas and the gauge coupling from Refs. [277–279] and the four-loop strong coupling beta function and quark mass anomalous dimension from Ref. [280]. These QCD corrections are implemented in DSixTools as well as the three-loop SM RGEs from Refs. [281–284].

The procedure depicted in Figure 5.1 does not apply to the observables defined above/at the EW scale, when running the SMEFT coefficients up to $\Lambda_{\rm UV}$ is the only necessary step. In some cases, previous studies and results in the literature allowed us to partially or completely skip some steps. These cases will be mentioned and discussed in the following.

Once we have expressed the low energy observables and pseudo-observables in terms of SMEFT Wilson coefficients, we build the log-likelihood:

$$-2\log\mathcal{L}(C_k) \equiv \chi^2(C_k) = \sum_{i,j}(\mathcal{O}_i(C_k) - \mu_i)\,(\sigma^2)^{-1}_{ij}\,(\mathcal{O}_j(C_k) - \mu_j)\,, \tag{5.2}$$

where $\mathcal{O}_i$ are the observables, C_k are the Wilson coefficients defined at the TeV scale, μ_i are the experimental values and $(\sigma^2)_{ij}$ is the corresponding covariance matrix. The likelihood is maximized by looking at the minimum of the chi-square, χ^2_0, so that the quantity $\Delta\chi^2 = \chi^2 - \chi^2_0$ allows to define the 68% or 95% CL regions. We use our global likelihood to perform individual, pairwise and global fits on Wilson coefficients. In practice, we allow only one, two or a subset of parameters in the global $\chi^2(C_i)$ to vary and set to zero all the remaining ones. Results and applications are discussed in Sections 5.4 and 5.5.

5.3 Observables

The up quark basis we employ for the left-handed quark doublet makes several top quark operators, such as the ones from Table 5.1, contribute to FCNC $d^i_L \to d^j_L$ transitions even at tree-level, only suppressed by $V^*_{tj}V_{ti}$ factors. Very strong bounds to such BSM contributions can be obtained from rare B and K decays as well as meson mixing observables. Operators with top quarks are also expected to give relevant contributions, via loop effects, to anomalous magnetic moments of leptons, tau decays, electroweak precision data, Higgs measurements and precision measurements entering in Cabibbo-angle analyses. Finally, operators that violate lepton flavor are constrained by lepton flavor violation (LFV) tests in lepton and meson decays. In the following subsections we provide some more details on these observables, postponing more detailed discussions to Appendix E.

5.3.1 B physics

SM-suppressed FCNC $b \to s$ transitions are powerful channels to probe new physics, in particular in those observables for which the SM prediction is free from poorly-known long-distance QCD effects. Among these, after the recent update by LHCb [21], the lepton flavor universality ratios R_K and R_{K^*}, defined in Eq. (4.1), provide stringent constraints on new physics coupled to light leptons, see Eq. (4.4).

Other powerful decay channels for testing new physics are the so-called *golden-channel* decays, for which it can be useful to define the ratios with the SM predictions as

$$R^{\nu}_{K^{(*)}} \equiv \frac{\mathcal{B}(B \to K^{(*)}\nu\bar{\nu})}{\mathcal{B}(B \to K^{(*)}\nu\bar{\nu})_{\rm SM}} \,, \tag{5.3}$$

using the updated SM predictions from Ref. [285]. Notably, the Belle-II experiment recently presented the first evidence for a signal in the $B^+ \to K^+\nu\bar{\nu}$ channel: $\mathcal{B}(B^+ \to K^+\nu\bar{\nu})_{\rm Belle-II} = (2.3 \pm 0.5^{+0.5}_{-0.4}) \times 10^{-5}$ [286]. Once combined with previous upper limits, this becomes $\mathcal{B}(B^+ \to K^+\nu\bar{\nu})_{\rm Comb.} = (1.3 \pm 0.4) \times 10^{-5}$, to be compared with the SM prediction $\mathcal{B}(B^+ \to K^+\nu\bar{\nu})_{\rm SM} = (0.444 \pm 0.030) \times 10^{-5}$.[2] The corresponding value for R^{ν}_K is reported in Table 5.2. On the other hand, the strongest upper limit on the K^* mode comes from Belle, with $R^{\nu}_{K^*} < 3.21$ at 95%CL [287] after combining the different modes. Several new physics models affect these decay modes as a rescaling of the SM short-distance amplitude, that involves only $V - A$ currents, in such a way that $R^{\nu}_K = R^{\nu}_{K^*}$. In this case it is interesting to combine the two modes, obtaining

$$R^{\nu}_{K^{(*)}} = 2.16 \pm 0.70 \,, \tag{5.4}$$

compatible with the SM value of 1 at 1.7σ. We emphasize that, since we are not assuming lepton flavor number conservation, the inclusive sum on neutrino final states takes into account LFV cases:

$$\mathcal{B}(B \to K^{(*)}\nu\bar{\nu}) = \sum_{\alpha,\beta=1}^{3} \mathcal{B}(B \to K^{(*)}\nu_\alpha\bar{\nu}_\beta) \,. \tag{5.5}$$

We conclude the list of B decays by including $B_s \to X_s\gamma$, the leptonic $B_s \to \ell_\alpha\ell_\beta$ decays as well as semileptonic and leptonic LFV modes. The complete list of B-physics observables we consider is displayed Table 5.2, together with measurements provided by the LHCb, Belle(-II) and BaBar experiments.

Theoretical predictions are extensively discussed in Appendix E, where branching ratios expressed in terms of low energy EFT coefficients are given. Here, we limit ourselves to show, in Table 5.3, a comprehensive sketch of SMEFT contributions to the observables we considered. We briefly discuss WC's relevance and interplay in the rest of this Section.

[2] This is the SM prediction with the long-distance $B^+ \to \bar{\nu}_\tau\tau^+ \to K^+\bar{\nu}_\tau\nu_\tau$ removed, since the experimental collaboration treats this as background.

Observable	Experimental value
$B \to X_s\gamma$	$(3.49 \pm 0.19) \times 10^{-4}$ [74]
R_K^ν	2.93 ± 0.90 [285, 286]
$R_{K^*}^\nu$	< 3.21 [285, 287]
$R_K[1.1, 6]$	0.949 ± 0.047 [21]
$R_{K^*}[1.1, 6]$	1.027 ± 0.077 [21]
$\mathcal{B}(B \to Ke\mu)$	$< 4.5 \times 10^{-8}$ [288]
$\mathcal{B}(B \to Ke\tau)$	$< 3.6 \times 10^{-5}$ [289]
$\mathcal{B}(B \to K\mu\tau)$	$< 4.5 \times 10^{-5}$ [290]

Observable	Experimental value
$\mathcal{B}(B_s \to ee)$	$< 11.2 \times 10^{-9}$ [291]
$\mathcal{B}(B_s \to \mu\mu)$	$(3.01 \pm 0.35) \times 10^{-9}$ [132]
$\mathcal{B}(B_s \to \tau\tau)$	$< 6.8 \times 10^{-3}$ [292]
$\mathcal{B}(B_s \to e\mu)$	$< 6.3 \times 10^{-9}$ [293]
$\mathcal{B}(B_s \to \mu\tau)$	$< 4.2 \times 10^{-5}$ [294]
$\mathcal{B}(B_d \to ee)$	$< 3.0 \times 10^{-9}$ [291]
$\mathcal{B}(B_d \to \mu\mu)$	$< 2.6 \times 10^{-10}$ [132]
$\mathcal{B}(B_d \to \tau\tau)$	$< 2.1 \times 10^{-3}$ [292]
$\mathcal{B}(B_d \to e\mu)$	$< 1.3 \times 10^{-9}$ [293]
$\mathcal{B}(B_d \to \mu\tau)$	$< 1.4 \times 10^{-5}$ [294]

Table 5.2: Experimental values for B-physics observables included in this work. Bounds are given at 95% CL.

The semileptonic C_{qe} and the combination $(C_{lq}^{(1)}+C_{lq}^{(3)})$ contribute at tree level to $b(d) \to s\ell_\alpha\ell_\beta$ processes, getting constrained by both rare meson $B_{s,d} \to \ell_\alpha\ell_\beta$ and semileptonic $B \to K\ell_\alpha\ell_\beta$ decays. Within these cases, the recent analysis of $R_{K^{(*)}}$ provides strong constraints on light lepton operators (see discussion in Section 5.4.2 and figures therein) up to the $|C_i| \leq 10^{-2}\,\text{TeV}^{-2}$ level. These bounds on semileptonic current-current operators are completed and complemented by dineutrino modes $B \to K\nu\bar{\nu}$, which are sensitive at tree level to the combination $(C_{lq}^{(1)} - C_{lq}^{(3)})$ and to the Higgs-top operators $C_{Hq}^{(1)}$ and $C_{Hq}^{(3)}$.

In general, contributions from 4-quark operators arise in radiative corrections, from both the one-loop matching and the RG evolution. Similarly, the up-type dipole operators C_{uG}, C_{uB} and C_{uW} enter the one-loop matching expression for down-type dipoles, contributing then to the $B \to X_s\gamma$ decays. Inclusive radiative decays and rare $B \to \ell_\alpha\ell_\beta$ decays also constrain the $C_{Hq}^{(1/3)}$ coefficients, making B physics bounds almost comparable to the EW precision tests (see Figure 5.4).

Remarkably, the lack of direct limits on semileptonic dimension-six operators from top-quark measurements, such as inclusive $t\bar{t}$ and single top productions, makes indirect bounds from B mesons crucial in interpreting top-philic BSM scenarios. At the same time, these flavor observables provide competitive or stronger constraints on 4-quark and Higgs-top operators, testing the robustness of global fits.

5.3.2 Kaon physics

Analogously to B physics, several operators in Table 5.1 induce $s \to d$ transitions, driving FCNC decays of kaons. The list of observables we considered in this work and the

	Tree level matching	RG and 1-loop matching
$B \to X_s\gamma$		$C_{Hq}^{(1,3)},\ C_{uB},\ C_{uW},\ C_{uG}$
$R_{K^{(*)}}^{\nu}$ $K \to \pi\nu\bar{\nu}$	$C_{Hq}^{(1,3)},\ C_{lq}^{(1,3),\alpha\beta}$	$C_{Hu},\ C_{qq}^{(1,3)},\ C_{lu}^{\alpha\beta},\ C_{qe}^{\alpha\beta}$ $C_{qu}^{(1,8)},\ C_{uu},\ C_{uW}$
$B \to K^{(*)}\ell_\alpha\ell_\beta$ $B_{s,d} \to \ell_\alpha\ell_\beta$ $K \to \pi\ell_\alpha\ell_\beta$ $K \to \ell_\alpha\ell_\beta$	$C_{lq}^{(1,3),\alpha\beta},\ C_{qe}^{\alpha\beta},\ C_{Hq}^{(1,3)}$	$C_{lu}^{\alpha\beta},\ C_{eu}^{\alpha\beta},\ C_{qq}^{(1,3)}$
$R_{K^{(*)}}$	$C_{lq}^{(1,3),\ell\ell},\ C_{qe}^{\ell\ell}$	$C_{lu}^{\ell\ell}$

Table 5.3: Most relevant WC to B and K physics observables. The operators that contribute at tree level are displayed in the left column, while operators generated by radiative corrections are listed in the right column. The indices take values α, β=1,2,3 and $\ell = e, \mu$. Transpose conjugate operators are not listed since related to the already mentioned ones, e.g. $C_{lq}^{(1),\beta\alpha} = C_{lq}^{(1),\alpha\beta *}$.

corresponding experimental measurements are reported in Table 5.4, while more details can be found in Appendix E. The discussion for kaon physics follows the same lines as the one above for B decays: the relevant coefficients constrained by each observables are reported in Table 5.3. Bounds on WC from rare kaon decays involving leptons are less relevant then the corresponding ones of B mesons, mainly due to the strong constraints from $R_{K^{(*)}}$ and $B_s \to \mu\mu$, while $K \to \pi\nu\bar{\nu}$ gives competitive bounds on $C_{lq}^{(1/3),33}$, see the relevant discussions in Section 5.4.

5.3.3 $\Delta F = 2$

Meson mixing observables offer some of the most stringent constraints for several BSM scenarios. Among the top quark operators we consider, $\mathcal{O}_{qq}^{(1,3)}$ induce tree-level contributions to these processes, while many more contribute at the loop level.

Model-independent expressions of new physics contributions to $\Delta F = 2$ amplitudes in terms of SMEFT coefficients have been derived in Ref. [306]. The authors considered hadronic matrix elements of the various LEFT operators at the low scale, the RG evolution to the electroweak scale, the matching to SMEFT coefficients in the Warsaw basis (and the up quark mass basis), and finally the SMEFT RG evolution up to a scale $\Lambda = 5\,\text{TeV}$. We neglect the small mismatch in the RG evolution between this scale and the scale at which we define our coefficients, 1 TeV, as this can be well included among the theory uncertainties of working with the LL RG evolution. For the predictions of the SM contribution to meson mixing we use the results of Ref. [305], specifically the values obtained with the exclusive V_{cb} measurements and the inclusive V_{ub} one (the so-called hybrid scenario). Finally, we take the experimental values for ϵ_K, ΔM_s, and ΔM_d from the PDG combination [74]. In

Observable	Experimental value
$\mathcal{B}(K^+ \to \pi^+ \nu\bar{\nu})$	$(1.14^{+0.4}_{-0.33}) \times 10^{-10}$ [295] [296]
$\mathcal{B}(K_L \to \pi^0 \nu\bar{\nu})$	$< 3.6 \times 10^{-9}$ [297]
$\mathcal{B}(K_S \to \mu^+\mu^-)$	$< 2.5 \times 10^{-10}$ [298]
$\mathcal{B}(K_L \to \mu^+\mu^-)_{SD}$	$< 2.5 \times 10^{-9}$ [299]
$\mathcal{B}(K_L \to \mu^\pm e^\mp)$	$< 5.6 \times 10^{-12}$ [300]
$\mathcal{B}(K_L \to \pi^0\mu^+\mu^-)$	$< 4.5 \times 10^{-10}$ [301]
$\mathcal{B}(K_L \to \pi^0 e^+ e^-)$	$< 3.3 \times 10^{-10}$ [302]
$\mathcal{B}(K_L \to \pi^0 e^+\mu^-)$	$< 9.1 \times 10^{-11}$ [303]
$\mathcal{B}(K^+ \to \pi^+ e^+\mu^-)$	$< 7.9 \times 10^{-11}$ [304]

Table 5.4: Experimental values for kaon physics observables included in this work. Bounds are given at 95% CL.

Observable	Experimental value	SM prediction
ϵ_K	$(2.228 \pm 0.011) \times 10^{-3}$	$(2.14 \pm 0.12) \times 10^{-3}$
ΔM_s	$(17.765 \pm 0.006)\,\text{ps}^{-1}$	$(17.35 \pm 0.94)\,\text{ps}^{-1}$
ΔM_d	$(0.5065 \pm 0.0019)\,\text{ps}^{-1}$	$(0.502 \pm 0.031)\,\text{ps}^{-1}$

Table 5.5: Experimental values [74] and SM predictions [305] for meson mixing observables.

Table 5.5 we collect the values employed in our analysis, where experimental and theory uncertainties are added in quadrature.

5.3.4 Cabibbo angle decays

Nuclear beta, baryon, pion, kaon decay and semileptonic tau decay data are also precise new physics probes. Since the studied decay modes in the SM are suppressed by $\mathcal{O}\left(\frac{1}{v^2}\right)$, new physics contributions to the observables are only suppressed with respect to the SM by $\mathcal{O}\left(\frac{v^2}{\Lambda^2}\right)$. Taking into account the per-mil level precision reached in some of the observables, potential new physics beyond the TeV scale is probed by these decays. Within the SM picture, this sector leads to the Cabibbo anomalies introduced in Section 2.1.3. It is then interesting to incorporate it to the analysis and to check whether, within our BSM set-up, constraints from other observables leave room for potential new physics explanations of these anomalies.

We make use the global analysis to those observables made in Ref. [307] in terms of low-energy EFT coefficients ϵ_i, which updates the EFT analyses made in Refs. [174, 308] and incorporates hadronic tau decays. Consistently with the assumptions of that analysis, we match the ϵ_i to the LEFT and then to the SMEFT at tree-level (see Appendix E.8).

Observable	Experimental value	
	$\ell = e$	$\ell = \mu$
Δa_ℓ	$(2.8 \pm 7.4) \times 10^{-13}$	$(20.0 \pm 8.4) \times 10^{-10}$
$g_\tau/g_\ell - 1$	$(2.7 \pm 1.4) \times 10^{-3}$	$(0.9 \pm 1.4) \times 10^{-3}$

Table 5.6: BSM contributions to anomalous magnetic moment of the leptons, $\Delta a_\ell \equiv a_\ell^{\rm exp} - a_\ell^{\rm SM}$, and LFU in τ decays [309], $g_\tau/g_\ell - 1$. The correlation between the g_τ/g_e and the g_τ/g_μ values is 51 %.

The leading contributions induced by the studied top operators appear through leading logs in the SMEFT running proportionally to the top Yukawa squared.

In our BSM set-up, the combined fit to this set of observables translates into $\mathcal{O}$(TeV) sensitivity to $C_{lq}^{(3),\ell\ell}$. At least part of the Cabibbo tension can in principle be alleviated by a nonzero $C_{lq}^{(3),22}$ value, which can play an important role in the unitarity relation. In Section 5.5.2 we discuss a UV model inspired by this anomaly. Currently, efforts in the area are focused in understanding whether the so-called Cabibbo anomalies are genuine new physics hints or due to underestimated uncertainties. Overall one may not expect any major improvement in the sensitivity to new physics with respect to the quoted precision from this sector in the short term.

5.3.5 Magnetic moments and LFU in τ decays

The anomalous magnetic moments of electrons and muons, $a_\ell = (g_\ell - 2)/2$, are among the most precisely measured quantities in experimental physics:

$$\begin{aligned} a_e^{\rm exp} &= (11596521807.3 \pm 2.8) \times 10^{-13}\,, \\ a_\mu^{\rm exp} &= (11659205.9 \pm 2.2) \times 10^{-10}\,. \end{aligned} \tag{5.6}$$

Remarkably, the theoretical precision of the corresponding SM predictions is similar, making them stringent SM tests. In practice, some tensions in the associated evaluations using different inputs slightly limit the current precision. Namely, as pointed out in Ref. [310], the value of $a_e^{\rm SM}$ is sensitive to the input value of the fine-structure constant, $\alpha_{\rm QED}$, and the two most precise determinations, based on Cesium and Rubidium atomic recoils [311, 312], differ by more than $5\,\sigma$. Similarly, the SM leading-order hadronic vacuum polarization (HVP) prediction quoted in the muon $g-2$ Theory White Paper (WP) [313–333], which constitutes the dominant source of uncertainty for $a_\mu^{\rm SM}$, is 2σ below the lattice BMW value [334] and new results on related observables [334–347] suggest that the source of the difference may go beyond a mere statistical fluctuation. We then take the weighted average of the $a_e^{\rm SM}$ result obtained from $\alpha_{\rm QED}^{\rm Cs}$ and $\alpha_{\rm QED}^{\rm Rb}$ and the weighted average of the $a_\mu^{\rm SM}$ one using $a_{\mu,\rm BMW}^{\rm HVP,LO}$ and $a_{\mu,\rm WP}^{\rm HVP,LO}$ as inputs, but adding half their differences as additional sources

of systematic uncertainties. The corresponding values of $\Delta a_\ell = a_\ell^{\rm exp} - a_e^{\rm SM}$ are reported in Table 5.6.

The main way to generate an extra a_ℓ contribution in our BSM set-up is through the $\mathcal{O}_{lequ}^{(3),\ell\ell}$ operator, since top-antitop annihilation will generate, through mixing, the dipole operator associated to the anomalous magnetic moment. The process has been recently studied within the LEFT-SMEFT framework in Ref. [310]. Using the results from that reference, running up to $\Lambda = 1\,\text{TeV}$ and keeping only the studied operators we find

$$\begin{aligned} \Delta a_e &= -4.8 \times 10^{-8}\, C_{lequ}^{(3),11} + 7.1 \times 10^{-11}\, C_{lequ}^{(1),11}, \\ \Delta a_\mu &= -1.0 \times 10^{-5}\, C_{lequ}^{(3),22} + 1.5 \times 10^{-8}\, C_{lequ}^{(1),22}. \end{aligned} \tag{5.7}$$

Thus, barring some bizarre cancellation mechanism, $|C_{lequ}^{(3),11}| \gtrsim 10^{-4}\,\text{TeV}^{-2}$ and $|C_{lequ}^{(3),22}| \gtrsim 10^{-3}\,\text{TeV}^{-2}$ at $\Lambda = 1\,\text{TeV}$ can already be excluded by current g-2 measurements.

Ratios of leptonic decays of τ and μ provide very clean tests of lepton flavor universality [309, 348]. Deviation from the SM predictions are often parameterized by ratios of effective charges, $g_\ell/g_{\ell'}$, which in the SM limit are equal to 1, and whose experimental values are given in Table 5.6. In the LEFT one has

$$\begin{aligned} \frac{g_\tau}{g_e} - 1 &= \frac{v^2}{2}\left(L^{V,LL}_{\substack{\nu e \\ \mu e e \mu}} - L^{V,LL}_{\substack{\nu e \\ \tau \mu \mu \tau}} \right), \\ \frac{g_\tau}{g_\mu} - 1 &= \frac{v^2}{2}\left(L^{V,LL}_{\substack{\nu e \\ \mu e e \mu}} - L^{V,LL}_{\substack{\nu e \\ \tau e e \tau}} \right). \end{aligned} \tag{5.8}$$

In our set-up this translates, for $\Lambda = 1\,\text{TeV}$, into

$$\begin{aligned} \frac{g_\tau}{g_e} - 1 &= 0.0038\,(C_{lq}^{(3),33} - C_{lq}^{(3),11}), \\ \frac{g_\tau}{g_\mu} - 1 &= 0.0038\,(C_{lq}^{(3),33} - C_{lq}^{(3),22}), \end{aligned} \tag{5.9}$$

where the C_{lq} coefficients are in TeV^{-2} units.

5.3.6 Charged lepton flavor violating decay modes

Experimental searches of neutrinoless lepton flavor violating decay modes of leptons are suitable to test potential BSM scenarios at energy scales beyond the reach of searches at high-energy colliders.

The very stringent limits on $\mu \to e\gamma$, $\mu \to 3e$ transitions and $\mu \to e$ conversion in nuclei, currently coming respectively from MEG at PSI and SINDRUM [349–351], constitute a BSM probe of scales of up to $\Lambda_{\rm BSM} \sim 10^3 - 10^4\,\text{TeV}$ [358]. They were studied within the LEFT in Ref. [359]. For our specific SMEFT set-up, the corresponding limits translate into limits on linear combinations of Wilson coefficients involving semileptonic operators that violate lepton flavor. They are the only operators that at the same time contain the needed BSM LFV insertion and satisfy the assumed top-philic condition. If only one (but

Observable	Experimental limit
$\mathcal{B}(\mu \to e\gamma)$	5.0×10^{-13} [349]
$\mathcal{B}(\mu \to 3e)$	1.2×10^{-12} [350]
$\mathcal{B}(\mu\,\mathrm{Au} \to e\,\mathrm{Au})$	8.3×10^{-13} [351]
$\mathcal{B}(\tau \to e\gamma)$	3.9×10^{-8} [352]
$\mathcal{B}(\tau \to 3e)$	3.2×10^{-8} [353]
$\mathcal{B}(\tau \to e\,\bar{\mu}\mu)$	3.2×10^{-8} [353]
$\mathcal{B}(\tau \to e\pi^0)$	9.5×10^{-8} [354]
$\mathcal{B}(\tau \to e\eta)$	1.1×10^{-7} [354]
$\mathcal{B}(\tau \to e\eta')$	1.9×10^{-7} [354]

Observable	Experimental limit
$\mathcal{B}(\tau \to e\pi^+\pi^-)$	2.7×10^{-8} [355]
$\mathcal{B}(\tau \to eK^+K^-)$	4.1×10^{-8} [355]
$\mathcal{B}(\tau \to \mu\gamma)$	5.0×10^{-8} [356]
$\mathcal{B}(\tau \to 3\mu)$	2.5×10^{-8} [353]
$\mathcal{B}(\tau \to \mu\,\bar{e}e)$	2.1×10^{-8} [353]
$\mathcal{B}(\tau \to \mu\pi^0)$	1.3×10^{-7} [357]
$\mathcal{B}(\tau \to \mu\eta)$	7.7×10^{-8} [354]
$\mathcal{B}(\tau \to \mu\eta')$	1.5×10^{-7} [354]
$\mathcal{B}(\tau \to \mu\pi^+\pi^-)$	2.5×10^{-8} [355]
$\mathcal{B}(\tau \to \mu K^+K^-)$	5.2×10^{-8} [355]

Table 5.7: Current 95% CL limits on studied LFV branching ratios.

any) parameter is switched on, one is able to constrain it at the $|C_i| \lesssim 10^{-4}\,\mathrm{TeV}^{-2}$ level. Studies at PSI, MEG II [360], Mu2e [361] and Mu3e [362], are expected to significantly improve these limits in the near future. We collect the present bounds in Table 5.7.

While the EFT description at the SMEFT-LEFT level of the tau decays is qualitatively equivalent, leading to bounds on Wilson coefficients of the same kind of semileptonic operators for our case, the underlying LFV studies are different [363–366]. With the existing and future probes one does not expect to test new physics much higher than $\Lambda_{\mathrm{BSM}} \sim 10\,\mathrm{TeV}$ [358]. However, many more potential decay channels can be experimentally accessed, as a consequence of a tau mass that is large enough to produce hadrons. In this sense, if charged LFV were discovered in the tau sector, the information from the different decay channels would unlock the full power of the EFT approach to stringently discriminate among different BSM scenarios, by having direct experimental access to the values of the different Wilson Coefficients. In the meantime we can use the existing limits to set bounds on different combinations of them. Current limits, coming from Belle and BaBar [74], are expected to be improved by Belle-II [367]. In Figure 5.2 we show the sensitivity of the different decay modes to the different studied operators.

5.3.7 Electroweak and Higgs data

Electroweak precision data (Z and W decays) and Higgs measurements provide strong indirect constraints on new physics involving the top quark, via loop effects. The authors of Ref. [368] performed a global SMEFT analysis of Z and W pole data, WW pair production data at LEP2, and Higgs signal strength measurements from ATLAS and CMS. SMEFT contributions in the Warsaw basis are included at the tree-level except for observables that

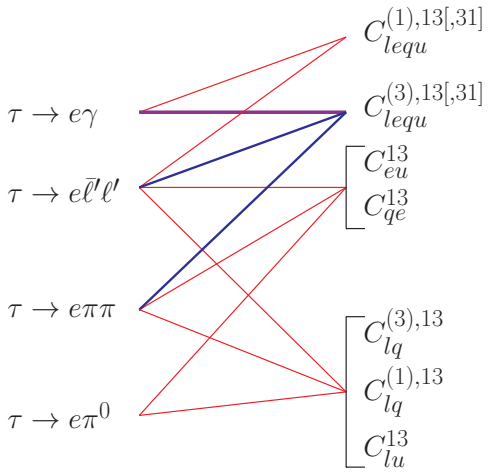

Figure 5.2: Sensitivity of the different $\tau \to e$ decay modes (similar hierarchy is observed for the $\tau \to \mu$ ones) to the different studied Wilson coefficients using the current experimental bounds. Red, blue and purple lines correspond, respectively, to upper bounds to the coefficient below 0.4, 4×10^{-3} and 4×10^{-4} (TeV^{-2} units), assuming one parameter is present at a time.

C_W	δc_z	$c_{z\Box}$	c_{gg}	$c_{\gamma\gamma}$	c_{zz}	$c_{z\gamma}$
$[\delta g_L^{W\ell}]_{\alpha\beta}$	$[\delta g_L^{Z\ell}]_{\alpha\beta}$	$[\delta g_R^{Z\ell}]_{\alpha\beta}$	$[\delta g_L^{Zd}]_{\alpha\alpha}$	$[\delta g_R^{Zd}]_{\alpha\alpha}$	$[\delta g_L^{Zu}]_{\alpha\alpha}$	$[\delta g_L^{Zu}]_{\alpha\alpha}$
$[C_{uH}]_{33}$	$[C_{dH}]_{33}$	$[C_{eH}]_{22}$	$[C_{eH}]_{33}$	$[C_{ll}]_{1221}$		

Table 5.8: List of Wilson coefficients used in the fit of Ref. [368]. The ones with capital C are already in the Warsaw basis, while the definition of the others is reported in Appendix E.9.

are loop-generated in the SM (such as $h \to \gamma\gamma, Z\gamma$ and $gg \to h$), in which case one-loop contributions are included as well. For our numerical analysis we use updated results for the global fit (including correlations), kindly provided by the authors of Ref. [368]. The constraints on LFV Z couplings to charged leptons are taken from the fit in Ref. [369], while LFV couplings to neutrinos are constrained via the measurement of the effective number of neutrinos N_ν updated in Ref. [370]. The fit is performed in terms of specific combinations of Wilson coefficients of the Warsaw basis evaluated at the weak scale shown in Table 5.8. Their definition is reported in Appendix E.9.

We interpret the resulting likelihood for SMEFT coefficients as evaluated at the EW scale, and then include the RG evolution up to 1 TeV to obtain the final likelihood for our analysis, in terms of the coefficients of the operators listed in Table 5.1. The coefficients that provide relevant constraints to our analysis are listed here, together with the TeV-scale

coefficients that contribute the most to each one:

EW/Higgs coeff.		TeV-scale coefficient
$\delta g_L^{Z\ell}$	$\longleftarrow$	$C_{uB},\ C_{uW}, C_{Hu},\ C_{Hq}^{(1,3)},\ C_{lq}^{(1,3),\ell\ell},\ C_{lu}^{\ell\ell},\ \ldots$
$\delta g_L^{W\ell}$	$\longleftarrow$	$C_{uB},\ C_{uW},\ C_{Hu},\ C_{Hq}^{(1,3)},\ C_{lq}^{(3),\ell\ell},\ \ldots$
$\delta g_R^{Z\ell}$	$\longleftarrow$	$C_{uB},\ C_{uW},\ C_{Hu},\ C_{Hq}^{(1,3)},\ C_{eu}^{\ell\ell},\ C_{qe}^{\ell\ell},\ \ldots$
δg_L^{Zb}	$\longleftarrow$	$C_{Hq}^{(1,3)},\ C_{Hu},\ C_{qq}^{(1,3)},\ \ldots$
δg_R^{Zb}	$\longleftarrow$	$C_{Hq}^{(1)},\ C_{Hu},\ C_{qq}^{(1,3)},\ C_{uB},\ C_{uW},\ \ldots$
$c_{\gamma\gamma}$	$\longleftarrow$	$C_{uB},\ C_{uW},\ C_{uG}$
c_{gg}	$\longleftarrow$	C_{uG}
$[C_{eH}]_{\alpha\alpha}$	$\longleftarrow$	$C_{lequ}^{(1),\alpha\alpha}$
$[C_{uH}]_{33}$	$\longleftarrow$	$C_{uH},\ C_{uG},\ C_{Hq}^{(1,3)},\ C_{qu}^{(1,8)},\ \ldots$

(5.10)

5.3.8 Direct bounds from LHC

SMEFT interpretations of top quark production and decay measurements at LHC have been discussed in several works [263, 265, 371–384], providing direct bounds on 4-quark, dipole and Higgs-top operators.

The analysis by the SMEFiT collaboration [377] includes observables from the LHC Run-II dataset and studies connections with Higgs and diboson data. The SMEFiT fitting framework has been released as a Python open source package [382]. We exploit the flexibility of this toolbox to perform a SMEFT analysis of Higgs, top quark and electroweak production data (see Section 3 of Ref. [377] for details) including our operators of Table 5.1, with exception of the semi-leptonic ones. The resulting constraints are reported in Appendix E.10. In the next section we compare these with the indirect constraints derived from our global analysis.

5.4 Global analysis

The observables described in the previous section, except for the direct constraints from LHC of Section 5.3.8, are used to build the log-likelihood as in Eq. (5.2). This provides global indirect constraints on top quark operators, that we can compare with the direct ones from measurements at LHC. In the following we present examples of fits derived using our global likelihood. For simplicity we assume all Wilson coefficients to be real in the following.

5.4.1 One-parameter fits

First, we perform one-parameter fits setting all the Wilson coefficients to zero except one. While such one-parameter set-up is not a realistic low-energy description of typical UV

Wilson	Global fit [TeV^{-2}]	Dominant
$C_{qq}^{(+)}$	$(-1.9 \pm 2.3) \times 10^{-3}$	ΔM_s
$C_{qq}^{(-)}$	$(-2.0 \pm 1.0) \times 10^{-1}$	$B_s \to \mu\mu$
$C_{qu}^{(1)}$	$(1.3 \pm 1.0) \times 10^{-1}$	ΔM_s
$C_{qu}^{(8)}$	$(-1.7 \pm 4.4) \times 10^{-1}$	ΔM_s
C_{uu}	$(-3.0 \pm 1.7) \times 10^{-1}$	$\delta g_{L,11}^{Ze}$
$C_{Hq}^{(+)}$	$(18.7 \pm 8.8) \times 10^{-3}$	$B_s \to \mu\mu$
$C_{Hq}^{(-)}$	$(5.8 \pm 4.5) \times 10^{-2}$	$\delta g_{L,11}^{Ze}$
C_{Hu}	$(-4.3 \pm 2.3) \times 10^{-2}$	$\delta g_{L,11}^{Ze}$
C_{uB}	$(-0.6 \pm 2.0) \times 10^{-2}$	$c_{\gamma\gamma}$
C_{uG}	$(-0.1 \pm 2.0) \times 10^{-2}$	c_{gg}
C_{uH}	$(-0.3 \pm 5.2) \times 10^{-1}$	$C_{uH,33}$
C_{uW}	$(-0.1 \pm 3.1) \times 10^{-2}$	$c_{\gamma\gamma}$

Table 5.9: Combined fit for one at a time Wilson coefficients for non-leptonic operators. The dominant observable giving the most precise bound is also displayed.

scenarios, it can provide meaningful information about the new physics scale that can be probed if that operator is generated. It also provides a way to compare the sensitivity of different observables or, alternatively, which observables/sectors one should look at first if a specific operator is induced by the studied UV model.

The results associated to the different operators, respectively non-leptonic, semileptonic lepton flavor conserving and semileptonic lepton flavor violating, are shown in Tables 5.9, 5.10 and 5.11, together with which (isolated) single observable currently gives the most precise determination of the associated Wilson coefficient. We have defined $C_{iq}^{(\pm)} \equiv C_{iq}^{(1)} \pm C_{iq}^{(3)}$ for $i = H, q, l$. As shown in Section 5.3, these linear combinations are typically the ones appearing at leading order in the most constraining observables.

We study next the complementarity of the indirect bounds with the direct LHC ones. In Figure 5.3 we show the results of the individual fits for Higgs-Top, dipoles and 4-quarks operators, together with corresponding bounds derived through the SMEFiT fitting framework. We stress that, exclusively in this plot, Wilson coefficients are displayed according to the SMEFiT basis (lower case c_{AB}), whose expression in terms of the Warsaw basis can be found in Table E.2.

A few comments are in order concerning the comparison of these bounds. The com-

Wilson	Global fit [TeV^{-2}]	Dominant
$C_{lq}^{(+),11}$	$(2.4 \pm 3.5) \times 10^{-3}$	R_K
$C_{lq}^{(+),22}$	$(-4.0 \pm 3.4) \times 10^{-3}$	R_K
$C_{lq}^{(+),33}$	$(7.2 \pm 4.4) \times 10^{-1}$	g_τ/g_i
$C_{lq}^{(-),11}$	$(10.9 \pm 7.6) \times 10^{-2}$	$R^{\nu}_{K^{(*)}}$
$C_{lq}^{(-),22}$	$(-6.0 \pm 7.0) \times 10^{-2}$	$R^{\nu}_{K^{(*)}}$
$C_{lq}^{(-),33}$	$(-1.8 \pm 1.0) \times 10^{-1}$	$R^{\nu}_{K^{(*)}}$
C_{lu}^{11}	$(-1.7 \pm 7.0) \times 10^{-2}$	$\delta g^{Ze}_{L,11}$
C_{lu}^{22}	$(-4.3 \pm 1.8) \times 10^{-1}$	$\delta g^{Ze}_{L,22}$, R_K
C_{lu}^{33}	$(0.5 \pm 2.4) \times 10^{-1}$	$\Delta g^{Ze}_{L,33}$
C_{qe}^{11}	$(-0.7 \pm 3.9) \times 10^{-2}$	R_{K^*}
C_{qe}^{22}	$(12.1 \pm 9.2) \times 10^{-3}$	$B_s \to \mu\mu$
C_{qe}^{33}	$(2.2 \pm 2.4) \times 10^{-1}$	$\delta g^{Ze}_{R,33}$

Wilson	Global fit [TeV^{-2}]	Dominant
C_{eu}^{11}	$(5.0 \pm 8.1) \times 10^{-2}$	$\Delta g_R^{Ze}{}_{11}$
C_{eu}^{22}	$(4.8 \pm 2.1) \times 10^{-1}$	$\Delta g_R^{Ze}{}_{22}$
C_{eu}^{33}	$(-2.3 \pm 2.5) \times 10^{-1}$	$\Delta g_R^{Ze}{}_{33}$
$C_{lequ}^{(1),11}$	$(0.4 \pm 1.0) \times 10^{-2}$	$(g-2)_e$
$C_{lequ}^{(1),22}$	$(1.8 \pm 1.6) \times 10^{-2}$	$C_{eH\,22}$
$C_{lequ}^{(1),33}$	$(8.0 \pm 9.1) \times 10^{-2}$	$C_{eH\,33}$
$C_{lequ}^{(3),11}$	$(-0.6 \pm 1.5) \times 10^{-5}$	$(g-2)_e$
$C_{lequ}^{(3),22}$	$(-19.3 \pm 8.1) \times 10^{-5}$	$(g-2)_\mu$
$C_{lequ}^{(3),33}$	$(-7.0 \pm 7.8) \times 10^{-1}$	$C_{eH\,33}$

Table 5.10: Combined fit for one at a time Wilson coefficients for semileptonic lepton flavor conserving operators. For reference, we also display the single observable giving the most precise bound.

binations involving the coefficients $C_{qq}^{(1/3)}$ are constrained up to the 10^{-2} level, due to the $\Delta F = 2$ meson mixing observables that strongly constrain their sum. This result remarkably improves the bounds derived by the ATLAS and CMS direct measurements of top quark cross-sections by 2-3 orders of magnitude. An improvement is also clear for the combinations of the Higgs-Top operators $C_{Hq}^{(1/3)}$ and C_{Hu} (c_{Ht}), mostly constrained in this analysis by the electroweak and Higgs observables discussed in Section 5.3.7. The C_{uG} (c_{tG}) coefficient represents the only exception to the general improvement trend observed in almost all the cases. However, as discussed in Ref. [377], the numerical fit of C_{uG} performed through the SMEFiT routine seems to be unstable, so that we do not consider this direct bound reliable (see Section 5.3 of Ref. [377] for an extended discussion).

5.4.2 Two-parameter fits

In this Section we carry out two-parameter fits, i.e. two Wilson coefficients at a time are allowed to vary under the assumption that they are generated at the same scale, while all the others are set to zero. These analyses can provide useful information on the interplay between pairs of coefficients, highlighting what are the most constrained combinations and giving thus intuition on their correlations. This is also the first step towards a UV

Wilson	$\mu \to e$		$\tau \to \mu$		$\tau \to e$	
	Limit	Dominant	Limit	Dominant	Limit	Dominant
$C_{lequ}^{(3)}$	3.9×10^{-9}	$\mu \to e\gamma$	5.0×10^{-5}	$\tau \to \mu\gamma$	4.4×10^{-5}	$\tau \to e\gamma$
$C_{lequ}^{(1)}$	3.6×10^{-5}	$\mu \to 3e, e\gamma$	2.7×10^{-2}	$\tau \to \mu\gamma$	2.4×10^{-2}	$\tau \to e\gamma$
$C_{lq}^{(3)}$	6.7×10^{-5}	$\mu\text{Au} \to e\text{Au}$	7.1×10^{-2}	$\tau \to \mu\pi\pi$	7.4×10^{-2}	$\tau \to e\pi\pi$
$C_{lq}^{(1)}$	4.0×10^{-5}	$\mu\text{Au} \to e\text{Au}$	1.1×10^{-1}	$\tau \to \mu\pi\pi$	1.1×10^{-1}	$\tau \to e\pi\pi$
C_{lu}	4.0×10^{-5}	$\mu\text{Au} \to e\text{Au}$	1.0×10^{-1}	$\tau \to \mu\pi\pi$	1.1×10^{-1}	$\tau \to e\pi\pi$
C_{eu}	3.6×10^{-5}	$\mu\text{Au} \to e\text{Au}$	1.0×10^{-1}	$\tau \to \mu\pi\pi$	1.1×10^{-1}	$\tau \to e\pi\pi$
C_{qe}	3.6×10^{-5}	$\mu\text{Au} \to e\text{Au}$	1.0×10^{-1}	$\tau \to \mu\pi\pi$	1.0×10^{-1}	$\tau \to e\pi\pi$

Table 5.11: Upper limits (68% CL) in TeV^{-2} for the different LFV Wilson coefficients. Family superscripts are omitted (in the working approximation bounds on $C_{lequ}^{(1,3),ij}$ and $C_{lequ}^{(1,3),ji}$ are found to be the same). For reference we also display the single observable giving the most precise bound.

interpretation, as WC's allowed regions can be contrasted with the relations predicted by specific UV scenarios. Among all the possible pairs we only show some interesting cases, e.g. when the importance of combining different sectors is highlighted and/or when the pair can be interesting from a new physics perspective.

The results of two-parameters fits are illustrated in Figures 5.4 - 5.9. We display the 68%CL regions obtained when different subsets of data are taken as input and the 68% and 95%CL regions resulting from the whole set of observables. In order to better understand the underlying phenomenology, in some plots we also show single-observable 1σ contours. In this way, we can investigate the constraining power of each sector/observable on coefficients pairs.

To start with, in Figure 5.4 we show the allowed regions for the $C_{Hq}^{(+)}$ and $C_{Hq}^{(-)}$ coefficients. Noteworthy, constraints from the B sector, mostly due to leptonic $B \to \ell\ell$ and radiative decays, are competitive to the EW and Higgs bounds, resulting in a (slightly more than) 2σ deviation from the SM prediction. This pull is mostly due to the Z boson coupling to right-handed electrons, $\delta g_R^{Ze} = (-7.3 \pm 4.4) \times 10^{-3}$ [368], as we show in the plot with the dot-dashed green line marking the 1σ bound. In the right panel, as an example of dipole operators, we show the C_{uW} vs C_{uB} plane. As expected, a strong constraint is set on the photon direction, whose main responsible is the $c_{\gamma\gamma}$ coefficient discussed in Section 5.3.7. The dominant constraints on the orthogonal direction are set again by the electroweak sector, as a combined effect of the deviations in the Z boson coupling to leptons and other (pseudo-)observables.

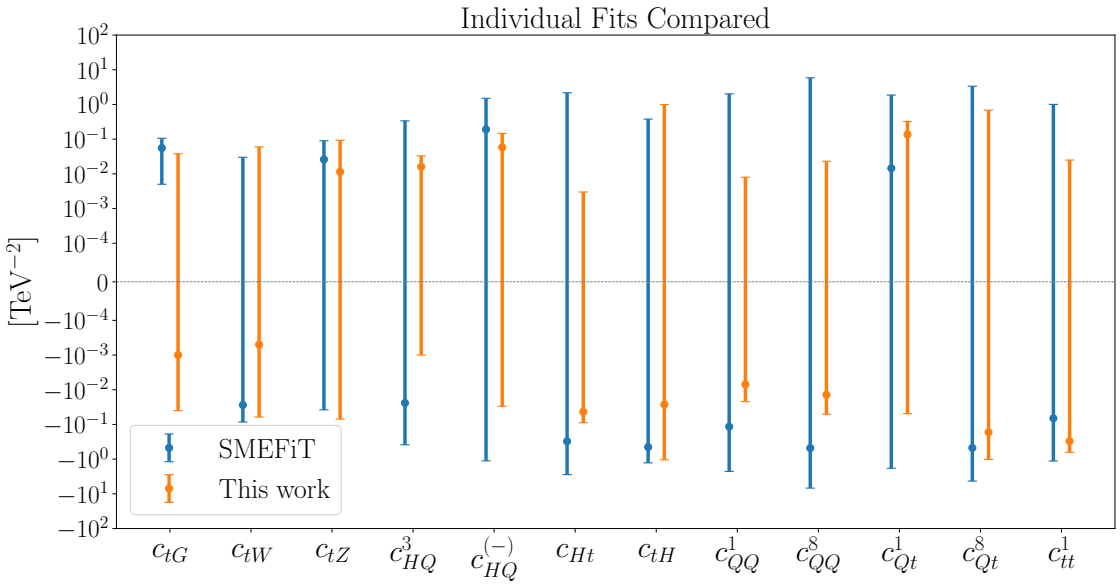

Figure 5.3: Comparison of the indirect constraints derived in this work and the direct bounds obtained through the SMEFiT toolbox. We display the 95% CL bounds for Wilson coefficients in the SMEFiT basis and notation (see Table E.2 for their expression in terms of the Warsaw basis).

In Figure 5.5 and the left panel of Figure 5.6, we show the two-parameters fits for the $C_{lq}^{(+/-),\alpha\alpha}$ coefficients. The existence of flat directions points out the importance of performing SMEFT analysis using various datasets, exploiting the complementarity between different physics sectors to constraint the EFT space. Focusing on B-physics, the strong bound on the positive combinations $C_{lq}^{(+),\alpha\alpha}$, with $\alpha = 1, 2$, can be ascribed to the $R_{K^{(*)}}$ measurements. In addition, the recently announced measurement of R_K^{ν}, with a pull from the SM, drives the allowed region for the negative combination, splitting the allowed band in two regions depending on the interference with the SM. Interestingly, in case of electrons and muons (Figure 5.5) the deviation in R_K^{ν} could be compatible with the Cabibbo angle anomaly but is in some tension with the bounds from EW precision data, which drives the global fit towards the SM. In case of tau leptons (Figure 5.6), instead, the looser EW bounds and the vanishing contribution to R_K allow the global analysis to overlap with the preferred region from R_K^{ν}. This feature is visible also in the right panel of Figure 5.6, where we display the allowed regions in the plane $C_{lq}^{(-),33}$ vs C_{lu}^{33}. The semileptonic coefficients $C_{lq}^{(1,3),33}$ will be further discussed in Section 5.5, where the scenario of a single scalar leptoquark S_1 coupling tau leptons and top quarks is explored. In Figure 5.7 we show the fit in the plane of C_{lu} vs. C_{qe} for both electrons (left panel) and muons (right panel). In both cases the global fit shows an interesting interplay of B and EW physics.

In Figure 5.8, we show the pairwise fits on the LFV coefficients $C_{lq,12}^{(+/-)}$ and $C_{lq,23}^{(+/-)}$. In the first case, the global fit is controlled entirely by the $\mu\mathrm{Au} \to e\mathrm{Au}$ measurement, as expected from Table 5.11. In the second case, the sensitivity of the coefficients is mostly driven by the tau LFV decays discussed in Section 5.3.6. However, LFV decay modes of

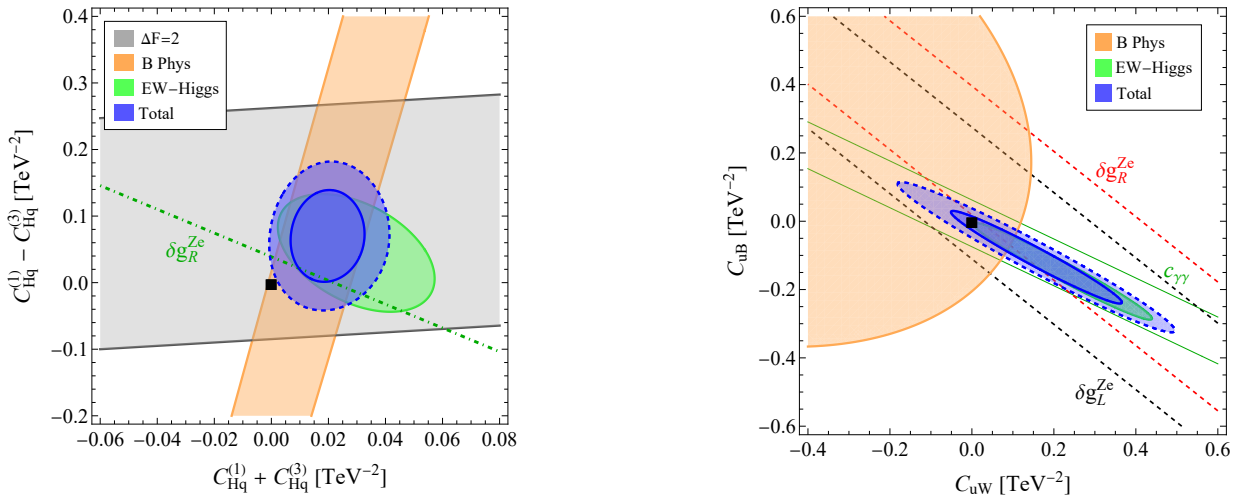

Figure 5.4: Left panel: Higgs-Top coefficients $C_{Hq}^{(+)}$ vs $C_{Hq}^{(-)}$. Right panel: dipole coefficients C_{uW} vs C_{uB}.

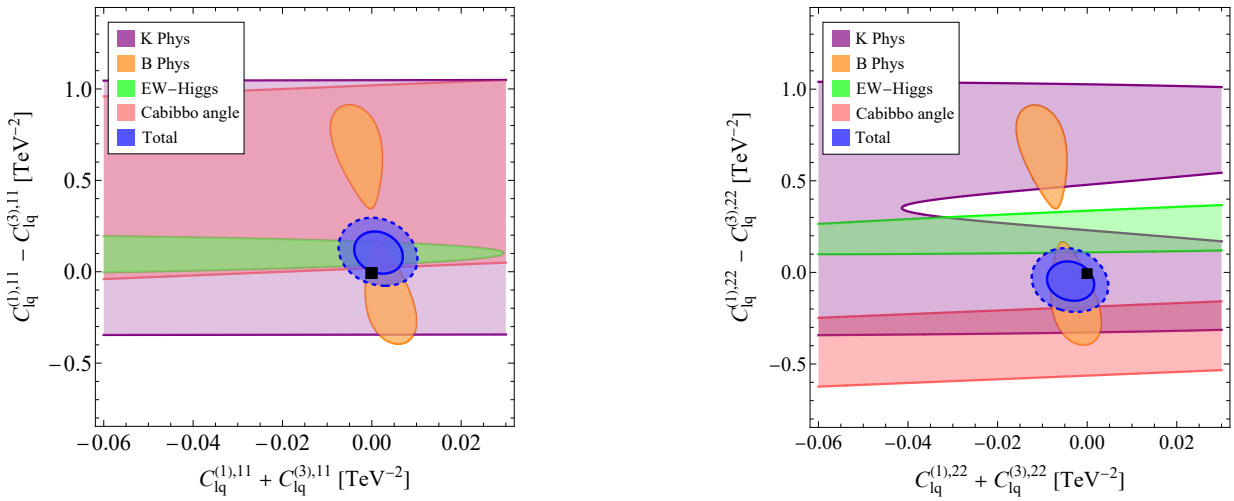

Figure 5.5: Semileptonic $C_{lq}^{(+)}$ vs $C_{lq}^{(-)}$ coefficients involving electrons and muons.

B and K mesons, as well as bounds on LFV Z decays, can improve the constraints. This discussion also applies to the $C_{lq,13}^{(+/-)}$ coefficients, whose bounds are very similar to the ones derived for $C_{lq,23}^{(+/-)}$.

Regarding four-quark operators, it is clear from the left panel of Figure 5.9 that the combinations $C_{qq}^{(+)}$ and $C_{qq}^{(-)}$ are the relevant degrees of freedom in the EFT space. In particular, the sum is severely constrained by meson oscillations, while the orthogonal combination is mainly constrained by $B_s \to \mu^+\mu^-$, kaon decays and EW and Higgs observables. In the right panel we display the $C_{qu}^{(1)}$ vs $C_{qq}^{(+)}$ pair. We illustrate the effect of the δg_R^{Ze} measurement, responsible again for the main discrepancy in the EW sector. The resulting allowed region shows a tension from the SM value within of slightly more than two sigmas.

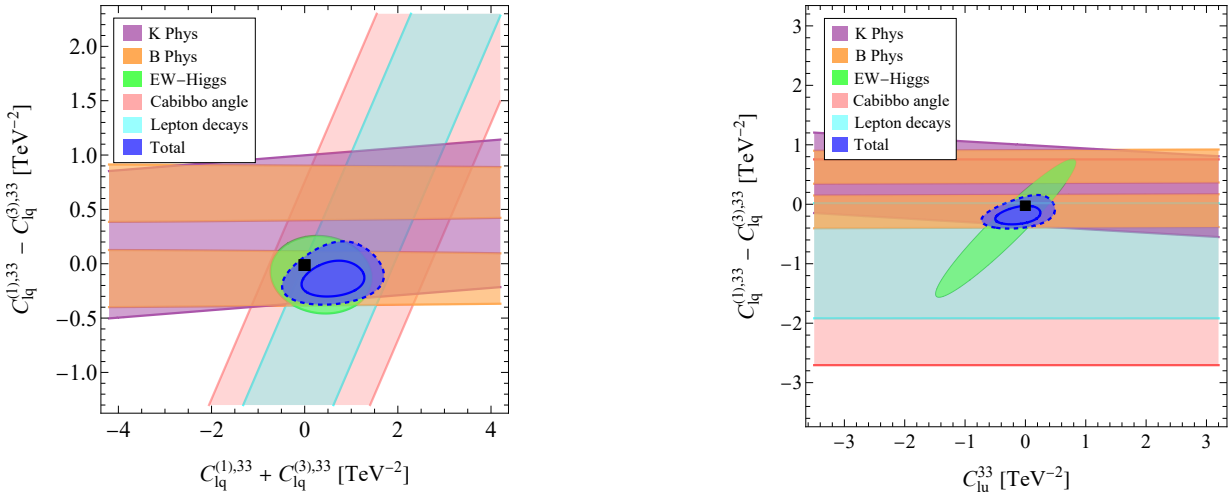

Figure 5.6: Left panel: semileptonic $C_{lq}^{(+)}$ vs $C_{lq}^{(-)}$ coefficients involving tau leptons. Bounds from the EW sector are improved by the synergy with the other sectors. Right panel: Semileptonic $C_{lq,33}^{(-)}$ vs $C_{lu,33}$ coefficients.

5.4.3 Gaussian fit with no semileptonic operators

Plots pose a limitation in only allowing fits to pairs of coefficients. There are two main possibilities to go beyond that: providing the complete likelihood or employing the Gaussian approximation around the global maximum of the likelihood to derive a multi-dimensional fit. While the former solution is more general, it is not a fit and the complexity of our analysis makes the resulting numerical function unwieldy to publish. Therefore, in this work we opt to perform a multi-dimensional Gaussian fit.

We consider all the operators in Table 5.1 except the semileptonic ones:[3]

$$\vec{C} = (C_{qq}^{(+)}, C_{qq}^{(-)}, C_{uu}, C_{qu}^{(1)}, C_{qu}^{(8)}, C_{Hq}^{(+)}, C_{Hq}^{(-)}, C_{Hu}, C_{uH}, C_{uG}, C_{uW}, C_{uB}) \ . \tag{5.11}$$

The best-fit point improves the χ^2 from the SM value by $\Delta\chi^2 \equiv \chi^2_{\rm SM} - \chi^2_{\rm best-fit} \approx 10.9$. This comes mostly from the EW-Higgs sector, however it is a result in mild improvements in several observables rather than a resolution of a specific large anomaly. The fit presents some almost flat directions, which imply correlations among some coefficients very close to ± 1. For this reason, we report the result in terms of the eigenvectors of the Hessian matrix around the best-fit minimum:

$$\chi^2 = \chi^2_{\rm best-fit} + (C_i - \mu_{C_i})(\sigma^2)^{-1}_{ij}(C_j - \mu_{C_j}) = \chi^2_{\rm best-fit} + \frac{(K_i - \mu_{K_i})^2}{\sigma^2_{K_i}}. \tag{5.12}$$

The results for the best-fit values μ_{K_i} and uncertainties σ_{K_i} are reported in Table 5.12,

[3] An analogous Gaussian fit including also semileptonic operators does not provide a physically meaningful result. This is due to the non-gaussianities, that become very important in light of the mild deviations from the SM expectation present in some observables. In this case, performing a Gaussian expansion around the global minimum provides a bad approximation to the full likelihood.

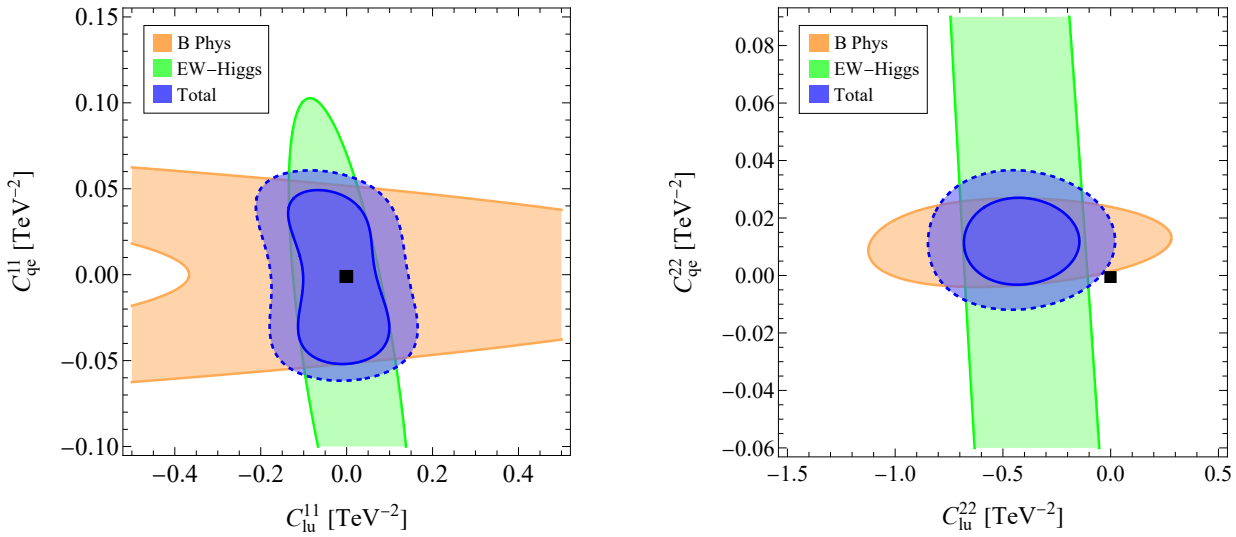

Figure 5.7: Here we show the semileptonic coefficients C_{lu} vs. C_{qe} for electrons (left) and muons (right).

Coefficient	Gaussian fit [TeV^{-2}]	Coefficient	Gaussian fit [TeV^{-2}]
K_1	0.0019 ± 0.0023	K_7	0.54 ± 0.79
K_2	0.0179 ± 0.0083	K_8	0.74 ± 0.88
K_3	-0.002 ± 0.015	K_9	-0.8 ± 1.3
K_4	-0.016 ± 0.021	K_{10}	-0.7 ± 1.8
K_5	0.044 ± 0.029	K_{11}	12 ± 13
K_6	-0.30 ± 0.38	K_{12}	-11 ± 16

Table 5.12: Result of our multidimensional gaussian fit of non-leptonic coefficients, in terms of the eigenvectors of the Hessian matrix.

while the rotation matrix from these coefficients to our C_i is given by $\vec{K} = U_{KC}\vec{C}$, with

$$U_{KC} = \begin{pmatrix}
-1.00 & 0.000 & 0.000 & -0.016 & -0.004 & -0.004 & 0.021 & -0.001 & 0.000 & 0.000 & 0.000 & 0.000 \\
-0.005 & -0.089 & -0.015 & 0.058 & 0.000 & 0.984 & -0.004 & -0.117 & 0.000 & -0.009 & 0.044 & 0.063 \\
0.004 & 0.011 & -0.039 & 0.018 & -0.001 & -0.1 & 0.145 & -0.28 & 0.015 & -0.494 & 0.447 & 0.667 \\
-0.007 & -0.013 & 0.09 & -0.053 & -0.003 & 0.081 & -0.316 & 0.64 & 0.024 & -0.673 & -0.126 & -0.059 \\
0.005 & 0.007 & -0.074 & 0.042 & -0.002 & -0.025 & 0.259 & -0.525 & 0.025 & -0.548 & -0.213 & -0.55 \\
-0.004 & -0.041 & 0.025 & 0.067 & 0.006 & -0.004 & -0.128 & 0.084 & 0.006 & 0.022 & 0.853 & -0.492 \\
-0.006 & -0.137 & 0.078 & 0.196 & 0.96 & -0.017 & 0.09 & 0.047 & -0.065 & -0.007 & -0.017 & 0.008 \\
0.002 & -0.349 & -0.006 & 0.646 & -0.248 & -0.029 & 0.545 & 0.318 & 0.014 & 0.001 & -0.012 & 0.006 \\
0.005 & 0.007 & 0.028 & -0.138 & 0.077 & 0.017 & 0.145 & 0.06 & 0.973 & 0.037 & 0.017 & -0.003 \\
0.023 & 0.221 & 0.074 & -0.569 & 0.053 & 0.092 & 0.684 & 0.292 & -0.212 & -0.002 & 0.095 & -0.057 \\
0.006 & -0.798 & 0.451 & -0.364 & -0.071 & -0.059 & -0.038 & -0.122 & -0.039 & 0.000 & -0.012 & 0.007 \\
-0.004 & 0.404 & 0.876 & 0.235 & -0.058 & 0.025 & 0.017 & -0.093 & 0.013 & 0.000 & -0.01 & 0.006
\end{pmatrix}. \tag{5.13}$$

The last two coefficients, K_{11} and K_{12}, correspond to two flat directions with only very weak constraints from our observables, given approximately by:

$$\begin{aligned}
K_{11} &\approx -0.80C_{qq}^{(-)} + 0.45C_{uu} - 0.36C_{qu}^{(1)} - 0.12C_{Hu} + \dots \ , \\
K_{12} &\approx +0.40C_{qq}^{(-)} + 0.88C_{uu} + 0.24C_{qu}^{(1)} - 0.09C_{Hu} + \dots \ .
\end{aligned} \tag{5.14}$$

Using the naive power counting of Ref. [385], one may estimate the allowed EFT hyper-volume spanned by the studied non-leptonic Wilson coefficients as $V_{\rm EFT} \sim$

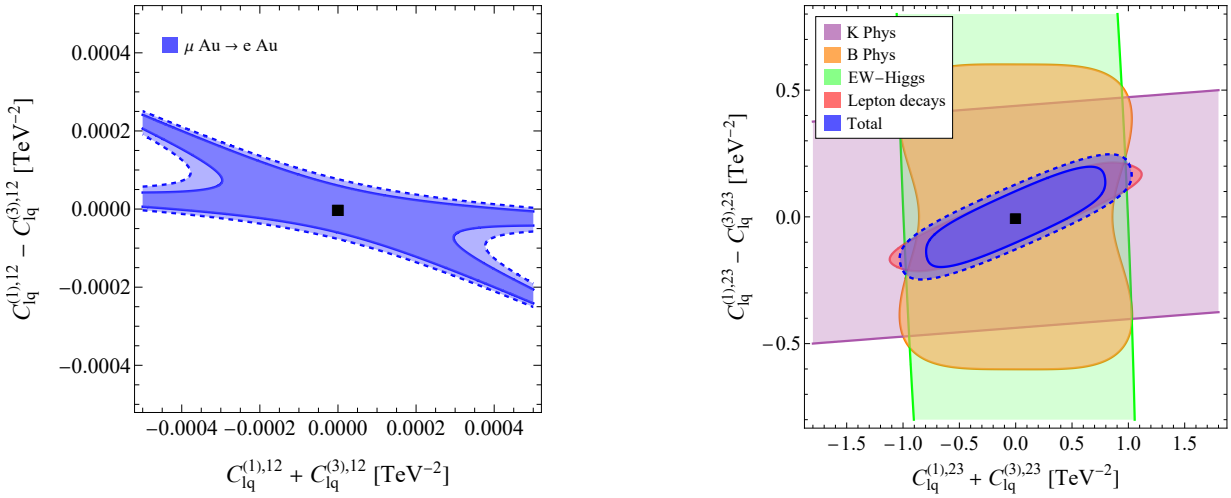

Figure 5.8: Two-parameters fit for the LFV semileptonic coefficients $C_{lq,12}^{(+/-)}$ and $C_{lq,23}^{(+/-)}$. The stronger constraints come from the LFV decay modes of tau lepton.

$\frac{\pi^6}{720}\left(\frac{(4\pi)}{\text{TeV}^2}\right)^3\left(\frac{(4\pi)^2}{\text{TeV}^2}\right)^8\left(\frac{(4\pi)^3}{\text{TeV}^2}\right)$, assuming $\Lambda = 1\,\text{TeV}$. From Table 5.12, experimental constraints restrict the potential SMEFT hyperspace to a very tiny fraction of its volume, $\sim 10^{-31}$.

5.5 Applications for UV models

In this Section we apply our global analysis to two UV scenarios of new physics at the TeV scale, coupled mainly to the top quark. The first is a simple minimal extension of the SM by one scalar leptoquark $S_1 \sim (\bar{\mathbf{3}}, \mathbf{1})_{+1/3}$ coupled only to the third generation quark and lepton doublets. The second scenario is an application guided by the Cabibbo anomaly, and it includes the scalar leptoquark $S_3 \sim (\bar{\mathbf{3}}, \mathbf{3})_{+1/3}$ as well as the vector leptoquark $U_1 \sim (\mathbf{3}, \mathbf{1})_{+2/3}$.

5.5.1 Single leptoquark S_1

Let us consider the scalar leptoquark $S_1 \sim (\bar{\mathbf{3}}, \mathbf{1})_{+1/3}$, coupled only to the third generation of quark and lepton $SU(2)_L$ doublets:

$$\mathcal{L} \supset \lambda_{t\tau}\, \bar{q^c}_3 i\sigma_2 l_3\, S_1 + \text{h.c.}\,, \tag{5.15}$$

where $q_3 = (t_L,\, V_{tj} d_L^j)$ and $l_3 = (\nu_\tau,\, \tau_L)$.

Matching at tree level this Lagrangian to the SMEFT gives [121, 386]

$$C_{lq}^{(1),33} = -C_{lq}^{(3),33} = \frac{|\lambda_{t\tau}|^2}{4M_{S_1}^2}\,. \tag{5.16}$$

For precision studies of such scenarios, however, the tree level matching is not sufficient since one-loop contributions can be important for some observables, as discussed

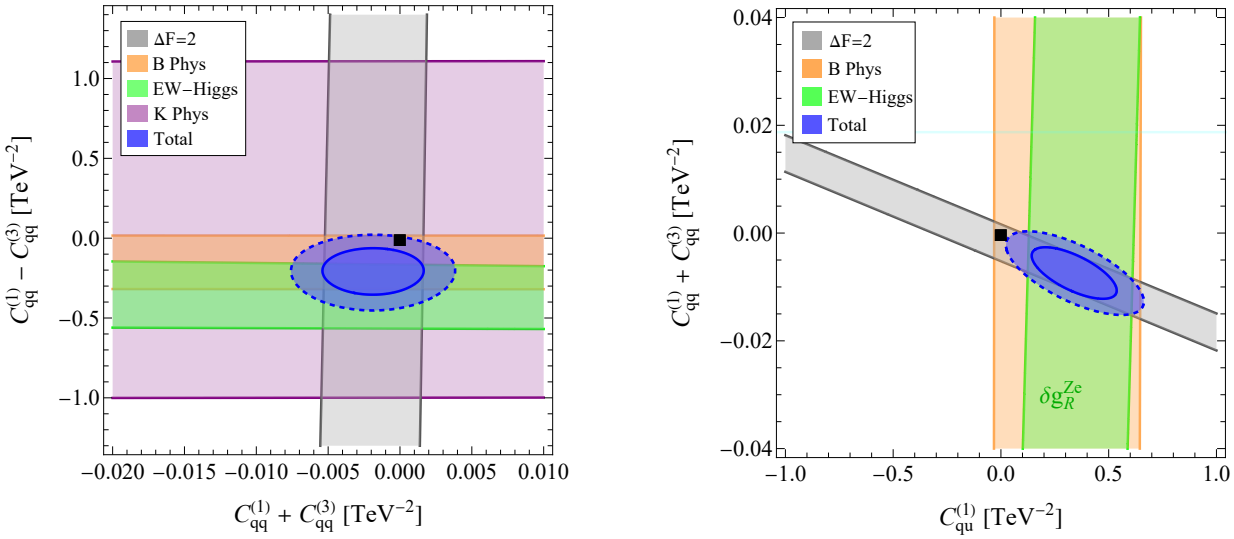

Figure 5.9: Left panel: four-quarks $C_{qq}^{(1)+(3)}$ vs $C_{qq}^{(1)-(3)}$ coefficients. $\Delta F = 2$ processes constraint the $C_{qq}^{(+)}$ combination up to the 10^{-3} level. The difference is constrained by the other sectors. Right panel: $C_{qu}^{(1)}$ and $C_{qq}^{(+)}$.

in Refs. [220, 227–229, 387, 388]. For our goal it is sufficient to add the leading contributions to four-quark operators, which induce contributions to meson-mixing observables. From the complete one-loop matching of this scalar leptoquark to the SMEFT, done in Ref. [389], we extract the relevant contribution:

$$C_{qq}^{(1)} = C_{qq}^{(3)} = -\frac{|\lambda_{t\tau}|^4}{256\pi^2 M_{S_1}^2} \,. \tag{5.17}$$

These coefficients are generated at the M_{S_1} scale, that we assume to be near 1 TeV, so that we neglect the RG evolution between M_{S_1} and 1 TeV.

The constraints from the global analysis, as well as from the most relevant observables, in the plane of the $\lambda_{t\tau}$ coupling vs. the leptoquark mass, are shown in Figure 5.10. The shaded gray region is excluded by ATLAS from leptoquark pair-production searches [390]. The regions preferred at 1σ and 2σ by the $R_{K^{(*)}}^{\nu}$ combination, Eq. (5.4), are show in green and yellow, respectively. Interestingly, the intermediate white region is disfavored at the 95%CL by $R_{K^{(*)}}^{\nu}$ due to the negative interference with the SM, which suppresses the branching ratio below the 2σ level. We observe an interesting interplay of constraints from different classes of observables: electroweak precision data and τ physics, meson mixing, B and kaon rare decays, as well as direct searches from LHC.

5.5.2 Two leptoquarks for the Cabibbo anomaly?

In this Section we illustrate how our combined likelihood may also be used to check whether experimental results in tension with the SM predictions can be partially accommodated in top-philic extensions (and which ones), taking into account the restrictions imposed by experimental results in other sectors. Here we focus on the longstanding tensions within

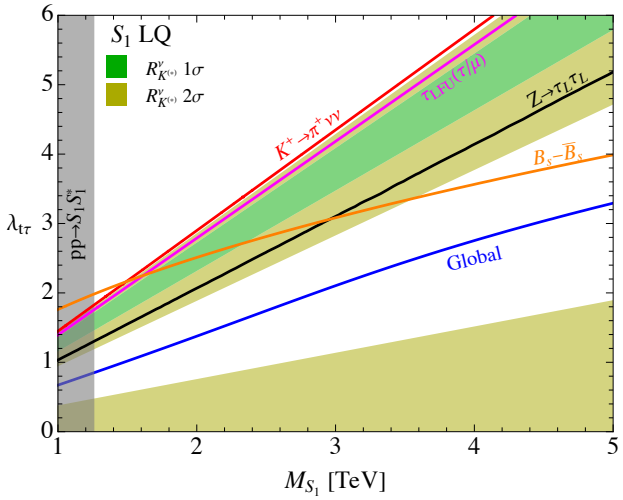

Figure 5.10: Present constraints on the S_1 leptoquark model, coupled only to third generation quark and lepton doublets. The green (yellow) region is preferred at 1σ (2σ) by $R^{\nu}_{K^{(*)}}$, while the gray region is excluded at 95%CL from direct searches at LHC. The region above each line is excluded at 95%CL by the corresponding observable, or by our global analysis (blue line).

the SM involving the determination of the inputs of the first row of the CKM matrix, known as Cabibbo anomalies.

Regardless of whether nonzero values are allowed or not for the remaining Wilson coefficients, the likelihood of the Cabibbo angle observables displays a $3\,\sigma$ preference for a nonzero value of $C_{lq}^{(3),22}$ at $\Lambda = 1\,\text{TeV}$:

$$[C_{lq}^{(3),22}]^{\text{Cabibbo}} = (0.19 \pm 0.06)\,\text{TeV}^{-2}\,. \tag{5.18}$$

Let us first develop on where this preferred nonzero value comes from. $C_{lq}^{(3),\alpha\alpha}$ induces an unusually large $C_{Hl}^{(3),\alpha\alpha}$ at the EW scale, due to a mixing that involves a double top Yukawa insertion. The leading log approximation, which one may expect to give a first approximation for $\Lambda \gtrsim$ TeV, is displayed in Eq. (E.41). After EWSB $C_{Hl}^{(3),\alpha\alpha}$ induces, at tree level, a re-scaling of the corresponding lepton charged current vertices, modifying the ratios of muon, beta and kaon decays. As a consequence, the corresponding apparent unitarity relation is[4]

$$\begin{aligned}\Delta_{\text{CKM}} &\equiv |V_{ud}^{\beta}|^2 + |V_{us}^{K_{\ell 3}}|^2 - 1 \approx -2v^2\,(|V_{ud}|^2 C_{Hl}^{(3),22} - |V_{us}|^2 (C_{Hl}^{(3),\ell\ell} - C_{Hl}^{(3),11} - C_{Hl}^{(3),22})) \\ &\approx -2v^2\,C_{Hl}^{(3),22} \sim -\left[\frac{N_c}{2\pi^2}\frac{m_t^2}{\Lambda_{\text{UV}}^2}\log\frac{\Lambda_{\text{UV}}}{M_Z}\right]\Lambda_{\text{UV}}^2 C_{lq}^{(3),22}(\Lambda_{\text{UV}}^2)\,.\end{aligned} \tag{5.19}$$

Experimentally Δ_{CKM} is known beyond the per-mil level and gives the main pull behind the result of Eq. (5.18).

[4] V_{ub} has a completely negligible numerical role in this relation.

If we set all the parameters to zero except for $C_{lq}^{(3),22}$ for the EW/Higgs likelihood, we also obtain a slight preference for nonzero values, but with the opposite sign:

$$[C_{lq}^{(3),22}]^{\text{EW/Higgs}} = (-0.11 \pm 0.06)\,\text{TeV}^{-2}\,. \tag{5.20}$$

This is to be expected, since it is well known that explaining Δ_{CKM} through increasing the muon decay matrix element is in tension with fits in other EWPOs, e.g. see Refs. [29, 391, 392]. We may yet respect CKM unitarity and decrease the muon decay rate with respect to the SM expectation by breaking LFU, with $0 < C_{Hl}^{(3),22} < -C_{Hl}^{(3),11}$. Let us then allow for nonzero values at the TeV scale for $C_{lq}^{(3),\alpha\alpha}$ for the first two lepton families and also for the corresponding $C_{lq}^{(1),\alpha\alpha}$, typically induced in UV models by the same couplings. The minimum χ^2 follows the expected pattern, plus a preference for $C_{lq}^{(1),11} \approx C_{lq}^{(3),11}$ and $C_{lq}^{(1),22} \approx 3C_{lq}^{(3),22}$. Both these relations and the obtained signs happen to match the couplings induced by top-philic U_1 and S_3 leptoquarks coupled, respectively, to the first and the second lepton family:

$$\mathcal{L} \supset \lambda_{U_1}\, \bar{q}_3 \gamma_\mu l_1\, U_1^\mu + \lambda_{S_3}\, \bar{q}_3^c i\sigma_2 \sigma_a l_2\, S_3^a + \text{h.c.}\,, \tag{5.21}$$

giving [121, 386]

$$C_{lq}^{(3),11} = -\frac{|\lambda_{U_1}|^2}{2M_{U_1}^2}\,, \quad C_{lq}^{(3),22} = \frac{|\lambda_{S_3}|^2}{4M_{S_3}^2}\,, \tag{5.22}$$

plus the relations with $C_{lq}^{(1)}$ above. Imposing them as strict equalities, in this two-parameter scenario one finds

$$C_{lq}^{(3),11} = (-0.19 \pm 0.06)\,\text{TeV}^{-2}\,,\; C_{lq}^{(3),22} = (0.14 \pm 0.04)\,\text{TeV}^{-2}\,. \tag{5.23}$$

With respect to the SM, this minimum has a $\Delta\chi^2 = 8.0$ preference for the Cabibbo sector and a $\Delta\chi^2 = 5.7$ for the EW/Higgs one.

It is only when adding constraints from B and K physics observables when this scenario becomes strongly disfavored. In a generic top-philic set-up defined in any specific flavor basis in which $C_{lq}^{(1,3),ii}$ are induced, FCNCs are generated when rotating to the mass basis. In the down sector FCNCs are very strongly constrained by the processes studied in this work, as we have explicitly shown when defining the top-philic condition in the up quark basis. Indeed we show in Figure 5.11 how including those constraints we can rule out this, and practically any, top-philic explanation to the Cabibbo anomaly.

Let us finish this section by remarking that there is, however, a possible way out to the strong constraints on FCNCs coming from K and B physics. Assuming that there exists some, admittedly bizarre from our infra-red perspective, mechanism in the UV theory to select a top-philic set-up in the only basis where this operator does not induce tree-level FCNCs in the down sector, i.e. the down-quark basis, the previous constraints from K and B physics do not hold, while the constraints on Cabibbo angle and EW/Higgs would give, in a first approximation, the same results, since the leading mechanism to modify the SM,

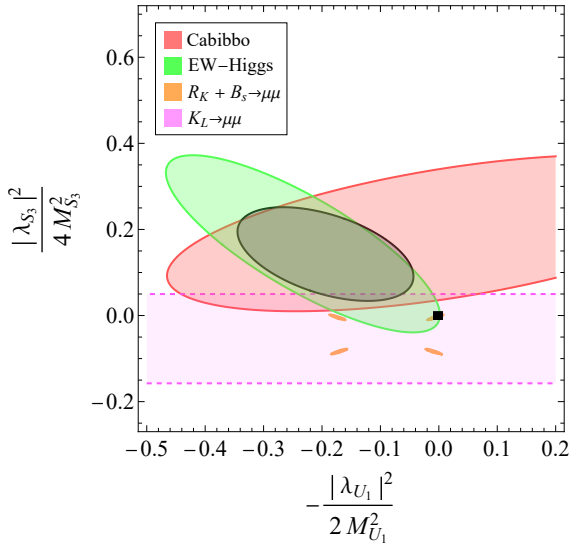

Figure 5.11: Allowed regions (95% CL) for the studied leptoquark couplings (see text) from the Cabibbo and the EW Higgs sector and combined, in black. Masses are in TeV units. The preferred nonzero values can be ruled out from B-physics and K-physics observables, unless one defines the top-philic set up in the down-quark basis.

through modifying lepton vertices, is largely independent on quark-basis rotation. In that scenario, this leptoquark model may still be a feasible (partial) solution to the Cabibbo anomaly. Complementary constraints on the space of parameters may come from $D - \bar{D}$ mixing (since FCNCs are yet induced in the up sector) and direct leptoquark searches, bounding the possible masses from below. Further studying this scenario is, however, well beyond the goals and the scope of this work.

5.6 Summary

In this Chapter we provided a global analysis of indirect constraints on SMEFT operators involving the top quark. In fact, several motivated UV scenarios predict new physics coupled mostly with the top.

We considered all dimension-6 operators involving the top quark and performed a global analysis that combines a large number of observables that do not involve directly the top quark. These include: B, K and τ decays, meson mixing observables, magnetic moments of leptons, measurements of the Cabibbo angle, EW precision measurements, Higgs physics, and LFV tests. Top quark operators contribute to these observables either at the tree-level via the $SU(2)_L$ connection with left-handed down quarks or via loop effects. Assuming that top quark operators are generated at the UV scale $\Lambda = 1$ TeV, we evolved them down to the scale relevant for each observable using the RG and matching equations. The result of this process is a global likelihood expressed in terms of the high-scale Wilson coefficients.

Using this likelihood we derived global indirect constraints on single coefficients, com-

paring the results with the bounds obtained from LHC analyses of processes involving top quarks. In all cases we found that the indirect constraints are stronger than the direct ones, often by several orders of magnitude. We then performed several 2D fits to study interesting correlations among coefficients and the complementarity between different observables, that showcase the importance of performing such global analyses. We also performed a multi-dimensional Gaussian fit of all the coefficients of non-leptonic operators, that can be useful to identify the directions in parameter space that have strongest or weakest constraints. Indeed, among these coefficients we identified two almost-flat directions.

Finally, as examples of possible applications of our analysis we studied the EFT coefficients generated by two simple UV models. The first includes a scalar singlet leptoquark coupled only to the third generation of quark and lepton doublets. We showed how the indirect constraints one can derive from different sectors combine in providing strong bounds on the model, and how these are complementary to direct searches at the LHC. As a second example we studied a two-leptoquark scenario inspired by the Cabibbo anomaly, with only two free couplings. This model accommodates the anomaly and improves the fit quality for the rest of EW-Higgs precision observables. However, B and kaon physics constraints are able to completely rule out this scenario unless a very specific flavor alignment is imposed.

Chapter 6

Conclusions

The near-term future of particle physics will be charted by precision measurements. The LHC has (almost) reached its nominal beam energy and is marching towards the high-luminosity phase. The long-term future of the field crucially depends on the decisions we make today about the next generation of high-energy colliders. The two most prominent options on the table are the future proton collider at 100 TeV (FCC-hh) and a multi-TeV muon collider. It is, therefore, necessary to thoroughly compare the two on a broad set of new physics hypotheses. Obtaining precise predictions for multi-TeV MuC, and lepton colliders in general, is a topic of active studies. In fact, while QCD radiation plays a minor role, in comparison to hadron colliders, electroweak corrections in this energy regime can become very large due to single and double logarithmic enhancements. Furthermore, the electroweak sector presents several features that are absent when dealing with QED or QCD radiation. Within this context, the resummation of a subset of large logarithms related to the factorisable emission of initial-state radiation can be viewed as an ingredient for a complete description of collider phenomenology at such machines. Precision measurements, in addition to setting the path to next generation colliders, can be used to constraint new physics scenarios. Even without explicit models at hand, they set bounds on the coefficients of higher-dimensional operators in the SMEFT and consequently on the scale of BSM particles.

In this thesis we collected some contributions in all these directions.
In Chapter 3 we computed PDFs for lepton colliders, showing the importance of EW symmetry breaking effects, especially in the gauge sector. In particular ultra-collinear splittings, proportional to the parton masses and not to the transverse momentum of the radiation emitted, give the most important contribution to longitudinal gauge bosons PDFs. We also discussed the importance double logarithms, that appear due to the violation of the Bloch-Nordsieck theorem. They play a crucial role in some splittings and represent the main source of deviation of our numerical results from the effective vector approximation implemented in many MonteCarlo generators, like MadGraph. The use of the full numerical results in studying the phenomenology at high-energy lepton colliders

is therefore necessary and the implementation in MonteCarlo generators, when available, would give a huge help in this sense. As a simple example of application, we concluded the Chapter studying the role of muon neutrino PDF at muon colliders. Thanks to the $\mu\nu_\mu W$ interaction, the $\mu\nu$ and $\nu\nu$ parton luminosities grow for invariant mass approaching the collider energy, offering a better sensitivity to neutrino-induced processes in such regimes. Indeed we showed that the impact of neutrino PDF can be measured through processes like $\mu\bar{\mu} \to e^-\bar{\nu}_e$ and $\mu\bar{\mu} \to W^-\gamma$. Furthermore the study of single Higgs production at muon colliders showed that neutrino-induced contributions must be taken into account when constraining new physics in the Higgs sector, since they exceed the expected sensitivity.

In Chapter 4 we compared FCC-hh and muon colliders in probing new physics scenarios relevant for $B-$meson decays. Motivated by the $R_{K^{(*)}}$ flavor anomalies present at the time of our work and now disappeared, we analysed models with Z' and leptoquarks, that represented excellent candidate to address such anomalies. We considered scenarios both neglecting and addressing the R_K anomaly and unfortunately only the former cases are currently meaningful. The prospects at the two machines are collected in Figures 4.18, showing that only a 10 TeV (or higher) MuC can cover all the parameter space for the models considered.

Finally in Chapter 5 we derived bounds on Wilson coefficients of top quark effective operators through a global analysis, going beyond previous analyses. We also compared our results with direct LHC bounds and showed applications to specific new physics models. Our results show how global indirect constraints on top quark operators can be powerful in constraining new physics scenarios coupled mainly to the top quark. Such constraints are often much stronger, or in any case complementary, to those derived from high-energy top quark physics at colliders. Furthermore, several of the observables providing the strongest indirect constraints are expected to be measured with a substantially better precision in the future: $R^{\nu}_{K^{(*)}}$ and τ decays at Belle-II, $R_{K^{(*)}}$ and $B_s \to \mu\mu$ by LHCb, ATLAS and CMS, $K \to \pi\nu\nu$ by NA62, and several experiments are expected to improve the sensitivity on $\mu \to e$ LFV by several orders of magnitude. All this will further increase the relevance of such global analysis of indirect bounds in the future.

Appendix A

SM interactions, splitting functions and DGLAP equations

In this Appendix we list the SM cubic interactions, the splitting functions and the SM DGLAP equations.

A.1 SM cubic interactions

Here we write down the cubic part of the SM Lagrangian. These interactions are the ones used for the computation of the splitting functions. According to our setup for the computation of LePDFs, we consider all fermions to be massless except for the top.

$$
\begin{aligned}
\mathcal{L}^{(3)}_{SM} = & -\frac{m_h^2}{2v} h(2h^+h^- + h^2 + \phi_3^2) \\
& + 2\frac{m_W^2}{v} h W_\mu^- W^{\mu+} + \frac{m_Z^2}{v} h Z_\mu Z^\mu + (e m_W A_\mu - g_2 m_Z s_W^2 Z_\mu)(W^{\mu-} h^+ + W^{\mu+} h^-) \\
& - i(eA_\mu + \frac{g_2 c_{2W}}{2c_W} Z_\mu) h^+ \overset{\leftrightarrow}{\partial^\mu} h^- - \frac{g_2}{2c_W} Z_\mu (h \overset{\leftrightarrow}{\partial^\mu} h_3) + \left[-i\frac{g_2}{2} W_\mu^+ (h - i h_3) \overset{\leftrightarrow}{\partial^\mu} h^- + \text{h.c.} \right] \\
& - i g_2 c_W \partial_\mu W_\nu^+ \left(Z^\mu W^{-\nu} - Z^\nu W^{-\mu} \right) - ie \partial_\mu W_\nu^+ \left(A^\mu W^{-\nu} - A^\nu W^{-\mu} \right) + \text{permutations} \\
& - \frac{g_3}{2} f_{ABC} \left(\partial_\mu G_\nu^A - \partial_\nu G_\mu^A \right) G_B^\mu G_C^\nu \\
& + g_3 G_\mu^A j_{sA}^\mu + e A_\mu j_{em}^\mu + \frac{g_2}{c_W} Z_\mu j_n^\mu + \frac{g_2}{\sqrt{2}} (W_\mu^+ j_-^\mu + \text{h.c.}) \\
& - \frac{y_t}{\sqrt{2}} (\bar{t}_R t_L + \bar{t}_L t_R) h + i \frac{y_t}{\sqrt{2}} (\bar{t}_R t_L - \bar{t}_L t_R) h_3 + y_t \bar{t}_R b_L h^+ + y_t \bar{b}_L t_R h^-.
\end{aligned}
\tag{A.1}
$$

The fermionic currents are defined in Eq. (2.18).

A.2 Splitting functions

Here we list all the splitting functions, including ultra-collinear ones. The $\bar{z}$ poles are regulated using the + distribution, defined in Eq. (2.65). As already discussed, since the SM is a chiral theory we separate vector polarizations and fermion helicities in the splitting functions.

A.2.1 Massless splitting functions

We start with the splitting functions of the form in Eq. (2.55). Here f labels a fermion, V a gauge boson and h a scalar. We do not specify the polarization of the particle C, since in the computation we sum over it.

$$\begin{aligned}
P^V_{ff}(z) &\equiv P^V_{f_L f_L}(z) = P^V_{f_R f_R}(z) = \frac{1+z^2}{\bar{z}_+} \,, \\
P^f_{V_+ f_L}(z) &= P^f_{V_- f_R}(z) = \frac{\bar{z}^2}{z} \,, \\
P^f_{V_- f_L}(z) &= P^f_{V_+ f_R}(z) = \frac{1}{z} \,, \\
P^f_{f_L V_+}(z) &= P^f_{f_R V_-}(z) = \bar{z}^2 \,, \\
P^f_{f_L V_-}(z) &= P^f_{f_R V_+}(z) = z^2 \,,
\end{aligned} \tag{A.2}$$

$$\begin{aligned}
P^h_{ff}(z) &\equiv P^h_{f_L f_R}(z) = P^h_{f_R f_L}(z) = \frac{\bar{z}}{2} \,, \\
P^f_{hf}(z) &\equiv P^f_{h f_L}(z) = P^f_{h f_R}(z) = \frac{z}{2} \,, \\
P^f_{fh}(z) &\equiv P^f_{f_L h}(z) = P^f_{f_R h}(z) = \frac{1}{2} \,,
\end{aligned} \tag{A.3}$$

$$\begin{aligned}
P^h_{V_\pm h}(z) &= \frac{\bar{z}}{z} \,, \\
P^h_{Vh}(z) &\equiv P^h_{V_+ h}(z) + P^h_{V_- h}(z) = \frac{2\bar{z}}{z} \,, \\
P^V_{hh}(z) &= \frac{2z}{\bar{z}_+} \,, \\
P^h_{hV}(z) &\equiv P^h_{hV_+}(z) = P^h_{hV_-}(z) = z\bar{z} \,,
\end{aligned} \tag{A.4}$$

$$\begin{aligned}
P^V_{V_+ V_+}(z) &= P^V_{V_- V_-}(z) = \frac{1+z^4}{z\bar{z}_+} \,, \\
P^V_{V_+ V_-}(z) &= P^V_{V_- V_+}(z) = \frac{\bar{z}^3}{z} \,.
\end{aligned} \tag{A.5}$$

Since QED and QCD are vectorlike theories, we also define the splitting functions properly summed over the vector polarizations and fermion helicities:

$$\begin{aligned}
P^f_{Vf}(z) &\equiv \frac{P^f_{V_+f_L}(z)+P^f_{V_+f_R}(z)+P^f_{V_-f_L}(z)+P^f_{V_-f_R}(z)}{2} = \frac{1+\bar{z}^2}{z} \ , \\
P^f_{fV}(z) &\equiv \frac{P^f_{f_LV_+}(z)+P^f_{f_RV_+}(z)+P^f_{f_LV_-}(z)+P^f_{f_RV_-}(z)}{2} = z^2+\bar{z}^2 \ , \\
P^V_{VV}(z) &\equiv \frac{P^V_{V_+V_+}(z)+P^V_{V_+V_-}(z)+P^V_{V_-V_+}(z)+P^V_{V_-V_-}(z)}{2} = 2\frac{(1-z\bar{z})^2}{z\bar{z}_+} \ .
\end{aligned} \tag{A.6}$$

Finally, we report here the integrals appearing in Eq. (3.6):

$$\begin{aligned}
I_{fVVf}(x) &= \int_x^1 \frac{dz}{z} P^f_{fV}(z) P^f_{Vf}\left(\frac{x}{z}\right) = \frac{4+3x-3x^2-4x^3}{3x} + 2(1+x)\log x \ , \\
I_{Vfff}(x) &= \int_x^1 \frac{dz}{z} P^f_{Vf}\left(\frac{x}{z}\right) P^V_{ff}(z) = \\
&= 2\log(1-x)P^f_{Vf}(x) + \frac{(1-x)(2x-3)}{x} + (2-x)\log x \ , \\
I_{ffff}(x) &= \int_x^1 \frac{dz}{z} P^V_{ff}\left(\frac{x}{z}\right) P^V_{ff}(z) = \\
&= \frac{-2(1-x)^2 + 4(1+x^2)\log(1-x) - (1+3x^2)\log x}{1-x} \ .
\end{aligned} \tag{A.7}$$

A.2.2 Ultra-collinear splitting functions

The top quark is explicitly written, while for other fermions we write f. $s = L, R$ is the helicity of the fermion, $T = \pm$ is a transverse polarization of the gauge bosons. If inside a splitting we write $f_s f_{-s}$ it means that the two fermions have opposite helicity (same for the gauge bosons). N_c^f is 1 for leptons and N_c for quarks.

Splitting $f \to f + V_T$ ($f = t, b$):

$$\begin{aligned}
U^{W^-_-}_{t_R b_L}(z) = U^{W^+_+}_{\bar{t}_R \bar{b}_L}(z) &= \frac{1}{2} g_2^2 y_t^2 \bar{z} \ , \\
U^{t_R}_{W^-_- b_L}(z) = U^{\bar{t}_R}_{W^+_+ \bar{b}_L}(z) &= \frac{1}{2} g_2^2 y_t^2 z \ , \\
U^{W^+_+}_{b_L t_R}(z) = U^{W^-_-}_{\bar{b}_L \bar{t}_R}(z) &= \frac{1}{2} g_2^2 y_t^2 \bar{z} z^2 \ , \\
U^{b_L}_{W^+_+ t_R}(z) = U^{\bar{b}_L}_{W^-_- \bar{t}_R}(z) &= \frac{1}{2} g_2^2 y_t^2 z \bar{z}^2 \ ,
\end{aligned} \tag{A.8}$$

$$\begin{aligned}
U^g_{tt}(z) &\equiv U^{g_-}_{t_R t_L}(z) = U^{g_+}_{\bar{t}_R \bar{t}_L}(z) = U^{g_+}_{t_L t_R}(z) = U^{g_-}_{\bar{t}_L \bar{t}_R}(z) = C_F g_3^2 y_t^2 \bar{z}^3 \ , \\
U^t_{gt}(z) &\equiv U^{t_R}_{g_- t_L}(z) = U^{\bar{t}_R}_{g_+ \bar{t}_L}(z) = U^{t_L}_{g_+ t_R}(z) = U^{\bar{t}_L}_{g_- \bar{t}_R}(z) = C_F g_3^2 y_t^2 z^3 \ , \\
U^\gamma_{tt}(z) &\equiv U^{\gamma_-}_{t_R t_L}(z) = U^{\gamma_+}_{\bar{t}_R \bar{t}_L}(z) = U^{\gamma_+}_{t_L t_R}(z) = U^{\gamma_-}_{\bar{t}_L \bar{t}_R}(z) = Q_u^2 e^2 y_t^2 \bar{z}^3 \ , \\
U^t_{\gamma t}(z) &\equiv U^{t_R}_{\gamma_- t_L}(z) = U^{\bar{t}_R}_{\gamma_+ \bar{t}_L}(z) = U^{t_L}_{\gamma_+ t_R}(z) = U^{\bar{t}_L}_{\gamma_- \bar{t}_R}(z) = Q_u^2 e^2 y_t^2 z^3 \ ,
\end{aligned} \tag{A.9}$$

$$
\begin{aligned}
U^{Z_-}_{t_R t_L}(z) = U^{Z_+}_{\bar{t}_R \bar{t}_L}(z) &= \frac{g_2^2 y_t^2}{c_W^2} \bar{z} \left(\frac{1}{2} - Q_u s_W^2 \bar{z} \right)^2 , \\
U^{t_R}_{Z_- t_L}(z) = U^{\bar{t}_R}_{Z_+ \bar{t}_L}(z) &= \frac{g_2^2 y_t^2}{c_W^2} z \left(\frac{1}{2} - Q_u s_W^2 z \right)^2 , \\
U^{Z_+}_{t_L t_R}(z) = U^{Z_-}_{\bar{t}_L \bar{t}_R}(z) &= \frac{g_2^2 y_t^2}{c_W^2} \bar{z} \left(\frac{z}{2} + Q_u s_W^2 \bar{z} \right)^2 , \\
U^{t_L}_{Z_+ t_R}(z) = U^{\bar{t}_L}_{Z_- \bar{t}_R}(z) &= \frac{g_2^2 y_t^2}{c_W^2} z \left(\frac{\bar{z}}{2} + Q_u s_W^2 z \right)^2 , \\
U^{t_R}_{Z/\gamma_- t_L}(z) = U^{\bar{t}_R}_{Z/\gamma_+ \bar{t}_L}(z) &= 2 Q_u \frac{e g_2}{c_W} y_t^2 z^2 \left(\frac{1}{2} - Q_u s_W^2 z \right) , \\
U^{t_L}_{Z/\gamma_+ t_R}(z) = U^{\bar{t}_L}_{Z/\gamma_- \bar{t}_R}(z) &= -2 Q_u \frac{e g_2}{c_W} y_t^2 z^2 \left(\frac{\bar{z}}{2} + Q_u s_W^2 z \right) .
\end{aligned}
\tag{A.10}
$$

Splitting $V_T \to f + \bar{f}$ ($f = t, b$):

$$
\begin{aligned}
U^{\bar{t}_R}_{b_L W_-^-}(z) = U^{t_R}_{\bar{b}_L W_+^+}(z) &= \frac{N_c}{2} g_2^2 y_t^2 z^2 , \\
U^{b_L}_{\bar{t}_R W_-^-}(z) = U^{\bar{b}_L}_{t_R W_+^+}(z) &= \frac{N_c}{2} g_2^2 y_t^2 \bar{z}^2 ,
\end{aligned}
\tag{A.11}
$$

$$
\begin{aligned}
U^t_{tg}(z) \equiv U^{\bar{t}_R}_{t_L g_-}(z) = U^{t_L}_{\bar{t}_R g_-}(z) = U^{\bar{t}_L}_{t_R g_+}(z) = U^{t_R}_{\bar{t}_L g_+}(z) &= T_F g_3^2 y_t^2 , \\
U^t_{t\gamma}(z) \equiv U^{\bar{t}_R}_{t_L \gamma_-}(z) = U^{t_L}_{\bar{t}_R \gamma_-}(z) = U^{\bar{t}_L}_{t_R \gamma_+}(z) = U^{t_R}_{\bar{t}_L \gamma_+}(z) &= N_c Q_u^2 e^2 y_t^2 ,
\end{aligned}
\tag{A.12}
$$

$$
\begin{aligned}
U^{\bar{t}_R}_{t_L Z_-}(z) = U^{t_R}_{\bar{t}_L Z_+}(z) &= N_c \frac{g_2^2 y_t^2}{c_W^2} \left(\frac{z}{2} - Q_u s_W^2 \right)^2 , \\
U^{t_L}_{\bar{t}_R Z_-}(z) = U^{\bar{t}_L}_{t_R Z_+}(z) &= N_c \frac{g_2^2 y_t^2}{c_W^2} \left(\frac{\bar{z}}{2} - Q_u s_W^2 \right)^2 , \\
U^{\bar{t}_R}_{t_L Z/\gamma_-}(z) = U^{t_R}_{\bar{t}_L Z/\gamma_+}(z) &= N_c Q_u e \frac{g_2}{c_W} y_t^2 \left(\frac{z}{2} - Q_u s_W^2 \right) , \\
U^{t_L}_{\bar{t}_R Z/\gamma_-}(z) = U^{\bar{t}_L}_{t_R Z/\gamma_+}(z) &= N_c Q_u e \frac{g_2}{c_W} y_t^2 \left(\frac{\bar{z}}{2} - Q_u s_W^2 \right) .
\end{aligned}
\tag{A.13}
$$

Splitting $f \to f + V_L$:

$$
\begin{aligned}
U^{Z_L}_{f_L f_L}(z) = U^{Z_L}_{\bar{f}_L \bar{f}_L}(z) &= \left(T_3 y_f^2 \bar{z}^2 + \frac{g_2^2}{c_W^2} Q^Z_{f_L} z \right)^2 \frac{1}{\bar{z}_+} , \\
U^{f_L}_{Z_L f_L}(z) = U^{\bar{f}_L}_{Z_L \bar{f}_L}(z) &= \left(T_3 y_f^2 z^2 + \frac{g_2^2}{c_W^2} Q^Z_{f_L} \bar{z} \right)^2 \frac{1}{z} , \\
U^{Z_L}_{f_R f_R}(z) = U^{Z_L}_{\bar{f}_R \bar{f}_R}(z) &= \left(T_3 y_f^2 \bar{z}^2 - \frac{g_2^2}{c_W^2} Q^Z_{f_R} z \right)^2 \frac{1}{\bar{z}_+} , \\
U^{f_R}_{Z_L f_R}(z) = U^{\bar{f}_R}_{Z_L \bar{f}_R}(z) &= \left(T_3 y_f^2 z^2 - \frac{g_2^2}{c_W^2} Q^Z_{f_R} \bar{z} \right)^2 \frac{1}{z} , \\
U^{W_L}_{f_L^{(2)} f_L^{(1)}}(z) = U^{W_L}_{\bar{f}_L^{(2)} \bar{f}_L^{(1)}}(z) &= \left(y_{f_1}^2 z \bar{z} - y_{f_2}^2 \bar{z} - g_2^2 z \right)^2 \frac{1}{2 \bar{z}_+} , \\
U^{f_L^{(2)}}_{W_L f_L^{(1)}}(z) = U^{\bar{f}_L^{(2)}}_{W_L \bar{f}_L^{(1)}}(z) &= \left(y_{f_1}^2 z \bar{z} - y_{f_2}^2 z - g_2^2 \bar{z} \right)^2 \frac{1}{2z} .
\end{aligned}
\tag{A.14}
$$

Splitting $V_L \to f + \bar{f}$:

$$\begin{aligned}
U^{\bar{f}_L}_{f_L Z_L}(z) = U^{f_L}_{\bar{f}_L Z_L}(z) &= N_c^f \left(T_3 y_f^2 - \frac{g_2^2}{c_W^2} Q^Z_{f_L} z\bar{z} \right)^2 , \\
U^{\bar{f}_R}_{f_R Z_L}(z) = U^{f_R}_{\bar{f}_R Z_L}(z) &= N_c^f \left(T_3 y_f^2 - \frac{g_2^2}{c_W^2} Q^Z_{f_R} z\bar{z} \right)^2 , \\
U^{\bar{f}^{(2)}_L}_{f^{(1)}_L W_L}(z) = U^{f^{(2)}_L}_{\bar{f}^{(1)}_L W_L}(z) &= \frac{N_c^f}{2} \left(y_{f_1}^2 \bar{z} + y_{f_2}^2 z - g_2^2 z\bar{z} \right)^2 .
\end{aligned} \tag{A.15}$$

Splitting $t \to t + h$:

$$\begin{aligned}
U^h_{tt}(z) \equiv U^h_{t_L t_L}(z) = U^h_{t_R t_R}(z) = U^h_{\bar{t}_R \bar{t}_R}(z) = U^h_{\bar{t}_L \bar{t}_L}(z) &= \frac{y_t^4}{4} \bar{z}(1+z)^2 , \\
U^t_{ht}(z) \equiv U^{t_L}_{h t_L}(z) = U^{t_R}_{h t_R}(z) = U^{\bar{t}_R}_{h \bar{t}_R}(z) = U^{\bar{t}_L}_{h \bar{t}_L}(z) &= \frac{y_t^4}{4} z(1+\bar{z})^2 .
\end{aligned} \tag{A.16}$$

Splitting $h \to t + \bar{t}$:

$$U^t_{th}(z) \equiv U^{\bar{t}_L}_{t_L h}(z) = U^{\bar{t}_R}_{t_R h}(z) = U^{t_R}_{\bar{t}_R h}(z) = U^{t_L}_{\bar{t}_L h}(z) = N_c \frac{y_t^4}{4} (\bar{z} - z)^2 . \tag{A.17}$$

Splitting $V_T \to V_L + V_T$:

$$\begin{aligned}
U^{\gamma_T}_{W_L W_T}(z) &= e^2 g_2^2 \frac{\bar{z}^3}{z} , \\
U^{W_L}_{\gamma_T W_T}(z) &= e^2 g_2^2 \frac{z^3}{\bar{z}_+} , \\
U^{Z_T}_{W_L W_T}(z) &= \frac{1}{4} c_W^2 g_2^4 (1 + \bar{z} + t_W^2 z)^2 \frac{\bar{z}}{z} , \\
U^{W_L}_{Z_T W_T}(z) &= \frac{1}{4} c_W^2 g_2^4 (1 + z + t_W^2 \bar{z})^2 \frac{z}{\bar{z}_+} , \\
U^{W_L}_{Z/\gamma_T W_T}(z) &= c_W e g_2^3 (1 + z + t_W^2 \bar{z}) \frac{z^2}{\bar{z}_+} , \\
U^{W_T}_{Z_L W_T}(z) &= \frac{1}{4} g_2^4 (1 + \bar{z})^2 \frac{\bar{z}}{z} , \\
U^{Z_L}_{W_T W_T}(z) &= \frac{1}{4} g_2^4 (1 + z)^2 \frac{z}{\bar{z}_+} , \\
U^{W_T}_{W_L \gamma_T}(z) &= e^2 g_2^2 \frac{\bar{z}}{z} , \\
U^{W_L}_{W_T \gamma_T}(z) &= e^2 g_2^2 \frac{z}{\bar{z}_+} , \\
U^{W_T}_{W_L Z_T}(z) &= \frac{1}{4} c_W^2 g_2^4 (1 + \bar{z} - t_W^2 z)^2 \frac{\bar{z}}{z} , \\
U^{W_L}_{W_T Z_T}(z) &= \frac{1}{4} c_W^2 g_2^4 (1 + z - t_W^2 \bar{z})^2 \frac{z}{\bar{z}_+} , \\
U^{W_T}_{W_L Z/\gamma_T}(z) &= \frac{1}{2} c_W e g_2^3 (1 + \bar{z} - t_W^2 z) \frac{\bar{z}}{z} , \\
U^{W_L}_{W_T Z/\gamma_T}(z) &= \frac{1}{2} c_W e g_2^3 (1 + z - t_W^2 \bar{z}) \frac{z}{\bar{z}_+} .
\end{aligned} \tag{A.18}$$

Splitting $V_L \to V_T + V_{-T}$:

$$\begin{aligned}
U^{W_{-T}}_{\gamma_T W_L}(z) &= e^2 g_2^2 z^3 \bar{z} \ , \\
U^{\gamma_{-T}}_{W_T W_L}(z) &= e^2 g_2^2 z \bar{z}^3 \ , \\
U^{W_{-T}}_{Z_T W_L}(z) &= \frac{1}{4} c_W^2 g_2^4 z\bar{z}(\bar{z} - z + t_W^2)^2 \ , \\
U^{Z_{-T}}_{W_T W_L}(z) &= \frac{1}{4} c_W^2 g_2^4 z\bar{z}(z - \bar{z} + t_W^2)^2 \ , \\
U^{W_{-T}}_{Z/\gamma_T W_L}(z) &= -c_W e g_2^3 z^2 \bar{z}(\bar{z} - z + t_W^2) \ , \\
U^{W_{-T}}_{W_T Z_L}(z) &= \frac{1}{4} g_2^4 z\bar{z}(\bar{z} - z)^2 \ .
\end{aligned} \tag{A.19}$$

Splitting $V_T \to h + V_T$:

$$\begin{aligned}
U^{W_T}_{hW_T}(z) = U^{h}_{W_T W_T}(z) &= \frac{1}{4} g_2^4 z\bar{z} \ , \\
U^{Z_T}_{hZ_T}(z) = U^{h}_{Z_T Z_T}(z) &= \frac{1}{4} \frac{g_2^4}{c_W^4} z\bar{z} \ .
\end{aligned} \tag{A.20}$$

Splitting $h \to V_T + V_{-T}$:

$$\begin{aligned}
U^{W_{-T}}_{W_T h}(z) &= \frac{1}{4} g_2^4 z\bar{z} \ , \\
U^{Z_{-T}}_{Z_T h}(z) &= \frac{1}{8} \frac{g_2^4}{c_W^4} z\bar{z} \ .
\end{aligned} \tag{A.21}$$

Splitting $V_L \to V_L + V_L$:

$$\begin{aligned}
U^{W_L}_{Z_L W_L}(z) &= \frac{1}{16} g_2^4 [(\bar{z} - z)(2 + z\bar{z}) - t_W^2 \bar{z}(1 + \bar{z})]^2 \frac{1}{z\bar{z}_+} \ , \\
U^{Z_L}_{W_L W_L}(z) &= \frac{1}{16} g_2^4 [(z - \bar{z})(2 + z\bar{z}) - t_W^2 z(1 + z)]^2 \frac{1}{z\bar{z}_+} \ , \\
U^{W_L}_{W_L Z_L}(z) &= \frac{1}{16} g_2^4 (z - \bar{z})^2 (2 + z\bar{z} - t_W^2 z\bar{z})^2 \frac{1}{z\bar{z}_+} \ .
\end{aligned} \tag{A.22}$$

Splitting $h \to V_L + V_L$:

$$\begin{aligned}
U^{Z_L}_{Z_L h}(z) &= \frac{1}{8} \left[\frac{g_2^2}{c_W^2} (1 - z\bar{z}) - 4\lambda_h z\bar{z} \right]^2 \frac{1}{z\bar{z}_+} \ , \\
U^{W_L}_{W_L h}(z) &= \frac{1}{4} [g_2^2 (1 - z\bar{z}) - 4\lambda_h z\bar{z}]^2 \frac{1}{z\bar{z}_+} \ .
\end{aligned} \tag{A.23}$$

Splitting $V_L \to h + V_L$:

$$\begin{aligned}
U^{Z_L}_{hZ_L}(z) &= \frac{1}{4} \left[\frac{g_2^2}{c_W^2} (1 - z\bar{z}) + 4\lambda_h \bar{z} \right]^2 \frac{z}{\bar{z}_+} \ , \\
U^{h}_{Z_L Z_L}(z) &= \frac{1}{4} \left[\frac{g_2^2}{c_W^2} (1 - z\bar{z}) + 4\lambda_h z \right]^2 \frac{\bar{z}}{z} \ , \\
U^{W_L}_{hW_L}(z) &= \frac{1}{4} [g_2^2 (1 - z\bar{z}) + 4\lambda_h \bar{z}]^2 \frac{z}{\bar{z}_+} \ , \\
U^{h}_{W_L W_L}(z) &= \frac{1}{4} [g_2^2 (1 - z\bar{z}) + 4\lambda_h z]^2 \frac{\bar{z}}{z} \ .
\end{aligned} \tag{A.24}$$

Splitting $h \to h + h$:

$$U^h_{hh}(z) = 18\lambda_h^2 z\bar{z} \ . \tag{A.25}$$

Splitting involving the mixed state hZ_L:

$$\begin{aligned}
U^{t_L}_{hZ_L t_L}(z) &= -U^{\bar{t}_L}_{hZ_L \bar{t}_L}(z) = y_t^2(1+\bar{z})\left(\frac{y_t^2}{2}z^2 + g_Z^2 Q^Z_{t_L}\bar{z}\right) \ , \\
U^{t_R}_{hZ_L t_R}(z) &= -U^{\bar{t}_R}_{hZ_L \bar{t}_R}(z) = -y_t^2(1+\bar{z})\left(\frac{y_t^2}{2}z^2 - g_Z^2 Q^Z_{t_R}\bar{z}\right) \ , \\
U^{\bar{t}_L}_{t_L hZ_L}(z) &= U^{t_L}_{\bar{t}_L hZ_L}(z) = -\frac{y_t^2}{2}(\bar{z}-z)\left(\frac{y_t^2}{2} - g_Z^2 Q^Z_{t_L} z\bar{z}\right) \ , \\
U^{\bar{t}_R}_{t_R hZ_L}(z) &= U^{t_R}_{\bar{t}_R hZ_L}(z) = \frac{y_t^2}{2}(\bar{z}-z)\left(\frac{y_t^2}{2} - g_Z^2 Q^Z_{t_R} z\bar{z}\right) \ ,
\end{aligned} \tag{A.26}$$

$$\begin{aligned}
U^{W_L}_{hZ_L W_L}(z) &\equiv U^{W_L^+}_{hZ_L W_L^+}(z) = -U^{W_L^-}_{hZ_L W_L^-}(z) \\
&= \frac{g_2^2}{4}[g_2^2(1-z\bar{z}) + 4\lambda_h\bar{z}][(\bar{z}-z)(2+z\bar{z}) - t_W^2\bar{z}(1-\bar{z})]\frac{1}{\bar{z}_+} \ , \\
U^{W_L}_{W_L hZ_L}(z) &\equiv U^{W_L^-}_{W_L^+ hZ_L}(z) = -U^{W_L^+}_{W_L^- hZ_L}(z) \\
&= \frac{g_2^2}{8}[g_2^2(1-z\bar{z}) - 4\lambda_h z\bar{z}](\bar{z}-z)[(2+(1-t_W^2)z\bar{z}]\frac{1}{z\bar{z}_+} \ ,
\end{aligned} \tag{A.27}$$

$$\begin{aligned}
U^{W_T}_{hZ_L W_T}(z) &\equiv U^{W_T^+}_{hZ_L W_T^+}(z) = U^{W_T^-}_{hZ_L W_T^-}(z) = \frac{g_2^4}{2}\bar{z}(1+\bar{z}) \ , \\
U^{W_T}_{W_T hZ_L}(z) &\equiv U^{W_T^-}_{W_T^+ hZ_L}(z) = -U^{W_T^+}_{W_T^- hZ_L}(z) = -\frac{g_2^4}{4}z\bar{z}(\bar{z}-z) \ .
\end{aligned} \tag{A.28}$$

A.3 SM DGLAP evolution equations

Here we list the full set of DGLAP equations valid above the EW scale. We use the following notation for transverse vector polarization:

$$P^C_{BV_s} \otimes f_{V_s} = P^C_{BV_+} \otimes f_{V_+} + P^C_{BV_-} \otimes f_{V_-} \ , \tag{A.29}$$

$$P^C_{BV_s} \otimes f_{V_{-s}} = P^C_{BV_+} \otimes f_{V_-} + P^C_{BV_-} \otimes f_{V_+} \ . \tag{A.30}$$

In the ultra-collinear terms the factor $v^2/(16\pi^2 Q(t)^2)$ appearing in front of each splitting function is omitted to shorten the notation. The mixed coupling for the Z/γ PDF is defined as

$$\alpha_{\gamma 2} = \sqrt{\alpha_\gamma \alpha_2}. \tag{A.31}$$

Several $SU(3)_c$ group factors, associated to QCD, appear in the equations. They are the quadratic Casimir in the fundamental and adjoint representations (C_F and C_A), and the Dynkin index in the fundamental representation (T_F). In the general case with N_c colors

they are given by

$$\begin{aligned} C_F &= \frac{N_c^2-1}{2N_c}, \\ C_A &= N_c, \\ T_F &= \frac{1}{2}. \end{aligned} \tag{A.32}$$

A.3.1 Leptons

$$\begin{aligned} \frac{df_{\nu_i}}{dt} &= P^v_{\nu_i} f_{\nu_i} + \frac{\alpha_2(t)}{2\pi c_W^2(t)} \left(Q^Z_\nu\right)^2 \left[\widetilde{P}^V_{ff} \otimes f_{\nu_i} + \widetilde{P}^f_{f_L V_s} \otimes f_{Z_s}\right] \\ &\quad + \frac{\alpha_2(t)}{2\pi} \frac{1}{2} \left[\widetilde{P}^V_{ff} \otimes f_{\ell_{L,i}} + \widetilde{P}^f_{f_L V_s} \otimes f_{W_s^+}\right] \\ &\quad + \widetilde{U}^{W_L^-}_{\nu \ell_L} \otimes f_{\ell_{L,i}} + \widetilde{U}^{\bar{\ell}_L}_{\nu W_L^+} \otimes f_{W_L^+} + \widetilde{U}^{Z_L}_{\nu\nu} \otimes f_{\nu_i} + \widetilde{U}^{\bar{\nu}}_{\nu Z_L} \otimes f_{Z_L} \ , \end{aligned} \tag{A.33}$$

$$\begin{aligned} \frac{df_{\bar{\nu}_i}}{dt} &= P^v_{\bar{\nu}_i} f_{\bar{\nu}_i} + \frac{\alpha_2(t)}{2\pi c_W^2(t)} \left(Q^Z_\nu\right)^2 \left[\widetilde{P}^V_{ff} \otimes f_{\bar{\nu}_i} + \widetilde{P}^f_{f_L V_s} \otimes f_{Z_{-s}}\right] \\ &\quad + \frac{\alpha_2(t)}{2\pi} \frac{1}{2} \left[\widetilde{P}^V_{ff} \otimes f_{\bar{\ell}_{L,i}} + \widetilde{P}^f_{f_L V_s} \otimes f_{W_{-s}^-}\right] \\ &\quad + \widetilde{U}^{W_L^+}_{\bar{\nu} \bar{\ell}_L} \otimes f_{\bar{\ell}_{L,i}} + \widetilde{U}^{\ell_L}_{\bar{\nu} W_L^-} \otimes f_{W_L^-} + \widetilde{U}^{Z_L}_{\bar{\nu}\bar{\nu}} \otimes f_{\bar{\nu}_i} + \widetilde{U}^{\nu}_{\bar{\nu} Z_L} \otimes f_{Z_L} \ , \end{aligned} \tag{A.34}$$

$$\begin{aligned} \frac{df_{\ell_{L,i}}}{dt} &= P^v_{\ell_{L,i}} f_{\ell_{L,i}} + \frac{\alpha_\gamma(t)}{2\pi} Q_\ell^2 \left[\widetilde{P}^V_{ff} \otimes f_{\ell_{L,i}} + \widetilde{P}^f_{f_L V_s} \otimes f_{\gamma_s}\right] \\ &\quad + \frac{\alpha_2(t)}{2\pi c_W^2(t)} \left(Q^Z_{\ell_L}\right)^2 \left[\widetilde{P}^V_{ff} \otimes f_{\ell_{L,i}} + \widetilde{P}^f_{f_L V_s} \otimes f_{Z_s}\right] \\ &\quad + \frac{\alpha_2(t)}{2\pi} \frac{1}{2} \left[\widetilde{P}^V_{ff} \otimes f_{\nu_i} + \widetilde{P}^f_{f_L V_s} \otimes f_{W_s^-}\right] \\ &\quad + \frac{\alpha_{\gamma 2}(t)}{2\pi c_W(t)} Q_\ell Q^Z_{\ell_L} \widetilde{P}^f_{f_L V_s} \otimes f_{Z\gamma_s} \\ &\quad + \widetilde{U}^{W_L^+}_{\ell_L \nu} \otimes f_{\nu_i} + \widetilde{U}^{\bar{\nu}}_{\ell_L W_L^-} \otimes f_{W_L^-} + \widetilde{U}^{Z_L}_{\ell_L \ell_L} \otimes f_{\ell_{L,i}} + \widetilde{U}^{\bar{\ell}_L}_{\ell_L Z_L} \otimes f_{Z_L} \ , \end{aligned} \tag{A.35}$$

$$\begin{aligned} \frac{df_{\bar{\ell}_{L,i}}}{dt} &= P^v_{\bar{\ell}_{L,i}} f_{\bar{\ell}_{L,i}} + \frac{\alpha_\gamma(t)}{2\pi} Q_\ell^2 \left[\widetilde{P}^V_{ff} \otimes f_{\bar{\ell}_{L,i}} + \widetilde{P}^f_{f_L V_s} \otimes f_{\gamma_{-s}}\right] \\ &\quad + \frac{\alpha_2(t)}{2\pi c_W^2(t)} \left(Q^Z_{\ell_L}\right)^2 \left[\widetilde{P}^V_{ff} \otimes f_{\bar{\ell}_{L,i}} + \widetilde{P}^f_{f_L V_s} \otimes f_{Z_{-s}}\right] \\ &\quad + \frac{\alpha_2(t)}{2\pi} \frac{1}{2} \left[\widetilde{P}^V_{ff} \otimes f_{\bar{\nu}_i} + \widetilde{P}^f_{f_L V_s} \otimes f_{W_{-s}^+}\right] \\ &\quad + \frac{\alpha_{\gamma 2}(t)}{2\pi c_W(t)} Q_\ell Q^Z_{\ell_L} \widetilde{P}^f_{f_L V_s} \otimes f_{Z\gamma_{-s}} \\ &\quad + \widetilde{U}^{W_L^-}_{\bar{\ell}_L \bar{\nu}} \otimes f_{\bar{\nu}_i} + \widetilde{U}^{\nu}_{\bar{\ell}_L W_L^+} \otimes f_{W_L^+} + \widetilde{U}^{Z_L}_{\bar{\ell}_L \bar{\ell}_L} \otimes f_{\bar{\ell}_{L,i}} + \widetilde{U}^{\ell_L}_{\bar{\ell}_L Z_L} \otimes f_{Z_L} \ , \end{aligned} \tag{A.36}$$

$$
\begin{aligned}
\frac{df_{\ell_{R,i}}}{dt} &= P^v_{\ell_{R,i}} f_{\ell_{R,i}} + \frac{\alpha_\gamma(t)}{2\pi} Q_\ell^2 \Big[\widetilde{P}^V_{ff} \otimes f_{\ell_{R,i}} + \widetilde{P}^f_{f_L V_s} \otimes f_{\gamma_{-s}} \Big] \\
&+ \frac{\alpha_2(t)}{2\pi c_W^2(t)} \left(Q^Z_{\ell_R}\right)^2 \Big[\widetilde{P}^V_{ff} \otimes f_{\ell_{R,i}} + \widetilde{P}^f_{f_L V_s} \otimes f_{Z_{-s}} \Big] \\
&+ \frac{\alpha_{\gamma 2}(t)}{2\pi c_W(t)} Q_\ell Q^Z_{\ell_R} \widetilde{P}^f_{f_L V_s} \otimes f_{Z\gamma_{-s}} \\
&+ \widetilde{U}^{Z_L}_{\ell_R \ell_R} \otimes f_{\ell_{R,i}} + \widetilde{U}^{\bar{\ell}_R}_{\ell_R Z_L} \otimes f_{Z_L} \ ,
\end{aligned}
\tag{A.37}
$$

$$
\begin{aligned}
\frac{df_{\bar{\ell}_{R,i}}}{dt} &= P^v_{\bar{\ell}_{R,i}} f_{\bar{\ell}_{R,i}} + \frac{\alpha_\gamma(t)}{2\pi} Q_\ell^2 \Big[\widetilde{P}^V_{ff} \otimes f_{\bar{\ell}_{R,i}} + \widetilde{P}^f_{f_L V_s} \otimes f_{\gamma_s} \Big] \\
&+ \frac{\alpha_2(t)}{2\pi c_W^2(t)} \left(Q^Z_{\ell_R}\right)^2 \Big[\widetilde{P}^V_{ff} \otimes f_{\bar{\ell}_{R,i}} + \widetilde{P}^f_{f_L V_s} \otimes f_{Z_s} \Big] \\
&+ \frac{\alpha_{\gamma 2}(t)}{2\pi c_W(t)} Q_\ell Q^Z_{\ell_R} \widetilde{P}^f_{f_L V_s} \otimes f_{Z\gamma_s} \\
&+ \widetilde{U}^{Z_L}_{\bar{\ell}_R \bar{\ell}_R} \otimes f_{\bar{\ell}_{R,i}} + \widetilde{U}^{\ell_R}_{\bar{\ell}_R Z_L} \otimes f_{Z_L} \ .
\end{aligned}
\tag{A.38}
$$

A.3.2 Quarks

$$
\begin{aligned}
\frac{df_{u_{L,i}}}{dt} &= P^v_{u_{L,i}} f_{u_{L,i}} + \frac{\alpha_\gamma(t)}{2\pi} Q_u^2 \Big[\widetilde{P}^V_{ff} \otimes f_{u_{L,i}} + N_c \widetilde{P}^f_{f_L V_s} \otimes f_{\gamma_s} \Big] \\
&+ \frac{\alpha_2(t)}{2\pi c_W^2(t)} \left(Q^Z_{u_L}\right)^2 \Big[\widetilde{P}^V_{ff} \otimes f_{u_{L,i}} + N_c \widetilde{P}^f_{f_L V_s} \otimes f_{Z_s} \Big] \\
&+ \frac{\alpha_2(t)}{2\pi} \frac{1}{2} \Big[\widetilde{P}^V_{ff} \otimes f_{d_{L,i}} + N_c \widetilde{P}^f_{f_L V_s} \otimes f_{W_s^+} \Big] \\
&+ \frac{\alpha_{\gamma 2}(t)}{2\pi} Q_u N_c Q^Z_{u_L} \widetilde{P}^f_{f_L V_s} \otimes f_{Z\gamma_s} \\
&+ \frac{\alpha_3(t)}{2\pi} \Big[C_F \widetilde{P}^V_{ff} \otimes f_{u_{L,i}} + T_F \widetilde{P}^f_{f_L V_s} \otimes f_{g_s} \Big] \\
&+ \widetilde{U}^{W_L^-}_{u_L d_L} \otimes f_{d_{L,i}} + \widetilde{U}^{\bar{d}_L}_{u_L W_L^+} \otimes f_{W_L^+} + \widetilde{U}^{Z_L}_{u_L u_L} \otimes f_{u_{L,i}} + \widetilde{U}^{\bar{u}_L}_{u_L Z_L} \otimes f_{Z_L} \ ,
\end{aligned}
\tag{A.39}
$$

$$
\begin{aligned}
\frac{df_{\bar{u}_{L,i}}}{dt} &= P^v_{\bar{u}_{L,i}} f_{\bar{u}_{L,i}} + \frac{\alpha_\gamma(t)}{2\pi} Q_u^2 \Big[\widetilde{P}^V_{ff} \otimes f_{\bar{u}_{L,i}} + N_c \widetilde{P}^f_{f_L V_s} \otimes f_{\gamma_{-s}} \Big] \\
&+ \frac{\alpha_2(t)}{2\pi c_W^2(t)} \left(Q^Z_{u_L}\right)^2 \Big[\widetilde{P}^V_{ff} \otimes f_{\bar{u}_{L,i}} + N_c \widetilde{P}^f_{f_L V_s} \otimes f_{Z_{-s}} \Big] \\
&+ \frac{\alpha_2(t)}{2\pi} \frac{1}{2} \Big[\widetilde{P}^V_{ff} \otimes f_{\bar{d}_{L,i}} + N_c \widetilde{P}^f_{f_L V_s} \otimes f_{W_{-s}^-} \Big] \\
&+ \frac{\alpha_{\gamma 2}(t)}{2\pi} Q_u N_c Q^Z_{u_L} \widetilde{P}^f_{f_L V_s} \otimes f_{Z\gamma_{-s}} \\
&+ \frac{\alpha_3(t)}{2\pi} \Big[C_F \widetilde{P}^V_{ff} \otimes f_{\bar{u}_{L,i}} + T_F \widetilde{P}^f_{f_L V_s} \otimes f_{g_{-s}} \Big] \\
&+ \widetilde{U}^{W_L^+}_{\bar{u}_L \bar{d}_L} \otimes f_{\bar{d}_{L,i}} + \widetilde{U}^{d_L}_{\bar{u}_L W_L^-} \otimes f_{W_L^-} + \widetilde{U}^{Z_L}_{\bar{u}_L \bar{u}_L} \otimes f_{\bar{u}_{L,i}} + \widetilde{U}^{u_L}_{\bar{u}_L Z_L} \otimes f_{Z_L} \ ,
\end{aligned}
\tag{A.40}
$$

$$
\begin{aligned}
\frac{df_{t_L}}{dt} &= P^v_{t_L} f_{t_L} + \frac{\alpha_\gamma(t)}{2\pi} Q_u^2 \Big[\widetilde{P}^V_{ff} \otimes f_{t_L} + N_c \widetilde{P}^f_{f_L V_s} \otimes f_{\gamma_s} \Big] \\
&+ \frac{\alpha_2(t)}{2\pi c_W^2(t)} \left(Q^Z_{u_L} \right)^2 \Big[\widetilde{P}^V_{ff} \otimes f_{t_L} + N_c \widetilde{P}^f_{f_L V_s} \otimes f_{Z_s} \Big] \\
&+ \frac{\alpha_2(t)}{2\pi} \frac{1}{2} \Big[\widetilde{P}^V_{ff} \otimes f_{b_L} + N_c \widetilde{P}^f_{f_L V_s} \otimes f_{W_s^+} \Big] \\
&+ \frac{\alpha_{\gamma 2}(t)}{2\pi} Q_u N_c Q^Z_{u_L} \widetilde{P}^f_{f_L V_s} \otimes f_{Z\gamma_s} \\
&+ \frac{\alpha_3(t)}{2\pi} \Big[C_F \widetilde{P}^V_{ff} \otimes f_{t_L} + T_F \widetilde{P}^f_{f_L V_s} \otimes f_{g_s} \Big] \\
&+ \frac{\alpha_y(t)}{2\pi} \frac{1}{2} \Big[\widetilde{P}^h_{ff} \otimes \left(f^{(h)}_{t_R} + f^{(Z_L)}_{t_R} \right) + N_c \widetilde{P}^f_{fh} \otimes \left(f_h + f_{Z_L} + f_{hZ_L} \right) \Big] \\
&+ \widetilde{U}^g_{tt} \otimes f_{t_R} + \widetilde{U}^t_{tg} \otimes f_{g_-} \\
&+ \widetilde{U}^\gamma_{tt} \otimes f_{t_R} + \widetilde{U}^t_{t\gamma} \otimes f_{\gamma_-} + \widetilde{U}^{Z_+}_{t_L t_R} \otimes f_{t_R} + \widetilde{U}^{\bar{t}_R}_{t_L Z_-} \otimes f_{Z_-} + \widetilde{U}^{\bar{t}_R}_{t_L Z/\gamma_-} \otimes f_{Z/\gamma_-} \\
&+ \widetilde{U}^{W_L^-}_{t_L b_L} \otimes f_{b_L} + \widetilde{U}^{\bar{b}_L}_{t_L W_L^+} \otimes f_{W_L^+} \\
&+ \widetilde{U}^{Z_L}_{t_L t_L} \otimes f_{t_L} + \widetilde{U}^{\bar{t}_L}_{t_L Z_L} \otimes f_{Z_L} + \widetilde{U}^h_{tt} \otimes f_{t_L} + \widetilde{U}^t_{th} \otimes f_h + \widetilde{U}^{\bar{t}_L}_{t_L h Z_L} \otimes f_{h Z_L} \ ,
\end{aligned}
\tag{A.41}
$$

$$
\begin{aligned}
\frac{df_{\bar{t}_L}}{dt} &= P^v_{\bar{t}_L} f_{\bar{t}_L} + \frac{\alpha_\gamma(t)}{2\pi} Q_u^2 \Big[\widetilde{P}^V_{ff} \otimes f_{\bar{t}_L} + N_c \widetilde{P}^f_{f_L V_s} \otimes f_{\gamma_{-s}} \Big] \\
&+ \frac{\alpha_2(t)}{2\pi c_W^2(t)} \left(Q^Z_{u_L} \right)^2 \Big[\widetilde{P}^V_{ff} \otimes f_{\bar{t}_L} + N_c \widetilde{P}^f_{f_L V_s} \otimes f_{Z_{-s}} \Big] \\
&+ \frac{\alpha_2(t)}{2\pi} \frac{1}{2} \Big[\widetilde{P}^V_{ff} \otimes f_{\bar{b}_L} + N_c \widetilde{P}^f_{f_L V_s} \otimes f_{W^-_{-s}} \Big] \\
&+ \frac{\alpha_{\gamma 2}(t)}{2\pi} Q_u N_c Q^Z_{u_L} \widetilde{P}^f_{f_L V_s} \otimes f_{Z\gamma_{-s}} \\
&+ \frac{\alpha_3(t)}{2\pi} \Big[C_F \widetilde{P}^V_{ff} \otimes f_{\bar{t}_L} + T_F \widetilde{P}^f_{f_L V_s} \otimes f_{g_{-s}} \Big] \\
&+ \frac{\alpha_y(t)}{2\pi} \frac{1}{2} \Big[\widetilde{P}^h_{ff} \otimes \left(f^{(h)}_{\bar{t}_R} + f^{(Z_L)}_{\bar{t}_R} \right) + N_c \widetilde{P}^f_{fh} \otimes \left(f_h + f_{Z_L} - f_{hZ_L} \right) \Big] \\
&+ \widetilde{U}^g_{tt} \otimes f_{\bar{t}_R} + \widetilde{U}^t_{tg} \otimes f_{g_+} \\
&+ \widetilde{U}^\gamma_{tt} \otimes f_{\bar{t}_R} + \widetilde{U}^t_{t\gamma} \otimes f_{\gamma_+} + \widetilde{U}^{Z_-}_{\bar{t}_L \bar{t}_R} \otimes f_{\bar{t}_R} + \widetilde{U}^{t_R}_{\bar{t}_L Z_+} \otimes f_{Z_+} + \widetilde{U}^{t_R}_{\bar{t}_L Z/\gamma_+} \otimes f_{Z/\gamma_+} \\
&+ \widetilde{U}^{W_L^+}_{\bar{t}_L \bar{b}_L} \otimes f_{\bar{b}_L} + \widetilde{U}^{b_L}_{\bar{t}_L W_L^-} \otimes f_{W_L^-} \\
&+ \widetilde{U}^{Z_L}_{\bar{t}_L \bar{t}_L} \otimes f_{\bar{t}_L} + \widetilde{U}^{t_L}_{\bar{t}_L Z_L} \otimes f_{Z_L} + \widetilde{U}^h_{tt} \otimes f_{\bar{t}_L} + \widetilde{U}^t_{th} \otimes f_h + \widetilde{U}^{t_L}_{\bar{t}_L h Z_L} \otimes f_{h Z_L} \ ,
\end{aligned}
\tag{A.42}
$$

$$
\begin{aligned}
\frac{df_{d_{L,i}}}{dt} &= P^v_{d_{L,i}} f_{d_{L,i}} + \frac{\alpha_\gamma(t)}{2\pi} Q_d^2 \Big[\widetilde{P}^V_{ff} \otimes f_{d_{L,i}} + N_c \widetilde{P}^f_{f_L V_s} \otimes f_{\gamma_s} \Big] \\
&+ \frac{\alpha_2(t)}{2\pi c_W^2(t)} \left(Q^Z_{d_L} \right)^2 \Big[\widetilde{P}^V_{ff} \otimes f_{d_{L,i}} + N_c \widetilde{P}^f_{f_L V_s} \otimes f_{Z_s} \Big] \\
&+ \frac{\alpha_2(t)}{2\pi} \frac{1}{2} \Big[\widetilde{P}^V_{ff} \otimes f_{u_{L,i}} + N_c \widetilde{P}^f_{f_L V_s} \otimes f_{W_s^-} \Big] \\
&+ \frac{\alpha_{\gamma 2}(t)}{2\pi} Q_d N_c Q^Z_{d_L} \widetilde{P}^f_{f_L V_s} \otimes f_{Z\gamma_s} \\
&+ \frac{\alpha_3(t)}{2\pi} \Big[C_F \widetilde{P}^V_{ff} \otimes f_{d_{L,i}} + T_F \widetilde{P}^f_{f_L V_s} \otimes f_{g_s} \Big] \\
&+ \widetilde{U}^{W_L^+}_{d_L u_L} \otimes f_{u_{L,i}} + \widetilde{U}^{\bar{u}_L}_{d_L W_L^-} \otimes f_{W_L^-} + \widetilde{U}^{Z_L}_{d_L d_L} \otimes f_{d_{L,i}} + \widetilde{U}^{\bar{d}_L}_{d_L Z_L} \otimes f_{Z_L} \ ,
\end{aligned}
\tag{A.43}
$$

$$
\begin{aligned}
\frac{df_{\bar{d}_{L,i}}}{dt} &= P^v_{\bar{d}_{L,i}} f_{\bar{d}_{L,i}} + \frac{\alpha_\gamma(t)}{2\pi} Q_d^2 \Big[\widetilde{P}^V_{ff} \otimes f_{\bar{d}_{L,i}} + N_c \widetilde{P}^f_{f_L V_s} \otimes f_{\gamma_{-s}} \Big] \\
&+ \frac{\alpha_2(t)}{2\pi c_W^2(t)} \left(Q^Z_{d_L} \right)^2 \Big[\widetilde{P}^V_{ff} \otimes f_{\bar{d}_{L,i}} + N_c \widetilde{P}^f_{f_L V_s} \otimes f_{Z_{-s}} \Big] \\
&+ \frac{\alpha_2(t)}{2\pi} \frac{1}{2} \Big[\widetilde{P}^V_{ff} \otimes f_{\bar{u}_{L,i}} + N_c \widetilde{P}^f_{f_L V_s} \otimes f_{W^+_{-s}} \Big] \\
&+ \frac{\alpha_{\gamma 2}(t)}{2\pi} Q_d N_c Q^Z_{d_L} \widetilde{P}^f_{f_L V_s} \otimes f_{Z\gamma_{-s}} \\
&+ \frac{\alpha_3(t)}{2\pi} \Big[C_F \widetilde{P}^V_{ff} \otimes f_{\bar{d}_{L,i}} + T_F \widetilde{P}^f_{f_L V_s} \otimes f_{g_{-s}} \Big] \\
&+ \widetilde{U}^{W_L^-}_{\bar{d}_L \bar{u}_L} \otimes f_{\bar{u}_{L,i}} + \widetilde{U}^{u_L}_{\bar{d}_L W_L^+} \otimes f_{W_L^+} + \widetilde{U}^{Z_L}_{\bar{d}_L \bar{d}_L} \otimes f_{\bar{d}_{L,i}} + \widetilde{U}^{d_L}_{\bar{d}_L Z_L} \otimes f_{Z_L} \ ,
\end{aligned}
\tag{A.44}
$$

$$
\begin{aligned}
\frac{df_{b_L}}{dt} &= P^v_{b_L} f_{b_L} + \frac{\alpha_\gamma(t)}{2\pi} Q_d^2 \Big[\widetilde{P}^V_{ff} \otimes f_{b_L} + N_c \widetilde{P}^f_{f_L V_s} \otimes f_{\gamma_s} \Big] \\
&+ \frac{\alpha_2(t)}{2\pi c_W^2(t)} \left(Q^Z_{d_L} \right)^2 \Big[\widetilde{P}^V_{ff} \otimes f_{b_L} + N_c \widetilde{P}^f_{f_L V_s} \otimes f_{Z_s} \Big] \\
&+ \frac{\alpha_2(t)}{2\pi} \frac{1}{2} \Big[\widetilde{P}^V_{ff} \otimes f_{t_L} + N_c \widetilde{P}^f_{f_L V_s} \otimes f_{W_s^-} \Big] \\
&+ \frac{\alpha_{\gamma 2}(t)}{2\pi} Q_d N_c Q^Z_{d_L} \widetilde{P}^f_{f_L V_s} \otimes f_{Z\gamma_s} \\
&+ \frac{\alpha_3(t)}{2\pi} \Big[C_F \widetilde{P}^V_{ff} \otimes f_{b_L} + T_F \widetilde{P}^f_{f_L V_s} \otimes f_{g_s} \Big] \\
&+ \frac{\alpha_y(t)}{2\pi} \Big[\widetilde{P}^h_{ff} \otimes f_{t_R} + N_c \widetilde{P}^f_{fh} \otimes f_{W_L^-} \Big] \\
&+ \widetilde{U}^{W_+^+}_{b_L t_R} \otimes f_{t_R} + \widetilde{U}^{\bar{t}_R}_{b_L W_-^-} \otimes f_{W_-^-} \\
&+ \widetilde{U}^{W_L^+}_{b_L t_L} \otimes f_{t_L} + \widetilde{U}^{\bar{t}_L}_{b_L W_L^-} \otimes f_{W_L^-} + \widetilde{U}^{Z_L}_{b_L b_L} \otimes f_{b_L} + \widetilde{U}^{\bar{b}_L}_{b_L Z_L} \otimes f_{Z_L} \ ,
\end{aligned}
\tag{A.45}
$$

$$
\begin{aligned}
\frac{df_{\bar{b}_L}}{dt} &= P^v_{\bar{b}_L} f_{\bar{b}_L} + \frac{\alpha_\gamma(t)}{2\pi} Q_d^2 \Big[\widetilde{P}^V_{ff} \otimes f_{\bar{b}_L} + N_c \widetilde{P}^f_{f_L V_s} \otimes f_{\gamma_{-s}} \Big] \\
&+ \frac{\alpha_2(t)}{2\pi c_W^2(t)} \left(Q^Z_{d_L} \right)^2 \Big[\widetilde{P}^V_{ff} \otimes f_{\bar{b}_L} + N_c \widetilde{P}^f_{f_L V_s} \otimes f_{Z_{-s}} \Big] \\
&+ \frac{\alpha_2(t)}{2\pi} \frac{1}{2} \Big[\widetilde{P}^V_{ff} \otimes f_{\bar{t}_L} + N_c \widetilde{P}^f_{f_L V_s} \otimes f_{W^+_{-s}} \Big] \\
&+ \frac{\alpha_{\gamma 2}(t)}{2\pi} Q_d N_c \left(Q^Z_{d_L} \right) \widetilde{P}^f_{f_L V_s} \otimes f_{Z\gamma_{-s}} \\
&+ \frac{\alpha_3(t)}{2\pi} \Big[C_F \widetilde{P}^V_{ff} \otimes f_{\bar{b}_L} + T_F \widetilde{P}^f_{f_L V_s} \otimes f_{g_{-s}} \Big] \\
&+ \frac{\alpha_y(t)}{2\pi} \Big[\widetilde{P}^h_{ff} \otimes f_{\bar{t}_R} + N_c \widetilde{P}^f_{fh} \otimes f_{W^+_L} \Big] \\
&+ \widetilde{U}^{W^-}_{\bar{b}_L \bar{t}_R} \otimes f_{\bar{t}_R} + \widetilde{U}^{t_R}_{\bar{b}_L W^+_+} \otimes f_{W^+_+} \\
&+ \widetilde{U}^{W^-_L}_{\bar{b}_L \bar{t}_L} \otimes f_{\bar{t}_L} + \widetilde{U}^{t_L}_{\bar{b}_L W^+_L} \otimes f_{W^+_L} + \widetilde{U}^{Z_L}_{\bar{b}_L \bar{b}_L} \otimes f_{\bar{b}_L} + \widetilde{U}^{t_L}_{\bar{b}_L Z_L} \otimes f_{Z_L} \ ,
\end{aligned}
\tag{A.46}
$$

$$
\begin{aligned}
\frac{df_{u_{R,i}}}{dt} &= P^v_{u_{R,i}} f_{u_{R,i}} + \frac{\alpha_\gamma(t)}{2\pi} Q_u^2 \Big[\widetilde{P}^V_{ff} \otimes f_{u_{R,i}} + N_c \widetilde{P}^f_{f_L V_s} \otimes f_{\gamma_{-s}} \Big] \\
&+ \frac{\alpha_2(t)}{2\pi c_W^2(t)} \left(Q^Z_{u_R} \right)^2 \Big[\widetilde{P}^V_{ff} \otimes f_{u_{R,i}} + N_c \widetilde{P}^f_{f_L V_s} \otimes f_{Z_{-s}} \Big] \\
&+ N_c \frac{\alpha_{\gamma 2}(t)}{2\pi c_W(t)} Q_u Q^Z_{u_R} \widetilde{P}^f_{f_L V_s} \otimes f_{Z\gamma_{-s}} \\
&+ \frac{\alpha_3(t)}{2\pi} \Big[C_F \widetilde{P}^V_{ff} \otimes f_{u_{R,i}} + T_F \widetilde{P}^f_{f_L V_s} \otimes f_{g_{-s}} \Big] \\
&+ \widetilde{U}^{Z_L}_{u_R u_R} \otimes f_{u_{R,i}} + \widetilde{U}^{\bar{u}_R}_{u_R Z_L} \otimes f_{Z_L},
\end{aligned}
\tag{A.47}
$$

$$
\begin{aligned}
\frac{df_{\bar{u}_{R,i}}}{dt} &= P^v_{\bar{u}_{R,i}} f_{\bar{u}_{R,i}} + \frac{\alpha_\gamma(t)}{2\pi} Q_u^2 \Big[\widetilde{P}^V_{ff} \otimes f_{\bar{u}_{R,i}} + N_c \widetilde{P}^f_{f_L V_s} \otimes f_{\gamma_s} \Big] \\
&+ \frac{\alpha_2(t)}{2\pi c_W^2(t)} \left(Q^Z_{u_R} \right)^2 \Big[\widetilde{P}^V_{ff} \otimes f_{\bar{u}_{R,i}} + N_c \widetilde{P}^f_{f_L V_s} \otimes f_{Z_s} \Big] \\
&+ N_c \frac{\alpha_{\gamma 2}(t)}{2\pi c_W(t)} Q_u Q^Z_{u_R} \widetilde{P}^f_{f_L V_s} \otimes f_{Z\gamma_s} \\
&+ \frac{\alpha_3(t)}{2\pi} \Big[C_F \widetilde{P}^V_{ff} \otimes f_{\bar{u}_{R,i}} + T_F \widetilde{P}^f_{f_L V_s} \otimes f_{g_s} \Big] \\
&+ \widetilde{U}^{Z_L}_{\bar{u}_R \bar{u}_R} \otimes f_{\bar{u}_{R,i}} + \widetilde{U}^{u_R}_{\bar{u}_R Z_L} \otimes f_{Z_L} \ ,
\end{aligned}
\tag{A.48}
$$

$$
\begin{aligned}
\frac{df_{t_R}}{dt} &= P^v_{t_R} f_{t_R} + \frac{\alpha_\gamma(t)}{2\pi} Q_u^2 \Big[\widetilde{P}^V_{ff} \otimes f_{t_R} + N_c \widetilde{P}^f_{f_L V_s} \otimes f_{\gamma_{-s}} \Big] \\
&+ \frac{\alpha_2(t)}{2\pi c_W^2(t)} \left(Q^Z_{u_R} \right)^2 \Big[\widetilde{P}^V_{ff} \otimes f_{t_R} + N_c \widetilde{P}^f_{f_L V_s} \otimes f_{Z_{-s}} \Big] \\
&+ N_c \frac{\alpha_{\gamma 2}(t)}{2\pi c_W(t)} Q_u Q^Z_{u_R} \widetilde{P}^f_{f_L V_s} \otimes f_{Z\gamma_{-s}} \\
&+ \frac{\alpha_3(t)}{2\pi} \Big[C_F \widetilde{P}^V_{ff} \otimes f_{t_R} + T_F \widetilde{P}^f_{f_L V_s} \otimes f_{g_{-s}} \Big] \\
&+ \frac{\alpha_y(t)}{2\pi} \left[\widetilde{P}^h_{ff} \otimes \left(\frac{f^{(h)}_{t_L} + f^{(Z_L)}_{t_L}}{2} + f_{b_L} \right) + N_c \widetilde{P}^f_{fh} \otimes \left(\frac{f_h + f_{Z_L} - f_{hZ_L}}{2} + f_{W^+_L} \right) \right] \\
&+ \widetilde{U}^g_{tt} \otimes f_{t_L} + \widetilde{U}^t_{tg} \otimes f_{g_+} \\
&+ \widetilde{U}^\gamma_{tt} \otimes f_{t_L} + \widetilde{U}^t_{t\gamma} \otimes f_{\gamma_+} + \widetilde{U}^{Z_-}_{t_R t_L} \otimes f_{t_L} + \widetilde{U}^{\bar{t}_L}_{t_R Z_+} \otimes f_{Z_+} + \widetilde{U}^{\bar{t}_L}_{t_R Z/\gamma_+} \otimes f_{Z/\gamma_+} \\
&+ \widetilde{U}^{W^-_-}_{t_R b_L} \otimes f_{b_L} + \widetilde{U}^{\bar{b}_L}_{t_R W^+_+} \otimes f_{W^+_+} \\
&+ \widetilde{U}^{Z_L}_{t_R t_R} \otimes f_{t_R} + \widetilde{U}^{\bar{t}_R}_{t_R Z_L} \otimes f_{Z_L} + \widetilde{U}^h_{tt} \otimes f_{t_R} + \widetilde{U}^t_{th} \otimes f_h + \widetilde{U}^{\bar{t}_R}_{t_R h Z_L} \otimes f_{hZ_L} \ ,
\end{aligned}
\tag{A.49}
$$

$$
\begin{aligned}
\frac{df_{\bar{t}_R}}{dt} &= P^v_{\bar{t}_R} f_{\bar{t}_R} + \frac{\alpha_\gamma(t)}{2\pi} Q_u^2 \Big[\widetilde{P}^V_{ff} \otimes f_{\bar{t}_R} + N_c \widetilde{P}^f_{f_L V_s} \otimes f_{\gamma_s} \Big] \\
&+ \frac{\alpha_2(t)}{2\pi c_W^2(t)} \left(Q^Z_{u_R} \right)^2 \Big[\widetilde{P}^V_{ff} \otimes f_{\bar{t}_R} + N_c \widetilde{P}^f_{f_L V_s} \otimes f_{Z_s} \Big] \\
&+ N_c \frac{\alpha_{\gamma 2}(t)}{2\pi c_W(t)} Q_u Q^Z_{u_R} \widetilde{P}^f_{f_L V_s} \otimes f_{Z\gamma_s} \\
&+ \frac{\alpha_3(t)}{2\pi} \Big[C_F \widetilde{P}^V_{ff} \otimes f_{\bar{t}_R} + T_F \widetilde{P}^f_{f_L V_s} \otimes f_{g_s} \Big] \\
&+ \frac{\alpha_y(t)}{2\pi} \left[\widetilde{P}^h_{ff} \otimes \left(\frac{f^{(h)}_{\bar{t}_L} + f^{(Z_L)}_{\bar{t}_L}}{2} + f_{\bar{b}_L} \right) + N_c \widetilde{P}^f_{fh} \otimes \left(\frac{f_h + f_{Z_L} + f_{hZ_L}}{2} + f_{W^-_L} \right) \right] \\
&+ \widetilde{U}^g_{tt} \otimes f_{\bar{t}_L} + \widetilde{U}^t_{tg} \otimes f_{g_-} \\
&+ \widetilde{U}^\gamma_{tt} \otimes f_{\bar{t}_L} + \widetilde{U}^t_{t\gamma} \otimes f_{\gamma_-} + \widetilde{U}^{Z_+}_{\bar{t}_R \bar{t}_L} \otimes f_{\bar{t}_L} + \widetilde{U}^{t_L}_{\bar{t}_R Z_-} \otimes f_{Z_-} + \widetilde{U}^{t_L}_{\bar{t}_R Z/\gamma_-} \otimes f_{Z/\gamma_-} \\
&+ \widetilde{U}^{W^+_+}_{\bar{t}_R \bar{b}_L} \otimes f_{\bar{b}_L} + \widetilde{U}^{b_L}_{\bar{t}_R W^-_-} \otimes f_{W^-_-} \\
&+ \widetilde{U}^{Z_L}_{\bar{t}_R \bar{t}_R} \otimes f_{\bar{t}_R} + \widetilde{U}^{t_R}_{\bar{t}_R Z_L} \otimes f_{Z_L} + \widetilde{U}^h_{tt} \otimes f_{\bar{t}_R} + \widetilde{U}^t_{th} \otimes f_h + \widetilde{U}^{t_R}_{\bar{t}_R h Z_L} \otimes f_{hZ_L} \ ,
\end{aligned}
\tag{A.50}
$$

$$
\begin{aligned}
\frac{df_{d_{R,i}}}{dt} &= P^v_{d_{R,i}} f_{d_{R,i}} + \frac{\alpha_\gamma(t)}{2\pi} Q_d^2 \Big[\widetilde{P}^V_{ff} \otimes f_{d_{R,i}} + N_c \widetilde{P}^f_{f_L V_s} \otimes f_{\gamma_{-s}} \Big] \\
&+ \frac{\alpha_2(t)}{2\pi c_W^2(t)} \left(Q^Z_{d_R} \right)^2 \Big[\widetilde{P}^V_{ff} \otimes f_{d_{R,i}} + N_c \widetilde{P}^f_{f_L V_s} \otimes f_{Z_{-s}} \Big] \\
&+ N_c \frac{\alpha_{\gamma 2}(t)}{2\pi c_W(t)} Q_d Q^Z_{d_R} \widetilde{P}^f_{f_L V_s} \otimes f_{Z\gamma_{-s}} \\
&+ \frac{\alpha_3(t)}{2\pi} \Big[C_F \widetilde{P}^V_{ff} \otimes f_{d_{R,i}} + T_F \widetilde{P}^f_{f_L V_s} \otimes f_{g_{-s}} \Big] \\
&+ \widetilde{U}^{Z_L}_{d_R d_R} \otimes f_{d_{R,i}} + \widetilde{U}^{\bar{d}_R}_{d_R Z_L} \otimes f_{Z_L} \ ,
\end{aligned}
\tag{A.51}
$$

$$
\begin{aligned}
\frac{df_{\bar{d}_{R,i}}}{dt} &= P^v_{\bar{d}_{R,i}} f_{\bar{d}_{R,i}} + \frac{\alpha_\gamma(t)}{2\pi} Q_d^2 \Big[\widetilde{P}^V_{ff} \otimes f_{\bar{d}_{R,i}} + N_c \widetilde{P}^f_{f_L V_s} \otimes f_{\gamma_s} \Big] \\
&+ \frac{\alpha_2(t)}{2\pi c^2_W(t)} \left(Q^Z_{d_R}\right)^2 \Big[\widetilde{P}^V_{ff} \otimes f_{\bar{d}_{R,i}} + N_c \widetilde{P}^f_{f_L V_s} \otimes f_{Z_s} \Big] \\
&+ N_c \frac{\alpha_{\gamma 2}(t)}{2\pi c_W(t)} Q_d Q^Z_{d_R} \widetilde{P}^f_{f_L V_s} \otimes f_{Z\gamma_s} \\
&+ \frac{\alpha_3(t)}{2\pi} \Big[C_F \widetilde{P}^V_{ff} \otimes f_{\bar{d}_{R,i}} + T_F \widetilde{P}^f_{f_L V_s} \otimes f_{g_s} \Big] \\
&+ \widetilde{U}^{Z_L}_{\bar{d}_R \bar{d}_R} \otimes f_{\bar{d}_{R,i}} + \widetilde{U}^{d_R}_{\bar{d}_R Z_L} \otimes f_{Z_L} \ .
\end{aligned}
\tag{A.52}
$$

A.3.3 Transverse gauge bosons

$$
\begin{aligned}
\frac{df_{g_+}}{dt} &= P^v_{g_+} f_{g_+} + \frac{\alpha_3(t)}{2\pi} \Big[C^{(3)}_A P^V_{V_+ V_s} \otimes f_{g_s} + C^{(3)}_F \widetilde{P}^f_{V_+ f_L} \otimes \sum_i \left(f_{u_L,i} + f_{d_L,i} + f_{\bar{u}_R,i} + f_{\bar{d}_R,i} \right) \\
&+ C^{(3)}_F \widetilde{P}^f_{V_- f_L} \otimes \sum_i \left(f_{u_R,i} + f_{d_R,i} + f_{\bar{u}_L,i} + f_{\bar{d}_L,i} \right) \Big] + \widetilde{U}^t_{gt} \otimes \left(f_{t_R} + f_{\bar{t}_L} \right) \ ,
\end{aligned}
\tag{A.53}
$$

$$
\begin{aligned}
\frac{df_{g_-}}{dt} &= P^v_{g_-} f_{g_-} + \frac{\alpha_3(t)}{2\pi} \Big[C^{(3)}_A P^V_{V_- V_s} \otimes f_{g_s} + C^{(3)}_F \widetilde{P}^f_{V_- f_L} \otimes \sum_i \left(f_{u_L,i} + f_{d_L,i} + f_{\bar{u}_R,i} + f_{\bar{d}_R,i} \right) \\
&+ C^{(3)}_F \widetilde{P}^f_{V_+ f_L} \otimes \sum_i \left(f_{u_R,i} + f_{d_R,i} + f_{\bar{u}_L,i} + f_{\bar{d}_L,i} \right) \Big] + \widetilde{U}^t_{gt} \otimes \left(f_{t_L} + f_{\bar{t}_R} \right) \ ,
\end{aligned}
\tag{A.54}
$$

$$
\begin{aligned}
\frac{df_{\gamma_+}}{dt} &= P^v_{\gamma_+} f_{\gamma_+} + \frac{\alpha_\gamma(t)}{2\pi} \widetilde{P}^V_{V_+ V_s} \otimes \left(f_{W^+_s} + f_{W^-_s} \right) + \frac{\alpha_\gamma(t)}{2\pi} \widetilde{P}^h_{V_+ h} \otimes \left(f_{W^+_L} + f_{W^-_L} \right) \\
&+ \frac{\alpha_\gamma(t)}{2\pi} \sum_f Q_f^2 \left[\widetilde{P}^f_{V_+ f_L} \otimes \left(f_{f_L} + f_{\bar{f}_R} \right) + \widetilde{P}^f_{V_- f_L} \otimes \left(f_{f_R} + f_{\bar{f}_L} \right) \right] \\
&+ \widetilde{U}^t_{\gamma t} \otimes \left(f_{t_R} + f_{\bar{t}_L} \right) + \widetilde{U}^{W_L}_{\gamma_T W_T} \otimes \left(f_{W^+_+} + f_{W^-_+} \right) + \widetilde{U}^{W_T}_{\gamma_T W_L} \otimes \left(f_{W^+_L} + f_{W^-_L} \right) \ ,
\end{aligned}
\tag{A.55}
$$

$$
\begin{aligned}
\frac{df_{\gamma_-}}{dt} &= P^v_{\gamma_-} f_{\gamma_-} + \frac{\alpha_\gamma(t)}{2\pi} \widetilde{P}^V_{V_- V_s} \otimes \left(f_{W^+_s} + f_{W^-_s} \right) + \frac{\alpha_\gamma(t)}{2\pi} \widetilde{P}^h_{V_- h} \otimes \left(f_{W^+_L} + f_{W^-_L} \right) \\
&+ \frac{\alpha_\gamma(t)}{2\pi} \sum_f Q_f^2 \left[\widetilde{P}^f_{V_- f_L} \otimes \left(f_{f_L} + f_{\bar{f}_R} \right) + \widetilde{P}^f_{V_+ f_L} \otimes \left(f_{f_R} + f_{\bar{f}_L} \right) \right] \\
&+ \widetilde{U}^t_{\gamma t} \otimes \left(f_{t_L} + f_{\bar{t}_R} \right) + \widetilde{U}^{W_L}_{\gamma_T W_T} \otimes \left(f_{W^+_-} + f_{W^-_-} \right) + \widetilde{U}^{W_T}_{\gamma_T W_L} \otimes \left(f_{W^+_L} + f_{W^-_L} \right) \ ,
\end{aligned}
\tag{A.56}
$$

$$
\begin{aligned}
\frac{df_{Z_+}}{dt} &= P^v_{Z_+} f_{Z_+} + \frac{\alpha_2(t)}{2\pi} c_W^2(t) \widetilde{P}^V_{V_+V_s} \otimes (f_{W_s^+} + f_{W_s^-}) \\
&+ \frac{\alpha_2(t)}{2\pi} \frac{c_{2W}^2}{4c_W^2} \widetilde{P}^h_{V_+h} \otimes (f_{W_L^+} + f_{W_L^-}) + \frac{\alpha_2(t)}{2\pi} \frac{1}{4c_W^2} \widetilde{P}^h_{V_+h} \otimes (f_h + f_{Z_L}) \\
&+ \frac{\alpha_2(t)}{2\pi c_W^2} \sum_f \left[\widetilde{P}^f_{V_+f_L} \otimes \left((Q^Z_{f_L})^2 f_{f_L} + (Q^Z_{f_R})^2 f_{\bar{f}_R} \right) + \widetilde{P}^f_{V_-f_L} \otimes \left((Q^Z_{f_R})^2 f_{f_R} + (Q^Z_{f_L})^2 f_{\bar{f}_L} \right) \right] \\
&+ \widetilde{U}^{t_L}_{Z_+t_R} \otimes f_{t_R} + \widetilde{U}^{t_R}_{Z_-t_L} \otimes f_{\bar{t}_L} \\
&+ \widetilde{U}^{W_L}_{Z_TW_T} \otimes (f_{W_+^+} + f_{W_+^-}) + \widetilde{U}^{W_T}_{Z_TW_L} \otimes (f_{W_L^+} + f_{W_L^-}) \\
&+ \widetilde{U}^h_{Z_TZ_T} \otimes f_{Z_+} + \widetilde{U}^{Z_T}_{Z_Th} \otimes f_h \ ,
\end{aligned}
\tag{A.57}
$$

$$
\begin{aligned}
\frac{df_{Z_-}}{dt} &= P^v_{Z_-} f_{Z_-} + \frac{\alpha_2(t)}{2\pi} c_W^2(t) \widetilde{P}^V_{V_-V_s} \otimes (f_{W_s^+} + f_{W_s^-}) \\
&+ \frac{\alpha_2(t)}{2\pi} \frac{c_{2W}^2}{4c_W^2} \widetilde{P}^h_{V_-h} \otimes (f_{W_L^+} + f_{W_L^-}) + \frac{\alpha_2(t)}{2\pi} \frac{1}{4c_W^2} \widetilde{P}^h_{V_-h} \otimes (f_h + f_{Z_L}) \\
&+ \frac{\alpha_2(t)}{2\pi c_W^2} \sum_f \left[\widetilde{P}^f_{V_-f_L} \otimes \left((Q^Z_{f_L})^2 f_{f_L} + (Q^Z_{f_R})^2 f_{\bar{f}_R} \right) + \widetilde{P}^f_{V_+f_L} \otimes \left((Q^Z_{f_R})^2 f_{f_R} + (Q^Z_{f_L})^2 f_{\bar{f}_L} \right) \right] \\
&+ \widetilde{U}^{t_R}_{Z_-t_L} \otimes f_{t_L} + \widetilde{U}^{t_L}_{Z_+t_R} \otimes f_{\bar{t}_R} \\
&+ \widetilde{U}^{W_L}_{Z_TW_T} \otimes (f_{W_-^+} + f_{W_-^-}) + \widetilde{U}^{W_T}_{Z_TW_L} \otimes (f_{W_L^+} + f_{W_L^-}) \\
&+ \widetilde{U}^h_{Z_TZ_T} \otimes f_{Z_-} + \widetilde{U}^{Z_T}_{Z_Th} \otimes f_h \ ,
\end{aligned}
\tag{A.58}
$$

$$
\begin{aligned}
\frac{df_{Z\gamma_+}}{dt} &= \frac{\alpha_{\gamma 2}(t)}{2\pi} 2c_W(t) \widetilde{P}^V_{V_+V_s} \otimes (f_{W_s^+} + f_{W_s^-}) + \frac{\alpha_{\gamma 2}(t)}{2\pi} \frac{c_{2W}(t)}{c_W(t)} \widetilde{P}^h_{V_+h} \otimes (f_{W_L^+} + f_{W_L^-}) \\
&+ \frac{\alpha_{\gamma 2}(t)}{2\pi} \frac{2}{c_W(t)} \sum_f Q_f \left[\widetilde{P}^f_{V_+f_L} \otimes \left(Q^Z_{f_L} f_{f_L} + Q^Z_{f_R} f_{\bar{f}_R} \right) + \widetilde{P}^f_{V_-f_L} \otimes \left(Q^Z_{f_R} f_{f_R} + Q^Z_{f_L} f_{\bar{f}_L} \right) \right] \\
&+ \widetilde{U}^{t_L}_{Z/\gamma_+t_R} \otimes f_{t_R} + \widetilde{U}^{t_R}_{Z/\gamma_-t_L} \otimes f_{\bar{t}_L} \\
&+ \widetilde{U}^{W_L}_{Z/\gamma_TW_T} \otimes (f_{W_+^+} + f_{W_+^-}) + \widetilde{U}^{W_T}_{Z/\gamma_TW_L} \otimes (f_{W_L^+} + f_{W_L^-}) \ ,
\end{aligned}
\tag{A.59}
$$

$$
\begin{aligned}
\frac{df_{Z\gamma_-}}{dt} &= \frac{\alpha_{\gamma 2}(t)}{2\pi} 2c_W(t) \widetilde{P}^V_{V_-V_s} \otimes (f_{W_s^+} + f_{W_s^-}) + \frac{\alpha_{\gamma 2}(t)}{2\pi} \frac{c_{2W}(t)}{c_W(t)} \widetilde{P}^h_{V_-h} \otimes (f_{W_L^+} + f_{W_L^-}) \\
&+ \frac{\alpha_{\gamma 2}(t)}{2\pi} \frac{2}{c_W(t)} \sum_f Q_f \left[\widetilde{P}^f_{V_-f_L} \otimes \left(Q^Z_{f_L} f_{f_L} + Q^Z_{f_R} f_{\bar{f}_R} \right) + \widetilde{P}^f_{V_+f_L} \otimes \left(Q^Z_{f_R} f_{f_R} + Q^Z_{f_L} f_{\bar{f}_L} \right) \right] \\
&+ \widetilde{U}^{t_R}_{Z/\gamma_-t_L} \otimes f_{t_L} + \widetilde{U}^{t_L}_{Z/\gamma_+t_R} \otimes f_{\bar{t}_R} \\
&+ \widetilde{U}^{W_L}_{Z/\gamma_TW_T} \otimes (f_{W_-^+} + f_{W_-^-}) + \widetilde{U}^{W_T}_{Z/\gamma_TW_L} \otimes (f_{W_L^+} + f_{W_L^-}) \ ,
\end{aligned}
\tag{A.60}
$$

$$
\begin{aligned}
\frac{df_{W_+^+}}{dt} &= P^v_{W_+^+} f_{W_+^+} + \frac{\alpha_2(t)}{2\pi} c_W^2(t) \widetilde{P}^V_{V_+V_s} \otimes (f_{W_s^+} + f_{Z_s}) + \frac{\alpha_\gamma(t)}{2\pi} \widetilde{P}^V_{V_+V_s} \otimes (f_{W_s^+} + f_{\gamma_s}) \\
&+ \frac{\alpha_{\gamma 2}(t)}{2\pi} c_W(t) \widetilde{P}^V_{V_+V_s} \otimes f_{Z\gamma_s} + \frac{\alpha_2(t)}{2\pi} \frac{1}{4} \widetilde{P}^h_{V_+h} \otimes (f_h + f_{Z_L} + f_{hZ_L} + f^{(h)}_{W_L^+} + f^{(Z_L)}_{W_L^+}) \\
&+ \frac{\alpha_2(t)}{2\pi} \frac{1}{2} \sum_i \left[\widetilde{P}^f_{V_+f_L} \otimes \left(f_{u_{L,i}} + f_{\nu_i} \right) + \widetilde{P}^f_{V_-f_L} \otimes \left(f_{\bar{d}_{L,i}} + f_{\bar{\ell}_{L,i}} \right) \right] \\
&+ \widetilde{U}^{b_L}_{W_+^+ t_R} \otimes f_{t_R} + \widetilde{U}^{t_R}_{W_-^- b_L} \otimes f_{\bar{b}_L} \\
&+ \left(\widetilde{U}^{\gamma_T}_{W_T W_L} + \widetilde{U}^{Z_T}_{W_T W_L} \right) \otimes f_{W_L^+} + \left(\widetilde{U}^{h}_{W_T W_T} + \widetilde{U}^{Z_L}_{W_T W_T} \right) \otimes f_{W_+^+} \\
&+ \widetilde{U}^{W_L}_{W_T \gamma_T} \otimes f_{\gamma_+} + \widetilde{U}^{W_L}_{W_T Z_T} \otimes f_{Z_+} + \widetilde{U}^{W_L}_{W_T Z \gamma_T} \otimes f_{Z\gamma_+} \\
&+ \widetilde{U}^{W_T}_{W_T h} \otimes f_h + \widetilde{U}^{W_T}_{W_T Z_L} \otimes f_{Z_L} + \widetilde{U}^{W_T}_{W_T h Z_L} \otimes f_{hZ_L} \ ,
\end{aligned}
\tag{A.61}
$$

$$
\begin{aligned}
\frac{df_{W_-^+}}{dt} &= P^v_{W_-^+} f_{W_-^+} + \frac{\alpha_2(t)}{2\pi} c_W^2(t) \widetilde{P}^V_{V_-V_s} \otimes (f_{W_s^+} + f_{Z_s}) + \frac{\alpha_\gamma(t)}{2\pi} \widetilde{P}^V_{V_-V_s} \otimes (f_{W_s^+} + f_{\gamma_s}) \\
&+ \frac{\alpha_{\gamma 2}(t)}{2\pi} c_W(t) \widetilde{P}^V_{V_-V_s} \otimes f_{Z\gamma_s} + \frac{\alpha_2(t)}{2\pi} \frac{1}{4} \widetilde{P}^h_{V_-h} \otimes (f_h + f_{Z_L} + f_{hZ_L} + f^{(h)}_{W_L^+} + f^{(Z_L)}_{W_L^+}) \\
&+ \frac{\alpha_2(t)}{2\pi} \frac{1}{2} \sum_i \left[\widetilde{P}^f_{V_-f_L} \otimes \left(f_{u_{L,i}} + f_{\nu_i} \right) + \widetilde{P}^f_{V_+f_L} \otimes \left(f_{\bar{d}_{L,i}} + f_{\bar{\ell}_{L,i}} \right) \right] \\
&+ \left(\widetilde{U}^{\gamma_T}_{W_T W_L} + \widetilde{U}^{Z_T}_{W_T W_L} \right) \otimes f_{W_L^+} + \left(\widetilde{U}^{h}_{W_T W_T} + \widetilde{U}^{Z_L}_{W_T W_T} \right) \otimes f_{W_-^+} \\
&+ \widetilde{U}^{W_L}_{W_T \gamma_T} \otimes f_{\gamma_-} + \widetilde{U}^{W_L}_{W_T Z_T} \otimes f_{Z_-} + \widetilde{U}^{W_L}_{W_T Z \gamma_T} \otimes f_{Z\gamma_-} \\
&+ \widetilde{U}^{W_T}_{W_T h} \otimes f_h + \widetilde{U}^{W_T}_{W_T Z_L} \otimes f_{Z_L} + \widetilde{U}^{W_T}_{W_T h Z_L} \otimes f_{hZ_L} \ ,
\end{aligned}
\tag{A.62}
$$

$$
\begin{aligned}
\frac{df_{W_+^-}}{dt} &= P^v_{W_+^-} f_{W_+^-} + \frac{\alpha_2(t)}{2\pi} c_W^2(t) \widetilde{P}^V_{V_+V_s} \otimes (f_{W_s^-} + f_{Z_s}) + \frac{\alpha_\gamma(t)}{2\pi} \widetilde{P}^V_{V_+V_s} \otimes (f_{W_s^-} + f_{\gamma_s}) \\
&+ \frac{\alpha_{\gamma 2}(t)}{2\pi} c_W(t) \widetilde{P}^V_{V_+V_s} \otimes f_{Z\gamma_s} + \frac{\alpha_2(t)}{2\pi} \frac{1}{4} \widetilde{P}^h_{V_+h} \otimes (f_h + f_{Z_L} - f_{hZ_L} + f^{(h)}_{W_L^-} + f^{(Z_L)}_{W_L^-}) \\
&+ \frac{\alpha_2(t)}{2\pi} \frac{1}{2} \sum_i \left[\widetilde{P}^f_{V_+f_L} \otimes \left(f_{d_{L,i}} + f_{\ell_{L,i}} \right) + \widetilde{P}^f_{V_-f_L} \otimes \left(f_{\bar{u}_{L,i}} + f_{\bar{\nu}_i} \right) \right] \\
&+ \left(\widetilde{U}^{\gamma_T}_{W_T W_L} + \widetilde{U}^{Z_T}_{W_T W_L} \right) \otimes f_{W_L^-} + \left(\widetilde{U}^{h}_{W_T W_T} + \widetilde{U}^{Z_L}_{W_T W_T} \right) \otimes f_{W_+^-} \\
&+ \widetilde{U}^{W_L}_{W_T \gamma_T} \otimes f_{\gamma_+} + \widetilde{U}^{W_L}_{W_T Z_T} \otimes f_{Z_+} + \widetilde{U}^{W_L}_{W_T Z \gamma_T} \otimes f_{Z\gamma_+} \\
&+ \widetilde{U}^{W_T}_{W_T h} \otimes f_h + \widetilde{U}^{W_T}_{W_T Z_L} \otimes f_{Z_L} - \widetilde{U}^{W_T}_{W_T h Z_L} \otimes f_{hZ_L} \ ,
\end{aligned}
\tag{A.63}
$$

$$
\begin{aligned}
\frac{df_{W_-^-}}{dt} &= P^v_{W_-^-} f_{W_-^-} + \frac{\alpha_2(t)}{2\pi} c_W^2(t) \widetilde{P}^V_{V_-V_s} \otimes (f_{W_s^-} + f_{Z_s}) + \frac{\alpha_\gamma(t)}{2\pi} \widetilde{P}^V_{V_-V_s} \otimes (f_{W_s^-} + f_{\gamma_s}) \\
&+ \frac{\alpha_{\gamma 2}(t)}{2\pi} c_W(t) \widetilde{P}^V_{V_-V_s} \otimes f_{Z\gamma_s} + \frac{\alpha_2(t)}{2\pi} \frac{1}{4} \widetilde{P}^h_{V_-h} \otimes (f_h + f_{Z_L} - f_{hZ_L} + f^{(h)}_{W_L^-} + f^{(Z_L)}_{W_L^-}) \\
&+ \frac{\alpha_2(t)}{2\pi} \frac{1}{2} \sum_i \Big[\widetilde{P}^f_{V_-f_L} \otimes \left(f_{d_{L,i}} + f_{\ell_{L,i}} \right) + \widetilde{P}^f_{V_+f_L} \otimes \left(f_{\bar{u}_{L,i}} + f_{\bar{\nu}_i} \right) \Big] \\
&+ \widetilde{P}^{t_R}_{W_-^- b_L} \otimes f_{b_L} + \widetilde{P}^{b_L}_{W_+^+ t_R} \otimes f_{\bar{t}_R} \\
&+ \left(\widetilde{U}^{\gamma_T}_{W_T W_L} + \widetilde{U}^{Z_T}_{W_T W_L} \right) \otimes f_{W_L^-} + \left(\widetilde{U}^h_{W_T W_T} + \widetilde{U}^{Z_L}_{W_T W_T} \right) \otimes f_{W_-^-} \\
&+ \widetilde{U}^{W_L}_{W_T \gamma_T} \otimes f_{\gamma_-} + \widetilde{U}^{W_L}_{W_T Z_T} \otimes f_{Z_-} + \widetilde{U}^{W_L}_{W_T Z \gamma_T} \otimes f_{Z\gamma_-} \\
&+ \widetilde{U}^{W_T}_{W_T h} \otimes f_h + \widetilde{U}^{W_T}_{W_T Z_L} \otimes f_{Z_L} - \widetilde{U}^{W_T}_{W_T h Z_L} \otimes f_{hZ_L} \ .
\end{aligned}
\tag{A.64}
$$

A.3.4 Higgs and longitudinal gauge bosons

$$
\begin{aligned}
\frac{df_h}{dt} &= P^v_h f_h + \frac{\alpha_2(t)}{2\pi} \frac{1}{4} \Big[\widetilde{P}^V_{hh} \otimes \left(f_{W_L^+} + f_{W_L^-} \right) + \widetilde{P}^h_{hV} \otimes \left(f_{W_+^+} + f_{W_-^+} + f_{W_+^-} + f_{W_-^-} \right) \Big] \\
&+ \frac{\alpha_2(t)}{2\pi} \frac{1}{4c_W^2} \Big[\widetilde{P}^V_{hh} \otimes f_{Z_L} + \widetilde{P}^h_{hV} \otimes \left(f_{Z_+} + f_{Z_-} \right) \Big] \\
&+ \frac{\alpha_y(t)}{2\pi} \frac{1}{2} \widetilde{P}^f_{hf} \otimes (f_{t_L} + f_{t_R} + f_{\bar{t}_L} + f_{\bar{t}_R}) \\
&+ \widetilde{U}^t_{ht} \otimes (f_{t_L} + f_{t_R} + f_{\bar{t}_L} + f_{\bar{t}_R}) \\
&+ \widetilde{U}^{W_T}_{hW_T} \otimes (f_{W_+^+} + f_{W_-^+} + f_{W_+^-} + f_{W_-^-}) + \widetilde{U}^{Z_T}_{hZ_T} \otimes (f_{Z_+} + f_{Z_-}) \\
&+ \widetilde{U}^{W_L}_{hW_L} \otimes (f_{W_L^+} + f_{W_L^-}) + \widetilde{U}^{Z_L}_{hZ_L} \otimes f_{Z_L} + \widetilde{U}^h_{hh} \otimes f_h \ ,
\end{aligned}
\tag{A.65}
$$

$$
\begin{aligned}
\frac{df_{Z_L}}{dt} &= P^v_{Z_L} f_{Z_L} + \frac{\alpha_2(t)}{2\pi} \frac{1}{4} \left[\widetilde{P}^V_{hh} \otimes (f_{W_L^+} + f_{W_L^-}) + \widetilde{P}^h_{hV} \otimes (f_{W_+^+} + f_{W_-^+} + f_{W_+^-} + f_{W_-^-}) \right] \\
&+ \frac{\alpha_2(t)}{2\pi} \frac{1}{4c_W^2} \left[\widetilde{P}^V_{hh} \otimes f_h + \widetilde{P}^h_{hV} \otimes (f_{Z_+} + f_{Z_-}) \right] \\
&+ \frac{\alpha_y(t)}{2\pi} \frac{1}{2} \widetilde{P}^f_{hf} \otimes (f_{t_L} + f_{t_R} + f_{\bar{t}_L} + f_{\bar{t}_R}) \\
&+ \sum_{f_L} \widetilde{U}^{f_L}_{Z_L f_L} \otimes f_{f_L} + \sum_{f_R} \widetilde{U}^{f_R}_{Z_L f_R} \otimes f_{f_R} \\
&+ \sum_{\bar{f}_L} \widetilde{U}^{\bar{f}_L}_{Z_L \bar{f}_L} \otimes f_{\bar{f}_L} + \sum_{\bar{f}_R} \widetilde{U}^{\bar{f}_R}_{Z_L \bar{f}_R} \otimes f_{\bar{f}_R} \\
&+ \widetilde{U}^{W_T}_{Z_L W_T} \otimes (f_{W_+^+} + f_{W_-^+} + f_{W_+^-} + f_{W_-^-}) \\
&+ \widetilde{U}^h_{Z_L Z_L} \otimes f_{Z_L} + \widetilde{U}^{Z_L}_{Z_L h} \otimes f_h + \widetilde{U}^{W_L}_{Z_L W_L} \otimes (f_{W_L^+} + f_{W_L^-}) \ ,
\end{aligned}
\tag{A.66}
$$

$$
\begin{aligned}
\frac{df_{W_L^+}}{dt} &= P^v_{W_L^+} f_{W_L^+} + \frac{\alpha_2(t)}{2\pi}\frac{1}{4}\left[\widetilde{P}^V_{hh}\otimes(f_h + f_{Z_L} - f_{hZ_L}) + \widetilde{P}^h_{hV}\otimes\left(f^{(h)}_{W_+^+} + f^{(Z_L)}_{W_+^+} + f^{(h)}_{W_-^+} + f^{(Z_L)}_{W_-^+}\right)\right] \\
&+ \frac{\alpha_2(t)}{2\pi}\frac{c_{2W}^2}{4c_W^2}\left[\widetilde{P}^V_{hh}\otimes f_{W_L^+} + \widetilde{P}^h_{hV}\otimes(f_{Z_+} + f_{Z_-})\right] \\
&+ \frac{\alpha_\gamma(t)}{2\pi}\left[\widetilde{P}^V_{hh}\otimes f_{W_L^+} + \widetilde{P}^h_{hV}\otimes(f_{\gamma_+} + f_{\gamma_-})\right] + \frac{\alpha_{\gamma 2}(t)}{2\pi}\frac{c_{2W}}{2c_W}\widetilde{P}^h_{hV}\otimes(f_{Z\gamma_+} + f_{Z\gamma_-}) \\
&+ \frac{\alpha_y(t)}{2\pi}\widetilde{P}^f_{hf}\otimes\left(f_{t_R} + f_{\bar{b}_L}\right) \\
&+ \sum_{f_L^{(1)}f_L^{(2)}}\widetilde{U}^{f_L^{(2)}}_{W_L^+ f_L^{(1)}}\otimes f_{f_L^{(1)}} + \sum_{\bar{f}_L^{(1)}\bar{f}_L^{(2)}}\widetilde{U}^{\bar{f}_L^{(2)}}_{W_L^+ \bar{f}_L^{(1)}}\otimes f_{\bar{f}_L^{(1)}} \\
&+ \widetilde{U}^{\gamma_T}_{W_L W_T}\otimes(f_{W_+^+} + f_{W_-^+}) + \widetilde{U}^{Z_T}_{W_L W_T}\otimes(f_{W_+^+} + f_{W_-^+}) \\
&+ \widetilde{U}^{W_T}_{W_L\gamma_T}\otimes(f_{\gamma_+} + f_{\gamma_-}) + \widetilde{U}^{W_T}_{W_L Z_T}\otimes(f_{Z_+} + f_{Z_-}) \\
&+ \widetilde{U}^{W_T}_{W_L Z_{\gamma_T}}\otimes(f_{Z\gamma_+} + f_{Z\gamma_-}) \\
&+ \widetilde{U}^{W_L}_{W_L h}\otimes f_h + \widetilde{U}^{W_L}_{W_L Z_L}\otimes f_{Z_L} + \widetilde{U}^{W_L}_{W_L hZ_L}\otimes f_{hZ_L} \\
&+ \widetilde{U}^{h}_{W_L W_L}\otimes f_{W_L^+} + \widetilde{U}^{Z_L}_{W_L W_L}\otimes f_{W_L^+}\ ,
\end{aligned}
\tag{A.67}
$$

$$
\begin{aligned}
\frac{df_{W_L^-}}{dt} &= P^v_{W_L^-} f_{W_L^-} + \frac{\alpha_2(t)}{2\pi}\frac{1}{4}\left[\widetilde{P}^V_{hh}\otimes(f_h + f_{Z_L} + f_{hZ_L}) + \widetilde{P}^h_{hV}\otimes\left(f^{(h)}_{W_+^-} + f^{(Z_L)}_{W_+^-} + f^{(h)}_{W_-^-} + f^{(Z_L)}_{W_-^-}\right)\right] \\
&+ \frac{\alpha_2(t)}{2\pi}\frac{c_{2W}^2}{4c_W^2}\left[\widetilde{P}^V_{hh}\otimes f_{W_L^-} + \widetilde{P}^h_{hV}\otimes(f_{Z_+} + f_{Z_-})\right] \\
&+ \frac{\alpha_\gamma(t)}{2\pi}\left[\widetilde{P}^V_{hh}\otimes f_{W_L^-} + \widetilde{P}^h_{hV}\otimes(f_{\gamma_+} + f_{\gamma_-})\right] + \frac{\alpha_{\gamma 2}(t)}{2\pi}\frac{c_{2W}}{2c_W}\widetilde{P}^h_{hV}\otimes(f_{Z\gamma_+} + f_{Z\gamma_-}) \\
&+ \frac{\alpha_y(t)}{2\pi}\widetilde{P}^f_{hf}\otimes(f_{b_L} + f_{\bar{t}_R}) \\
&+ \sum_{f_L^{(1)}f_L^{(2)}}\widetilde{U}^{f_L^{(2)}}_{W_L^- f_L^{(1)}}\otimes f_{f_L^{(1)}} + \sum_{\bar{f}_L^{(1)}\bar{f}_L^{(2)}}\widetilde{U}^{\bar{f}_L^{(2)}}_{W_L^- \bar{f}_L^{(1)}}\otimes f_{\bar{f}_L^{(1)}} \\
&+ \widetilde{U}^{\gamma_T}_{W_L W_T}\otimes(f_{W_+^-} + f_{W_-^-}) + \widetilde{U}^{Z_T}_{W_L W_T}\otimes(f_{W_+^-} + f_{W_-^-}) \\
&+ \widetilde{U}^{W_T}_{W_L\gamma_T}\otimes(f_{\gamma_+} + f_{\gamma_-}) + \widetilde{U}^{W_T}_{W_L Z_T}\otimes(f_{Z_+} + f_{Z_-}) \\
&+ \widetilde{U}^{W_T}_{W_L Z_{\gamma_T}}\otimes(f_{Z\gamma_+} + f_{Z\gamma_-}) \\
&+ \widetilde{U}^{W_L}_{W_L h}\otimes f_h + \widetilde{U}^{W_L}_{W_L Z_L}\otimes f_{Z_L} - \widetilde{U}^{W_L}_{W_L hZ_L}\otimes f_{hZ_L} \\
&+ \widetilde{U}^{h}_{W_L W_L}\otimes f_{W_L^-} + \widetilde{U}^{Z_L}_{W_L W_L}\otimes f_{W_L^-}\ ,
\end{aligned}
\tag{A.68}
$$

$$
\begin{aligned}
\frac{df_{hZ_L}}{dt} &= \frac{\alpha_y(t)}{2\pi}\widetilde{P}^f_{hf}\otimes(f_{t_L+} + f_{\bar{t}_R} - f_{t_R} - f_{\bar{t}_L}) \\
&+ \frac{\alpha_2(t)}{2\pi}\frac{1}{4}\left[\widetilde{P}^V_{hh}\otimes(f_{W_L^-} - f_{W_L^+}) + \widetilde{P}^h_{hV}\otimes(f_{W_+^+} + f_{W_-^+} - f_{W_+^-} - f_{W_-^-})\right] \\
&+ \widetilde{U}^{t_L}_{hZ_L t_L}\otimes(f_{t_L} - f_{\bar{t}_L}) + \widetilde{U}^{t_R}_{hZ_L t_R}\otimes(f_{t_R} - f_{\bar{t}_R}) \\
&+ \widetilde{U}^{W_L}_{hZ_L W_L}\otimes(f_{W_L^+} - f_{W_L^-}) + \widetilde{U}^{W_T}_{hZ_L W_T}\otimes(f_{W_+^+} + f_{W_-^+} - f_{W_+^-} - f_{W_-^-})\ .
\end{aligned}
\tag{A.69}
$$

Appendix B

Numerical calculation of LePDF

In this Appendix we collect useful information to understand the structure of our code and of the output files, and some examples on how to use it. We recall our numerical strategy and we explain in details how the code works and how the results are saved. For practical reasons the notation used in this Appendix, which is the one present in our code, may vary wrt Chapter 3. All the files mentioned in the following can be found at `https://github.com/DavidMarzocca/LePDF`.

B.1 Using LePDFs

B.1.1 Structure of the PDFs sets

We discretize the x-space from a minimum value x_0 up to 1 using a grid of N_x points, $x_j = \{x_0, x_1, \dots, x_{N_x-1} \equiv 1\}$, with spacing $\delta x_j = x_j - x_{j-1}$.[1]
We choose a spacing that is denser near $x = 1$ and sparser at small values, in practice we set

$$x_j = 10^{-6((N_x-1-j)/(N_x-1))^{2.5}}, \qquad j = 1, \dots, N_x \tag{B.1}$$

to get values from $x_0 = 10^{-6}$ to $x_{N_x-1} = 1$. We choose $N_x = 1001$, since the relative difference with finer grids would be at most of order $\mathcal{O}(10^{-2})$, see the discussion in Section 3.3.7. This discretization allows us to obtain a set of ODEs, where the integrals are computed using the rectangles method.
We discretize the energy variable t with spacing dt_0 below the EW scale $t_0 = \log(m_W^2/m_{\ell_v}^2)$. dt_0 is then fixed by the number N_{t_0} of grid points needed to reach the electroweak scale[2]:

$$dt_0 = \frac{t_0}{N_{t_0} - 1}. \tag{B.2}$$

[1] Notice that here N_x is just the length of the grid, while in Chapter 3 we used it to count the number of bins. We also set $\delta x_0 = x_0$.

[2] Here $t = 0$ and $t = t_0$ are included in the counting. This means that the EW scale is reached with $N_{t_0} - 1$ steps of the algorithm.

We choose $N_{t_0} = 351$ for the electron and $N_{t_0} = 201$ for the muon, in order to have a similar dt_0 in both cases. In the second phase of the evolution we use N_t grid points with spacing dt, starting from t_0. In our implementation we set $N_t = 150$ for the electron and $N_t = 200$ for the muon, with $dt = dt_0$.
The results are then exported in a format inspired by the LHAPDF6 one used for proton PDFs. The structure of the output files is reported below.

- The first three lines just specify the format.
- In the fourth and fifth lines are reported respectively the grids in x and in Q. In order to make lighter files, the grids (and the corresponding values of the PDFs) are a subset of the ones used in the code: we save 1 every 6 points for the Q-grid and 1 every 5 points for the x-grid, except for the last 100, that are all reported. We saved the x-grid with more significant digits than the other outputs in order to properly reconstruct the grid spacings in the region where the points are denser.
- The next three lines report the particles' list as in Table B.1: name, PDG ID (for the Z/γ and h/Z_L interference we join the PDG ID of the two states) and the additional label specifying the helicity (it is understood that for fermions or transverse vectors it will be $\pm 1/2$ or ± 1, respectively). This last line represents the main difference with the standard LHAPDF6 format.
- In all the remaining lines we report the quantities $xf(x, Q)$: each column corresponds to a particle, following the order of the previous lines. We start at $x = x_0$ increasing Q at each row and repeating for each x, so that the data have the form reported in Table B.2.

B.1.2 Use in Mathematica

LePDFs can be directly used in Mathematica for analytical studies. In LePDF_examples.nb, that can be found together with the code and the outputs, we show how this can be done. We load the files with PDFs and use a linear interpolation in x and Q to get $f_A(x, Q)$, which in the example correspond to the function μPDFpart[part,Q][x]. A couple of considerations are in order:

- Due to the sharp growth of the valence lepton PDF around $x = 1$, to reconstruct it properly it is important to use many grid points in that region. This is why we used a denser grid around $x = 1$ and we reported all the last 100 points in the outputs.
- For the same reason, performing integrals involving the valence PDF with NIntegrate may give wrong results. We then recommend to use the rectangles method with x-grid to compute such integrals, or to use zeroth order interpolation around $x = 1$ for

e_L	eL	11	-
e_R	eR	11	+
ν_e	nue	12	-
μ_L	muL	13	-
μ_R	muR	13	+
ν_μ	numu	14	-
τ_L	taL	15	-
τ_R	taR	15	+
ν_τ	nuta	16	-
$\bar{e}_L$	eLb	-11	+
$\bar{e}_R$	eRb	-11	-
$\bar{\nu}_e$	nueb	-12	+
$\bar{\mu}_L$	muLb	-13	+
$\bar{\mu}_R$	muRb	-13	-
$\bar{\nu}_\mu$	numub	-14	+
$\bar{\tau}_L$	taLb	-15	+
$\bar{\tau}_R$	taRb	-15	-
$\bar{\nu}_\tau$	nutab	-16	+

d_L	dL	1	-
d_R	dR	1	+
u_L	uL	2	-
u_R	uR	2	+
s_L	sL	3	-
s_R	sR	3	+
c_L	cL	4	-
c_R	cR	4	+
b_L	bL	5	-
b_R	bR	5	+
t_L	tL	6	-
t_R	tR	6	+
$\bar{d}_L$	dLb	-1	+
$\bar{d}_R$	dRb	-1	-
$\bar{u}_L$	uLb	-2	+
$\bar{u}_R$	uRb	-2	-
$\bar{s}_L$	sLb	-3	+
$\bar{s}_R$	sRb	-3	-
$\bar{c}_L$	cLb	-4	+
$\bar{c}_R$	cRb	-4	-
$\bar{b}_L$	bLb	-5	+
$\bar{b}_R$	bRb	-5	-
$\bar{t}_L$	tLb	-6	+
$\bar{t}_R$	tRb	-6	-

g_+	gp	21	+
g_-	gm	21	-
γ_+	gap	22	+
γ_-	gam	22	-
Z_+	Zp	23	+
Z_-	Zm	23	-
Z_L	ZL	23	0
Z/γ_+	Zgap	2223	+
Z/γ_-	Zgam	2223	-
W_+^+	Wpp	24	+
W_-^+	Wpm	24	-
W_L^+	WpL	24	0
W_+^-	Wmp	-24	+
W_-^-	Wmm	-24	-
W_L^-	WmL	-24	0
h	h	25	0
h/Z_L	hZL	2523	0

Table B.1: Names, PDG IDs and polarizations of the particles. In particular, the second, third and fourth columns of the tables correspond to the sixth, seventh and eighth lines of the output file.

consistency. In Table B.3 we report an example of this issue in the calculation of the momentum fraction carried by the various partons at $Q = 3$ TeV: while for other partons the two methods are compatible, NIntegrate does not work for the valence lepton.

We provide outputs both for particles and antiparticles, which can be loaded in Mathematica and interpolated as discussed above. Notice that since the PDFs for an antiparticle as valence lepton are equal to the ones of the corresponding particle with CP conjugated partons, the former can be obtained directly from the interpolated version of the latter:

$$\mu b\text{PDFpart[part,Q][x]} = \mu\text{PDFpart[CP(part),Q][x]}.$$

$x_0 f_{e_L}(x_0, Q_0)$	$\dots$	$\dots$	$x_0 f_{h/Z_L}(x_0, Q_0)$
$x_0 f_{e_L}(x_0, Q_1)$	$\dots$	$\dots$	$x_0 f_{h/Z_L}(x_0, Q_1)$
$\vdots$	$\vdots$	$\vdots$	$\vdots$
$x_0 f_{e_L}(x_0, Q_{N_Q-1})$	$\dots$	$\dots$	$x_0 f_{h/Z_L}(x_0, Q_{N_Q-1})$
$x_1 f_{e_L}(x_1, Q_0)$	$\dots$	$\dots$	$x_1 f_{h/Z_L}(x_1, Q_0)$
$x_1 f_{e_L}(x_1, Q_1)$	$\dots$	$\dots$	$x_1 f_{h/Z_L}(x_1, Q_1)$
$\vdots$	$\vdots$	$\vdots$	$\vdots$
$x_1 f_{e_L}(x_1, Q_{N_Q-1})$	$\dots$	$\dots$	$x_1 f_{h/Z_L}(x_1, Q_{N_Q-1})$
$\vdots$	$\vdots$	$\vdots$	$\vdots$
$\vdots$	$\vdots$	$\vdots$	$\vdots$
$x_{N_x-1} f_{e_L}(x_{N_x-1}, Q_0)$	$\dots$	$\dots$	$x_{N_x-1} f_{h/Z_L}(x_{N_x-1}, Q_0)$
$x_{N_x-1} f_{e_L}(x_{N_x-1}, Q_1)$	$\dots$	$\dots$	$x_{N_x-1} f_{h/Z_L}(x_{N_x-1}, Q_1)$
$\vdots$	$\vdots$	$\vdots$	$\vdots$
$x_{N_x-1} f_{e_L}(x_{N_x-1}, Q_{N_Q-1})$	$\dots$	$\dots$	$x_{N_x-1} f_{h/Z_L}(x_{N_x-1}, Q_{N_Q-1})$

Table B.2: Structure of our PDF data in the LHAPDF6 format. The labels for x and Q are referred to the reduced grids reported in the fourth and fifth lines of the output files.

Parton	NIntegrate	Rectangles
μ_L	36.22	48.03
μ_R	34.03	45.54
ν_μ	1.72	1.75
ν_ℓ	0.0076	0.0075
ℓ	0.074	0.073
q	0.154	0.152
γ	3.01	3.00
W^-	1.287	1.281
W^+	0.098	0.096
Z	0.418	0.416
g	0.0192	0.0187
h	0.0032	0.0031
Total	77.04	100.37

Table B.3: Fraction of the momentum carried by each parton at $Q = 3$ TeV, computed using NIntegrate and the rectangles method. Here the muon is the valence lepton.

B.1.3 Use in MonteCarlo generators

At the moment there is no implementation of LePDFs into MonteCarlo generators, such as MadGraph5_aMC, due to the added difficulty of having polarized PDFs. Work on preparing such an implementation is in progress.

B.2 DGLAP evolution code

B.2.1 The Runge-Kutta algorithm

Given the differential equation $y'(t) = F(t, y)$ we can solve it numerically with a 4^{th}-order Runge-Kutta algorithm as follows:

$$\begin{aligned} k_1(t) &= dtF(t, y(t)) \\ k_2(t) &= dtF(t + \frac{dt}{2}, y(t) + \frac{k_1(t)}{2}) \\ k_3(t) &= dtF(t + \frac{dt}{2}, y(t) + \frac{k_2(t)}{2}) \\ k_4(t) &= dtF(t + dt, y(t) + k_3(t)) \\ y(t + dt) &= y(t) + \frac{k_1(t)}{6} + \frac{k_2(t)}{3} + \frac{k_3(t)}{3} + \frac{k_4(t)}{6} + \mathcal{O}(dt^5) \ . \end{aligned} \tag{B.3}$$

This means that starting with the initial condition $y(t_0)$ we can obtain the solution at any t through the proper number of steps in dt.
In the code we solve the DGLAP equations

$$\frac{df_B(x,t)}{dt} = P_B^v(t)\, f_B(x,t) + \sum_{A,C} \frac{\alpha_{ABC}}{2\pi} \widetilde{P}_{BA}^C(t) \otimes f_A + \frac{v^2}{16\pi^2 m_0^2 e^t} \sum_{A,C} \widetilde{U}_{BA}^C(t) \otimes f_A(t) \ , \tag{B.4}$$

where the indices A, B, C label the N partons we consider and m_0 is the valence lepton mass (electron or muon). After the discretization of the x-space, we obtain a set of $N \times N_x$ ordinary differential equations for the variables $f_{Bj}(t) \equiv f_B(x_j, t)$. The discretized equations have the following form:

$$\begin{aligned} &\frac{df_{Bj}(t)}{dt} = P_B^v(t) f_{Bj}(t) \\ &+ (\log(1 - x_j) - X_j) \sum_{A,C} \left[\frac{\alpha_{ABC}(t)}{2\pi} \widetilde{D}_{BA}^C(1) + \frac{v^2}{16\pi^2 m_0^2 e^t} \widetilde{V}_{BA}^C(1) \right] f_{Aj}(t) \\ &+ \sum_{k=j+1}^{N_x - 1} \frac{\delta x_k}{x_k} \sum_{A,C} \left[\frac{\alpha_{ABC}(t)}{2\pi} \widetilde{P}_{BA}^C \left(\frac{x_j}{x_k} \right) + \frac{v^2}{16\pi^2 m_0^2 e^t} \widetilde{U}_{BA}^C(t) \left(\frac{x_j}{x_k} \right) \right] f_{Ak}(t) \ , \end{aligned} \tag{B.5}$$

where D and V are obtained removing the factor $1 - x$ at the denominator of the splitting functions divergent at $x \to 1$

$$\widetilde{P}_{BA}^C(x) = \frac{\widetilde{D}_{BA}^C(x)}{(1-x)_+} \ , \qquad \widetilde{U}_{BA}^C(x) = \frac{\widetilde{V}_{BA}^C(x)}{(1-x)_+} \ , \tag{B.6}$$

and X_j is given by

$$X_j \equiv x_j \sum_{k=j+1}^{N_x-1} \frac{\delta x_k}{x_k^2} \frac{1}{1-\frac{x_j}{x_k}} \ . \tag{B.7}$$

The first two lines, which we call j-terms, come from the virtual corrections and from the definition of the plus distribution, Eq. (2.65). In particular, X_j comes from the discretization of the $-f(1)$ part. The last line of Eq. (B.5), which we call k-terms, contains instead the contribution of all the higher grid points. The number of equations is then reduced using momentum conservation:

$$\sum_A \int_0^1 dx\, x f_A(x,t) = 1 \quad \Longrightarrow \quad \sum_A \sum_{j=0}^{N_x-1} \delta x_j x_j f_{Aj}(t) = 1 \quad \forall t, \tag{B.8}$$

In the first phase of the evolution, since the initial conditions on PDFs are given by (for concreteness we consider the muon as the valence lepton)

$$f_\mu(0,x_j) = \delta(1-x_j) = \frac{1}{\delta x_{N_x-1}} \delta_{jN_x-1} \ , \qquad f_{i\neq\mu}(0,x) = 0 \ , \tag{B.9}$$

only $f_{\mu j}$ will be nonzero for $j = N_x - 1$ (i.e. for $x = 1$) throughout the evolution. Then we fix

$$f_{iN_x-1}(t) = \begin{cases} \frac{L(t)}{\delta x_{N_x-1}} & i = \mu \\ 0 & i \neq \mu \end{cases} \ , \tag{B.10}$$

reducing by N the number of variables and solving the remaining equations. The factor $L(t)$ is computed using Eq. (B.8):

$$L(t) = 1 - \sum_A \sum_{j=0}^{N_x-2} \delta x_j x_j f_{Aj}(t) \ . \tag{B.11}$$

For the second phase, the computation of $L(t)$ is analogous, but now both left- and right-handed muon PDFs are nonzero for $x = 1$, so we fix $f_{\mu_{L,R}N_x-1} = L(t)/2\delta x_{N_x-1}$. The Runge-Kutta coefficients are then computed for all the $N \times (N_x - 1)$ variables $f_{B,j}$ using Eq. (B.3), with the right hand side of Eq. (B.5) as the function F. This is done with three different functions (see Section B.2.2 for details): **Rj** and **Rjuc** calculate the j terms for massless and ultra-collinear contributions respectively and **RK** computes the k terms. The coefficients are collected in four $(N_t - 1) \times N_x N$ matrices, each row corresponding to a given step of the algorithm. For each row, the first N_x entries correspond to the first parton and so on until the last one.

B.2.2 File list

The code for the computation of LePDFs consists of the following files:

- **Main.cpp**: it is the file to be run, containing the calculations.

- **Matrix_alloc.cpp**: to allocate and free $n \times m$ matrices. When allocated, all the entries of the matrix are set to zero.

- **Couplings_RG.cpp**: it contains the one-loop running coupling of α_γ, α_1 and α_2. α_s instead is obtained through a linear interpolation starting from a matrix with the scale t in the first column and the corresponding value of the coupling in the second one. The file ends with functions calculating the running of other couplings starting from α_1, α_2 and α_s.

- **Cuts.cpp**: it contains the function to impose the cut $z_{\rm MAX}$ [3] and the definition of the $\theta-$function, which is used to insert the mass thresholds.

- **EVA.cpp**: here we write the formulas for the PDFs of W^- and Z in Effective Vector Approximation, which are used at $t = t_0$ to match between the two phases.

- **Prop_corr.cpp**: it contains the mass corrections to the splitting functions coming from the propagators, including the one for the mixed PDFs.

- **Massless_splitting.cpp** and **Uc_splitting.cpp**: they collect all the splitting functions.

- **QED_QCD.cpp**: it contains the functions to implement the Runge-Kutta algorithm for the first phase of the evolution (the formulas for the coefficients of the algorithm, the implementation of the step and the imposition of momentum conservation).

- **Massless_DGLAP.cpp**: it contains the recurring massless splittings contributing to the DGLAP equations.

- **Massless_eqs.cpp**: it contains the expressions for the k-term massless contributions to the evolution coefficients for the SM degrees of freedom.

- **Uc_eqs.cpp**: same as the one above, but for ultra-collinear contributions.

- **RK_sum.cpp**: here is reported the function RK, which is used to update the matrices of the evolution coefficients adding both the massless and ultra-collinear k contributions (see Section B.2.3 for its usage).

- **Massless_virt.cpp** and **Uc_virtual.cpp**: they contain the contributions to the virtual coefficients P_B^v from massless and ultra-collinear terms respectively.

[3] In the code we use the DGLAP equations with the splitting functions computed in x/z and the PDFs in z, while is the opposite in the discussion in Chapter 3. In this way the upper bound $z_{\rm MAX}$ becomes a lower bound, which is the one implemented in the code.

- **RK_virtual.cpp** and **RK_virtual_uc.cpp**: as in "RK-sum.cpp", here are reported the functions to update the matrices with the evolution coefficients adding the j-terms, massless and ultra-collinear respectively. The former contains also the imposition of momentum conservation.

- **Writing.cpp**: it contains the functions used to write the results in LHAPDF format, both for the particle and the antiparticle.

B.2.3 Structure of "Main.cpp"

"Main.cpp" is the actual code to be run. The structure of the file is as follows.

- In order to be used by all the files in the code, we declare as global variables all the constants we need: charges, group factors, masses, energy scales, beta function coefficients, initial conditions for running couplings and discretization constants such as the number of points in t and x. The constants depending on the choice of the valence lepton and of the flavor scheme are set through functions.

- We allocate the matrices containing the PDFs, for both phases, with the rows corresponding to the energy scale t and the columns to the point of the x-grid. For QED+QCD the first row contains the initial conditions at $t = 0$ and in the last one are reported the PDFs at $t = t_0$. We then use the last row to generate the initial conditions for the second phase. We then allocate the matrices for the evolution coefficients.

- The output files are opened with name "LePDF_ℓ_nFS_0000.dat" (ℓ = e, mu is the valence lepton and $n = 5, 6$ is the flavor scheme). The code compiles the name automatically depending on the choice of the valence lepton and of the flavor scheme.

- α_s is imported from the file "alphas_NNLO.dat" and interpolated.

- The grid in x is generated through Eq. (B.1)[4] and the grid spacings are computed.

- We perform the first phase of the evolution, for QED+QCD, with three for-cycles: the first one spans the scale t through $i = 0, \ldots, N_{t_0} - 1$ and for each i we compute the $(j + nN_x)^{\text{th}}$ entries of the matrices ($j = 0, \ldots, N_x - 2$ and n runs from zero to the number of partons) with the functions RKj0, and RK0 (no ultra-collinear contributions in this phase). The latter, giving the k terms, is summed over k with the last cycle (for $k > j$). The PDFs at the scale $i + 1$ are then computed summing the coefficients according to Eq. (B.3). We do not consider $j = N_x - 1$, since at $x = 1$ we use momentum conservation, which is imposed through the function $Lt0$.

[4]We use a formula to generate the grid, but it can also be imported from a file.

- After the first phase we match the PDFs of QED+QCD to the full set of SM variables of the second one, including the EVA, and we repeat the three for-cycles to perform the Runge-Kutta.

- The PDFs are saved in LHAPDF format. The code generates two files, one with the PDFs for the lepton (electron or muon) and one with the PDFs for the antiparticle, obtained through CP conjugation. Notice that the output is different for the two flavor schemes, since in the 5FS the top is absent and we do not report it.

B.2.4 The choice of the parameters

Most of the parameters used in the code are fixed and must be left unchanged. Here we list the ones that can be modified.

- Choice of the valence lepton, through the integer variable **lepton**: 0 corresponds to the electron, any other value to the muon. The code is exactly the same, with a different value of the valence mass m_0 (set automatically by the function "leptonmass"), since the equations are the same. We use the same notation for both cases, labelling the valence lepton as the muon: then, when we insert the results in the output files, we do it accordingly to what the valence lepton actually is.[5]

- Choice of the flavor scheme, through the integer variable **FS**: 5 means 5FS (without the top quark), while any other integer corresponds to the 6FS. Again the code is the same and the 5FS is obtained setting the top threshold **tt** to a value above the maximum t reached during the evolution: this is done by the function "ttchoice".

- α_s: the strong coupling is loaded from a file, which can be changed if a different order approximation is needed (one can even insert an analytic formula, without using a file with points, but in this case the code must be modified accordingly). In case of modifications in the loaded file, also the variables **Na** and **dta**, corresponding to the number of points in the file and their spacing in t, should be modified.

- QCD starts contributing at **tQCD**. In our implementation it corresponds to 0.7 GeV, but it can be changed.

- Grid in x: the discretization is arbitrary and it can be chosen by changing the formula which generates the grid (function **xgrid**) or loading it from a file. The number of points **Nx** must be changed accordingly.

- Evolution steps: the number of steps can be changed modifying the variables **Nt0** and **Nt**. This is done through the functions "Nt0choice" and "Ntchoice".

[5]For instance, fml is written in the column corresponding to e_L if lepton = 0 and in the one corresponding to μ_L otherwise.

- Finally one can change what is written in the output files: one can print the results only for a subset of values of (x,t) and also change the value of t at which data start to be saved (this is done through the variable **twrite**, we start from 10 GeV, safely above the non-perturbative regime of QCD). By default, we save the PDFs every 6 values of t and every 5 values of x, with the exception of the last 100, which are all saved. These parameters can be modified through the variables **itSteps**, **ixStep** and **NixLast** respectively.

Appendix C

Partonic and total cross sections

In this Appendix we report the formulas we used to convolute partonic cross sections with PDFs. We also report two examples of calculations of partonic cross sections.

C.1 Convolution with PDFs

For the production of two final state objects $X_{3,4}$, assuming that the energy of the hard-scattering is much larger than the transverse momentum of the initial state collinear radiation and the masses of all objects, the triple differential cross section is given in terms of a convolution of the partonic cross section $d\hat{\sigma}/d\hat{t}$ with the initial state PDFs:

$$\frac{d^3\sigma}{dy_3 dy_4 dp_T} = \sum_{i,j} f_i(x_1) f_j(x_2) \left(\frac{2p_T\hat{s}}{s_0}\right) \frac{d\hat{\sigma}_{ij}}{d\hat{t}}(\hat{s},\hat{t}) \ , \tag{C.1}$$

where s_0 is the collider center-of-mass energy squared, $\hat{s}$ and $\hat{t}$ are the partonic Mandelstam variables and $\hat{\sigma}_{ij}$ is the cross section for the partonic process $i+j \to X_3X_4$. $y_{3,4}$ are the rapidities of the two outgoing particles, defined as

$$y = \frac{1}{2}\log\left(\frac{E+p_z}{E-p_z}\right), \tag{C.2}$$

where z is the direction of the beam. A more geometrical quantity is the pseudo-rapidity η, directly related to the scattering angle θ:

$$\eta = \frac{1}{2}\log\left(\frac{|\vec{p}|+p_z}{|\vec{p}|-p_z}\right) = -\log\left[\tan\left(\frac{\theta}{2}\right)\right]. \tag{C.3}$$

The two quantities, for a particle of mass m, are related as follows:

$$y = \log\left(\frac{\sqrt{m^2+p_T^2\cosh^2\eta}+p_T\sinh\eta}{\sqrt{m^2+p_T^2}}\right), \tag{C.4}$$

that simply reduces to $y=\eta$ for massless particles.

All the kinematical variables can be expressed in terms of the two rapidities $y_{3,4}$ of the final state particles and their p_T, that is the same for both by momentum conservation:

$$\begin{aligned} y &\equiv \frac{y_3 - y_4}{2} \ , \qquad Y \equiv \frac{y_3 + y_4}{2} \ , \\ \hat{s} &= x_1 x_2 s_0 = 4p_T^2 \cosh^2 y \ , \qquad \hat{t} = -2p_T^2 e^{-y} \cosh y \ , \\ x_1 &= \frac{2p_T \cosh y}{\sqrt{s_0}} e^{Y} \ , \qquad x_2 = \frac{2p_T \cosh y}{\sqrt{s_0}} e^{-Y} \ . \end{aligned} \tag{C.5}$$

Being $x_{1,2} \leq 1$, the kinematic constraints on p_T, y_3 and y_4 are

$$p_T \leq \frac{\sqrt{s_0}}{2} \frac{e^{\pm Y}}{\cosh y}. \tag{C.6}$$

Fixing y_3, the two functions at the RHS of Eq. (C.6) intersect at $(y_4, p_T) = (-y_3, \sqrt{s_0}/2 \cosh y_3)$. Then after integration on y_4 the following region is kinematically forbidden $\forall (y_3, p_T)$:

$$p_T > \frac{\sqrt{s_0}}{2 \cosh y_3}. \tag{C.7}$$

The analogous formula to Eq. (C.1) in terms of the invariant mass of the products, $m = \sqrt{\hat{s}}$, is

$$\frac{d^3\sigma}{dy_3 dy_4 dm} = \sum_{i,j} f_i(x_1) f_j(x_2) \frac{m^3}{2s} \frac{1}{\cosh^2 y} \frac{d\hat{\sigma}_{ij}}{d\hat{t}}(\hat{s}, \hat{t}) \ , \tag{C.8}$$

In absence of divergences at the parton level, one can directly integrate in $\hat{t}$ and work with the total cross sections. The convolution of PDFs in this case becomes simply

$$\sigma(s_0) = \sum_{i,j} \int_0^1 dx_1 \int_0^1 dx_2 \, f_i\left(x_1, \sqrt{\hat{s}}/2\right) f_j\left(x_2, \sqrt{\hat{s}}/2\right) \hat{\sigma}_{ij}(\hat{s}), \tag{C.9}$$

where $\hat{s} = x_1 x_2 s_0$. Instead of directly use PDFs, one can first compute parton luminosities, defined in Eq. (3.21), and then perform the convolution with the partonic cross section. The formula for the total cross section becomes in this case

$$\sigma(s_0) = \sum_{i,j} \int_0^{\sqrt{s_0}} dm \frac{2m}{s_0} \mathcal{L}_{ij}(m, s_0) \hat{\sigma}_{ij}(m^2). \tag{C.10}$$

C.2 Partonic cross sections

We derived analytic expressions for the total polarized partonic cross sections (not averaged over initial spins) for all the $2 \to 2$ processes considered in Chapters 3 and 4. As an example, we give here the result for $\mu_L^+ \mu_L^- \to \bar{q}_L q_L$ in the limit of vanishing fermion masses for the case where the new physics effect is mediated by a Z', a S_3 leptoquark, as well as a contact

interaction $C_{\mu_L\mu_L q_L q_L}$ in Eq. (4.8):

$$\sigma(\mu_L^+\mu_L^- \to \bar{q}_L q_L) = \frac{3}{16\pi s^2}\left[\frac{4s^3}{3}\left|\frac{Q_q Q_\mu}{s} + \frac{g_q^Z g_\mu^Z}{s - m_Z^2 + i\Gamma_Z m_Z} + \frac{g_{q_L}^{Z'} g_{\mu_L}^{Z'}}{s - M_{Z'}^2 + i\Gamma_{Z'} M_{Z'}} + C_{\mu_L\mu_L q_L q_L}\right|^2\right.$$
$$- 2\,|\lambda_{q\mu}|^2\,\mathrm{Re}\left[\left(\frac{Q_q Q_\mu}{s} + \frac{g_q^Z g_\mu^Z}{s - m_Z^2 + i\Gamma_Z m_Z}\right)\left(2M_{S_3}^2 s - s^2 + 2M_{S_3}^4 \log\left(\frac{M_{S_3}^2}{M_{S_3}^2 + s}\right)\right)\right]$$
$$\left. + |\lambda_{q\mu}|^4\left(\frac{s(2M_{S_3}^2 + s)}{M_{S_3}^2 + s} + 2M_{S_3}^2 \log\left(\frac{M_{S_3}^2}{M_{S_3}^2 + s}\right)\right)\right]\ , \tag{C.11}$$

where the equation above can be used directly for the up quarks with the coupling convention of Eq. (4.19), while for the down quarks one should multiply the leptoquark coupling by a factor of $\sqrt{2}$ (see Eq. (4.20)). The cross section for the vector leptoquark is:

$$\sigma(\mu_L^+\mu_L^- \to \bar{q}_L q_L^-) = \frac{3}{16\pi s^2}\left[\frac{4s^3}{3}\left|\frac{Q_q Q_\mu}{s} + \frac{g_q^Z g_q^\mu}{s - m_Z^2 + i\Gamma_Z m_Z}\right|^2\right.$$
$$+ 4|\lambda_{q\mu}|^2\mathrm{Re}\left[\left(\frac{Q_q Q_\mu}{s} + \frac{g_q^Z g_q^\mu}{s - m_Z^2 + i\Gamma_Z m_Z}\right)\left(2M_{U_1}^2 s + 3s^2 + 2(M_{U_1}^2 + s)^2 \log\left(\frac{M_{U_1}^2}{M_{U_1}^2 + s}\right)\right)\right]$$
$$\left. + 4|\lambda_{q\mu}|^4\left(s(2 + \frac{s}{M_{U_1}^2}) + 2(M_{U_1}^2 + s)\log\left(\frac{M_{U_1}^2}{M_{U_1}^2 + s}\right)\right)\right]\ . \tag{C.12}$$

Appendix D

Collider analysis

In this Appendix we collect the details of the analysis at future colliders described in Chapter 4. We describe the statistical procedure used, our assumptions on the detectors and the recast of signatures at hadron colliders.

D.1 Statistical procedure

To derive the expected exclusion or discovery reach we construct our test statistic as $-2\log L = -2\sum_{i\in\text{bins}}\log L_i$, where

$$\begin{aligned} &\text{if } N_i^{\text{obs}} \geq 100 \ : \qquad -2\log L_i = \frac{(N_i - N_i^{\text{obs}})^2}{N_i + \epsilon^2 N_i^2} \ , \\ &\text{if } N_i^{\text{obs}} < 100 \ : \qquad -2\log L_i = -2\log \frac{N_i^{N_i^{\text{obs}}} e^{-N_i}}{N_i^{\text{obs}}!} \ , \end{aligned} \tag{D.1}$$

where N_i^{obs} (N_i) is the observed (expected) number of events in each bin and ϵ is the relative systematic uncertainty. We assume that our test statistic follows a χ^2 distribution. In case of exclusion reach the observed number of events is derived assuming the SM, while the expected one is expressed in the new physics model. For the discovery reach, the expected number of events is given assuming the SM, while the observed one is derived assuming new physics.

For the systematic uncertainty we assume an uncorrelated value of $\epsilon = 2\%$. This is increased to 10% in the case of $\mu q \to \mu q$ process, due to our estimation of QCD uncertainties in quark PDFs inside the muon. The 2% experimental systematic uncertainty is rather conservative according to some literature. For instance a value of 1% is taken in [64], while Refs. [113, 393] assume a systematic uncertainty of only 0.1%.

D.2 Detector performance

A detailed study of the FCC-hh detector system has been collected in the design report [5], from which we take the expected performances relevant for the processes considered in

Chapter 4. Specifically, for the energy resolution of the hadronic calorimeter we take the baseline performance of the reference detector (c.f. Table 7.3):

$$\frac{\sigma_E}{E} = \frac{50\%}{\sqrt{E[\mathrm{GeV}]}} \oplus 3\% \,, \tag{D.2}$$

where $\oplus$ means the two terms are added in quadrature. For the muon p_T resolution we take the combined resolution from the muon system and the tracker, assuming 25 μm position resolution (c.f. Figure 7.21(a) of Ref. [5]). This is $\approx 2\%$ at 1 TeV and $\approx 5\%$ at 10 TeV.

For all MuCs considered, we assume that the hadronic calorimeter and muon system performances are the same as for the FCC-hh. However, when relevant, we limit the maximum rapidity to $|y|_{\max} = 2$, due to the rapid degradation of tracking efficiency closer to the beamline [100]. Our tracking and hadronic calorimeter resolutions are conservative with respect to the ones required for the CLIC detector [394] in the corresponding energy range.

The LHC performance specifications are detailed in the CMS paper [191]. The jet and muon triggering, identification, and reconstruction efficiencies are assumed to be 100% in our analyses for FCC-hh and MuC.

D.3 (HL-)LHC and FCC-hh analyses

$pp \to \mu^+\mu^-$

The analysis of the di-muon signatures at the hadron colliders is based on the recent CMS search [211]. For each benchmark model, we calculate the leading-order Drell-Yan cross section analytically on parton level which is then numerically convoluted with the `NNPDF30_nnlo_as_0118` PDF set [395] using Mathematica. The CMS collaboration reported the SM expected number of DY and other background events in the binned $m_{\mu\mu}$ distribution. Their DY prediction is calculated at NNLO QCD and NLO EW precision.

The present observed 95% CL limits on all benchmark models come from assuming the number of expected DY events in each bin reported by the CMS collaboration is rescaled by the ratio of leading-order BSM and SM cross sections [171]. The systematic uncertainty on the number of DY events is as reported by the CMS collaboration. The statistical analysis takes into account the number of SM+BSM DY events, as well as events coming from non-DY backgrounds. We note that neglecting the subleading contribution of non-DY backgrounds has a negligible effect on the derived bounds.

In order to obtain the projections for the HL-LHC and the FCC-hh, we translated the $m_{\mu\mu}$ distribution into $\tau = m^2_{\mu\mu}/s_0$ distribution and rescaled the CMS prediction by the ratio

$$\sigma_i(s) = \sigma_i^{\mathrm{SM\,CMS}}(s_0) \frac{\sigma_i^{\mathrm{SM\,LO}}(s)}{\sigma_i^{\mathrm{SM\,LO}}(s_0)} \frac{L}{L_0} \,, \tag{D.3}$$

where the index i labels the bin, $s_{(0)}$ is the future (present) center-of-mass energy and $L_{(0)}$ is the future (present) luminosity. The validity of such scaling for DY cross section was checked at LO using `MadGraph5` [396]. The non-DY backgrounds, however, do not scale in the same way. While $t\bar{t}$ and VV backgrounds remain subleading at the FCC-hh (directly checked by `MadGraph5`), the tW background becomes relevant (less than an order of magnitude times the SM DY). However, the presence of jets and missing energy in the final state allows for designing cuts that can easily suppress this background. We therefore neglect any non-DY backgrounds in the derivation of the future projections.

In all non-resonant searches, as well as resonant search at the LHC and the HL-LHC, the CMS binning of the τ distribution was used. On the other hand, similarly to the MuC searches, the resonant search at FCC-hh uses bins constructed following the hadronic calorimeter resolution described in Eq. (D.2). For HL-LHC and FCC-hh we assign 2% systematic uncertainty.

$pp \to 4\mu$

In the case of multilepton signature for $L_\mu - L_\tau$ model, we derive the exclusion limits and discovery reach by calculating the significance of the signal as

$$Z(M_{Z'}, g_{Z'}) = \frac{s(M_{Z'}, g_{Z'})}{\sqrt{b}} = \sqrt{L}\, \frac{g_{Z'}^2 \sigma_{Z'}(M_{Z'}, 1)}{\sigma_{\rm SM}}\,. \tag{D.4}$$

where both cross sections were calculated using `MadGraph5` applying the following set of standard cuts: $p_T^\mu > 20$ GeV (leading muon), $p_T^\mu > 10$ GeV (subleading muon), $p_T^\mu > 5$ GeV (other muons), $|\eta_\mu| < 2.7$ and $\Delta R_{\mu\mu} > 0.05$. Additionally, in order to suppress the SM background, we applied the cut $m_{\mu^+\mu^-} > \min(800\ \text{GeV}, 0.8 M_{Z'})$ on any oppositely-charged muon pair.

Appendix E

Low-energy observables

In this Appendix we collect all the low-energy observables we used for the global analysis described in Chapter 5. We also show the direct constraints from LHC on Wilson coefficient of the top quark effective operators we considered. In Table E.3 we report the list of LEFT operators.

E.1 $B \to K^{(*)}\nu\bar{\nu}$ and $K \to \pi\nu\bar{\nu}$

The Standard Model prediction and SMEFT parametrization of dineutrino modes $B \to K^{(*)}\nu\bar{\nu}$ are deeply discussed in Ref. [397]. The effective Hamiltonian for these processes reads

$$\begin{aligned}\mathcal{H}_{eff} &= -\frac{4G_F}{\sqrt{2}}\frac{\alpha}{4\pi}\sum_{i,j} V_{ti}^* V_{tj}\left(C_L^{ij\alpha\beta}O_L^{ij\alpha\beta} + C_R^{ij\alpha\beta}O_R^{ij\alpha\beta}\right) \\ &= -\sum_{i,j}\left(\frac{1}{2}L^{V,LL}_{\substack{\nu d\\ \alpha\beta ij}}O_L^{ij\alpha\beta} + \frac{1}{2}L^{V,LR}_{\substack{\nu d\\ \alpha\beta ij}}O_R^{ij\alpha\beta}\right)\,,\end{aligned} \tag{E.1}$$

where

$$O_L^{ij\alpha\beta} = (\bar{d}_i\gamma_\mu P_L d_j)(\bar{\nu}_\alpha\gamma^\mu(1-\gamma_5)\nu_\beta)\,, \quad O_R^{ij\alpha\beta} = (\bar{d}_i\gamma_\mu P_R d_j)(\bar{\nu}_\alpha\gamma^\mu(1-\gamma_5)\nu_\beta)\,. \tag{E.2}$$

and $L^{V,LL(R)}_{\nu d}$ are LEFT coefficients given in Table E.3. The ratios

$$R_K^\nu = \frac{\mathcal{B}(B\to K\nu\bar{\nu})}{\mathcal{B}(B\to K\nu\bar{\nu})_{\rm SM}}\,, \quad R_{K^*}^\nu = \frac{\mathcal{B}(B\to K^*\nu\bar{\nu})}{\mathcal{B}(B\to K^*\nu\bar{\nu})_{\rm SM}}\,, \tag{E.3}$$

can be expressed in terms of two parameters $\epsilon > 0$ and $\eta \in [-1/2, 1/2]$ as:

$$\begin{aligned}R_K^\nu &= \sum_{\alpha\beta}\frac{1}{3}(1-2\eta_{\alpha,\beta})\epsilon_{\alpha\beta}^2\,, \quad R_{K^*}^\nu = \sum_{\alpha\beta}\frac{1}{3}(1+\kappa_\eta\eta_{\alpha,\beta})\epsilon_{\alpha\beta}^2, \\ \epsilon_{\alpha\beta} &= \frac{\sqrt{|C^{sb}_{L,\rm SM}\delta_{\alpha\beta} + C_L^{sb\alpha\beta}|^2 + |C_R^{sb\alpha\beta}|^2}}{|C^{sb}_{L,\rm SM}|}, \\ \eta_{\alpha\beta} &= -\frac{{\rm Re}\left[\left(C^{sb}_{L,\rm SM}\delta_{\alpha\beta} + C_L^{sb\alpha\beta}\right)\left(C_R^{sb\alpha\beta}\right)^*\right]}{|C^{sb}_{L,\rm SM}\delta_{\alpha\beta} + C_L^{sb\alpha\beta}|^2 + |C_R^{sb\alpha\beta}|^2}\,,\end{aligned} \tag{E.4}$$

where the parameter κ_η depends on form factors. There are not isospin asymmetries between the charged and neutral meson decays to neutrinos, so that the only difference between $\mathcal{B}(B^\pm \to K^{\pm(*)}\nu\bar{\nu})$ and $\mathcal{B}(B^0 \to K^{0(*)}\nu\bar{\nu})$ is in the lifetime $\tau_{B^\pm}$ and τ_{B^0}, that cancel in the ratio. Remarkably, in our setup the coefficient C_R is zero at the level of dimension-six SMEFT contributions, so that $\eta_{\alpha\beta} = 0$ and then the theoretical predictions for R^ν_K and $R^\nu_{K^*}$ coincide.

For kaons, we use directly the branching ratios. Since $C_R = 0$ in our setup, we can just write them in terms of the SM values rescaling the C_L coefficients

$$\begin{aligned}\mathcal{B}(K^+ \to \pi^+\nu\bar{\nu})_{th} = \mathcal{B}(K^+ \to \pi^+\nu_e\bar{\nu}_e)_{\rm SM} \sum_{\alpha,\beta=1,2} \left|\delta_{\alpha\beta} + \frac{C_L^{ds\alpha\beta}}{C_{L,\rm SM}^{ds11}}\right|^2 \\ + \mathcal{B}(K^+ \to \pi^+\nu_\tau\bar{\nu}_\tau)_{\rm SM} \left[\left|1 + \frac{C_L^{ds33}}{C_{L,\rm SM}^{ds33}}\right|^2 + \sum_{\alpha=1,2}\left(\left|\frac{C_L^{ds\alpha3}}{C_{L,\rm SM}^{ds33}}\right|^2 + \left|\frac{C_L^{ds3\alpha}}{C_{L,\rm SM}^{ds33}}\right|^2\right)\right],\end{aligned} \tag{E.5}$$

$$\begin{aligned}\mathcal{B}(K_L \to \pi^0\nu\bar{\nu})_{th} = \frac{1}{3}\mathcal{B}(K_L \to \pi^0\nu\bar{\nu})_{\rm SM}\left[\sum_{\alpha,\beta=1,2}\left(\delta_{\alpha\beta} + \frac{\mathrm{Im}[N_{ds}^{-1}C_L^{ds\alpha\beta}]}{\mathrm{Im}[N_{ds}^{-1}C_{L,\rm SM}^{ds11}]}\right)^2\right. \\ \left. + \left(1 + \frac{\mathrm{Im}[N_{ds}^{-1}C_L^{ds33}]}{\mathrm{Im}[N_{ds}^{-1}C_{L,\rm SM}^{ds33}]}\right) + \sum_{\alpha=1,2}\left(\left(\frac{\mathrm{Im}[N_{ds}^{-1}C_L^{ds\alpha3}]}{\mathrm{Im}[N_{ds}^{-1}C_{L,\rm SM}^{ds33}]}\right) + \left(\frac{\mathrm{Im}[N_{ds}^{-1}C_L^{ds3\alpha}]}{\mathrm{Im}[N_{ds}^{-1}C_{L,\rm SM}^{ds33}]}\right)\right)\right],\end{aligned} \tag{E.6}$$

where we defined $N_{ds} = (\sqrt{2}G_F\alpha V_{td}^* V_{ts}/\pi)^{-1}$ and the SM values for the branching ratios and Wilson coefficients are

$$\begin{aligned}\mathcal{B}(K^+ \to \pi^+\nu_e\bar{\nu}_e)_{\rm SM} &= 3.06 \times 10^{-11}\,, \\ \mathcal{B}(K^+ \to \pi^+\nu_\tau\bar{\nu}_\tau)_{\rm SM} &= 2.52 \times 10^{-11}\,, \\ \mathcal{B}(K_L \to \pi^0\nu\bar{\nu})_{\rm SM} &= 3.4 \times 10^{-11}\,,\end{aligned} \tag{E.7}$$

$$C_{L,\rm SM}^{ds\alpha\beta} = -\frac{1}{s_W^2}\left(X_t + \frac{V_{cd}^* V_{cs}}{V_{td}^* V_{ts}} X_c^\alpha\right)\delta_{\alpha\beta}\,, \tag{E.8}$$

with $X_\tau = 1.481$, $X_c^e = X_c^\mu = 1.053 \times 10^{-3}$ and $X_c^t = 0.711 \times 10^{-3}$.

E.2 $B_s \to \ell_\alpha^- \ell_\beta^+$ and $K_{L,S} \to \ell_\alpha^- \ell_\beta^+$

The branching ratio for rare leptonic B decays is discussed, for example, in Ref. [398] and the same description holds also for kaons. In our framework, these processes are induced by the operators

$$O_9^{ij\alpha\beta} = (\bar{d}_i\gamma_\mu P_L d_j)(\bar{\ell}_\alpha\gamma^\mu\ell_\beta)\,, \quad O_{10}^{ij\alpha\beta} = (\bar{d}_i\gamma_\mu P_L d_j)(\bar{\ell}_\alpha\gamma^\mu\gamma_5\ell_\beta)\,, \tag{E.9}$$

appearing in the effective Hamiltonian

$$\mathcal{H}_{eff} = -\frac{4G_F}{\sqrt{2}}\frac{\alpha}{4\pi}\sum_{k=9,10} V_{ti}^* V_{tj} \mathcal{C}_k^{ij\alpha\beta} \mathcal{O}_k^{ij\alpha\beta}. \tag{E.10}$$

We do not take into account the other possible contributions: the operators $O_{9',10'}$, with $P_L \to P_R$, are identically zero in our setup and we do not consider the usual scalar and pseudoscalar operators O_S and O_P (see e.g. in Ref. [398]), since they are generated with negligible coefficients with respect to O_9 and O_{10}. The relation between these coefficients and the LEFT ones is

$$C_{9(10)}^{ij\alpha\beta} = \frac{\sqrt{2}\pi}{G_F \alpha V_{ti}^* V_{tj}} \left(L^{V,LR}_{\substack{de \\ ij\alpha\beta}} \pm L^{V,LL}_{\substack{ed \\ \alpha\beta ij}} \right) . \tag{E.11}$$

The branching ratio for the leptonic B_s decays is given by

$$\begin{aligned} \mathcal{B}(B_s \to \ell_\alpha^- \ell_\beta^+)_{th} = {} & \frac{\tau_{B_s}}{64\pi^3}\frac{\alpha^2 G_F^2}{m_{B_s}^3} f_{B_s}^2 |V_{tb}V_{ts}^*|^2 \lambda^{1/2}(m_{B_s}, m_\alpha, m_\beta) \times \\ & \times \Bigg[\left[m_{B_s}^2 - (m_\alpha + m_\beta)^2\right] \times \left| (C_{9,\mathrm{SM}}^{sb\alpha\beta} + C_9^{sb\alpha\beta})(m_\alpha - m_\beta) \right|^2 + \\ & + \left[m_{B_s}^2 - (m_\alpha - m_\beta)^2\right] \times \left| (C_{10,\mathrm{SM}}^{sb\alpha\beta} + C_{10}^{sb\alpha\beta})(m_\alpha + m_\beta) \right|^2 \Bigg] , \end{aligned} \tag{E.12}$$

where $\lambda(a,b,c) = [a^2 - (b-c)^2][a^2 - (b+c)^2]$. When comparing the theoretical prediction of B decays to untagged experimental data, the sizeable decay width differences in the $B_s^0 - \bar{B_s}^0$ system must be taken into account. This is done by using an effective lifetime. To a good approximation one has [399, 400]

$$\mathcal{B}(B_s \to \ell_\alpha^- \ell_\beta^+)_{\mathrm{eff}} \simeq \frac{1}{1-y_s} \mathcal{B}(B_s \to \ell_\alpha^- \ell_\beta^+)_{\mathrm{th}} , \tag{E.13}$$

with $y_s = \Delta\Gamma_{B_s}/(2\Gamma_{B_s}) = 0.064(4)$, according to the current PDG and HFLAV average [74]. Numerical values for couplings and parameters appearing in the formula can be found in Refs. [74, 401]. The expression in Eq. (E.12) can be applied to $B_d \to \ell_\alpha^- \ell_\beta^+$ with the obvious $s \to d$ replacement.

The leptonic kaon decays are instead given by

$$\begin{aligned} \mathcal{B}(K_{L(S)} \to \ell_\alpha^- \ell_\beta^+)_{th} = {} & \frac{\tau_{K_L}}{128\pi^3}\frac{\alpha^2 G_F^2}{m_{K_0}^3} f_K^2 |V_{td}V_{ts}^*|^2 \lambda^{1/2}(m_K, m_\alpha, m_\beta) \times \\ & \times \Bigg[\left[m_{K_0}^2 - (m_\alpha + m_\beta)^2\right] \times \left| \left(C_{9,\mathrm{SM}}^{ds\alpha\beta} \pm C_{9,\mathrm{SM}}^{sd\alpha\beta} + C_9^{ds\alpha\beta} \pm C_9^{sd\alpha\beta} \right) \right|^2 (m_\alpha - m_\beta)^2 + \\ & + \left[m_{K_0}^2 - (m_\alpha - m_\beta)^2\right] \times \left| \left(C_{10,\mathrm{SM}}^{ds\alpha\beta} \pm C_{10,\mathrm{SM}}^{sd\alpha\beta} + C_{10}^{ds\alpha\beta} \pm C_{10}^{sd\alpha\beta} \right) \right|^2 (m_\alpha + m_\beta)^2 \Bigg] . \end{aligned} \tag{E.14}$$

Notice that for kaons both ds and sd indices appear, since $K_{L,S}$ are linear combinations of K^0 and $\bar{K}^0$

$$|K_{L(S)}\rangle = \frac{|K^0\rangle \pm |\bar{K}^0\rangle}{\sqrt{2}}\,. \tag{E.15}$$

In all cases, as one can expect, for $\ell_\alpha = \ell_\beta = \ell$ the coefficient C_9 does not contribute.

E.3 $B \to K^{(*)}\ell^+\ell^-$

In Ref. [402], the leading contributions to the decay width of $B \to K^{(*)}\ell^+\ell^-$ are computed. Under some justified assumptions, the R_K and R_{K^*} ratios read

$$\begin{aligned} R_K([1.1,6]) \approx & 1.00 + 0.24\text{Re}[C_9 - C_{10}] + 0.24\text{Re}[C'_9 - C'_{10}] + 0.058\text{Re}[C_9^* C'_9 + \\ & + C_{10}^* C'_{10}] + 0.029\left(|C_9|^2 + |C'_9|^2 + |C_{10}|^2 + |C'_{10}|^2\right)\,, \end{aligned}$$

$$\begin{aligned} R_{K^*}([1.1,6]) \approx & 1.00 + 0.24\text{Re}[C_9 - C_{10}] - 0.18\text{Re}[C'_9] + 0.17\text{Re}[C'_{10}] - 0.042\text{Re}[C_9^* C'_9 + \\ & + C_{10}^* C'_{10}] + +0.029\left(|C_9|^2 + |C'_9|^2 + |C_{10}|^2 + |C'_{10}|^2\right)\,, \end{aligned}$$

where the operators and the Hamiltonian are defined as in Appendix E.9-E.10. The numerical coefficients are compatible with the ones computed, for example, in Refs. [232, 403, 404] and with our calculation of R_{K^*}, derived using expressions and form factors provided in Refs. [405, 406]. The primed coefficients C'_9 and C'_{10} are displayed for completeness, but they are anyway set to zero as they are not generated by the operators in Table 5.1.

E.4 $K_L \to \pi^0\ell^+\ell^-$

We consider again the Hamiltonian in Eq. (E.10) and we define $\tilde{C}_k^{ij\alpha\beta} = V_{ti}^* V_{tj} C_k^{ij\alpha\beta}$. Rearranging the formula given in Ref. [407] to fit our notation, we obtain for the branching ratio

$$\mathcal{B}(K_L \to \pi^0\ell^+\ell^-)_{th} = a_\ell\left[(\omega_{7V}^\ell)^2 + (\omega_{7A}^\ell)^2\right] + b_\ell\omega_{7V}^\ell + c_\ell, \tag{E.16}$$

where

$$\begin{aligned} \omega_{7V}^\ell &= \frac{1}{2\pi}\frac{1}{1.407\times10^{-4}}\left[P_0\text{Im}(V_{ts}^*V_{td}) + \text{Im}(C_{9,\text{SM}}^{sd\ell\ell} + C_9^{sd\ell\ell})\right], \\ \omega_{7A}^\ell &= \frac{1}{2\pi}\frac{1}{1.407\times10^{-4}}\text{Im}(C_{10,\text{SM}}^{sd\ell\ell} + C_{10}^{sd\ell\ell}). \end{aligned} \tag{E.17}$$

The numerical coefficients a, b and c are given by

$$\begin{aligned} a_e &= 4.62\times10^{-12}, & a_\mu &= 1.09\times10^{-12}, \\ b_e &= 13.56\times10^{-12}, & b_\mu &= 3.156\times10^{-12}, \\ c_e &= 20.88\times10^{-12}, & c_\mu &= 10.0384\times10^{-12}. \end{aligned} \tag{E.18}$$

E.5 $P \to M\ell_\alpha^-\ell_\beta^+$

We consider here the semileptonic decay of a meson $P = \{B, K_L, K^+\}$ into $M = \{K^{(*)}, \pi\}$ and two different leptons. The branching ratios for the decays are [178, 398]

$$\mathcal{B}(P \to M\ell_\alpha^-\ell_\beta^+)_{th} = \frac{1}{8G_F^2}\left(\alpha_V^+\left|L^{V,LR}_{\substack{de\\ij\alpha\beta}} + L^{V,LL}_{\substack{ed\\\alpha\beta ij}}\right|^2 + \alpha_V^-\left|L^{V,LR}_{\substack{de\\ij\alpha\beta}} - L^{V,LL}_{\substack{ed\\\alpha\beta ij}}\right|^2\right) . \tag{E.19}$$

Numerical values for the multiplicative coefficients are given in Table E.1. The indices ij correspond to the transition $q_j \to q_i\ell_\alpha^-\ell_\beta^+$ and for K_L it is understood the average $(ds + sd)/2$.

Process	α_V^+	α_V^-
$B \to Ke^+\mu^-$	8.2(6)	8.2(6)
$B \to Ke^+\tau^-$	5.3(2)	5.3(2)
$B \to K\mu^+\tau^-$	5.2(2)	5.2(2)
$B \to K^*e^+\mu^-$	2.8(5)	2.8(5)
$B \to K^*e^+\tau^-$	1.4(2)	1.4(2)
$B \to K^*\mu^+\tau^-$	1.5(2)	1.3(2)
$K^+ \to \pi^+e^+\mu^-$	0.596(4)	0.598(4)
$K_L \to \pi^0e^+\mu^-$	2.75(2)	2.76(2)

Table E.1: Values for the factors defined in Eq. (E.19), for all the possible final states. Details on their computation can be found in Ref. [178].

E.6 $B \to X_s\gamma$

The inclusive radiative B decays can be parametrized in terms of the operators

$$O_7 = \frac{e}{16\pi^2}m_b(\bar{s}\sigma_{\alpha\beta}P_{R(L)}b)F^{\alpha\beta}\,, \quad O_8 = \frac{g}{16\pi^2}m_b(\bar{s}\sigma_{\alpha\beta}P_{R(L)}T^a b)G_a^{\alpha\beta}\,, \tag{E.20}$$

and the effective Hamiltonian

$$\mathcal{H}_{eff} = -\frac{4G_F}{\sqrt{2}}V_{ts}^*V_{tb}\sum_i \mathcal{C}_i\mathcal{O}_i\,. \tag{E.21}$$

The branching ratio is given then by [408, 409]

$$\mathcal{B}(\bar{B} \to X_s\gamma)_{E_\gamma > 1.6\,\mathrm{GeV}} = 10^{-4} \times (3.36 \pm 0.23 - 8.22C_7 - 1.99C_8)\ , \tag{E.22}$$

where the coefficients are defined at the matching scale $\mu_0 = 160$ GeV [408]. In terms of LEFT coefficients, we have:

$$C_7 = \frac{N_{sb}^{-1} e}{m_b} \times L_{\underset{sb}{d\gamma}}\,, \qquad C_8 = \frac{N_{sb}^{-1} e^2}{g m_b} L_{\underset{sb}{dG}}\,, \\ N_{sb} = \frac{4G_F}{\sqrt{2}} \frac{\alpha_{em}}{4\pi} V_{ts}^* V_{tb}\,. \tag{E.23}$$

E.7 Charged lepton flavor violation

For charged lepton flavor violation processes we employ the expressions from Refs. [359, 364], after translating them to the LEFT basis. In the following we give the explicit expressions used in this work.

- $\ell_H \to \ell_L \gamma$

  We may take a reference renormalization scale $\mu = 2\,\text{GeV}$, where the LEFT is yet well defined. One has [359, 364, 410]

  $$\Gamma_{\ell\to\ell'\gamma} = \frac{m_\ell^3}{4\pi}[|L_{\underset{\ell'\ell}{e\gamma}}|^2 + |L_{\underset{\ell\ell'}{e\gamma}}|^2]\,. \tag{E.24}$$

  The (non-perturbative) effect of four-fermion operators involving tensor light-quark currents can be taken into account by making the following substitutions

  $$L_{\underset{\ell'\ell}{e\gamma}} \to L_{\underset{\ell'\ell}{e\gamma}} - e\left(c_3^{\ell'\ell} + \frac{c_8^{\ell'\ell}}{\sqrt{3}}\right) i\Pi_{VT}(0)\,, \tag{E.25}$$

  $$L_{\underset{\ell\ell'}{e\gamma}} \to L_{\underset{\ell\ell'}{e\gamma}} + e\left(c_3^{\ell\ell'} + \frac{c_8^{\ell\ell'}}{\sqrt{3}}\right) i\Pi_{VT}(0)\,, \tag{E.26}$$

  with

  $$c_3^{ij} = L^{T,RR}_{\underset{ij11}{eu}} - L^{T,RR}_{\underset{ij11}{ed}}\,, \tag{E.27}$$

  $$c_8^{ij} = \frac{1}{\sqrt{3}}\left[L^{T,RR}_{\underset{ij11}{eu}} + L^{T,RR}_{\underset{ij11}{ed}} - 2L^{T,RR}_{\underset{ij22}{ed}}\right]\,. \tag{E.28}$$

  As in Ref. [364] we take $i\Pi_{VT}(0) \approx 0.04\,\text{GeV}$.

- $\tau \to 3e$, $\tau \to 3\mu$, $\mu \to 3e$

  We use the analytic expressions given in Ref. [364], adapting them to the LEFT normalization of this work. Numerically we find, in GeV units,

  $$\begin{aligned}\mathcal{B}(\tau \to 3e) \approx\ & 1.6\times 10^8(|L^{S,RR}_{\underset{1113}{ee}}|^2 + |L^{V,LR}_{\underset{1113}{ee}}|^2 + |L^{V,LR}_{\underset{1311}{ee}}|^2) \\ & + 1.3\times 10^9(|L^{V,LL}_{\underset{1311}{ee}}|^2 + |L^{V,RR}_{\underset{1311}{ee}}|^2) + 2.1\times 10^9(|L_{\underset{31}{e\gamma}}|^2 + |L_{\underset{13}{e\gamma}}|^2) \\ & + [L_{\underset{31}{e\gamma}}(-4.5\times 10^8 L^{V,LL}_{\underset{1113}{ee}} - 1.1\times 10^8 L^{V,LR}_{\underset{1311}{ee}}) + c.c.] \\ & + [L^*_{\underset{13}{e\gamma}}(-4.5\times 10^8 L^{V,RR}_{\underset{1113}{ee}} - 1.1\times 10^8 L^{V,LR}_{\underset{1113}{ee}}) + c.c.]\,.\end{aligned} \tag{E.29}$$

The analytic expressions trivially generalize for $\tau \to 3\mu$, $\mu \to 3e$. Numerically one finds

$$\begin{aligned}\mathcal{B}(\tau \to 3\mu) \approx\ & 1.6 \times 10^8 (|L^{S,RR}_{ee\,1123}|^2 + |L^{V,LR}_{ee\,1123}|^2 + |L^{V,LR}_{ee\,2311}|^2) \\ & + 1.3 \times 10^9 (|L^{V,LL}_{ee\,2311}|^2 + |L^{V,RR}_{ee\,2311}|^2) + 4.4 \times 10^8 (|L_{e\gamma\,32}|^2 + |L_{e\gamma\,23}|^2) \\ & + [L_{e\gamma\,32}(-4.5 \times 10^8 L^{V,LL}_{ee\,1123} - 1.1 \times 10^8 L^{V,LR}_{ee\,2311}) + c.c.] \\ & + [L^*_{e\gamma\,23}(-4.5 \times 10^8 L^{V,RR}_{ee\,1123} - 1.1 \times 10^8 L^{V,LR}_{ee\,1123}) + c.c.]\,, \end{aligned} \tag{E.30}$$

and

$$\begin{aligned}\mathcal{B}(\mu \to 3e) \approx\ & 9.2 \times 10^8 (|L^{S,RR}_{ee\,1112}|^2 + |L^{V,LR}_{ee\,1112}|^2 + |L^{V,LR}_{ee\,1211}|^2) \\ & + 7.4 \times 10^9 (|L^{V,LL}_{ee\,1211}|^2 + |L^{V,RR}_{ee\,1211}|^2) + 1.9 \times 10^{12} (|L_{e\gamma\,21}|^2 + |L_{e\gamma\,12}|^2) \\ & + [L_{e\gamma\,21}(-4.2 \times 10^{10} L^{V,LL}_{ee\,1112} - 1.1 \times 10^{10} L^{V,LR}_{ee\,1211}) + c.c.] \\ & + [L^*_{e\gamma\,12}(-4.2 \times 10^{10} L^{V,RR}_{ee\,1112} - 1.1 \times 10^{10} L^{V,LR}_{ee\,1112}) + c.c.]\,, \end{aligned} \tag{E.31}$$

- $\tau \to e\bar{\mu}\mu$, $\tau \to \mu\bar{e}e$.

  Once again we adapt the analytic results as given in Ref. [364], finding

$$\begin{aligned}\mathcal{B}(\tau \to e\bar{\mu}\mu) \approx\ & 2.5 \times 10^9 (|L^{V,LL}_{ee\,1223}|^2 + |L^{V,RR}_{ee\,1223}|^2) \\ & + 1.6 \times 10^8 (|L^{V,LR}_{ee\,2213}|^2 + |L^{V,LR}_{ee\,1322}|^2) + 1.0 \times 10^8 (|L_{e\gamma\,31}|^2 + |L_{e\gamma\,13}|^2) \\ & - 2.1 \times 10^8 [L_{e\gamma\,31} L^{V,LL}_{ee\,1223} + c.c.] \\ & + [L^*_{e\gamma\,13}(-5.2 \times 10^7 L^{*V,LR}_{ee\,1322} - 2.6 \times 10^8 L^{V,RR}_{ee\,1223}) + c.c.]\,, \end{aligned} \tag{E.32}$$

  and

$$\begin{aligned}\mathcal{B}(\tau \to \mu\bar{e}e) \approx\ & 2.6 \times 10^9 (|L^{V,LL}_{ee\,1123}|^2 + |L^{V,RR}_{ee\,1123}|^2) \\ & + 1.6 \times 10^8 (|L^{V,LR}_{ee\,1123}|^2 + |L^{V,LR}_{ee\,2311}|^2) + 5.0 \times 10^8 (|L_{e\gamma\,32}|^2 + |L_{e\gamma\,23}|^2) \\ & - 2.2 \times 10^8 [L_{e\gamma\,32} L^{V,LL}_{ee\,1123} + c.c.] \\ & + [L^*_{e\gamma\,23}(-5.5 \times 10^7 L^{*V,LR}_{ee\,2311} - 2.8 \times 10^8 L^{V,RR}_{ee\,1123}) + c.c.]\,. \end{aligned} \tag{E.33}$$

- $\mu\mathrm{Au} \to e\mathrm{Au}$.

  We adapt the results of Ref. [359], neglecting the power-suppressed contributions from c and b quarks. In principle they are given at a $\mu = 1\,\mathrm{GeV}$, but within the theoretical uncertainties the same expressions can also be used at $\mu = 2\,\mathrm{GeV}$.[1] We have also

[1]The large QCD running of the scalar quark current is fully taken into account by simply taking as input $m_q(\mu = 2\,\mathrm{GeV})$ instead of $m_q(\mu = 1\,\mathrm{GeV})$.

checked that we agree with the adaptation given in Ref. [410]. The numerical result is rather large. For reference, the first quadratic coefficients are

$$\mathcal{B}(\mu\mathrm{Au}\to e\mathrm{Au}) \approx 1.1\times 10^{13}[(L^{S,RL}_{\substack{ed\\1211}})^2+(L^{S,RL}_{\substack{ed\\2111}})^2+(L^{S,RR}_{\substack{ed\\2111}})^2+(L^{S,RR}_{\substack{ed\\1211}})^2+(d\to u)] \tag{E.34}$$

- $\tau\to\ell\pi^0$

  We take the numerical result of Ref. [364]. Adapting it to the normalization of this work we have

$$\mathcal{B}(\tau\to\ell\pi^0)\approx B_1(\tau\to\ell\pi^0)+B_2(\tau\to\ell\pi^0)\,,$$

  with

$$\begin{aligned}\mathcal{B}_1(\tau\to\ell\pi^0) \approx\ & 1.3\times 10^8|L^{S,RL}_{\substack{ed\\\ell311}}-L^{S,RL}_{\substack{eu\\\ell311}}-L^{S,RR}_{\substack{ed\\\ell311}}+L^{S,RR}_{\substack{eu\\\ell311}}|^2\\ &+5.1\times 10^7|L^{V,LL}_{\substack{ed\\3\ell11}}-L^{V,LL}_{\substack{eu\\3\ell11}}-L^{V,LR}_{\substack{ed\\3\ell11}}+L^{V,LR}_{\substack{eu\\3\ell11}}|^2\,,\end{aligned} \tag{E.35}$$

  and $\mathcal{B}_2(\tau\to\ell\pi^0)$ can be obtained from the $B_1(\tau\to\ell\pi^0)$ expression by making the following substitutions

$$L^{V,LL}_{\substack{eq\\3\ell11}}\to L^{V,RR}_{\substack{eq\\3\ell11}}, L^{V,LR}_{\substack{eq\\3\ell11}}\to L^{V,LR}_{\substack{qe\\113\ell}}, L^{S,RR}_{\substack{eq\\\ell3qq}}\to L^{S,RR^*}_{\substack{eq\\3\ell qq}}, L^{S,RL}_{\substack{eq\\\ell3qq}}\to L^{S,RL^*}_{\substack{eq\\3\ell qq}}. \tag{E.36}$$

- $\tau\to\ell\pi^+\pi^-$

  Once again we use the numerical results from Ref. [364]. We find

$$\mathcal{B}(\tau\to\ell\pi\pi)=\mathcal{B}_1(\tau\to\ell\pi\pi)+\mathcal{B}_2(\tau\to\ell\pi\pi)\,.$$

$$\begin{aligned}\mathcal{B}_1(\tau\to\ell\pi\pi) \approx\ & 9.2\times 10^8|L^{T,RR}_{\substack{ed\\3\ell11}}-L^{T,RR}_{\substack{eu\\3\ell11}}|^2+4.6\times 10^8|L^{V,LL}_{\substack{ed\\3\ell11}}-L^{V,LL}_{\substack{eu\\3\ell11}}+L^{V,LR}_{\substack{ed\\3\ell11}}-L^{V,LR}_{\substack{eu\\3\ell11}}|^2\\ &+5.0\times 10^8|L_{\substack{e\gamma\\3\ell}}|^2+1.6\times 10^8|L^{S,RL}_{\substack{ed\\3\ell11}}+L^{S,RL}_{\substack{eu\\3\ell11}}+L^{S,RR}_{\substack{ed\\3\ell11}}+L^{S,RR}_{\substack{eu\\3\ell11}}|^2\\ &+1.2\times 10^8|L^{S,RL}_{\substack{ed\\3\ell22}}+L^{S,RR}_{\substack{ed\\3\ell22}}|^2\,,\end{aligned} \tag{E.37}$$

  and $\mathcal{B}_2(\tau\to\ell\pi\pi)$ can be obtained from the $B_1(\tau\to\ell\pi\pi)$ expression by making the following substitutions

$$\begin{aligned}L^{T,RR}_{\substack{eq\\3\ell11}}\to L^{T,RR}_{\substack{eq\\\ell311}}, L^{V,LL}_{\substack{eq\\3\ell11}}\to L^{V,RR}_{\substack{eq\\3\ell11}}, L^{V,LR}_{\substack{eq\\3\ell11}}\to L^{V,LR}_{\substack{qe\\113\ell}},\\ L_{\substack{e\gamma\\3\ell}}\to L_{\substack{e\gamma\\\ell3}}, L^{S,RR}_{\substack{eq\\3\ell qq}}\to L^{S,RR^*}_{\substack{eq\\\ell3qq}}, L^{S,RL}_{\substack{eq\\3\ell qq}}\to L^{S,RL^*}_{\substack{eq\\\ell3qq}}.\end{aligned} \tag{E.38}$$

$\tau\to\ell\eta, \tau\to\ell\eta', \tau\to\ell K, \tau\to\ell\pi K, \tau\to\ell KK$ are also included in our χ^2, adapting the compilation of Ref. [364]. However they play a marginal phenomenological role in our analysis and thus we refrain from giving the explicit expressions.

E.8 Matching relations for the Cabibbo angle observables

The running of the chirality-flipping low-energy couplings to the M_Z mass is large and needs to be taken into account. From Ref. [411], which includes higher-order QCD running effects, one has

$$\begin{pmatrix}\epsilon_S\\ \epsilon_P\\ \epsilon_T\end{pmatrix}_{\mu=2\,\mathrm{GeV}} = \begin{pmatrix}1.72 & 2.46\times10^{-6} & -0.0242\\ 2.46\times10^{-6} & 1.72 & -0.0242\\ -2.17\times10^{-4} & -2.17\times10^{-4} & 0.825\end{pmatrix}\begin{pmatrix}\epsilon_S\\ \epsilon_P\\ \epsilon_T\end{pmatrix}_{\mu=M_Z}. \tag{E.39}$$

At M_Z at tree-level one has

$$\begin{aligned}
-\frac{2\hat{V}_{ud}}{v^2}\epsilon_L^{dse} &= 2\left(C^{(3)}_{\substack{Hl\\22}} - C^{(3)}_{\substack{Hq\\11}} - C_{\substack{ll\\1221}} + C^{(3)}_{\substack{lq\\1111}}\right)\\
-\frac{2\hat{V}_{ud}}{v^2}\epsilon_L^{d\ell'/\ell} &= L^{V,LL}_{\substack{\nu edu\\ \ell'\ell'11}} - L^{V,LL}_{\substack{\nu edu\\ \ell\ell11}} = 2V_{ud}(C^{(3)}_{\substack{Hl\\ \ell\ell}} - C^{(3)}_{\substack{Hl\\ \ell'\ell'}} - C^{(3)}_{\substack{lq\\ \ell\ell11}} + C^{(3)}_{\substack{lq\\ \ell'\ell'11}}) - 2V_{us}(-C^{(3)}_{\substack{lq\\ \ell\ell21}} + C^{(3)}_{\substack{lq\\ \ell'\ell'21}}),\\
-\frac{2\hat{V}_{us}}{v^2}\epsilon_L^{s\ell'/\ell} &= L^{V,LL}_{\substack{\nu edu\\ \ell'\ell'21}} - L^{V,LL}_{\substack{\nu edu\\ \ell\ell21}} = 2V_{us}(C^{(3)}_{\substack{Hl\\ \ell\ell}} - C^{(3)}_{\substack{Hl\\ \ell'\ell'}} - C^{(3)}_{\substack{lq\\ \ell\ell11}} + C^{(3)}_{\substack{lq\\ \ell'\ell'11}}) + 2V_{ud}(-C^{(3)}_{\substack{lq\\ \ell\ell21}} + C^{(3)}_{\substack{lq\\ \ell'\ell'21}}),\\
-\frac{2\hat{V}_{uD}}{v^2}\epsilon_R^{D} &= L^{V,LR}_{\substack{\nu edu\\ \ell\ell D1}} = -C_{\substack{Hud\\1D}},\\
-\frac{2\hat{V}_{ud}}{v^2}\epsilon_S^{d\ell} &= L^{S,RR}_{\substack{\nu edu\\ \ell\ell11}} + L^{S,RL}_{\substack{\nu edu\\ \ell\ell11}} = C_{\substack{ledq\\ \ell\ell11}} + V_{ud}C^{(1)}_{\substack{lequ\\ \ell\ell11}} - V_{us}C^{(1)}_{\substack{lequ\\ \ell\ell21}},\\
-\frac{2\hat{V}_{us}}{v^2}\epsilon_S^{s\ell} &= L^{S,RR}_{\substack{\nu edu\\ \ell\ell21}} + L^{S,RL}_{\substack{\nu edu\\ \ell\ell21}} = C_{\substack{ledq\\ \ell\ell21}} + V_{us}C^{(1)}_{\substack{lequ\\ \ell\ell11}} + V_{ud}C^{(1)}_{\substack{lequ\\ \ell\ell21}},\\
-\frac{2\hat{V}_{ud}}{v^2}\epsilon_P^{d\ell} &= L^{S,RR}_{\substack{\nu edu\\ \ell\ell11}} - L^{S,RL}_{\substack{\nu edu\\ \ell\ell11}} = -C_{\substack{ledq\\ \ell\ell11}} + V_{ud}C^{(1)}_{\substack{lequ\\ \ell\ell11}} - V_{us}C^{(1)}_{\substack{lequ\\ \ell\ell21}},\\
-\frac{2\hat{V}_{us}}{v^2}\epsilon_P^{s\ell} &= L^{S,RR}_{\substack{\nu edu\\ \ell\ell21}} - L^{S,RL}_{\substack{\nu edu\\ \ell\ell21}} = -C_{\substack{ledq\\ \ell\ell21}} + V_{us}C^{(1)}_{\substack{lequ\\ \ell\ell11}} + V_{ud}C^{(1)}_{\substack{lequ\\ \ell\ell21}},\\
-\frac{2\hat{V}_{ud}}{v^2}\frac{1}{4}\hat{\epsilon}_T^{d\ell} &= L^{T,RR}_{\substack{\nu edu\\ \ell\ell11}} = V_{ud}C^{(3)}_{\substack{lequ\\ \ell\ell11}} - V_{us}C^{(3)}_{\substack{lequ\\ \ell\ell21}},\\
-\frac{2\hat{V}_{us}}{v^2}\frac{1}{4}\hat{\epsilon}_T^{s\ell} &= L^{T,RR}_{\substack{\nu edu\\ \ell\ell21}} = V_{us}C^{(3)}_{\substack{lequ\\ \ell\ell11}} + V_{ud}C^{(3)}_{\substack{lequ\\ \ell\ell21}}.
\end{aligned} \tag{E.40}$$

The leading mechanism to generate a top operator is through the large mixing of $C^{(3)}_{\substack{Hl\\ \alpha\alpha}}$

with $C^{(3)}_{\substack{lq\\ \alpha\alpha 33}}$ through a double top-Yukawa insertion [272],[2]

$$v^2 C^{(3)}_{\substack{Hl\\ \alpha\alpha}}(M_Z^2) \approx v^2 4N_c \frac{m_t^2}{(4\pi v)^2} C^{(3)}_{\substack{lq\\ \alpha\alpha 33}}(\Lambda_{\rm UV}^2) \log\frac{\Lambda_{\rm UV}}{M_Z} = \left[\frac{N_c}{4\pi^2}\frac{m_t^2}{\Lambda_{\rm UV}^2}\log\frac{\Lambda_{\rm UV}}{M_Z}\right] \Lambda_{\rm UV}^2 C^{(3)}_{\substack{lq\\ \alpha\alpha 33}}(\Lambda_{\rm UV}^2)\,. \tag{E.41}$$

E.9 Higgs basis used for EWPT and Higgs fit

The fit performed in Ref. [368] employs a specific combinations of Wilson coefficients of the Warsaw basis, called *Higgs basis*. This allows to reduce the correlations between the directions mostly constrained by EW precision data and those constrained by Higgs data, which differ strongly in the precision. The combinations used are the following:

$$\begin{aligned}
\delta g_L^{W\ell} &= C_{Hl}^{(3)} + f(1/2,0) - f(-1/2,-1),\\
\delta g_L^{Z\ell} &= -\frac{1}{2}C_{Hl}^{(3)} - \frac{1}{2}C_{Hl}^{(1)} + f(-1/2,-1),\\
\delta g_R^{Z\ell} &= -\frac{1}{2}C_{He}^{(1)} + f(0,-1),\\
\delta g_L^{Zu} &= \frac{1}{2}C_{Hq}^{(3)} - \frac{1}{2}C_{Hq}^{(1)} + f(1/2,2/3),\\
\delta g_L^{Zd} &= -\frac{1}{2}C_{Hq}^{(3)} - \frac{1}{2}C_{Hq}^{(1)} + f(-1/2,-1/3),\\
\delta g_R^{Zu} &= -\frac{1}{2}C_{Hu} + f(0,2/3),\\
\delta g_R^{Zd} &= -\frac{1}{2}C_{Hd} + f(0,-1/3),\\
\delta c_z &= C_{H\Box} - \frac{1}{4}C_{HD} - \frac{3}{2}\Delta_{G_F},\\
c_{z\Box} &= \frac{1}{2g_L^2}\left(C_{HD} + 2\Delta_{G_F}\right),\\
c_{gg} &= \frac{4}{g_s^2}C_{HG},\\
c_{\gamma\gamma} &= 4\left(\frac{1}{g_L^2}C_{HW} + \frac{1}{g_Y^2}C_{HB} - \frac{1}{g_L g_Y}C_{HWB}\right),\\
c_{zz} &= 4\left(\frac{g_L^2 C_{HW} + g_Y^2 C_{HB} + g_L g_Y C_{HWB}}{(g_L^2+g_Y^2)^2}\right),\\
c_{z\gamma} &= 4\left(\frac{C_{HW} - C_{HB} - \frac{g_L^2-g_Y^2}{2g_L g_Y}C_{HWB}}{g_L^2+g_Y^2}\right),
\end{aligned} \tag{E.42}$$

where

$$f(T^3,Q) \equiv \left\{ -Q\frac{g_L g_Y}{g_L^2-g_Y^2}C_{HWB} - \mathbf{1}\left(\frac{1}{4}C_{HD} + \frac{1}{2}\Delta_{G_F}\right)\left(T^3 + Q\frac{g_Y^2}{g_L^2-g_Y^2}\right)\right\}\mathbf{1}\,, \tag{E.43}$$

[2] As in the rest of this work, the DSixTools package has been used to perform the full one-loop running. We have also checked that the loop-induced top operators in the SMEFT-LEFT matching play a marginal role in this sector and, in first approximation, can be neglected.

Class	Coefficients	Warsaw basis	95% CL Individual	95% CL Marginalised
Dipoles	c_{tG}	C_{uG}	[0.01,0.11]	[0.01,0.23]
	c_{tW}	C_{uW}	[-0.085,0.030]	[-0.28,0.13]
	c_{tZ}	$-\mathrm{s}_\theta\, C_{uB} + \mathrm{c}_\theta\, C_{uW}$	[-0.038,0.090]	[-0.50,0.14]
Higgs-Top	c^3_{HQ}	$C^{(3)}_{Hq}$	[-0.39,0.34]	[-0.42,0.31]
	$c^{(-)}_{HQ}$	$C^{(1)}_{Hq} - C^{(3)}_{Hq}$	[-1.1,1.5]	[-2.7,2.7]
	c_{Ht}	C_{Hu}	[-2.8,2.2]	[-15,4]
	c_{tH}	C_{uH}	[-1.3,0.4]	[-0.5,2.9]
4 quarks	c^1_{QQ}	$2C^{(1)}_{qq} - \frac{2}{3}C^{(3)}_{qq}$	[-2.3,2.0]	[-3.7,4.4]
	c^8_{QQ}	$8C^{(3)}_{qq}$	[-6.8,5.9]	[-13,10]
	c^1_{Qt}	$C^{(1)}_{qu}$	[-1.8,1.9]	[-1.5,1.4]
	c^8_{Qt}	$C^{(8)}_{qu}$	[-4.3,3.3]	[-3.4,2.5]
	c^1_{tt}	C_{uu}	[-1.1,1.0]	[-0.88,0.81]

Table E.2: The 95% CL bounds from SMEFiT for individual and global fits obtained using quadratic EFT calculations. Top quark, Higgs and diboson data have been used, as discussed in Ref. [377]. Coefficients are expressed in both the SMEFiT and the Warsaw basis conventions.

and $\Delta_{G_F} = [C^{(3)}_{Hl}]_{11} + [C^{(3)}_{Hl}]_{22} - \frac{1}{2}[C_{ll}]_{1221}$. To these coefficients, the fit in Ref. [368] also adds those for the dimension-6 Yukawa-like operators of top, bottom, muon and tau fermions, as well as the one responsible for modifying the muon decay: $[C_{uH}]_{33}$, $[C_{dH}]_{33}$, $[C_{eH}]_{22}$, $[C_{eH}]_{33}$, $[C_{ll}]_{1221}$.

The set of $\delta g_{V\psi}$ parametrize the corresponding vertex corrections of Z and W bosons, and are mostly constrained by electroweak data from LEP. As mentioned, the coefficient $[C_{ll}]_{1221}$ enters the EW fit by its impact in the muon decay. Finally, the other coefficients do not affect EW observables at tree level and are only constrained by Higgs data.

E.10 Direct constraints from LHC

Here we provide the 95% CL bounds on Wilson coefficients, from both individual and global marginalised fits obtained from SMEFiT [377]. These are illustrated in Table E.2. Single parameter fits match the findings of Ref. [377] (see Table 5.4 therein).

Even though it is reasonable to expect that individual bounds are comparable or more severe than the global ones, we observe the latter to be stronger in the case of the $C^{(1/8)}_{qu}$ and C_{uu} coefficients. This surprising trend was also observed in Ref. [377], where the global

analysis involved a larger set of operators.

The direct bounds shown in Table E.2 are compared to the indirect limits computed in this work in Section 5.4.

$\boldsymbol{\nu\nu + h.c.}$	
$\mathcal{O}_\nu$	$(\nu_{Lp}^T C \nu_{Lr})$

$\boldsymbol{(\nu\nu)X + h.c.}$	
$\mathcal{O}_{\nu\gamma}$	$(\nu_{Lp}^T C \sigma^{\mu\nu} \nu_{Lr}) F_{\mu\nu}$

$\boldsymbol{(\overline{L}R)X + h.c.}$	
$\mathcal{O}_{e\gamma}$	$\bar{e}_{Lp} \sigma^{\mu\nu} e_{Rr} \, F_{\mu\nu}$
$\mathcal{O}_{u\gamma}$	$\bar{u}_{Lp} \sigma^{\mu\nu} u_{Rr} \, F_{\mu\nu}$
$\mathcal{O}_{d\gamma}$	$\bar{d}_{Lp} \sigma^{\mu\nu} d_{Rr} \, F_{\mu\nu}$
$\mathcal{O}_{uG}$	$\bar{u}_{Lp} \sigma^{\mu\nu} T^A u_{Rr} \, G^A_{\mu\nu}$
$\mathcal{O}_{dG}$	$\bar{d}_{Lp} \sigma^{\mu\nu} T^A d_{Rr} \, G^A_{\mu\nu}$

$\boldsymbol{X^3}$	
$\mathcal{O}_G$	$f^{ABC} G_\mu^{A\nu} G_\nu^{B\rho} G_\rho^{C\mu}$
$\mathcal{O}_{\widetilde{G}}$	$f^{ABC} \widetilde{G}_\mu^{A\nu} G_\nu^{B\rho} G_\rho^{C\mu}$

$\boldsymbol{(\overline{L}L)(\overline{L}L)}$	
$\mathcal{O}_{\nu\nu}^{V,LL}$	$(\bar{\nu}_{Lp} \gamma^\mu \nu_{Lr})(\bar{\nu}_{Ls} \gamma_\mu \nu_{Lt})$
$\mathcal{O}_{ee}^{V,LL}$	$(\bar{e}_{Lp} \gamma^\mu e_{Lr})(\bar{e}_{Ls} \gamma_\mu e_{Lt})$
$\mathcal{O}_{\nu e}^{V,LL}$	$(\bar{\nu}_{Lp} \gamma^\mu \nu_{Lr})(\bar{e}_{Ls} \gamma_\mu e_{Lt})$
$\mathcal{O}_{\nu u}^{V,LL}$	$(\bar{\nu}_{Lp} \gamma^\mu \nu_{Lr})(\bar{u}_{Ls} \gamma_\mu u_{Lt})$
$\mathcal{O}_{\nu d}^{V,LL}$	$(\bar{\nu}_{Lp} \gamma^\mu \nu_{Lr})(\bar{d}_{Ls} \gamma_\mu d_{Lt})$
$\mathcal{O}_{eu}^{V,LL}$	$(\bar{e}_{Lp} \gamma^\mu e_{Lr})(\bar{u}_{Ls} \gamma_\mu u_{Lt})$
$\mathcal{O}_{ed}^{V,LL}$	$(\bar{e}_{Lp} \gamma^\mu e_{Lr})(\bar{d}_{Ls} \gamma_\mu d_{Lt})$
$\mathcal{O}_{\nu edu}^{V,LL}$	$(\bar{\nu}_{Lp} \gamma^\mu e_{Lr})(\bar{d}_{Ls} \gamma_\mu u_{Lt}) + h.c.$
$\mathcal{O}_{uu}^{V,LL}$	$(\bar{u}_{Lp} \gamma^\mu u_{Lr})(\bar{u}_{Ls} \gamma_\mu u_{Lt})$
$\mathcal{O}_{dd}^{V,LL}$	$(\bar{d}_{Lp} \gamma^\mu d_{Lr})(\bar{d}_{Ls} \gamma_\mu d_{Lt})$
$\mathcal{O}_{ud}^{V1,LL}$	$(\bar{u}_{Lp} \gamma^\mu u_{Lr})(\bar{d}_{Ls} \gamma_\mu d_{Lt})$
$\mathcal{O}_{ud}^{V8,LL}$	$(\bar{u}_{Lp} \gamma^\mu T^A u_{Lr})(\bar{d}_{Ls} \gamma_\mu T^A d_{Lt})$

$\boldsymbol{(\overline{R}R)(\overline{R}R)}$	
$\mathcal{O}_{ee}^{V,RR}$	$(\bar{e}_{Rp} \gamma^\mu e_{Rr})(\bar{e}_{Rs} \gamma_\mu e_{Rt})$
$\mathcal{O}_{eu}^{V,RR}$	$(\bar{e}_{Rp} \gamma^\mu e_{Rr})(\bar{u}_{Rs} \gamma_\mu u_{Rt})$
$\mathcal{O}_{ed}^{V,RR}$	$(\bar{e}_{Rp} \gamma^\mu e_{Rr})(\bar{d}_{Rs} \gamma_\mu d_{Rt})$
$\mathcal{O}_{uu}^{V,RR}$	$(\bar{u}_{Rp} \gamma^\mu u_{Rr})(\bar{u}_{Rs} \gamma_\mu u_{Rt})$
$\mathcal{O}_{dd}^{V,RR}$	$(\bar{d}_{Rp} \gamma^\mu d_{Rr})(\bar{d}_{Rs} \gamma_\mu d_{Rt})$
$\mathcal{O}_{ud}^{V1,RR}$	$(\bar{u}_{Rp} \gamma^\mu u_{Rr})(\bar{d}_{Rs} \gamma_\mu d_{Rt})$
$\mathcal{O}_{ud}^{V8,RR}$	$(\bar{u}_{Rp} \gamma^\mu T^A u_{Rr})(\bar{d}_{Rs} \gamma_\mu T^A d_{Rt})$

$\boldsymbol{(\overline{L}L)(\overline{R}R)}$	
$\mathcal{O}_{\nu e}^{V,LR}$	$(\bar{\nu}_{Lp} \gamma^\mu \nu_{Lr})(\bar{e}_{Rs} \gamma_\mu e_{Rt})$
$\mathcal{O}_{ee}^{V,LR}$	$(\bar{e}_{Lp} \gamma^\mu e_{Lr})(\bar{e}_{Rs} \gamma_\mu e_{Rt})$
$\mathcal{O}_{\nu u}^{V,LR}$	$(\bar{\nu}_{Lp} \gamma^\mu \nu_{Lr})(\bar{u}_{Rs} \gamma_\mu u_{Rt})$
$\mathcal{O}_{\nu d}^{V,LR}$	$(\bar{\nu}_{Lp} \gamma^\mu \nu_{Lr})(\bar{d}_{Rs} \gamma_\mu d_{Rt})$
$\mathcal{O}_{eu}^{V,LR}$	$(\bar{e}_{Lp} \gamma^\mu e_{Lr})(\bar{u}_{Rs} \gamma_\mu u_{Rt})$
$\mathcal{O}_{ed}^{V,LR}$	$(\bar{e}_{Lp} \gamma^\mu e_{Lr})(\bar{d}_{Rs} \gamma_\mu d_{Rt})$
$\mathcal{O}_{ue}^{V,LR}$	$(\bar{u}_{Lp} \gamma^\mu u_{Lr})(\bar{e}_{Rs} \gamma_\mu e_{Rt})$
$\mathcal{O}_{de}^{V,LR}$	$(\bar{d}_{Lp} \gamma^\mu d_{Lr})(\bar{e}_{Rs} \gamma_\mu e_{Rt})$
$\mathcal{O}_{\nu edu}^{V,LR}$	$(\bar{\nu}_{Lp} \gamma^\mu e_{Lr})(\bar{d}_{Rs} \gamma_\mu u_{Rt}) + h.c.$
$\mathcal{O}_{uu}^{V1,LR}$	$(\bar{u}_{Lp} \gamma^\mu u_{Lr})(\bar{u}_{Rs} \gamma_\mu u_{Rt})$
$\mathcal{O}_{uu}^{V8,LR}$	$(\bar{u}_{Lp} \gamma^\mu T^A u_{Lr})(\bar{u}_{Rs} \gamma_\mu T^A u_{Rt})$
$\mathcal{O}_{ud}^{V1,LR}$	$(\bar{u}_{Lp} \gamma^\mu u_{Lr})(\bar{d}_{Rs} \gamma_\mu d_{Rt})$
$\mathcal{O}_{ud}^{V8,LR}$	$(\bar{u}_{Lp} \gamma^\mu T^A u_{Lr})(\bar{d}_{Rs} \gamma_\mu T^A d_{Rt})$
$\mathcal{O}_{du}^{V1,LR}$	$(\bar{d}_{Lp} \gamma^\mu d_{Lr})(\bar{u}_{Rs} \gamma_\mu u_{Rt})$
$\mathcal{O}_{du}^{V8,LR}$	$(\bar{d}_{Lp} \gamma^\mu T^A d_{Lr})(\bar{u}_{Rs} \gamma_\mu T^A u_{Rt})$
$\mathcal{O}_{dd}^{V1,LR}$	$(\bar{d}_{Lp} \gamma^\mu d_{Lr})(\bar{d}_{Rs} \gamma_\mu d_{Rt})$
$\mathcal{O}_{dd}^{V8,LR}$	$(\bar{d}_{Lp} \gamma^\mu T^A d_{Lr})(\bar{d}_{Rs} \gamma_\mu T^A d_{Rt})$
$\mathcal{O}_{uddu}^{V1,LR}$	$(\bar{u}_{Lp} \gamma^\mu d_{Lr})(\bar{d}_{Rs} \gamma_\mu u_{Rt}) + h.c.$
$\mathcal{O}_{uddu}^{V8,LR}$	$(\bar{u}_{Lp} \gamma^\mu T^A d_{Lr})(\bar{d}_{Rs} \gamma_\mu T^A u_{Rt}) + h.c.$

$\boldsymbol{(\overline{L}R)(\overline{L}R) + h.c.}$	
$\mathcal{O}_{ee}^{S,RR}$	$(\bar{e}_{Lp} e_{Rr})(\bar{e}_{Ls} e_{Rt})$
$\mathcal{O}_{eu}^{S,RR}$	$(\bar{e}_{Lp} e_{Rr})(\bar{u}_{Ls} u_{Rt})$
$\mathcal{O}_{eu}^{T,RR}$	$(\bar{e}_{Lp} \sigma^{\mu\nu} e_{Rr})(\bar{u}_{Ls} \sigma_{\mu\nu} u_{Rt})$
$\mathcal{O}_{ed}^{S,RR}$	$(\bar{e}_{Lp} e_{Rr})(\bar{d}_{Ls} d_{Rt})$
$\mathcal{O}_{ed}^{T,RR}$	$(\bar{e}_{Lp} \sigma^{\mu\nu} e_{Rr})(\bar{d}_{Ls} \sigma_{\mu\nu} d_{Rt})$
$\mathcal{O}_{\nu edu}^{S,RR}$	$(\bar{\nu}_{Lp} e_{Rr})(\bar{d}_{Ls} u_{Rt})$
$\mathcal{O}_{\nu edu}^{T,RR}$	$(\bar{\nu}_{Lp} \sigma^{\mu\nu} e_{Rr})(\bar{d}_{Ls} \sigma_{\mu\nu} u_{Rt})$
$\mathcal{O}_{uu}^{S1,RR}$	$(\bar{u}_{Lp} u_{Rr})(\bar{u}_{Ls} u_{Rt})$
$\mathcal{O}_{uu}^{S8,RR}$	$(\bar{u}_{Lp} T^A u_{Rr})(\bar{u}_{Ls} T^A u_{Rt})$
$\mathcal{O}_{ud}^{S1,RR}$	$(\bar{u}_{Lp} u_{Rr})(\bar{d}_{Ls} d_{Rt})$
$\mathcal{O}_{ud}^{S8,RR}$	$(\bar{u}_{Lp} T^A u_{Rr})(\bar{d}_{Ls} T^A d_{Rt})$
$\mathcal{O}_{dd}^{S1,RR}$	$(\bar{d}_{Lp} d_{Rr})(\bar{d}_{Ls} d_{Rt})$
$\mathcal{O}_{dd}^{S8,RR}$	$(\bar{d}_{Lp} T^A d_{Rr})(\bar{d}_{Ls} T^A d_{Rt})$
$\mathcal{O}_{uddu}^{S1,RR}$	$(\bar{u}_{Lp} d_{Rr})(\bar{d}_{Ls} u_{Rt})$
$\mathcal{O}_{uddu}^{S8,RR}$	$(\bar{u}_{Lp} T^A d_{Rr})(\bar{d}_{Ls} T^A u_{Rt})$

$\boldsymbol{(\overline{L}R)(\overline{R}L) + h.c.}$	
$\mathcal{O}_{eu}^{S,RL}$	$(\bar{e}_{Lp} e_{Rr})(\bar{u}_{Rs} u_{Lt})$
$\mathcal{O}_{ed}^{S,RL}$	$(\bar{e}_{Lp} e_{Rr})(\bar{d}_{Rs} d_{Lt})$
$\mathcal{O}_{\nu edu}^{S,RL}$	$(\bar{\nu}_{Lp} e_{Rr})(\bar{d}_{Rs} u_{Lt})$

Table E.3: LEFT operators of dimension three and five, as well as LEFT operators of dimension six that conserve baryon and lepton number, reproduced from Ref. [268].

Bibliography

[1] Georges Aad et al. "Observation of a new particle in the search for the Standard Model Higgs boson with the ATLAS detector at the LHC". In: *Phys. Lett. B* 716 (2012), pp. 1–29. DOI: 10.1016/j.physletb.2012.08.020. arXiv: 1207.7214 [hep-ex].

[2] Serguei Chatrchyan et al. "Observation of a New Boson at a Mass of 125 GeV with the CMS Experiment at the LHC". In: *Phys. Lett. B* 716 (2012), pp. 30–61. DOI: 10.1016/j.physletb.2012.08.021. arXiv: 1207.7235 [hep-ex].

[3] C. Adolphsen et al. "European Strategy for Particle Physics – Accelerator R&D Roadmap". In: *CERN Yellow Rep. Monogr.* 1 (2022). Ed. by N. Mounet, pp. 1–270. DOI: 10.23731/CYRM-2022-001. arXiv: 2201.07895 [physics.acc-ph].

[4] A. Abada et al. "FCC Physics Opportunities: Future Circular Collider Conceptual Design Report Volume 1". In: *Eur. Phys. J. C* 79.6 (2019), p. 474. DOI: 10.1140/epjc/s10052-019-6904-3.

[5] A. Abada et al. "FCC-hh: The Hadron Collider: Future Circular Collider Conceptual Design Report Volume 3". In: *Eur. Phys. J. ST* 228.4 (2019), pp. 755–1107. DOI: 10.1140/epjst/e2019-900087-0.

[6] G. Bernardi et al. "The Future Circular Collider: a Summary for the US 2021 Snowmass Process". In: (Mar. 2022). arXiv: 2203.06520 [hep-ex].

[7] A. Abada et al. "FCC-ee: The Lepton Collider: Future Circular Collider Conceptual Design Report Volume 2". In: *Eur. Phys. J. ST* 228.2 (2019), pp. 261–623. DOI: 10.1140/epjst/e2019-900045-4.

[8] Mingyi Dong et al. "CEPC Conceptual Design Report: Volume 2 - Physics & Detector". In: (Nov. 2018). Ed. by João Barreiro Guimarães da Costa et al. arXiv: 1811.10545 [hep-ex].

[9] "The International Linear Collider Technical Design Report - Volume 1: Executive Summary". In: (June 2013). Ed. by Ties Behnke et al. arXiv: 1306.6327 [physics.acc-ph].

[10] J. de Blas et al. "The CLIC Potential for New Physics". In: 3/2018 (Dec. 2018). DOI: 10.23731/CYRM-2018-003. arXiv: 1812.02093 [hep-ph].

[11] Mei Bai et al. "C^3: A "Cool" Route to the Higgs Boson and Beyond". In: *Snowmass 2021*. Oct. 2021. arXiv: 2110.15800 [hep-ex].

[12] D. Stratakis et al. "A Muon Collider Facility for Physics Discovery". In: (Mar. 2022). arXiv: 2203.08033 [physics.acc-ph].

[13] S. Jindariani et al. "Promising Technologies and R&D Directions for the Future Muon Collider Detectors". In: (Mar. 2022). arXiv: 2203.07224 [physics.ins-det].

[14] Chiara Aime et al. "Muon Collider Physics Summary". In: (Mar. 2022). arXiv: 2203.07256 [hep-ph].

[15] Jorge de Blas et al. "The physics case of a 3 TeV muon collider stage". In: (Mar. 2022). arXiv: 2203.07261 [hep-ph].

[16] Carlotta Accettura et al. "Towards a Muon Collider". In: (Mar. 2023). arXiv: 2303.08533 [physics.acc-ph].

[17] C. Accettura et al. "Interim report for the International Muon Collider Collaboration (IMCC)". In: (July 2024). arXiv: 2407.12450 [physics.acc-ph].

[18] Antonio Costantini et al. "Vector boson fusion at multi-TeV muon colliders". In: *JHEP* 09 (2020), p. 080. DOI: 10.1007/JHEP09(2020)080. arXiv: 2005.10289 [hep-ph].

[19] R. Aaij et al. "Test of lepton universality with $B^0 \to K^{*0}\ell^+\ell^-$ decays". In: *JHEP* 08 (2017), p. 055. DOI: 10.1007/JHEP08(2017)055. arXiv: 1705.05802 [hep-ex].

[20] Roel Aaij et al. "Test of lepton universality in beauty-quark decays". In: *Nature Phys.* 18.3 (2022), pp. 277–282. DOI: 10.1038/s41567-021-01478-8. arXiv: 2103.11769 [hep-ex].

[21] R. Aaij et al. "Test of lepton universality in $b \to s\ell^+\ell^-$ decays". In: *Phys. Rev. Lett.* 131.5 (2023), p. 051803. DOI: 10.1103/PhysRevLett.131.051803. arXiv: 2212.09152 [hep-ex].

[22] S. L. Glashow. "Partial Symmetries of Weak Interactions". In: *Nucl. Phys.* 22 (1961), pp. 579–588. DOI: 10.1016/0029-5582(61)90469-2.

[23] Steven Weinberg. "A Model of Leptons". In: *Phys. Rev. Lett.* 19 (1967), pp. 1264–1266. DOI: 10.1103/PhysRevLett.19.1264.

[24] Abdus Salam. "Weak and Electromagnetic Interactions". In: *Conf. Proc. C* 680519 (1968), pp. 367–377. DOI: 10.1142/9789812795915_0034.

[25] Peter W. Higgs. "Broken Symmetries and the Masses of Gauge Bosons". In: *Phys. Rev. Lett.* 13 (1964). Ed. by J. C. Taylor, pp. 508–509. DOI: 10.1103/PhysRevLett.13.508.

[26] F. Englert and R. Brout. "Broken Symmetry and the Mass of Gauge Vector Mesons". In: *Phys. Rev. Lett.* 13 (1964). Ed. by J. C. Taylor, pp. 321–323. DOI: 10.1103/PhysRevLett.13.321.

[27] Makoto Kobayashi and Toshihide Maskawa. "CP Violation in the Renormalizable Theory of Weak Interaction". In: *Prog. Theor. Phys.* 49 (1973), pp. 652–657. DOI: 10.1143/PTP.49.652.

[28] S. Navas et al. "Review of particle physics". In: *Phys. Rev. D* 110.3 (2024), p. 030001. DOI: 10.1103/PhysRevD.110.030001.

[29] Andreas Crivellin. "Explaining the Cabibbo Angle Anomaly". In: July 2022. arXiv: 2207.02507 [hep-ph].

[30] Riccardo Barbieri et al. "$U(2)$ and Minimal Flavour Violation in Supersymmetry". In: *Eur. Phys. J. C* 71 (2011), p. 1725. DOI: 10.1140/epjc/s10052-011-1725-z. arXiv: 1105.2296 [hep-ph].

[31] Riccardo Barbieri et al. "Flavour physics from an approximate $U(2)^3$ symmetry". In: *JHEP* 07 (2012), p. 181. DOI: 10.1007/JHEP07(2012)181. arXiv: 1203.4218 [hep-ph].

[32] Riccardo Barbieri et al. "A 125 GeV composite Higgs boson versus flavour and electroweak precision tests". In: *JHEP* 05 (2013), p. 069. DOI: 10.1007/JHEP05(2013)069. arXiv: 1211.5085 [hep-ph].

[33] Christian W. Bauer, Nicolas Ferland, and Bryan R. Webber. "Standard Model Parton Distributions at Very High Energies". In: *JHEP* 08 (2017), p. 036. DOI: 10.1007/JHEP08(2017)036. arXiv: 1703.08562 [hep-ph].

[34] Zamiul Alam and Stephen P. Martin. "Standard model at 200 GeV". In: *Phys. Rev. D* 107.1 (2023), p. 013010. DOI: 10.1103/PhysRevD.107.013010. arXiv: 2211.08576 [hep-ph].

[35] E. Fermi. "On the Theory of the impact between atoms and electrically charged particles". In: *Z. Phys.* 29 (1924), pp. 315–327. DOI: 10.1007/BF03184853.

[36] C. F. von Weizsacker. "Radiation emitted in collisions of very fast electrons". In: *Z. Phys.* 88 (1934), pp. 612–625. DOI: 10.1007/BF01333110.

[37] E. J. Williams. "Nature of the high-energy particles of penetrating radiation and status of ionization and radiation formulae". In: *Phys. Rev.* 45 (1934), pp. 729–730. DOI: 10.1103/PhysRev.45.729.

[38] Lev Davidovich Landau and Evgeny Mikhailovich Lifschitz. "ON THE PRODUCTION OF ELECTRONS AND POSITRONS BY A COLLISION OF TWO PARTICLES". In: *Phys. Z. Sowjetunion* 6 (1934). Ed. by D. ter Haar, p. 244. DOI: 10.1016/B978-0-08-010586-4.50021-3.

[39] V. N. Gribov and L. N. Lipatov. "Deep inelastic e p scattering in perturbation theory". In: *Sov. J. Nucl. Phys.* 15 (1972), pp. 438–450.

[40] Yuri L. Dokshitzer. "Calculation of the Structure Functions for Deep Inelastic Scattering and e+ e- Annihilation by Perturbation Theory in Quantum Chromodynamics." In: *Sov. Phys. JETP* 46 (1977), pp. 641–653.

[41] Guido Altarelli and G. Parisi. "Asymptotic Freedom in Parton Language". In: *Nucl. Phys. B* 126 (1977), pp. 298–318. DOI: 10.1016/0550-3213(77)90384-4.

[42] Gabriel Cuomo, Luca Vecchi, and Andrea Wulzer. "Goldstone Equivalence and High Energy Electroweak Physics". In: *SciPost Phys.* 8.5 (2020), p. 078. DOI: 10.21468/SciPostPhys.8.5.078. arXiv: 1911.12366 [hep-ph].

[43] Stefano Frixione. "Initial conditions for electron and photon structure and fragmentation functions". In: *JHEP* 11 (2019), p. 158. DOI: 10.1007/JHEP11(2019)158. arXiv: 1909.03886 [hep-ph].

[44] V. Bertone et al. "The partonic structure of the electron at the next-to-leading logarithmic accuracy in QED". In: *JHEP* 03 (2020). [Erratum: JHEP 08, 108 (2022)], p. 135. DOI: 10.1007/JHEP03(2020)135. arXiv: 1911.12040 [hep-ph].

[45] V. Bertone et al. "Improving methods and predictions at high-energy e^+e^- colliders within collinear factorisation". In: *JHEP* 10 (2022), p. 089. DOI: 10.1007/JHEP10(2022)089. arXiv: 2207.03265 [hep-ph].

[46] Paolo Ciafaloni and Denis Comelli. "Electroweak evolution equations". In: *JHEP* 11 (2005), p. 022. DOI: 10.1088/1126-6708/2005/11/022. arXiv: hep-ph/0505047.

[47] Valerio Bertone et al. "On the Impact of Lepton PDFs". In: *JHEP* 11 (2015), p. 194. DOI: 10.1007/JHEP11(2015)194. arXiv: 1508.07002 [hep-ph].

[48] Aneesh Manohar et al. "How bright is the proton? A precise determination of the photon parton distribution function". In: *Phys. Rev. Lett.* 117.24 (2016), p. 242002. DOI: 10.1103/PhysRevLett.117.242002. arXiv: 1607.04266 [hep-ph].

[49] Aneesh V. Manohar et al. "The Photon Content of the Proton". In: *JHEP* 12 (2017), p. 046. DOI: 10.1007/JHEP12(2017)046. arXiv: 1708.01256 [hep-ph].

[50] Bartosz Fornal, Aneesh V. Manohar, and Wouter J. Waalewijn. "Electroweak Gauge Boson Parton Distribution Functions". In: *JHEP* 05 (2018), p. 106. DOI: 10.1007/JHEP05(2018)106. arXiv: 1803.06347 [hep-ph].

[51] Luca Buonocore et al. "Leptons in the proton". In: *JHEP* 08.08 (2020), p. 019. DOI: 10.1007/JHEP08(2020)019. arXiv: 2005.06477 [hep-ph].

[52] P. Ciafaloni and D. Comelli. "Sudakov enhancement of electroweak corrections". In: *Phys. Lett. B* 446 (1999), pp. 278–284. DOI: 10.1016/S0370-2693(98)01541-X. arXiv: hep-ph/9809321.

[53] Marcello Ciafaloni, Paolo Ciafaloni, and Denis Comelli. "Bloch-Nordsieck violating electroweak corrections to inclusive TeV scale hard processes". In: *Phys. Rev. Lett.* 84 (2000), pp. 4810–4813. DOI: 10.1103/PhysRevLett.84.4810. arXiv: hep-ph/0001142.

[54] Marcello Ciafaloni, Paolo Ciafaloni, and Denis Comelli. "Bloch-Nordsieck violation in spontaneously broken Abelian theories". In: *Phys. Rev. Lett.* 87 (2001), p. 211802. DOI: 10.1103/PhysRevLett.87.211802. arXiv: hep-ph/0103315.

[55] Junmou Chen, Tao Han, and Brock Tweedie. "Electroweak Splitting Functions and High Energy Showering". In: *JHEP* 11 (2017), p. 093. DOI: 10.1007/JHEP11(2017)093. arXiv: 1611.00788 [hep-ph].

[56] Christian W. Bauer and Bryan R. Webber. "Polarization Effects in Standard Model Parton Distributions at Very High Energies". In: *JHEP* 03 (2019), p. 013. DOI: 10.1007/JHEP03(2019)013. arXiv: 1808.08831 [hep-ph].

[57] W. Buchmuller and D. Wyler. "Effective Lagrangian Analysis of New Interactions and Flavor Conservation". In: *Nucl. Phys. B* 268 (1986), pp. 621–653. DOI: 10.1016/0550-3213(86)90262-2.

[58] B. Grzadkowski et al. "Dimension-Six Terms in the Standard Model Lagrangian". In: *JHEP* 10 (2010), p. 085. DOI: 10.1007/JHEP10(2010)085. arXiv: 1008.4884 [hep-ph].

[59] S. L. Glashow, J. Iliopoulos, and L. Maiani. "Weak Interactions with Lepton-Hadron Symmetry". In: *Phys. Rev. D* 2 (1970), pp. 1285–1292. DOI: 10.1103/PhysRevD.2.1285.

[60] G. D'Ambrosio et al. "Minimal flavor violation: An Effective field theory approach". In: *Nucl. Phys. B* 645 (2002), pp. 155–187. DOI: 10.1016/S0550-3213(02)00836-2. arXiv: hep-ph/0207036.

[61] Wolfgang Altmannshofer and Peter Stangl. "New physics in rare B decays after Moriond 2021". In: *Eur. Phys. J. C* 81.10 (2021), p. 952. DOI: 10.1140/epjc/s10052-021-09725-1. arXiv: 2103.13370 [hep-ph].

[62] Tao Han, Yang Ma, and Keping Xie. "High energy leptonic collisions and electroweak parton distribution functions". In: *Phys. Rev. D* 103.3 (2021), p. L031301. DOI: 10.1103/PhysRevD.103.L031301. arXiv: 2007.14300 [hep-ph].

[63] Tao Han, Yang Ma, and Keping Xie. "Quark and gluon contents of a lepton at high energies". In: *JHEP* 02 (2022), p. 154. DOI: 10.1007/JHEP02(2022)154. arXiv: 2103.09844 [hep-ph].

[64] Hind Al Ali et al. "The muon Smasher's guide". In: *Rept. Prog. Phys.* 85.8 (2022), p. 084201. DOI: 10.1088/1361-6633/ac6678. arXiv: 2103.14043 [hep-ph].

[65] Richard Ruiz et al. "The Effective Vector Boson Approximation in high-energy muon collisions". In: *JHEP* 06 (2022), p. 114. DOI: 10.1007/JHEP06(2022)114. arXiv: 2111.02442 [hep-ph].

[66] S. Coleman and R. E. Norton. "Singularities in the physical region". In: *Nuovo Cim.* 38 (1965), pp. 438–442. DOI: 10.1007/BF02750472.

[67] I. F. Ginzburg. "Initial particle instability in muon collisions". In: *Nucl. Phys. B Proc. Suppl.* 51 (1996). Ed. by D. B. Cline, pp. 85–89. DOI: 10.1016/0920-5632(96)00418-5. arXiv: hep-ph/9601272.

[68] K. Melnikov and V. G. Serbo. "New type of beam size effect and the W boson production at mu+ mu- colliders". In: *Phys. Rev. Lett.* 76 (1996), pp. 3263–3266. DOI: 10.1103/PhysRevLett.76.3263. arXiv: hep-ph/9601221.

[69] Francesca Borzumati and Gerhard A. Schuler. "Real and virtual photon contributions to inelastic e p scattering". In: *Z. Phys. C* 58 (1993), pp. 139–152. DOI: 10.1007/BF01554087. arXiv: hep-ph/9211271.

[70] P. Aurenche et al. "Jets in photon-photon collisions: from TRISTAN to J/N-LC". In: *Prog. Theor. Phys.* 92 (1994), pp. 175–188. DOI: 10.1143/PTP.92.175. arXiv: hep-ph/9401269.

[71] Manuel Drees and Rohini M. Godbole. "Virtual photon structure functions and the parton content of the electron". In: *Phys. Rev. D* 50 (1994), pp. 3124–3133. DOI: 10.1103/PhysRevD.50.3124. arXiv: hep-ph/9403229.

[72] Gerhard A. Schuler and Torbjorn Sjostrand. "Low and high mass components of the photon distribution functions". In: *Z. Phys. C* 68 (1995), pp. 607–624. DOI: 10.1007/BF01565260. arXiv: hep-ph/9503384.

[73] Gerhard A. Schuler and Torbjorn Sjostrand. "Parton distributions of the virtual photon". In: *Phys. Lett. B* 376 (1996), pp. 193–200. DOI: 10.1016/0370-2693(96)00265-1. arXiv: hep-ph/9601282.

[74] R. L. Workman et al. "Review of Particle Physics". In: *PTEP* 2022 (2022), p. 083C01. DOI: 10.1093/ptep/ptac097.

[75] Marcello Ciafaloni, Paolo Ciafaloni, and Denis Comelli. "Towards collinear evolution equations in electroweak theory". In: *Phys. Rev. Lett.* 88 (2002), p. 102001. DOI: 10.1103/PhysRevLett.88.102001. arXiv: hep-ph/0111109.

[76] F. Bloch and A. Nordsieck. "Note on the Radiation Field of the electron". In: *Phys. Rev.* 52 (1937), pp. 54–59. DOI: 10.1103/PhysRev.52.54.

[77] Marcello Ciafaloni, Paolo Ciafaloni, and Denis Comelli. "Electroweak double logarithms in inclusive observables for a generic initial state". In: *Phys. Lett. B* 501 (2001), pp. 216–222. DOI: 10.1016/S0370-2693(01)00127-7. arXiv: hep-ph/0007096.

[78] Marcello Ciafaloni, Paolo Ciafaloni, and Denis Comelli. "Electroweak Bloch-Nordsieck violation at the TeV scale: 'Strong' weak interactions?" In: *Nucl. Phys. B* 589 (2000), pp. 359–380. DOI: 10.1016/S0550-3213(00)00508-3. arXiv: hep-ph/0004071.

[79] D. Amati et al. "A Treatment of Hard Processes Sensitive to the Infrared Structure of QCD". In: *Nucl. Phys. B* 173 (1980), pp. 429–455. DOI: 10.1016/0550-3213(80)90012-7.

[80] Christian W. Bauer, Nicolas Ferland, and Bryan R. Webber. "Combining initial-state resummation with fixed-order calculations of electroweak corrections". In: *JHEP* 04 (2018), p. 125. DOI: 10.1007/JHEP04(2018)125. arXiv: 1712.07147 [hep-ph].

[81] Aneesh V. Manohar and Wouter J. Waalewijn. "Electroweak Logarithms in Inclusive Cross Sections". In: *JHEP* 08 (2018), p. 137. DOI: 10.1007/JHEP08(2018)137. arXiv: 1802.08687 [hep-ph].

[82] Ansgar Denner and Stefano Pozzorini. "One loop leading logarithms in electroweak radiative corrections. 1. Results". In: *Eur. Phys. J. C* 18 (2001), pp. 461–480. DOI: 10.1007/s100520100551. arXiv: hep-ph/0010201.

[83] Ansgar Denner. "Electroweak radiative corrections at high-energies". In: *PoS* HEP2001 (2001). Ed. by Dezsõ Horváth, Péter Lévai, and András Patkós, p. 129. DOI: 10.22323/1.007.0129. arXiv: hep-ph/0110155.

[84] Davide Pagani and Marco Zaro. "One-loop electroweak Sudakov logarithms: a revisitation and automation". In: *JHEP* 02 (2022), p. 161. DOI: 10.1007/JHEP02(2022)161. arXiv: 2110.03714 [hep-ph].

[85] Siyu Chen et al. "Learning from radiation at a very high energy lepton collider". In: *JHEP* 05 (2022), p. 180. DOI: 10.1007/JHEP05(2022)180. arXiv: 2202.10509 [hep-ph].

[86] Junegone Chay and Taehyun Kwon. "N-jettiness for muon jet pairs in electroweak high-energy processes". In: *JHEP* 12 (2022), p. 091. DOI: 10.1007/JHEP12(2022)091. arXiv: 2207.05425 [hep-ph].

[87] Christian W. Bauer, Davide Provasoli, and Bryan R. Webber. "Standard Model Fragmentation Functions at Very High Energies". In: *JHEP* 11 (2018), p. 030. DOI: 10.1007/JHEP11(2018)030. arXiv: 1806.10157 [hep-ph].

[88] R. Michael Barnett, Howard E. Haber, and Davison E. Soper. "Ultraheavy Particle Production from Heavy Partons at Hadron Colliders". In: *Nucl. Phys. B* 306 (1988), pp. 697–745. DOI: 10.1016/0550-3213(88)90440-3.

[89] Fredrick I. Olness and Wu-Ki Tung. "When Is a Heavy Quark Not a Parton? Charged Higgs Production and Heavy Quark Mass Effects in the QCD Based Parton Model". In: *Nucl. Phys. B* 308 (1988), p. 813. DOI: 10.1016/0550-3213(88)90129-0.

[90] S. Dawson, A. Ismail, and Ian Low. "Redux on "When is the top quark a parton?"". In: *Phys. Rev. D* 90.1 (2014), p. 014005. DOI: 10.1103/PhysRevD.90.014005. arXiv: 1405.6211 [hep-ph].

[91] Tao Han, Joshua Sayre, and Susanne Westhoff. "Top-Quark Initiated Processes at High-Energy Hadron Colliders". In: *JHEP* 04 (2015), p. 145. DOI: 10.1007/JHEP04(2015)145. arXiv: 1411.2588 [hep-ph].

[92] R. N. Cahn and Sally Dawson. "Production of Very Massive Higgs Bosons". In: *Phys. Lett. B* 136 (1984). [Erratum: Phys.Lett.B 138, 464 (1984)], p. 196. DOI: 10.1016/0370-2693(84)91180-8.

[93] Sally Dawson. "The Effective W Approximation". In: *Nucl. Phys. B* 249 (1985), pp. 42–60. DOI: 10.1016/0550-3213(85)90038-0.

[94] Michael S. Chanowitz and Mary K. Gaillard. "Multiple Production of W and Z as a Signal of New Strong Interactions". In: *Phys. Lett. B* 142 (1984), pp. 85–90. DOI: 10.1016/0370-2693(84)91141-9.

[95] Gordon L. Kane, W. W. Repko, and W. B. Rolnick. "The Effective W+-, Z0 Approximation for High-Energy Collisions". In: *Phys. Lett. B* 148 (1984), pp. 367–372. DOI: 10.1016/0370-2693(84)90105-9.

[96] Zoltan Kunszt and Davison E. Soper. "On the Validity of the Effective W Approximation". In: *Nucl. Phys. B* 296 (1988), pp. 253–289. DOI: 10.1016/0550-3213(88)90673-6.

[97] Pascal Borel et al. "Probing the Scattering of Equivalent Electroweak Bosons". In: *JHEP* 06 (2012), p. 122. DOI: 10.1007/JHEP06(2012)122. arXiv: 1202.1904 [hep-ph].

[98] Dario Buttazzo et al. "Fusing Vectors into Scalars at High Energy Lepton Colliders". In: *JHEP* 11 (2018), p. 144. DOI: 10.1007/JHEP11(2018)144. arXiv: 1807.04743 [hep-ph].

[99] David Marzocca and Alfredo Stanzione. "On the impact of the mixed Z/γ PDF at muon colliders". In: *In progress* (2024).

[100] Nazar Bartosik et al. "Detector and Physics Performance at a Muon Collider". In: *JINST* 15.05 (2020), P05001. DOI: 10.1088/1748-0221/15/05/P05001. arXiv: 2001.04431 [hep-ex].

[101] Paolo Andreetto et al. "Higgs Physics at a $\sqrt{s} = 3$ TeV Muon Collider with detailed detector simulation". In: (May 2024). arXiv: 2405.19314 [hep-ex].

[102] Tao Han et al. "Electroweak couplings of the Higgs boson at a multi-TeV muon collider". In: *Phys. Rev. D* 103.1 (2021), p. 013002. DOI: 10.1103/PhysRevD.103.013002. arXiv: 2008.12204 [hep-ph].

[103] Matthew Forslund and Patrick Meade. "High precision higgs from high energy muon colliders". In: *JHEP* 08 (2022), p. 185. DOI: 10.1007/JHEP08(2022)185. arXiv: 2203.09425 [hep-ph].

[104] Matthew Forslund and Patrick Meade. "Precision Higgs width and couplings with a high energy muon collider". In: *JHEP* 01 (2024), p. 182. DOI: 10.1007/JHEP01(2024)182. arXiv: 2308.02633 [hep-ph].

[105] B. C. Allanach, Ben Gripaios, and Tevong You. "The case for future hadron colliders from $B \to K^{(*)}\mu^+\mu^-$ decays". In: *JHEP* 03 (2018), p. 021. DOI: 10.1007/JHEP03(2018)021. arXiv: 1710.06363 [hep-ph].

[106] B. C. Allanach et al. "Hadron collider sensitivity to fat flavourful Z's for $R_{K^{(*)}}$". In: *JHEP* 03 (2019), p. 137. DOI: 10.1007/JHEP03(2019)137. arXiv: 1810.02166 [hep-ph].

[107] B. C. Allanach, Tyler Corbett, and Maeve Madigan. "Sensitivity of Future Hadron Colliders to Leptoquark Pair Production in the Di-Muon Di-Jets Channel". In: *Eur. Phys. J. C* 80.2 (2020), p. 170. DOI: 10.1140/epjc/s10052-020-7722-3. arXiv: 1911.04455 [hep-ph].

[108] Bradley Garland et al. "Probing B-Anomalies via Dimuon Tails at a Future Collider". In: (Dec. 2021). arXiv: 2112.05127 [hep-ph].

[109] Clement Helsens et al. "Heavy resonances at energy-frontier hadron colliders". In: *Eur. Phys. J. C* 79 (2019), p. 569. DOI: 10.1140/epjc/s10052-019-7062-3. arXiv: 1902.11217 [hep-ph].

[110] Priyotosh Bandyopadhyay et al. "Distinguishing Leptoquarks at the LHC/FCC". In: *Nucl. Phys. B* 971 (2021), p. 115524. DOI: 10.1016/j.nuclphysb.2021.115524. arXiv: 2007.12997 [hep-ph].

[111] Priyotosh Bandyopadhyay, Anirban Karan, and Rusa Mandal. "Distinguishing signatures of scalar leptoquarks at hadron and muon colliders". In: (Aug. 2021). arXiv: 2108.06506 [hep-ph].

[112] Pouya Asadi et al. "Searching for leptoquarks at future muon colliders". In: *JHEP* 10 (2021), p. 182. DOI: 10.1007/JHEP10(2021)182. arXiv: 2104.05720 [hep-ph].

[113] Guo-yuan Huang, Farinaldo S. Queiroz, and Werner Rodejohann. "Gauged $L_\mu - L_\tau$ at a muon collider". In: *Phys. Rev. D* 103.9 (2021), p. 095005. DOI: 10.1103/PhysRevD.103.095005. arXiv: 2101.04956 [hep-ph].

[114] Guo-yuan Huang et al. "Probing the RK(*) anomaly at a muon collider". In: *Phys. Rev. D* 105.1 (2022), p. 015013. DOI: 10.1103/PhysRevD.105.015013. arXiv: 2103.01617 [hep-ph].

[115] Sitian Qian et al. "Searching for heavy leptoquarks at a muon collider". In: *JHEP* 12 (2021), p. 047. DOI: 10.1007/JHEP12(2021)047. arXiv: 2109.01265 [hep-ph].

[116] Rodolfo Capdevilla et al. "No-lose theorem for discovering the new physics of $(g-2)_\mu$ at muon colliders". In: *Phys. Rev. D* 105.1 (2022), p. 015028. DOI: 10.1103/PhysRevD.105.015028. arXiv: 2101.10334 [hep-ph].

[117] Jorge De Blas et al. "The physics case of a 3 TeV muon collider stage". In: *2022 Snowmass Summer Study*. Mar. 2022. arXiv: 2203.07261 [hep-ph].

[118] Wolfgang Altmannshofer, Sri Aditya Gadam, and Stefano Profumo. "Snowmass White Paper: Probing New Physics with $\mu^+\mu^- \to bs$ at a Muon Collider". In: *2022 Snowmass Summer Study*. Mar. 2022. arXiv: 2203.07495 [hep-ph].

[119] A. Cerri et al. "Report from Working Group 4: Opportunities in Flavour Physics at the HL-LHC and HE-LHC". In: *CERN Yellow Rep. Monogr.* 7 (2019). Ed. by Andrea Dainese et al., pp. 867–1158. DOI: 10.23731/CYRM-2019-007.867. arXiv: 1812.07638 [hep-ph].

[120] Xabier Cid Vidal et al. "Report from Working Group 3: Beyond the Standard Model physics at the HL-LHC and HE-LHC". In: *CERN Yellow Rep. Monogr.* 7 (2019). Ed. by Andrea Dainese et al., pp. 585–865. DOI: 10.23731/CYRM-2019-007.585. arXiv: 1812.07831 [hep-ph].

[121] I. Doršner et al. "Physics of leptoquarks in precision experiments and at particle colliders". In: *Phys. Rept.* 641 (2016), pp. 1–68. DOI: 10.1016/j.physrep.2016.06.001. arXiv: 1603.04993 [hep-ph].

[122] R Aaij et al. "Measurement of Form-Factor-Independent Observables in the Decay $B^0 \to K^{*0}\mu^+\mu^-$". In: *Phys. Rev. Lett.* 111 (2013), p. 191801. DOI: 10.1103/PhysRevLett.111.191801. arXiv: 1308.1707 [hep-ex].

[123] R. Aaij et al. "Differential branching fractions and isospin asymmetries of $B \to K^{(*)}\mu^+\mu^-$ decays". In: *JHEP* 06 (2014), p. 133. DOI: 10.1007/JHEP06(2014)133. arXiv: 1403.8044 [hep-ex].

[124] Roel Aaij et al. "Angular analysis and differential branching fraction of the decay $B_s^0 \to \phi\mu^+\mu^-$". In: *JHEP* 09 (2015), p. 179. DOI: 10.1007/JHEP09(2015)179. arXiv: 1506.08777 [hep-ex].

[125] Roel Aaij et al. "Angular analysis of the $B^0 \to K^{*0}\mu^+\mu^-$ decay using 3 fb^{-1} of integrated luminosity". In: *JHEP* 02 (2016), p. 104. DOI: 10.1007/JHEP02(2016)104. arXiv: 1512.04442 [hep-ex].

[126] Roel Aaij et al. "Measurements of the S-wave fraction in $B^0 \to K^+\pi^-\mu^+\mu^-$ decays and the $B^0 \to K^*(892)^0\mu^+\mu^-$ differential branching fraction". In: *JHEP* 11 (2016). [Erratum: JHEP 04, 142 (2017)], p. 047. DOI: 10.1007/JHEP11(2016)047. arXiv: 1606.04731 [hep-ex].

[127] Morad Aaboud et al. "Study of the rare decays of B_s^0 and B^0 mesons into muon pairs using data collected during 2015 and 2016 with the ATLAS detector". In: *JHEP* 04 (2019), p. 098. DOI: 10.1007/JHEP04(2019)098. arXiv: 1812.03017 [hep-ex].

[128] Roel Aaij et al. "Measurement of CP-Averaged Observables in the $B^0 \to K^{*0}\mu^+\mu^-$ Decay". In: *Phys. Rev. Lett.* 125.1 (2020), p. 011802. DOI: 10.1103/PhysRevLett.125.011802. arXiv: 2003.04831 [hep-ex].

[129] "Combination of the ATLAS, CMS and LHCb results on the $B^0_{(s)} \to \mu^+\mu^-$ decays". In: (2020).

[130] Roel Aaij et al. "Angular Analysis of the $B^+ \to K^{*+}\mu^+\mu^-$ Decay". In: *Phys. Rev. Lett.* 126.16 (2021), p. 161802. DOI: 10.1103/PhysRevLett.126.161802. arXiv: 2012.13241 [hep-ex].

[131] Roel Aaij et al. "Branching Fraction Measurements of the Rare $B_s^0 \to \phi\mu^+\mu^-$ and $B_s^0 \to f_2'(1525)\mu^+\mu^-$ Decays". In: *Phys. Rev. Lett.* 127.15 (2021), p. 151801. DOI: 10.1103/PhysRevLett.127.151801. arXiv: 2105.14007 [hep-ex].

[132] Roel Aaij et al. "Measurement of the $B_s^0 \to \mu^+\mu^-$ decay properties and search for the $B^0 \to \mu^+\mu^-$ and $B_s^0 \to \mu^+\mu^-\gamma$ decays". In: *Phys. Rev. D* 105.1 (2022), p. 012010. DOI: 10.1103/PhysRevD.105.012010. arXiv: 2108.09283 [hep-ex].

[133] R. Aaij et al. "Analysis of Neutral B-Meson Decays into Two Muons". In: *Phys. Rev. Lett.* 128.4 (2022), p. 041801. DOI: 10.1103/PhysRevLett.128.041801. arXiv: 2108.09284 [hep-ex].

[134] Roel Aaij et al. "Test of lepton universality using $B^+ \to K^+\ell^+\ell^-$ decays". In: *Phys. Rev. Lett.* 113 (2014), p. 151601. DOI: 10.1103/PhysRevLett.113.151601. arXiv: 1406.6482 [hep-ex].

[135] Roel Aaij et al. "Search for lepton-universality violation in $B^+ \to K^+\ell^+\ell^-$ decays". In: *Phys. Rev. Lett.* 122.19 (2019), p. 191801. DOI: 10.1103/PhysRevLett.122.191801. arXiv: 1903.09252 [hep-ex].

[136] A. Abdesselam et al. "Test of Lepton-Flavor Universality in $B \to K^*\ell^+\ell^-$ Decays at Belle". In: *Phys. Rev. Lett.* 126.16 (2021), p. 161801. DOI: 10.1103/PhysRevLett.126.161801. arXiv: 1904.02440 [hep-ex].

[137] J. P. Lees et al. "Evidence for an excess of $\bar{B} \to D^{(*)}\tau^-\bar{\nu}_\tau$ decays". In: *Phys. Rev. Lett.* 109 (2012), p. 101802. DOI: 10.1103/PhysRevLett.109.101802. arXiv: 1205.5442 [hep-ex].

[138] Marzia Bordone, Gino Isidori, and Andrea Pattori. "On the Standard Model predictions for R_K and R_{K^*}". In: *Eur. Phys. J. C* 76.8 (2016), p. 440. DOI: 10.1140/epjc/s10052-016-4274-7. arXiv: 1605.07633 [hep-ph].

[139] Aleksandr Azatov et al. "New physics in b $\to$ s$\mu\mu$: FCC-hh or a muon collider?" In: *JHEP* 10 (2022), p. 149. DOI: 10.1007/JHEP10(2022)149. arXiv: 2205.13552 [hep-ph].

[140] Gino Isidori et al. "On the significance of new physics in $b \to \ell^+\ell^-$ decays". In: *Phys. Lett. B* 822 (2021), p. 136644. DOI: 10.1016/j.physletb.2021.136644. arXiv: 2104.05631 [hep-ph].

[141] Luca Di Luzio and Marco Nardecchia. "What is the scale of new physics behind the B-flavour anomalies?" In: *Eur. Phys. J. C* 77.8 (2017), p. 536. DOI: 10.1140/epjc/s10052-017-5118-9. arXiv: 1706.01868 [hep-ph].

[142] Andrzej J. Buras and Jennifer Girrbach. "Left-handed Z' and Z FCNC quark couplings facing new $b \to s\mu^+\mu^-$ data". In: *JHEP* 12 (2013), p. 009. DOI: 10.1007/JHEP12(2013)009. arXiv: 1309.2466 [hep-ph].

[143] Wolfgang Altmannshofer et al. "Quark flavor transitions in $L_\mu - L_\tau$ models". In: *Phys. Rev. D* 89 (2014), p. 095033. DOI: 10.1103/PhysRevD.89.095033. arXiv: 1403.1269 [hep-ph].

[144] Admir Greljo, Gino Isidori, and David Marzocca. "On the breaking of Lepton Flavor Universality in B decays". In: *JHEP* 07 (2015), p. 142. DOI: 10.1007/JHEP07(2015)142. arXiv: 1506.01705 [hep-ph].

[145] Andreas Crivellin, Giancarlo D'Ambrosio, and Julian Heeck. "Explaining $h \to \mu^\pm\tau^\mp$, $B \to K^*\mu^+\mu^-$ and $B \to K\mu^+\mu^-/B \to Ke^+e^-$ in a two-Higgs-doublet model with gauged $L_\mu - L_\tau$". In: *Phys. Rev. Lett.* 114 (2015), p. 151801. DOI: 10.1103/PhysRevLett.114.151801. arXiv: 1501.00993 [hep-ph].

[146] Alejandro Celis et al. "Family nonuniversal Z' models with protected flavor-changing interactions". In: *Phys. Rev. D* 92.1 (2015), p. 015007. DOI: 10.1103/PhysRevD.92.015007. arXiv: 1505.03079 [hep-ph].

[147] Adam Falkowski, Marco Nardecchia, and Robert Ziegler. "Lepton Flavor Non-Universality in B-meson Decays from a U(2) Flavor Model". In: *JHEP* 11 (2015), p. 173. DOI: 10.1007/JHEP11(2015)173. arXiv: 1509.01249 [hep-ph].

[148] Andreas Crivellin et al. "Lepton Flavor Non-Universality in B decays from Dynamical Yukawas". In: *Phys. Lett. B* 766 (2017), pp. 77–85. DOI: 10.1016/j.physletb.2016.12.057. arXiv: 1611.02703 [hep-ph].

[149] Sofiane M. Boucenna et al. "Phenomenology of an $SU(2) \times SU(2) \times U(1)$ model with lepton-flavour non-universality". In: *JHEP* 12 (2016), p. 059. DOI: 10.1007/JHEP12(2016)059. arXiv: 1608.01349 [hep-ph].

[150] P. Ko et al. "LHCb anomaly and B physics in flavored Z' models with flavored Higgs doublets". In: *Phys. Rev. D* 95.11 (2017), p. 115040. DOI: 10.1103/PhysRevD.95.115040. arXiv: 1702.08666 [hep-ph].

[151] Rodrigo Alonso et al. "Flavoured $B - L$ local symmetry and anomalous rare B decays". In: *Phys. Lett. B* 774 (2017), pp. 643–648. DOI: 10.1016/j.physletb.2017.10.027. arXiv: 1705.03858 [hep-ph].

[152] Rodrigo Alonso et al. "Anomaly-free local horizontal symmetry and anomaly-full rare B-decays". In: *Phys. Rev. D* 96.7 (2017), p. 071701. DOI: 10.1103/PhysRevD.96.071701. arXiv: 1704.08158 [hep-ph].

[153] Disha Bhatia, Sabyasachi Chakraborty, and Amol Dighe. "Neutrino mixing and R_K anomaly in $U(1)_X$ models: a bottom-up approach". In: *JHEP* 03 (2017), p. 117. DOI: 10.1007/JHEP03(2017)117. arXiv: 1701.05825 [hep-ph].

[154] Ligong Bian, Hyun Min Lee, and Chan Beom Park. "B-meson anomalies and Higgs physics in flavored $U(1)'$ model". In: *Eur. Phys. J. C* 78.4 (2018), p. 306. DOI: 10.1140/epjc/s10052-018-5777-1. arXiv: 1711.08930 [hep-ph].

[155] Stephen F. King. "$R_{K^{(*)}}$ and the origin of Yukawa couplings". In: *JHEP* 09 (2018), p. 069. DOI: 10.1007/JHEP09(2018)069. arXiv: 1806.06780 [hep-ph].

[156] Cesar Bonilla et al. "$U(1)_{B_3-3L_\mu}$ gauge symmetry as a simple description of $b \to s$ anomalies". In: *Phys. Rev. D* 98.9 (2018), p. 095002. DOI: 10.1103/PhysRevD.98.095002. arXiv: 1705.00915 [hep-ph].

[157] Lorenzo Calibbi et al. "Z' models with less-minimal flavour violation". In: *Phys. Rev. D* 101.9 (2020), p. 095003. DOI: 10.1103/PhysRevD.101.095003. arXiv: 1910.00014 [hep-ph].

[158] John Ellis, Malcolm Fairbairn, and Patrick Tunney. "Anomaly-Free Models for Flavour Anomalies". In: *Eur. Phys. J. C* 78.3 (2018), p. 238. DOI: 10.1140/epjc/s10052-018-5725-0. arXiv: 1705.03447 [hep-ph].

[159] B. C. Allanach and Joe Davighi. "Third family hypercharge model for $R_{K^{(*)}}$ and aspects of the fermion mass problem". In: *JHEP* 12 (2018), p. 075. DOI: 10.1007/JHEP12(2018)075. arXiv: 1809.01158 [hep-ph].

[160] Wolfgang Altmannshofer, Joe Davighi, and Marco Nardecchia. "Gauging the accidental symmetries of the standard model, and implications for the flavor anomalies". In: *Phys. Rev. D* 101.1 (2020), p. 015004. DOI: 10.1103/PhysRevD.101.015004. arXiv: 1909.02021 [hep-ph].

[161] B. C. Allanach. "$U(1)_{B_3-L_2}$ explanation of the neutral current B-anomalies". In: *Eur. Phys. J. C* 81.1 (2021). [Erratum: Eur.Phys.J.C 81, 321 (2021)], p. 56. DOI: 10.1140/epjc/s10052-021-08855-w. arXiv: 2009.02197 [hep-ph].

[162] B. C. Allanach, J. M. Butterworth, and Tyler Corbett. "Large hadron collider constraints on some simple Z' models for $b \to s\mu^+\mu^-$ anomalies". In: *Eur. Phys. J. C* 81.12 (2021), p. 1126. DOI: 10.1140/epjc/s10052-021-09919-7. arXiv: 2110.13518 [hep-ph].

[163] Joe Davighi. "Anomalous Z' bosons for anomalous B decays". In: *JHEP* 08 (2021), p. 101. DOI: 10.1007/JHEP08(2021)101. arXiv: 2105.06918 [hep-ph].

[164] Rigo Bause et al. "B-anomalies from flavorful U(1)′ extensions, safely". In: *Eur. Phys. J. C* 82.1 (2022), p. 42. DOI: 10.1140/epjc/s10052-021-09957-1. arXiv: 2109.06201 [hep-ph].

[165] Andrei Angelescu et al. "Single leptoquark solutions to the B-physics anomalies". In: *Phys. Rev. D* 104.5 (2021), p. 055017. DOI: 10.1103/PhysRevD.104.055017. arXiv: 2103.12504 [hep-ph].

[166] Dario Buttazzo, Roberto Franceschini, and Andrea Wulzer. "Two Paths Towards Precision at a Very High Energy Lepton Collider". In: *JHEP* 05 (2021), p. 219. DOI: 10.1007/JHEP05(2021)219. arXiv: 2012.11555 [hep-ph].

[167] Diego Becciolini et al. "Constraining new colored matter from the ratio of 3 to 2 jets cross sections at the LHC". In: *Phys. Rev. D* 91.1 (2015). [Addendum: Phys.Rev.D 92, 079905 (2015)], p. 015010. DOI: 10.1103/PhysRevD.91.015010. arXiv: 1403.7411 [hep-ph].

[168] Daniele S. M. Alves et al. "Running Electroweak Couplings as a Probe of New Physics". In: *JHEP* 02 (2015), p. 007. DOI: 10.1007/JHEP02(2015)007. arXiv: 1410.6810 [hep-ph].

[169] Darius A. Faroughy, Admir Greljo, and Jernej F. Kamenik. "Confronting lepton flavor universality violation in B decays with high-p_T tau lepton searches at LHC". In: *Phys. Lett. B* 764 (2017), pp. 126–134. DOI: 10.1016/j.physletb.2016.11.011. arXiv: 1609.07138 [hep-ph].

[170] Rodolfo Capdevilla et al. "Systematically testing singlet models for $(g-2)_\mu$". In: *JHEP* 04 (2022), p. 129. DOI: 10.1007/JHEP04(2022)129. arXiv: 2112.08377 [hep-ph].

[171] Admir Greljo and David Marzocca. "High-p_T dilepton tails and flavor physics". In: *Eur. Phys. J. C* 77.8 (2017), p. 548. DOI: 10.1140/epjc/s10052-017-5119-8. arXiv: 1704.09015 [hep-ph].

[172] Vincenzo Cirigliano, Martin Gonzalez-Alonso, and Michael L. Graesser. "Non-standard Charged Current Interactions: beta decays versus the LHC". In: *JHEP* 02 (2013), p. 046. DOI: 10.1007/JHEP02(2013)046. arXiv: 1210.4553 [hep-ph].

[173] Jorge de Blas, Mikael Chala, and Jose Santiago. "Global Constraints on Lepton-Quark Contact Interactions". In: *Phys. Rev. D* 88 (2013), p. 095011. DOI: 10.1103/PhysRevD.88.095011. arXiv: 1307.5068 [hep-ph].

[174] Martín González-Alonso and Jorge Martin Camalich. "Global Effective-Field-Theory analysis of New-Physics effects in (semi)leptonic kaon decays". In: *JHEP* 12 (2016), p. 052. DOI: 10.1007/JHEP12(2016)052. arXiv: 1605.07114 [hep-ph].

[175] Vincenzo Cirigliano et al. "Hadronic τ Decays as New Physics Probes in the LHC Era". In: *Phys. Rev. Lett.* 122.22 (2019), p. 221801. DOI: 10.1103/PhysRevLett.122.221801. arXiv: 1809.01161 [hep-ph].

[176] Admir Greljo, Jorge Martin Camalich, and José David Ruiz-Álvarez. "Mono-τ Signatures at the LHC Constrain Explanations of B-decay Anomalies". In: *Phys. Rev. Lett.* 122.13 (2019), p. 131803. DOI: 10.1103/PhysRevLett.122.131803. arXiv: 1811.07920 [hep-ph].

[177] Saurabh Bansal et al. "Hunting leptoquarks in monolepton searches". In: *Phys. Rev. D* 98.1 (2018), p. 015037. DOI: 10.1103/PhysRevD.98.015037. arXiv: 1806.02370 [hep-ph].

[178] Andrei Angelescu, Darius A. Faroughy, and Olcyr Sumensari. "Lepton Flavor Violation and Dilepton Tails at the LHC". In: *Eur. Phys. J. C* 80.7 (2020), p. 641. DOI: 10.1140/epjc/s10052-020-8210-5. arXiv: 2002.05684 [hep-ph].

[179] Marco Farina et al. "Energy helps accuracy: electroweak precision tests at hadron colliders". In: *Phys. Lett. B* 772 (2017), pp. 210–215. DOI: 10.1016/j.physletb.2017.06.043. arXiv: 1609.08157 [hep-ph].

[180] Simone Alioli et al. "Catching a New Force by the Tail". In: *Phys. Rev. Lett.* 120.10 (2018), p. 101801. DOI: 10.1103/PhysRevLett.120.101801. arXiv: 1712.02347 [hep-ph].

[181] Nirmal Raj. "Anticipating nonresonant new physics in dilepton angular spectra at the LHC". In: *Phys. Rev. D* 95.1 (2017), p. 015011. DOI: 10.1103/PhysRevD.95.015011. arXiv: 1610.03795 [hep-ph].

[182] Martin Schmaltz and Yi-Ming Zhong. "The leptoquark Hunter's guide: large coupling". In: *JHEP* 01 (2019), p. 132. DOI: 10.1007/JHEP01(2019)132. arXiv: 1810.10017 [hep-ph].

[183] G. Brooijmans et al. "Les Houches 2019 Physics at TeV Colliders: New Physics Working Group Report". In: *11th Les Houches Workshop on Physics at TeV Colliders: PhysTeV Les Houches*. Feb. 2020. arXiv: 2002.12220 [hep-ph].

[184] Riccardo Torre, Lorenzo Ricci, and Andrea Wulzer. "On the W&Y interpretation of high-energy Drell-Yan measurements". In: *JHEP* 02 (2021), p. 144. DOI: 10.1007/JHEP02(2021)144. arXiv: 2008.12978 [hep-ph].

[185] Javier Fuentes-Martin et al. "Charm physics confronts high-p_T lepton tails". In: *JHEP* 11 (2020), p. 080. DOI: 10.1007/JHEP11(2020)080. arXiv: 2003.12421 [hep-ph].

[186] S. Alioli et al. "Right-handed charged currents in the era of the Large Hadron Collider". In: *JHEP* 05 (2017), p. 086. DOI: 10.1007/JHEP05(2017)086. arXiv: 1703.04751 [hep-ph].

[187] Simone Alioli et al. "Precision Probes of QCD at High Energies". In: *JHEP* 07 (2017), p. 097. DOI: 10.1007/JHEP07(2017)097. arXiv: 1706.03068 [hep-ph].

[188] Simone Alioli et al. "NLO QCD corrections to SM-EFT dilepton and electroweak Higgs boson production, matched to parton shower in POWHEG". In: *JHEP* 08 (2018), p. 205. DOI: 10.1007/JHEP08(2018)205. arXiv: 1804.07407 [hep-ph].

[189] Simone Alioli et al. "Novel angular dependence in Drell-Yan lepton production via dimension-8 operators". In: *Phys. Lett. B* 809 (2020), p. 135703. DOI: 10.1016/j.physletb.2020.135703. arXiv: 2003.11615 [hep-ph].

[190] Giuliano Panico, Lorenzo Ricci, and Andrea Wulzer. "High-energy EFT probes with fully differential Drell-Yan measurements". In: *JHEP* 07 (2021), p. 086. DOI: 10.1007/JHEP07(2021)086. arXiv: 2103.10532 [hep-ph].

[191] Albert M Sirunyan et al. "Search for resonant and nonresonant new phenomena in high-mass dilepton final states at $\sqrt{s} = 13$ TeV". In: *JHEP* 07 (2021), p. 208. DOI: 10.1007/JHEP07(2021)208. arXiv: 2103.02708 [hep-ex].

[192] "Search for new phenomena in final states with two leptons and one or no b-tagged jets at $\sqrt{s} = 13$ TeV using the ATLAS detector". In: (Mar. 2021).

[193] David Marzocca, Ui Min, and Minho Son. "Bottom-Flavored Mono-Tau Tails at the LHC". In: *JHEP* 12 (2020), p. 035. DOI: 10.1007/JHEP12(2020)035. arXiv: 2008.07541 [hep-ph].

[194] Yoav Afik et al. "Searching for New Physics with $b\bar{b}\ell^+\ell^-$ contact interactions". In: *Phys. Lett. B* 807 (2020), p. 135541. DOI: 10.1016/j.physletb.2020.135541. arXiv: 1912.00425 [hep-ex].

[195] Alexandre Alves et al. "Indirect and monojet constraints on scalar leptoquarks". In: *Phys. Rev. D* 99.9 (2019), p. 095005. DOI: 10.1103/PhysRevD.99.095005. arXiv: 1812.08632 [hep-ph].

[196] Admir Greljo et al. "Parton distributions in the SMEFT from high-energy Drell-Yan tails". In: *JHEP* 07 (2021), p. 122. DOI: 10.1007/JHEP07(2021)122. arXiv: 2104.02723 [hep-ph].

[197] Johannes Blumlein, Edward Boos, and Alexander Kryukov. "Leptoquark pair production in hadronic interactions". In: *Z. Phys. C* 76 (1997), pp. 137–153. DOI: 10.1007/s002880050538. arXiv: hep-ph/9610408.

[198] M. Kramer et al. "Pair production of scalar leptoquarks at the Tevatron". In: *Phys. Rev. Lett.* 79 (1997), pp. 341–344. DOI: 10.1103/PhysRevLett.79.341. arXiv: hep-ph/9704322.

[199] M. Kramer et al. "Pair production of scalar leptoquarks at the CERN LHC". In: *Phys. Rev. D* 71 (2005), p. 057503. DOI: 10.1103/PhysRevD.71.057503. arXiv: hep-ph/0411038.

[200] Bastian Diaz, Martin Schmaltz, and Yi-Ming Zhong. "The leptoquark Hunter's guide: Pair production". In: *JHEP* 10 (2017), p. 097. DOI: 10.1007/JHEP10(2017)097. arXiv: 1706.05033 [hep-ph].

[201] Ilja Doršner and Admir Greljo. "Leptoquark toolbox for precision collider studies". In: *JHEP* 05 (2018), p. 126. DOI: 10.1007/JHEP05(2018)126. arXiv: 1801.07641 [hep-ph].

[202] Christoph Borschensky et al. "Scalar leptoquark pair production at hadron colliders". In: *Phys. Rev. D* 101.11 (2020), p. 115017. DOI: 10.1103/PhysRevD.101.115017. arXiv: 2002.08971 [hep-ph].

[203] Ilja Dorsner, Svjetlana Fajfer, and Admir Greljo. "Cornering Scalar Leptoquarks at LHC". In: *JHEP* 10 (2014), p. 154. DOI: 10.1007/JHEP10(2014)154. arXiv: 1406.4831 [hep-ph].

[204] Christoph Borschensky et al. "Scalar leptoquark pair production at the LHC: precision predictions in the era of flavour anomalies". In: *JHEP* 02 (2022), p. 157. DOI: 10.1007/JHEP02(2022)157. arXiv: 2108.11404 [hep-ph].

[205] J. B. Hammett and D. A. Ross. "NLO Leptoquark Production and Decay: The Narrow-Width Approximation and Beyond". In: *JHEP* 07 (2015), p. 148. DOI: 10.1007/JHEP07(2015)148. arXiv: 1501.06719 [hep-ph].

[206] Tanumoy Mandal, Subhadip Mitra, and Satyajit Seth. "Single Productions of Colored Particles at the LHC: An Example with Scalar Leptoquarks". In: *JHEP* 07 (2015), p. 028. DOI: 10.1007/JHEP07(2015)028. arXiv: 1503.04689 [hep-ph].

[207] J. Ohnemus et al. "Single leptoquark production at hadron colliders". In: *Phys. Lett. B* 334 (1994), pp. 203–207. DOI: 10.1016/0370-2693(94)90612-2. arXiv: hep-ph/9406235.

[208] Luca Buonocore et al. "Lepton-Quark Collisions at the Large Hadron Collider". In: *Phys. Rev. Lett.* 125.23 (2020), p. 231804. DOI: 10.1103/PhysRevLett.125.231804. arXiv: 2005.06475 [hep-ph].

[209] Admir Greljo and Nudzeim Selimovic. "Lepton-Quark Fusion at Hadron Colliders, precisely". In: *JHEP* 03 (2021), p. 279. DOI: 10.1007/JHEP03(2021)279. arXiv: 2012.02092 [hep-ph].

[210] Riccardo Barbieri et al. "Electroweak symmetry breaking after LEP-1 and LEP-2". In: *Nucl. Phys. B* 703 (2004), pp. 127–146. DOI: 10.1016/j.nuclphysb.2004.10.014. arXiv: hep-ph/0405040.

[211] Albert M Sirunyan et al. "Search for resonant and nonresonant new phenomena in high-mass dilepton final states at $\sqrt{s} = 13$ TeV". In: *JHEP* 07 (2021), p. 208. DOI: 10.1007/JHEP07(2021)208. arXiv: 2103.02708 [hep-ex].

[212] Rodrigo Alonso et al. "Renormalization Group Evolution of the Standard Model Dimension Six Operators III: Gauge Coupling Dependence and Phenomenology". In: *JHEP* 04 (2014), p. 159. DOI: 10.1007/JHEP04(2014)159. arXiv: 1312.2014 [hep-ph].

[213] Alejandro Celis et al. "Gauge-invariant implications of the LHCb measurements on lepton-flavor nonuniversality". In: *Phys. Rev. D* 96.3 (2017), p. 035026. DOI: 10.1103/PhysRevD.96.035026. arXiv: 1704.05672 [hep-ph].

[214] M. Bona et al. "Model-independent constraints on $\Delta F = 2$ operators and the scale of new physics". In: *JHEP* 03 (2008), p. 049. DOI: 10.1088/1126-6708/2008/03/049. arXiv: 0707.0636 [hep-ph].

[215] Luca Silvestrini and Mauro Valli. "Model-independent Bounds on the Standard Model Effective Theory from Flavour Physics". In: *Phys. Lett. B* 799 (2019), p. 135062. DOI: 10.1016/j.physletb.2019.135062. arXiv: 1812.10913 [hep-ph].

[216] Admir Greljo et al. "Muonic force behind flavor anomalies". In: *JHEP* 04 (2022), p. 151. DOI: 10.1007/JHEP04(2022)151. arXiv: 2107.07518 [hep-ph].

[217] Marzia Bordone, Gino Isidori, and Sokratis Trifinopoulos. "Semileptonic B-physics anomalies: A general EFT analysis within $U(2)^n$ flavor symmetry". In: *Phys. Rev. D* 96.1 (2017), p. 015038. DOI: 10.1103/PhysRevD.96.015038. arXiv: 1702.07238 [hep-ph].

[218] Dario Buttazzo et al. "B-physics anomalies: a guide to combined explanations". In: *JHEP* 11 (2017), p. 044. DOI: 10.1007/JHEP11(2017)044. arXiv: 1706.07808 [hep-ph].

[219] Javier Fuentes-Martín et al. "With or without U(2)? Probing non-standard flavor and helicity structures in semileptonic B decays". In: *Phys. Lett. B* 800 (2020), p. 135080. DOI: 10.1016/j.physletb.2019.135080. arXiv: 1909.02519 [hep-ph].

[220] David Marzocca, Sokratis Trifinopoulos, and Elena Venturini. "From B-meson anomalies to Kaon physics with scalar leptoquarks". In: *Eur. Phys. J. C* 82.4 (2022), p. 320. DOI: 10.1140/epjc/s10052-022-10271-7. arXiv: 2106.15630 [hep-ph].

[221] Gudrun Hiller and Martin Schmaltz. "R_K and future $b \to s\ell\ell$ physics beyond the standard model opportunities". In: *Phys. Rev. D* 90 (2014), p. 054014. DOI: 10.1103/PhysRevD.90.054014. arXiv: 1408.1627 [hep-ph].

[222] Ben Gripaios, Marco Nardecchia, and S. A. Renner. "Composite leptoquarks and anomalies in B-meson decays". In: *JHEP* 05 (2015), p. 006. DOI: 10.1007/JHEP05(2015)006. arXiv: 1412.1791 [hep-ph].

[223] Ben Gripaios, M. Nardecchia, and S. A. Renner. "Linear flavour violation and anomalies in B physics". In: *JHEP* 06 (2016), p. 083. DOI: 10.1007/JHEP06(2016)083. arXiv: 1509.05020 [hep-ph].

[224] Ilja Doršner et al. "The role of the S_3 GUT leptoquark in flavor universality and collider searches". In: *JHEP* 10 (2017), p. 188. DOI: 10.1007/JHEP10(2017)188. arXiv: 1706.07779 [hep-ph].

[225] Jacky Kumar, David London, and Ryoutaro Watanabe. "Combined Explanations of the $b \to s\mu^+\mu^-$ and $b \to c\tau^-\bar{\nu}$ Anomalies: a General Model Analysis". In: *Phys. Rev. D* 99.1 (2019), p. 015007. DOI: 10.1103/PhysRevD.99.015007. arXiv: 1806.07403 [hep-ph].

[226] Ivo de Medeiros Varzielas and Jim Talbert. "Simplified Models of Flavourful Leptoquarks". In: *Eur. Phys. J. C* 79.6 (2019), p. 536. DOI: 10.1140/epjc/s10052-019-7047-2. arXiv: 1901.10484 [hep-ph].

[227] Andreas Crivellin, Dario Müller, and Francesco Saturnino. "Flavor Phenomenology of the Leptoquark Singlet-Triplet Model". In: *JHEP* 06 (2020), p. 020. DOI: 10.1007/JHEP06(2020)020. arXiv: 1912.04224 [hep-ph].

[228] Shaikh Saad. "Combined explanations of $(g-2)_\mu$, $R_{D^{(*)}}$, $R_{K^{(*)}}$ anomalies in a two-loop radiative neutrino mass model". In: *Phys. Rev. D* 102.1 (2020), p. 015019. DOI: 10.1103/PhysRevD.102.015019. arXiv: 2005.04352 [hep-ph].

[229] Valerio Gherardi, David Marzocca, and Elena Venturini. "Low-energy phenomenology of scalar leptoquarks at one-loop accuracy". In: *JHEP* 01 (2021), p. 138. DOI: 10.1007/JHEP01(2021)138. arXiv: 2008.09548 [hep-ph].

[230] Hyun Min Lee. "Leptoquark option for B-meson anomalies and leptonic signatures". In: *Phys. Rev. D* 104.1 (2021), p. 015007. DOI: 10.1103/PhysRevD.104.015007. arXiv: 2104.02982 [hep-ph].

[231] Andreas Crivellin, Dario Müller, and Toshihiko Ota. "Simultaneous explanation of $R(D^{(*)})$ and $b \to s\mu^+\mu^-$: the last scalar leptoquarks standing". In: *JHEP* 09 (2017), p. 040. DOI: 10.1007/JHEP09(2017)040. arXiv: 1703.09226 [hep-ph].

[232] Gudrun Hiller and Ivan Nisandzic. "R_K and R_{K^*} beyond the standard model". In: *Phys. Rev. D* 96.3 (2017), p. 035003. DOI: 10.1103/PhysRevD.96.035003. arXiv: 1704.05444 [hep-ph].

[233] David Marzocca. "Addressing the B-physics anomalies in a fundamental Composite Higgs Model". In: *JHEP* 07 (2018), p. 121. DOI: 10.1007/JHEP07(2018)121. arXiv: 1803.10972 [hep-ph].

[234] K. S. Babu et al. "Unified framework for B-anomalies, muon $g-2$ and neutrino masses". In: *JHEP* 03 (2021), p. 179. DOI: 10.1007/JHEP03(2021)179. arXiv: 2009.01771 [hep-ph].

[235] Shaikh Saad and Anil Thapa. "Common origin of neutrino masses and $R_{D^{(*)}}$, $R_{K^{(*)}}$ anomalies". In: *Phys. Rev. D* 102.1 (2020), p. 015014. DOI: 10.1103/PhysRevD.102.015014. arXiv: 2004.07880 [hep-ph].

[236] Admir Greljo, Peter Stangl, and Anders Eller Thomsen. "A model of muon anomalies". In: *Phys. Lett. B* 820 (2021), p. 136554. DOI: 10.1016/j.physletb.2021.136554. arXiv: 2103.13991 [hep-ph].

[237] Joe Davighi, Matthew Kirk, and Marco Nardecchia. "Anomalies and accidental symmetries: charging the scalar leptoquark under $L_\mu - L_\tau$". In: *JHEP* 12 (2020), p. 111. DOI: 10.1007/JHEP12(2020)111. arXiv: 2007.15016 [hep-ph].

[238] Claudia Cornella et al. "Reading the footprints of the B-meson flavor anomalies". In: *JHEP* 08 (2021), p. 050. DOI: 10.1007/JHEP08(2021)050. arXiv: 2103.16558 [hep-ph].

[239] Riccardo Barbieri et al. "Anomalies in B-decays and $U(2)$ flavour symmetry". In: *Eur. Phys. J. C* 76.2 (2016), p. 67. DOI: 10.1140/epjc/s10052-016-3905-3. arXiv: 1512.01560 [hep-ph].

[240] Rodrigo Alonso, Benjamín Grinstein, and Jorge Martin Camalich. "Lepton universality violation and lepton flavor conservation in B-meson decays". In: *JHEP* 10 (2015), p. 184. DOI: 10.1007/JHEP10(2015)184. arXiv: 1505.05164 [hep-ph].

[241] Lorenzo Calibbi, Andreas Crivellin, and Toshihiko Ota. "Effective Field Theory Approach to $b \to s\ell\ell^{(')}$, $B \to K^{(*)}\nu\overline{\nu}$ and $B \to D^{(*)}\tau\nu$ with Third Generation Couplings". In: *Phys. Rev. Lett.* 115 (2015), p. 181801. DOI: 10.1103/PhysRevLett.115.181801. arXiv: 1506.02661 [hep-ph].

[242] Bhubanjyoti Bhattacharya et al. "Simultaneous Explanation of the R_K and $R_{D^{(*)}}$ Puzzles: a Model Analysis". In: *JHEP* 01 (2017), p. 015. DOI: 10.1007/JHEP01(2017)015. arXiv: 1609.09078 [hep-ph].

[243] Luca Di Luzio, Admir Greljo, and Marco Nardecchia. "Gauge leptoquark as the origin of B-physics anomalies". In: *Phys. Rev. D* 96.11 (2017), p. 115011. DOI: 10.1103/PhysRevD.96.115011. arXiv: 1708.08450 [hep-ph].

[244] Admir Greljo and Ben A. Stefanek. "Third family quark–lepton unification at the TeV scale". In: *Phys. Lett. B* 782 (2018), pp. 131–138. DOI: 10.1016/j.physletb.2018.05.033. arXiv: 1802.04274 [hep-ph].

[245] Marzia Bordone et al. "A three-site gauge model for flavor hierarchies and flavor anomalies". In: *Phys. Lett. B* 779 (2018), pp. 317–323. DOI: 10.1016/j.physletb.2018.02.011. arXiv: 1712.01368 [hep-ph].

[246] Marzia Bordone et al. "Low-energy signatures of the PS^3 model: from B-physics anomalies to LFV". In: *JHEP* 10 (2018), p. 148. DOI: 10.1007/JHEP10(2018)148. arXiv: 1805.09328 [hep-ph].

[247] Claudia Cornella, Javier Fuentes-Martin, and Gino Isidori. "Revisiting the vector leptoquark explanation of the B-physics anomalies". In: *JHEP* 07 (2019), p. 168. DOI: 10.1007/JHEP07(2019)168. arXiv: 1903.11517 [hep-ph].

[248] Bartosz Fornal, Sri Aditya Gadam, and Benjamin Grinstein. "Left-Right SU(4) Vector Leptoquark Model for Flavor Anomalies". In: *Phys. Rev. D* 99.5 (2019), p. 055025. DOI: 10.1103/PhysRevD.99.055025. arXiv: 1812.01603 [hep-ph].

[249] Monika Blanke and Andreas Crivellin. "B Meson Anomalies in a Pati-Salam Model within the Randall-Sundrum Background". In: *Phys. Rev. Lett.* 121.1 (2018), p. 011801. DOI: 10.1103/PhysRevLett.121.011801. arXiv: 1801.07256 [hep-ph].

[250] Javier Fuentes-Martín et al. "Vector Leptoquarks Beyond Tree Level". In: *Phys. Rev. D* 101.3 (2020), p. 035024. DOI: 10.1103/PhysRevD.101.035024. arXiv: 1910.13474 [hep-ph].

[251] Diego Guadagnoli, Meril Reboud, and Peter Stangl. "The Dark Side of 4321". In: *JHEP* 10 (2020), p. 084. DOI: 10.1007/JHEP10(2020)084. arXiv: 2005.10117 [hep-ph].

[252] Javier Fuentes-Martín and Peter Stangl. "Third-family quark-lepton unification with a fundamental composite Higgs". In: *Phys. Lett. B* 811 (2020), p. 135953. DOI: 10.1016/j.physletb.2020.135953. arXiv: 2004.11376 [hep-ph].

[253] Javier Fuentes-Martín, Mario Reig, and Avelino Vicente. "Strong CP problem with low-energy emergent QCD: The 4321 case". In: *Phys. Rev. D* 100.11 (2019), p. 115028. DOI: 10.1103/PhysRevD.100.115028. arXiv: 1907.02550 [hep-ph].

[254] Jordan Bernigaud et al. "LHC Signatures of τ-Flavoured Vector Leptoquarks". In: (Dec. 2021). arXiv: 2112.12129 [hep-ph].

[255] Javier Fuentes-Martín et al. "Vector leptoquarks beyond tree level. II. $\mathcal{O}(\alpha_s)$ corrections and radial modes". In: *Phys. Rev. D* 102.3 (2020), p. 035021. DOI: 10.1103/PhysRevD.102.035021. arXiv: 2006.16250 [hep-ph].

[256] Javier Fuentes-Martín et al. "Vector Leptoquarks Beyond Tree Level III: Vector-like Fermions and Flavor-Changing Transitions". In: *Phys. Rev. D* 102 (2020), p. 115015. DOI: 10.1103/PhysRevD.102.115015. arXiv: 2009.11296 [hep-ph].

[257] Javier Fuentes-Martin et al. "Flavor hierarchies, flavor anomalies, and Higgs mass from a warped extra dimension". In: (Mar. 2022). arXiv: 2203.01952 [hep-ph].

[258] Luca Di Luzio et al. "Maximal Flavour Violation: a Cabibbo mechanism for leptoquarks". In: *JHEP* 11 (2018), p. 081. DOI: 10.1007/JHEP11(2018)081. arXiv: 1808.00942 [hep-ph].

[259] Patrick J. Fox et al. "Deciphering top flavor violation at the LHC with B factories". In: *Phys. Rev. D* 78 (2008), p. 054008. DOI: 10.1103/PhysRevD.78.054008. arXiv: 0704.1482 [hep-ph].

[260] Bohdan Grzadkowski and Mikolaj Misiak. "Anomalous Wtb coupling effects in the weak radiative B-meson decay". In: *Phys. Rev. D* 78 (2008). [Erratum: Phys.Rev.D 84, 059903 (2011)], p. 077501. DOI: 10.1103/PhysRevD.78.077501. arXiv: 0802.1413 [hep-ph].

[261] Jure Drobnak, Svjetlana Fajfer, and Jernej F. Kamenik. "Probing anomalous tWb interactions with rare B decays". In: *Nucl. Phys. B* 855 (2012), pp. 82–99. DOI: 10.1016/j.nuclphysb.2011.10.004. arXiv: 1109.2357 [hep-ph].

[262] Joachim Brod et al. "Probing anomalous $t\bar{t}Z$ interactions with rare meson decays". In: *JHEP* 02 (2015), p. 141. DOI: 10.1007/JHEP02(2015)141. arXiv: 1408.0792 [hep-ph].

[263] Wolfgang Altmannshofer et al. "UV physics from IR features: New prospects from top flavor violation". In: *Phys. Rev. D* 107.9 (2023), p. 095025. DOI: 10.1103/PhysRevD.107.095025. arXiv: 2303.00781 [hep-ph].

[264] V. Cirigliano et al. "Constraining the top-Higgs sector of the Standard Model Effective Field Theory". In: *Phys. Rev. D* 94.3 (2016), p. 034031. DOI: 10.1103/PhysRevD.94.034031. arXiv: 1605.04311 [hep-ph].

[265] Stefan Bißmann et al. "Constraining top-quark couplings combining top-quark and $\boldsymbol{B}$ decay observables". In: *Eur. Phys. J. C* 80.2 (2020), p. 136. DOI: 10.1140/epjc/s10052-020-7680-9. arXiv: 1909.13632 [hep-ph].

[266] Stefan Bißmann et al. "Top and Beauty synergies in SMEFT-fits at present and future colliders". In: *JHEP* 06 (2021), p. 010. DOI: 10.1007/JHEP06(2021)010. arXiv: 2012.10456 [hep-ph].

[267] Roberto Franceschini. "Beyond-Standard-Model Physics Associated with the Top Quark". In: (Jan. 2023). arXiv: 2301.04407 [hep-ph].

[268] Elizabeth E. Jenkins, Aneesh V. Manohar, and Peter Stoffer. "Low-Energy Effective Field Theory below the Electroweak Scale: Operators and Matching". In: *JHEP* 03 (2018), p. 016. DOI: 10.1007/JHEP03(2018)016. arXiv: 1709.04486 [hep-ph].

[269] Alejandro Celis et al. "DsixTools: The Standard Model Effective Field Theory Toolkit". In: *Eur. Phys. J. C* 77.6 (2017), p. 405. DOI: 10.1140/epjc/s10052-017-4967-6. arXiv: 1704.04504 [hep-ph].

[270] Javier Fuentes-Martin et al. "DsixTools 2.0: The Effective Field Theory Toolkit". In: *Eur. Phys. J. C* 81.2 (2021), p. 167. DOI: 10.1140/epjc/s10052-020-08778-y. arXiv: 2010.16341 [hep-ph].

[271] Elizabeth E. Jenkins, Aneesh V. Manohar, and Michael Trott. "Renormalization Group Evolution of the Standard Model Dimension Six Operators I: Formalism and lambda Dependence". In: *JHEP* 10 (2013), p. 087. DOI: 10.1007/JHEP10(2013)087. arXiv: 1308.2627 [hep-ph].

[272] Elizabeth E. Jenkins, Aneesh V. Manohar, and Michael Trott. "Renormalization Group Evolution of the Standard Model Dimension Six Operators II: Yukawa Dependence". In: *JHEP* 01 (2014), p. 035. DOI: 10.1007/JHEP01(2014)035. arXiv: 1310.4838 [hep-ph].

[273] Johannes Braathen et al. "N-loop running should be combined with N-loop matching". In: *Phys. Rev. D* 97.1 (2018), p. 015011. DOI: 10.1103/PhysRevD.97.015011. arXiv: 1711.08460 [hep-ph].

[274] Wouter Dekens and Peter Stoffer. "Low-energy effective field theory below the electroweak scale: matching at one loop". In: *JHEP* 10 (2019). [Erratum: JHEP 11, 148 (2022)], p. 197. DOI: 10.1007/JHEP10(2019)197. arXiv: 1908.05295 [hep-ph].

[275] Jason Aebischer et al. "Matching of gauge invariant dimension-six operators for $b \to s$ and $b \to c$ transitions". In: *JHEP* 05 (2016), p. 037. DOI: 10.1007/JHEP05(2016)037. arXiv: 1512.02830 [hep-ph].

[276] Elizabeth E. Jenkins, Aneesh V. Manohar, and Peter Stoffer. "Low-Energy Effective Field Theory below the Electroweak Scale: Anomalous Dimensions". In: *JHEP* 01 (2018), p. 084. DOI: 10.1007/JHEP01(2018)084. arXiv: 1711.05270 [hep-ph].

[277] T. van Ritbergen, J. A. M. Vermaseren, and S. A. Larin. "The Four loop beta function in quantum chromodynamics". In: *Phys. Lett. B* 400 (1997), pp. 379–384. DOI: 10.1016/S0370-2693(97)00370-5. arXiv: hep-ph/9701390.

[278] J. A. M. Vermaseren, S. A. Larin, and T. van Ritbergen. "The four loop quark mass anomalous dimension and the invariant quark mass". In: *Phys. Lett. B* 405 (1997), pp. 327–333. DOI: 10.1016/S0370-2693(97)00660-6. arXiv: hep-ph/9703284.

[279] P. A. Baikov, K. G. Chetyrkin, and J. H. Kühn. "Five-loop fermion anomalous dimension for a general gauge group from four-loop massless propagators". In: *JHEP* 04 (2017), p. 119. DOI: 10.1007/JHEP04(2017)119. arXiv: 1702.01458 [hep-ph].

[280] K. G. Chetyrkin, Johann H. Kuhn, and M. Steinhauser. "RunDec: A Mathematica package for running and decoupling of the strong coupling and quark masses". In: *Comput. Phys. Commun.* 133 (2000), pp. 43–65. DOI: 10.1016/S0010-4655(00)00155-7. arXiv: hep-ph/0004189.

[281] A. V. Bednyakov, A. F. Pikelner, and V. N. Velizhanin. "Anomalous dimensions of gauge fields and gauge coupling beta-functions in the Standard Model at three loops". In: *JHEP* 01 (2013), p. 017. DOI: 10.1007/JHEP01(2013)017. arXiv: 1210.6873 [hep-ph].

[282] A. V. Bednyakov, A. F. Pikelner, and V. N. Velizhanin. "Yukawa coupling beta-functions in the Standard Model at three loops". In: *Phys. Lett. B* 722 (2013), pp. 336–340. DOI: 10.1016/j.physletb.2013.04.038. arXiv: 1212.6829 [hep-ph].

[283] A. V. Bednyakov, A. F. Pikelner, and V. N. Velizhanin. "Higgs self-coupling beta-function in the Standard Model at three loops". In: *Nucl. Phys. B* 875 (2013), pp. 552–565. DOI: 10.1016/j.nuclphysb.2013.07.015. arXiv: 1303.4364 [hep-ph].

[284] A. V. Bednyakov, A. F. Pikelner, and V. N. Velizhanin. "Three-loop SM beta-functions for matrix Yukawa couplings". In: *Phys. Lett. B* 737 (2014), pp. 129–134. DOI: 10.1016/j.physletb.2014.08.049. arXiv: 1406.7171 [hep-ph].

[285] Damir Bečirević, Gioacchino Piazza, and Olcyr Sumensari. "Revisiting $B \to K^{(*)}\nu\bar{\nu}$ decays in the Standard Model and beyond". In: *Eur. Phys. J. C* 83.3 (2023), p. 252. DOI: 10.1140/epjc/s10052-023-11388-z. arXiv: 2301.06990 [hep-ph].

[286] I. Adachi et al. "Evidence for $B^+ \to K^+\nu\bar{\nu}$ Decays". In: (Nov. 2023). arXiv: 2311.14647 [hep-ex].

[287] J. Grygier et al. "Search for $\boldsymbol{B \to h\nu\bar{\nu}}$ decays with semileptonic tagging at Belle". In: *Phys. Rev. D* 96.9 (2017). [Addendum: Phys.Rev.D 97, 099902 (2018)], p. 091101. DOI: 10.1103/PhysRevD.96.091101. arXiv: 1702.03224 [hep-ex].

[288] S. Choudhury et al. "Test of lepton flavor universality and search for lepton flavor violation in $B \to K\ell\ell$ decays". In: *JHEP* 03 (2021), p. 105. DOI: 10.1007/JHEP03(2021)105. arXiv: 1908.01848 [hep-ex].

[289] J. P. Lees et al. "A search for the decay modes $B^{+-} \to h^{+-}\tau^{+-}l$". In: *Phys. Rev. D* 86 (2012), p. 012004. DOI: 10.1103/PhysRevD.86.012004. arXiv: 1204.2852 [hep-ex].

[290] Roel Aaij et al. "Search for the lepton flavour violating decay $B^+ \to K^+\mu^-\tau^+$ using B^{*0}_{s2} decays". In: *JHEP* 06 (2020), p. 129. DOI: 10.1007/JHEP06(2020)129. arXiv: 2003.04352 [hep-ex].

[291] Roel Aaij et al. "Search for the Rare Decays $B^0_s \to e^+e^-$ and $B^0 \to e^+e^-$". In: *Phys. Rev. Lett.* 124.21 (2020), p. 211802. DOI: 10.1103/PhysRevLett.124.211802. arXiv: 2003.03999 [hep-ex].

[292] Roel Aaij et al. "Search for the decays $B^0_s \to \tau^+\tau^-$ and $B^0 \to \tau^+\tau^-$". In: *Phys. Rev. Lett.* 118.25 (2017), p. 251802. DOI: 10.1103/PhysRevLett.118.251802. arXiv: 1703.02508 [hep-ex].

[293] Roel Aaij et al. "Search for the lepton-flavour violating decays $\mathrm{B}^0_{(s)} \to e^{\pm}\mu^{\mp}$". In: *JHEP* 03 (2018), p. 078. DOI: 10.1007/JHEP03(2018)078. arXiv: 1710.04111 [hep-ex].

[294] Roel Aaij et al. "Search for the lepton-flavour-violating decays $B_s^0 \to \tau^\pm\mu^\mp$ and $B^0 \to \tau^\pm\mu^\mp$". In: *Phys. Rev. Lett.* 123.21 (2019), p. 211801. DOI: 10.1103/PhysRevLett.123.211801. arXiv: 1905.06614 [hep-ex].

[295] Eduardo Cortina Gil et al. "Measurement of the very rare $K^+ \to \pi^+\nu\overline{\nu}$ decay". In: *JHEP* 06 (2021), p. 093. DOI: 10.1007/JHEP06(2021)093. arXiv: 2103.15389 [hep-ex].

[296] A. V. Artamonov et al. "New measurement of the $K^+ \to \pi^+\nu\bar{\nu}$ branching ratio". In: *Phys. Rev. Lett.* 101 (2008), p. 191802. DOI: 10.1103/PhysRevLett.101.191802. arXiv: 0808.2459 [hep-ex].

[297] J. K. Ahn et al. "Search for the $K_L \to \pi^0\nu\overline{\nu}$ and $K_L \to \pi^0 X^0$ decays at the J-PARC KOTO experiment". In: *Phys. Rev. Lett.* 122.2 (2019), p. 021802. DOI: 10.1103/PhysRevLett.122.021802. arXiv: 1810.09655 [hep-ex].

[298] Roel Aaij et al. "Constraints on the $K_S^0 \to \mu^+\mu^-$ Branching Fraction". In: *Phys. Rev. Lett.* 125.23 (2020), p. 231801. DOI: 10.1103/PhysRevLett.125.231801. arXiv: 2001.10354 [hep-ex].

[299] Gino Isidori and Rene Unterdorfer. "On the short distance constraints from K(L,S) —> mu+ mu-". In: *JHEP* 01 (2004), p. 009. DOI: 10.1088/1126-6708/2004/01/009. arXiv: hep-ph/0311084.

[300] D. Ambrose et al. "New limit on muon and electron lepton number violation from K0(L) —> mu+- e-+ decay". In: *Phys. Rev. Lett.* 81 (1998), pp. 5734–5737. DOI: 10.1103/PhysRevLett.81.5734. arXiv: hep-ex/9811038.

[301] A. Alavi-Harati et al. "Search for the Decay $K_L \to \pi^0\mu^+\mu^-$". In: *Phys. Rev. Lett.* 84 (2000), pp. 5279–5282. DOI: 10.1103/PhysRevLett.84.5279. arXiv: hep-ex/0001006.

[302] A. Alavi-Harati et al. "Search for the rare decay K(L) —> pi0 e+ e-". In: *Phys. Rev. Lett.* 93 (2004), p. 021805. DOI: 10.1103/PhysRevLett.93.021805. arXiv: hep-ex/0309072.

[303] E. Abouzaid et al. "Search for lepton flavor violating decays of the neutral kaon". In: *Phys. Rev. Lett.* 100 (2008), p. 131803. DOI: 10.1103/PhysRevLett.100.131803. arXiv: 0711.3472 [hep-ex].

[304] Eduardo Cortina Gil et al. "Search for Lepton Number and Flavor Violation in K^+ and π^0 Decays". In: *Phys. Rev. Lett.* 127.13 (2021), p. 131802. DOI: 10.1103/PhysRevLett.127.131802. arXiv: 2105.06759 [hep-ex].

[305] Andrzej J. Buras and Elena Venturini. "The exclusive vision of rare K and B decays and of the quark mixing in the standard model". In: *Eur. Phys. J. C* 82.7 (2022), p. 615. DOI: 10.1140/epjc/s10052-022-10583-8. arXiv: 2203.11960 [hep-ph].

[306] Jason Aebischer et al. "SMEFT ATLAS of $\Delta F = 2$ transitions". In: *JHEP* 12 (2020), p. 187. DOI: 10.1007/JHEP12(2020)187. arXiv: 2009.07276 [hep-ph].

[307] Vincenzo Cirigliano et al. "Semileptonic tau decays beyond the Standard Model". In: *JHEP* 04 (2022), p. 152. DOI: 10.1007/JHEP04(2022)152. arXiv: 2112.02087 [hep-ph].

[308] Adam Falkowski, Martín González-Alonso, and Oscar Naviliat-Cuncic. "Comprehensive analysis of beta decays within and beyond the Standard Model". In: *JHEP* 04 (2021), p. 126. DOI: 10.1007/JHEP04(2021)126. arXiv: 2010.13797 [hep-ph].

[309] Yasmine Sara Amhis et al. "Averages of b-hadron, c-hadron, and τ-lepton properties as of 2021". In: *Phys. Rev. D* 107.5 (2023), p. 052008. DOI: 10.1103/PhysRevD.107.052008. arXiv: 2206.07501 [hep-ex].

[310] Jason Aebischer et al. "Effective field theory interpretation of lepton magnetic and electric dipole moments". In: *JHEP* 07 (2021), p. 107. DOI: 10.1007/JHEP07(2021)107. arXiv: 2102.08954 [hep-ph].

[311] Léo Morel et al. "Determination of the fine-structure constant with an accuracy of 81 parts per trillion". In: *Nature* 588.7836 (2020), pp. 61–65. DOI: 10.1038/s41586-020-2964-7.

[312] Richard H. Parker et al. "Measurement of the fine-structure constant as a test of the Standard Model". In: *Science* 360 (2018), p. 191. DOI: 10.1126/science.aap7706. arXiv: 1812.04130 [physics.atom-ph].

[313] T. Aoyama et al. "The anomalous magnetic moment of the muon in the Standard Model". In: *Phys. Rept.* 887 (2020), pp. 1–166. DOI: 10.1016/j.physrep.2020.07.006. arXiv: 2006.04822 [hep-ph].

[314] Tatsumi Aoyama et al. "Complete Tenth-Order QED Contribution to the Muon g-2". In: *Phys. Rev. Lett.* 109 (2012), p. 111808. DOI: 10.1103/PhysRevLett.109.111808. arXiv: 1205.5370 [hep-ph].

[315] Tatsumi Aoyama, Toichiro Kinoshita, and Makiko Nio. "Theory of the Anomalous Magnetic Moment of the Electron". In: *Atoms* 7.1 (2019), p. 28. DOI: 10.3390/atoms7010028.

[316] Andrzej Czarnecki, William J. Marciano, and Arkady Vainshtein. "Refinements in electroweak contributions to the muon anomalous magnetic moment". In: *Phys. Rev. D* 67 (2003). [Erratum: Phys.Rev.D 73, 119901 (2006)], p. 073006. DOI: 10.1103/PhysRevD.67.073006. arXiv: hep-ph/0212229.

[317] C. Gnendiger, D. Stöckinger, and H. Stöckinger-Kim. "The electroweak contributions to $(g-2)_\mu$ after the Higgs boson mass measurement". In: *Phys. Rev. D* 88 (2013), p. 053005. DOI: 10.1103/PhysRevD.88.053005. arXiv: 1306.5546 [hep-ph].

[318] Michel Davier et al. "Reevaluation of the hadronic vacuum polarisation contributions to the Standard Model predictions of the muon $g-2$ and $\alpha(m_Z^2)$ using newest hadronic cross-section data". In: *Eur. Phys. J. C* 77.12 (2017), p. 827. DOI: 10.1140/epjc/s10052-017-5161-6. arXiv: 1706.09436 [hep-ph].

[319] Alexander Keshavarzi, Daisuke Nomura, and Thomas Teubner. "Muon $g-2$ and $\alpha(M_Z^2)$: a new data-based analysis". In: *Phys. Rev. D* 97.11 (2018), p. 114025. DOI: 10.1103/PhysRevD.97.114025. arXiv: 1802.02995 [hep-ph].

[320] Gilberto Colangelo, Martin Hoferichter, and Peter Stoffer. "Two-pion contribution to hadronic vacuum polarization". In: *JHEP* 02 (2019), p. 006. DOI: 10.1007/JHEP02(2019)006. arXiv: 1810.00007 [hep-ph].

[321] Martin Hoferichter, Bai-Long Hoid, and Bastian Kubis. "Three-pion contribution to hadronic vacuum polarization". In: *JHEP* 08 (2019), p. 137. DOI: 10.1007/JHEP08(2019)137. arXiv: 1907.01556 [hep-ph].

[322] M. Davier et al. "A new evaluation of the hadronic vacuum polarisation contributions to the muon anomalous magnetic moment and to $\boldsymbol{\alpha(m_Z^2)}$". In: *Eur. Phys. J. C* 80.3 (2020). [Erratum: Eur.Phys.J.C 80, 410 (2020)], p. 241. DOI: 10.1140/epjc/s10052-020-7792-2. arXiv: 1908.00921 [hep-ph].

[323] Alexander Keshavarzi, Daisuke Nomura, and Thomas Teubner. "$g-2$ of charged leptons, $\alpha(M_Z^2)$, and the hyperfine splitting of muonium". In: *Phys. Rev. D* 101.1 (2020), p. 014029. DOI: 10.1103/PhysRevD.101.014029. arXiv: 1911.00367 [hep-ph].

[324] Alexander Kurz et al. "Hadronic contribution to the muon anomalous magnetic moment to next-to-next-to-leading order". In: *Phys. Lett. B* 734 (2014), pp. 144–147. DOI: 10.1016/j.physletb.2014.05.043. arXiv: 1403.6400 [hep-ph].

[325] Kirill Melnikov and Arkady Vainshtein. "Hadronic light-by-light scattering contribution to the muon anomalous magnetic moment revisited". In: *Phys. Rev. D* 70 (2004), p. 113006. DOI: 10.1103/PhysRevD.70.113006. arXiv: hep-ph/0312226.

[326] Pere Masjuan and Pablo Sanchez-Puertas. "Pseudoscalar-pole contribution to the $(g_\mu-2)$: a rational approach". In: *Phys. Rev. D* 95.5 (2017), p. 054026. DOI: 10.1103/PhysRevD.95.054026. arXiv: 1701.05829 [hep-ph].

[327] Gilberto Colangelo et al. "Dispersion relation for hadronic light-by-light scattering: two-pion contributions". In: *JHEP* 04 (2017), p. 161. DOI: 10.1007/JHEP04(2017)161. arXiv: 1702.07347 [hep-ph].

[328] Martin Hoferichter et al. "Dispersion relation for hadronic light-by-light scattering: pion pole". In: *JHEP* 10 (2018), p. 141. DOI: 10.1007/JHEP10(2018)141. arXiv: 1808.04823 [hep-ph].

[329] Antoine Gérardin, Harvey B. Meyer, and Andreas Nyffeler. "Lattice calculation of the pion transition form factor with $N_f = 2 + 1$ Wilson quarks". In: *Phys. Rev. D* 100.3 (2019), p. 034520. DOI: 10.1103/PhysRevD.100.034520. arXiv: 1903.09471 [hep-lat].

[330] Johan Bijnens, Nils Hermansson-Truedsson, and Antonio Rodríguez-Sánchez. "Short-distance constraints for the HLbL contribution to the muon anomalous magnetic moment". In: *Phys. Lett. B* 798 (2019), p. 134994. DOI: 10.1016/j.physletb.2019.134994. arXiv: 1908.03331 [hep-ph].

[331] Gilberto Colangelo et al. "Longitudinal short-distance constraints for the hadronic light-by-light contribution to $(g-2)_\mu$ with large-N_c Regge models". In: *JHEP* 03 (2020), p. 101. DOI: 10.1007/JHEP03(2020)101. arXiv: 1910.13432 [hep-ph].

[332] Thomas Blum et al. "Hadronic Light-by-Light Scattering Contribution to the Muon Anomalous Magnetic Moment from Lattice QCD". In: *Phys. Rev. Lett.* 124.13 (2020), p. 132002. DOI: 10.1103/PhysRevLett.124.132002. arXiv: 1911.08123 [hep-lat].

[333] Gilberto Colangelo et al. "Remarks on higher-order hadronic corrections to the muon g−2". In: *Phys. Lett. B* 735 (2014), pp. 90–91. DOI: 10.1016/j.physletb.2014.06.012. arXiv: 1403.7512 [hep-ph].

[334] Sz. Borsanyi et al. "Leading hadronic contribution to the muon magnetic moment from lattice QCD". In: *Nature* 593.7857 (2021), pp. 51–55. DOI: 10.1038/s41586-021-03418-1. arXiv: 2002.12347 [hep-lat].

[335] Christoph Lehner and Aaron S. Meyer. "Consistency of hadronic vacuum polarization between lattice QCD and the R-ratio". In: *Phys. Rev. D* 101 (2020), p. 074515. DOI: 10.1103/PhysRevD.101.074515. arXiv: 2003.04177 [hep-lat].

[336] Marco Cè et al. "The hadronic running of the electromagnetic coupling and the electroweak mixing angle from lattice QCD". In: *JHEP* 08 (2022), p. 220. DOI: 10.1007/JHEP08(2022)220. arXiv: 2203.08676 [hep-lat].

[337] Marco Cè et al. "Window observable for the hadronic vacuum polarization contribution to the muon g-2 from lattice QCD". In: *Phys. Rev. D* 106.11 (2022), p. 114502. DOI: 10.1103/PhysRevD.106.114502. arXiv: 2206.06582 [hep-lat].

[338] Gen Wang et al. "Muon g-2 with overlap valence fermions". In: *Phys. Rev. D* 107.3 (2023), p. 034513. DOI: 10.1103/PhysRevD.107.034513. arXiv: 2204.01280 [hep-lat].

[339] C. Alexandrou et al. "Lattice calculation of the short and intermediate time-distance hadronic vacuum polarization contributions to the muon magnetic moment using twisted-mass fermions". In: *Phys. Rev. D* 107.7 (2023), p. 074506. DOI: 10.1103/PhysRevD.107.074506. arXiv: 2206.15084 [hep-lat].

[340] G. Colangelo et al. "Data-driven evaluations of Euclidean windows to scrutinize hadronic vacuum polarization". In: *Phys. Lett. B* 833 (2022), p. 137313. DOI: 10.1016/j.physletb.2022.137313. arXiv: 2205.12963 [hep-ph].

[341] Christopher Aubin et al. "Muon anomalous magnetic moment with staggered fermions: Is the lattice spacing small enough?" In: *Phys. Rev. D* 106.5 (2022), p. 054503. DOI: 10.1103/PhysRevD.106.054503. arXiv: 2204.12256 [hep-lat].

[342] T. Blum et al. "An update of Euclidean windows of the hadronic vacuum polarization". In: (Jan. 2023). arXiv: 2301.08696 [hep-lat].

[343] Alexei Bazavov et al. "Light-quark connected intermediate-window contributions to the muon g-2 hadronic vacuum polarization from lattice QCD". In: *Phys. Rev. D* 107.11 (2023), p. 114514. DOI: 10.1103/PhysRevD.107.114514. arXiv: 2301.08274 [hep-lat].

[344] M. Davier et al. "The Euclidean Adler function and its interplay with $\Delta\alpha^{\rm had}_{\rm QED}$ and α_s". In: *JHEP* 04 (2023), p. 067. DOI: 10.1007/JHEP04(2023)067. arXiv: 2302.01359 [hep-ph].

[345] F. V. Ignatov et al. "Measurement of the $e^+e^- \to \pi^+\pi^-$ cross section from threshold to 1.2 GeV with the CMD-3 detector". In: (Feb. 2023). arXiv: 2302.08834 [hep-ex].

[346] Genessa Benton et al. "Data-driven determination of the light-quark connected component of the intermediate-window contribution to the muon $g-2$". In: (June 2023). arXiv: 2306.16808 [hep-ph].

[347] Michel Davier et al. "Hadronic vacuum polarization: comparing lattice QCD and data-driven results in systematically improvable ways". In: (Aug. 2023). arXiv: 2308.04221 [hep-ph].

[348] Antonio Pich. "Precision Tau Physics". In: *Prog. Part. Nucl. Phys.* 75 (2014), pp. 41–85. DOI: 10.1016/j.ppnp.2013.11.002. arXiv: 1310.7922 [hep-ph].

[349] A. M. Baldini et al. "Search for the lepton flavour violating decay $\mu^+ \to e^+\gamma$ with the full dataset of the MEG experiment". In: *Eur. Phys. J. C* 76.8 (2016), p. 434. DOI: 10.1140/epjc/s10052-016-4271-x. arXiv: 1605.05081 [hep-ex].

[350] U. Bellgardt et al. "Search for the Decay mu+ —> e+ e+ e-". In: *Nucl. Phys. B* 299 (1988), pp. 1–6. DOI: 10.1016/0550-3213(88)90462-2.

[351] Wilhelm H. Bertl et al. "A Search for muon to electron conversion in muonic gold". In: *Eur. Phys. J. C* 47 (2006), pp. 337–346. DOI: 10.1140/epjc/s2006-02582-x.

[352] Bernard Aubert et al. "Searches for Lepton Flavor Violation in the Decays tau+- —> e+- gamma and tau+- —> mu+- gamma". In: *Phys. Rev. Lett.* 104 (2010), p. 021802. DOI: 10.1103/PhysRevLett.104.021802. arXiv: 0908.2381 [hep-ex].

[353] K. Hayasaka et al. "Search for Lepton Flavor Violating Tau Decays into Three Leptons with 719 Million Produced Tau+Tau- Pairs". In: *Phys. Lett. B* 687 (2010), pp. 139–143. DOI: 10.1016/j.physletb.2010.03.037. arXiv: 1001.3221 [hep-ex].

[354] Y. Miyazaki et al. "Search for lepton flavor violating tau- decays into l- eta, l- eta-prime and l- pi0". In: *Phys. Lett. B* 648 (2007), pp. 341–350. DOI: 10.1016/j.physletb.2007.03.027. arXiv: hep-ex/0703009.

[355] Y. Miyazaki et al. "Search for Lepton-Flavor-Violating and Lepton-Number-Violating $\tau \to \ell hh'$ Decay Modes". In: *Phys. Lett. B* 719 (2013), pp. 346–353. DOI: 10.1016/j.physletb.2013.01.032. arXiv: 1206.5595 [hep-ex].

[356] A. Abdesselam et al. "Search for lepton-flavor-violating tau-lepton decays to $\ell\gamma$ at Belle". In: *JHEP* 10 (2021), p. 19. DOI: 10.1007/JHEP10(2021)019. arXiv: 2103.12994 [hep-ex].

[357] Bernard Aubert et al. "Search for Lepton Flavor Violating Decays $\tau^\pm \to \ell^\pm\pi^0$, $\ell^\pm\eta$, $\ell^\pm\eta'$". In: *Phys. Rev. Lett.* 98 (2007), p. 061803. DOI: 10.1103/PhysRevLett.98.061803. arXiv: hep-ex/0610067.

[358] Sacha Davidson et al. "Charged Lepton Flavor Violation". In: (Aug. 2022). arXiv: 2209.00142 [hep-ex].

[359] Andreas Crivellin et al. "Renormalisation-group improved analysis of $\mu \to e$ processes in a systematic effective-field-theory approach". In: *JHEP* 05 (2017), p. 117. DOI: 10.1007/JHEP05(2017)117. arXiv: 1702.03020 [hep-ph].

[360] A. M. Baldini et al. "The design of the MEG II experiment". In: *Eur. Phys. J. C* 78.5 (2018), p. 380. DOI: 10.1140/epjc/s10052-018-5845-6. arXiv: 1801.04688 [physics.ins-det].

[361] L. Bartoszek et al. "Mu2e Technical Design Report". In: (Oct. 2014). DOI: 10.2172/1172555. arXiv: 1501.05241 [physics.ins-det].

[362] K. Arndt et al. "Technical design of the phase I Mu3e experiment". In: *Nucl. Instrum. Meth. A* 1014 (2021), p. 165679. DOI: 10.1016/j.nima.2021.165679. arXiv: 2009.11690 [physics.ins-det].

[363] Alejandro Celis, Vincenzo Cirigliano, and Emilie Passemar. "Model-discriminating power of lepton flavor violating τ decays". In: *Phys. Rev. D* 89.9 (2014), p. 095014. DOI: 10.1103/PhysRevD.89.095014. arXiv: 1403.5781 [hep-ph].

[364] Vincenzo Cirigliano et al. "Charged Lepton Flavor Violation at the EIC". In: *JHEP* 03 (2021), p. 256. DOI: 10.1007/JHEP03(2021)256. arXiv: 2102.06176 [hep-ph].

[365] Tomas Husek, Kevin Monsalvez-Pozo, and Jorge Portoles. "Lepton-flavour violation in hadronic tau decays and $\mu - \tau$ conversion in nuclei". In: *JHEP* 01 (2021), p. 059. DOI: 10.1007/JHEP01(2021)059. arXiv: 2009.10428 [hep-ph].

[366] Swagato Banerjee et al. "Snowmass 2021 White Paper: Charged lepton flavor violation in the tau sector". In: (Mar. 2022). arXiv: 2203.14919 [hep-ph].

[367] Latika Aggarwal et al. "Snowmass White Paper: Belle II physics reach and plans for the next decade and beyond". In: (July 2022). arXiv: 2207.06307 [hep-ex].

[368] Adam Falkowski and David Straub. "Flavourful SMEFT likelihood for Higgs and electroweak data". In: *JHEP* 04 (2020), p. 066. DOI: 10.1007/JHEP04(2020)066. arXiv: 1911.07866 [hep-ph].

[369] Aielet Efrati, Adam Falkowski, and Yotam Soreq. "Electroweak constraints on flavorful effective theories". In: *JHEP* 07 (2015), p. 018. DOI: 10.1007/JHEP07(2015)018. arXiv: 1503.07872 [hep-ph].

[370] Patrick Janot and Stanisław Jadach. "Improved Bhabha cross section at LEP and the number of light neutrino species". In: *Phys. Lett. B* 803 (2020), p. 135319. DOI: 10.1016/j.physletb.2020.135319. arXiv: 1912.02067 [hep-ph].

[371] D. Barducci et al. "Interpreting top-quark LHC measurements in the standard-model effective field theory". In: (Feb. 2018). Ed. by Juan Antonio Aguilar-Saavedra et al. arXiv: 1802.07237 [hep-ph].

[372] Fabio Maltoni, Luca Mantani, and Ken Mimasu. "Top-quark electroweak interactions at high energy". In: *JHEP* 10 (2019), p. 004. DOI: 10.1007/JHEP10(2019)004. arXiv: 1904.05637 [hep-ph].

[373] Ilaria Brivio et al. "O new physics, where art thou? A global search in the top sector". In: *JHEP* 02 (2020), p. 131. DOI: 10.1007/JHEP02(2020)131. arXiv: 1910.03606 [hep-ph].

[374] Gauthier Durieux et al. "The electro-weak couplings of the top and bottom quarks — Global fit and future prospects". In: *JHEP* 12 (2019). [Erratum: JHEP 01, 195 (2021)], p. 98. DOI: 10.1007/JHEP12(2019)098. arXiv: 1907.10619 [hep-ph].

[375] Nathan P. Hartland et al. "A Monte Carlo global analysis of the Standard Model Effective Field Theory: the top quark sector". In: *JHEP* 04 (2019), p. 100. DOI: 10.1007/JHEP04(2019)100. arXiv: 1901.05965 [hep-ph].

[376] Sebastian Bruggisser et al. "The Flavor of UV Physics". In: *JHEP* 05 (2021), p. 257. DOI: 10.1007/JHEP05(2021)257. arXiv: 2101.07273 [hep-ph].

[377] Jacob J. Ethier et al. "Combined SMEFT interpretation of Higgs, diboson, and top quark data from the LHC". In: *JHEP* 11 (2021), p. 089. DOI: 10.1007/JHEP11(2021)089. arXiv: 2105.00006 [hep-ph].

[378] Víctor Miralles et al. "The top quark electro-weak couplings after LHC Run 2". In: *JHEP* 02 (2022), p. 032. DOI: 10.1007/JHEP02(2022)032. arXiv: 2107.13917 [hep-ph].

[379] Gauthier Durieux et al. "Snowmass White Paper: prospects for the measurement of top-quark couplings". In: *Snowmass 2021*. May 2022. arXiv: 2205.02140 [hep-ph].

[380] Jorge de Blas et al. "Global SMEFT Fits at Future Colliders". In: *Snowmass 2021*. June 2022. arXiv: 2206.08326 [hep-ph].

[381] Sebastian Bruggisser, Danny van Dyk, and Susanne Westhoff. "Resolving the flavor structure in the MFV-SMEFT". In: *JHEP* 02 (2023), p. 225. DOI: 10.1007/JHEP02(2023)225. arXiv: 2212.02532 [hep-ph].

[382] Tommaso Giani, Giacomo Magni, and Juan Rojo. "SMEFiT: a flexible toolbox for global interpretations of particle physics data with effective field theories". In: *Eur. Phys. J. C* 83.5 (2023), p. 393. DOI: 10.1140/epjc/s10052-023-11534-7. arXiv: 2302.06660 [hep-ph].

[383] Zahari Kassabov et al. "The top quark legacy of the LHC Run II for PDF and SMEFT analyses". In: *JHEP* 05 (2023), p. 205. DOI: 10.1007/JHEP05(2023)205. arXiv: 2303.06159 [hep-ph].

[384] Cornelius Grunwald et al. "More Synergies from Beauty, Top, Z and Drell-Yan Measurements in SMEFT". In: (Apr. 2023). arXiv: 2304.12837 [hep-ph].

[385] B. M. Gavela et al. "Analysis of General Power Counting Rules in Effective Field Theory". In: *Eur. Phys. J. C* 76.9 (2016), p. 485. DOI: 10.1140/epjc/s10052-016-4332-1. arXiv: 1601.07551 [hep-ph].

[386] J. de Blas et al. "Effective description of general extensions of the Standard Model: the complete tree-level dictionary". In: *JHEP* 03 (2018), p. 109. DOI: 10.1007/JHEP03(2018)109. arXiv: 1711.10391 [hep-ph].

[387] P. Arnan et al. "Probing low energy scalar leptoquarks by the leptonic W and Z couplings". In: *JHEP* 02 (2019), p. 109. DOI: 10.1007/JHEP02(2019)109. arXiv: 1901.06315 [hep-ph].

[388] Andreas Crivellin, Dario Müller, and Francesco Saturnino. "Leptoquarks in oblique corrections and Higgs signal strength: status and prospects". In: *JHEP* 11 (2020), p. 094. DOI: 10.1007/JHEP11(2020)094. arXiv: 2006.10758 [hep-ph].

[389] Valerio Gherardi, David Marzocca, and Elena Venturini. "Matching scalar leptoquarks to the SMEFT at one loop". In: *JHEP* 07 (2020). [Erratum: JHEP 01, 006 (2021)], p. 225. DOI: 10.1007/JHEP07(2020)225. arXiv: 2003.12525 [hep-ph].

[390] Georges Aad et al. "Search for new phenomena in pp collisions in final states with tau leptons, b-jets, and missing transverse momentum with the ATLAS detector". In: *Phys. Rev. D* 104.11 (2021), p. 112005. DOI: 10.1103/PhysRevD.104.112005. arXiv: 2108.07665 [hep-ex].

[391] Benedetta Belfatto, Revaz Beradze, and Zurab Berezhiani. "The CKM unitarity problem: A trace of new physics at the TeV scale?" In: *Eur. Phys. J. C* 80.2 (2020), p. 149. DOI: 10.1140/epjc/s10052-020-7691-6. arXiv: 1906.02714 [hep-ph].

[392] Vincenzo Cirigliano et al. "Beta-decay implications for the W-boson mass anomaly". In: *Phys. Rev. D* 106.7 (2022), p. 075001. DOI: 10.1103/PhysRevD.106.075001. arXiv: 2204.08440 [hep-ph].

[393] Tao Han et al. "WIMPs at High Energy Muon Colliders". In: *Phys. Rev. D* 103.7 (2021), p. 075004. DOI: 10.1103/PhysRevD.103.075004. arXiv: 2009.11287 [hep-ph].

[394] D. Dannheim et al. "Detector Technologies for CLIC". In: (). https://edms.cern.ch/document/2053288/.

[395] Richard D. Ball et al. "Parton distributions for the LHC Run II". In: *JHEP* 04 (2015), p. 040. DOI: 10.1007/JHEP04(2015)040. arXiv: 1410.8849 [hep-ph].

[396] J. Alwall et al. "The automated computation of tree-level and next-to-leading order differential cross sections, and their matching to parton shower simulations". In: *JHEP* 07 (2014), p. 079. DOI: 10.1007/JHEP07(2014)079. arXiv: 1405.0301 [hep-ph].

[397] Andrzej J. Buras et al. "$B \to K^{(*)}\nu\overline{\nu}$ decays in the Standard Model and beyond". In: *JHEP* 02 (2015), p. 184. DOI: 10.1007/JHEP02(2015)184. arXiv: 1409.4557 [hep-ph].

[398] Damir Bečirević, Olcyr Sumensari, and Renata Zukanovich Funchal. "Lepton flavor violation in exclusive $b \to s$ decays". In: *Eur. Phys. J. C* 76.3 (2016), p. 134. DOI: 10.1140/epjc/s10052-016-3985-0. arXiv: 1602.00881 [hep-ph].

[399] Kristof De Bruyn et al. "Branching Ratio Measurements of B_s Decays". In: *Phys. Rev. D* 86 (2012), p. 014027. DOI: 10.1103/PhysRevD.86.014027. arXiv: 1204.1735 [hep-ph].

[400] Kristof De Bruyn et al. "Probing New Physics via the $B_s^0 \to \mu^+\mu^-$ Effective Lifetime". In: *Phys. Rev. Lett.* 109 (2012), p. 041801. DOI: 10.1103/PhysRevLett.109.041801. arXiv: 1204.1737 [hep-ph].

[401] S. Aoki et al. "Review of lattice results concerning low-energy particle physics". In: *Eur. Phys. J. C* 77.2 (2017), p. 112. DOI: 10.1140/epjc/s10052-016-4509-7. arXiv: 1607.00299 [hep-lat].

[402] Gudrun Hiller and Martin Schmaltz. "Diagnosing lepton-nonuniversality in $b \to s\ell\ell$". In: *JHEP* 02 (2015), p. 055. DOI: 10.1007/JHEP02(2015)055. arXiv: 1411.4773 [hep-ph].

[403] Marco Ciuchini et al. "New Physics in $b \to s\ell^+\ell^-$ confronts new data on Lepton Universality". In: *Eur. Phys. J. C* 79.8 (2019), p. 719. DOI: 10.1140/epjc/s10052-019-7210-9. arXiv: 1903.09632 [hep-ph].

[404] Li-Sheng Geng et al. "Towards the discovery of new physics with lepton-universality ratios of $b \to s\ell\ell$ decays". In: *Phys. Rev. D* 96.9 (2017), p. 093006. DOI: 10.1103/PhysRevD.96.093006. arXiv: 1704.05446 [hep-ph].

[405] Wolfgang Altmannshofer et al. "Symmetries and Asymmetries of $B \to K^*\mu^+\mu^-$ Decays in the Standard Model and Beyond". In: *JHEP* 01 (2009), p. 019. DOI: 10.1088/1126-6708/2009/01/019. arXiv: 0811.1214 [hep-ph].

[406] Aoife Bharucha, David M. Straub, and Roman Zwicky. "$B \to V\ell^+\ell^-$ in the Standard Model from light-cone sum rules". In: *JHEP* 08 (2016), p. 098. DOI: 10.1007/JHEP08(2016)098. arXiv: 1503.05534 [hep-ph].

[407] Jason Aebischer, Andrzej J. Buras, and Jacky Kumar. "On the Importance of Rare Kaon Decays: A Snowmass 2021 White Paper". In: *Snowmass 2021*. Mar. 2022. arXiv: 2203.09524 [hep-ph].

[408] M. Misiak et al. "Updated NNLO QCD predictions for the weak radiative B-meson decays". In: *Phys. Rev. Lett.* 114.22 (2015), p. 221801. DOI: 10.1103/PhysRevLett.114.221801. arXiv: 1503.01789 [hep-ph].

[409] Michał Czakon et al. "The $(Q_7, Q_{1,2})$ contribution to $\overline{B} \to X_s\gamma$ at $\mathcal{O}(\alpha_s^2)$". In: *JHEP* 04 (2015), p. 168. DOI: 10.1007/JHEP04(2015)168. arXiv: 1503.01791 [hep-ph].

[410] Wouter Dekens et al. "Non-perturbative effects in $\mu \to e\gamma$". In: *JHEP* 01 (2019), p. 088. DOI: 10.1007/JHEP01(2019)088. arXiv: 1810.05675 [hep-ph].

[411] Martín González-Alonso, Jorge Martin Camalich, and Kin Mimouni. "Renormalization-group evolution of new physics contributions to (semi)leptonic meson decays". In: *Phys. Lett. B* 772 (2017), pp. 777–785. DOI: 10.1016/j.physletb.2017.07.003. arXiv: 1706.00410 [hep-ph].